

DOCTORAL THESIS

Detection of Changes in Tissue State with the Aid of Electromagnetic Interaction

Eiko Priidel

TALLINN UNIVERSITY OF TECHNOLOGY
DOCTORAL THESIS
51/2022

Detection of Changes in Tissue State with the Aid of Electromagnetic Interaction

EIKO PRIIDEL



TALLINN UNIVERSITY OF TECHNOLOGY
School of Information Technologies
Thomas Johann Seebeck Department of Electronics
This dissertation was accepted for the defence of the degree 09/06/2022

Supervisor: Professor Mart Min
School of Information Technologies
Tallinn University of Technology
Tallinn, Estonia

Co-supervisor: Dr. Jaan Ojarand
School of Information Technologies
Tallinn University of Technology
Tallinn, Estonia

Opponents: Prof. Dr. Eng. Jari Hyttinen
BioMediTech Unit, Faculty of Medicine and Health Technology
University of Tampere
Tampere, Finland

Assoc. Prof. Dr.-Ing. Daniel Teichmann
Center for Health Informatics and Technology
The Maersk Mc-Kinney Moller Institute
University of Southern Denmark
Odense, Denmark

Defence of the thesis: 09/09/2022, Tallinn

Declaration:

Hereby I declare that this doctoral thesis, my original investigation and achievement, submitted for the doctoral degree at Tallinn University of Technology has not been submitted for doctoral or equivalent academic degree.

Eiko Priidel

Signature



European Union
European Regional
Development Fund



Investing
in your future

Copyright: Eiko Priidel, 2022
ISSN 2585-6898 (publication)
ISBN 978-9949-83-889-9 (publication)
ISSN 2585-6901 (PDF)
ISBN 978-9949-83-890-5 (PDF)
Printed by Koopia Niini & Rauam

TALLINNA TEHNIKAÜLIKOOL
DOKTORITÖÖ
51/2022

Koe seisundi muutuste detekteerimine elektromagnetilise vastastikmõju abil

EIKO PRIIDEL



Contents

List of Publications.....	7
Author’s Contribution to the Publications.....	9
Abbreviations	10
Introduction	12
Overview of the Thesis Work.....	13
The Methodology Used in the Thesis	14
Objectives of the Thesis and Research Questions	15
Contributions of the Thesis	16
1 Measurement with Radio Waves	17
1.1 Continuous Wave Radar.....	17
1.2 Ultra Wide Band Radar.....	18
1.2.1 Experimental results with UWB radar and multisensory device.....	21
1.3 Summary of Chapter	24
2 Bioimpedance Sensing.....	25
2.1 Electrical Bioimpedance	25
2.1.1 Electrical impedance	25
2.1.2 Electrical model of the tissue	26
2.1.3 Electrical properties of biological tissue – dispersion regions	30
2.2 Measurement of the Electrical Bioimpedance	32
2.2.1 Impact of the measurement setup and environment	32
2.2.2 Impedance of electrodes.....	34
2.2.3 Electrode-tissue system	35
2.2.4 Instrumentation	36
2.3 Summary of Chapter	38
3 Detection of Bioimpedance Variations in Resource Constrained Environments	39
3.1 Basic Configurations for Impedance Measurements.....	39
3.2 Cardiorespiratory Activity Monitoring	39
3.2.1 The origin of the bioimpedance signal	41
3.2.2 Central aortic pressure of blood – detection and methods.....	42
3.3 Methods and a Device for Bioimpedance-based Cardiovascular Activity Monitoring.....	43
3.4 Summary of Chapter	49
4 Compact Impedance Analyzer (CIA)	50
4.1 Introduction	50
4.1.1 Commercially available analyzers.....	50
4.2 Developed Wearable Impedance Analyzer	51
4.2.1 The digital board of the analyzer.....	52
4.2.2 The analog board of the analyzer	54
4.2.3 Input signal path.....	55
4.2.4 Excitation signal path	56
4.2.5 Digital signal processing in the FPGA.....	57
4.3 Performance of Digital Board.....	61
4.4 Measurement Part Instrumentation	63

4.4.1 Initial calibration and corrections.....	64
4.4.2 Resolution and accuracy.....	66
4.5 Experimental Measurements of Bioimpedance	69
4.5.1 Capacitive electrodes	69
4.5.2 Excitation voltage control via digital feedback	74
4.6 Summary of Chapter	75
5 Magnetic Induction Based Measurement of Electrical Bioimpedance Variations	76
5.1 Introduction	76
5.1.1 The rationale for the investigation of electromagnetic induction methods	76
5.1.2 Methods of the Inductive coupling	76
5.1.3 Impact of magnetic cores.....	83
5.2 Excitation and Acquisition of the Response via Inductive Coupling	84
5.2.1 Impedance transformation via inductive coupling	84
5.2.2 Finding mutual inductance and coupling factor	86
5.2.3 Impedance transformation and sensitivity.....	88
5.2.4 Detection of the impedance change with a resonance circuit.....	92
5.3 Experimental Results with U-shaped and Rod Sensors	95
5.3.1 Detection of the impedance change with a U-shaped sensor	95
5.3.2 Experimental pulse sensing results with a rod-shaped sensor	96
5.4 Toroidal Sensor with a Closing Loop of the Induced Current	99
5.4.1 Measurement strategy.....	99
5.4.2 Experimental results obtained with the local closing loop method.....	100
5.5 Summary of Chapter	102
6 Conclusions.....	104
6.1 General Conclusions and Directions for Further Research.....	105
References.....	106
Acknowledgements	115
Abstract	116
Lühikokkuvõte	118
Appendix 1	121
Appendix 2	129
Appendix 3	135
Appendix 4	141
Appendix 5	151
Appendix 6	169
Curriculum vitae	176
Elulookirjeldus.....	177

List of Publications

The list of author's publications, on the basis of which the thesis has been prepared:

- I Priidel, E.; Land, R.; Sinivee, V.; Annus, P.; Min, M. (2017). Comparative Measurement of Cardiac Cycle by Means of Different Sensors. *IEEE Conference Proceedings, Lithuania, Palanga, 19–21 June, 2017: 21st International Conference ELECTRONICS 2017, Palanga, Lithuania from 19th to 21st June, 2017*. Palanga: IEEE Conference Publications, 1–5. DOI: [10.1109/ELECTRONICS.2017.7995221](https://doi.org/10.1109/ELECTRONICS.2017.7995221).
- II Annus, P.; Land, R.; Priidel, E.; Metshein, M.; Min, M.; Märtens, O. (2017). Quantization of the response signal differences for the electrical bioimpedance measurement. *EMBECE & NBC 2017: European Medical and Biological Engineering Conference (EMBECE) and the Nordic-Baltic Conference on Biomedical Engineering and Medical Physics (NBC)*. Ed. Eskola H., Väisänen O., Viik J., Hyttinen J. Springer, 290–293. (IFMBE Proceedings; 65). DOI: [10.1007/978-981-10-5122-7_73](https://doi.org/10.1007/978-981-10-5122-7_73).
- III Priidel, E.; Annus, P.; Metshein, M.; Land, R.; Märtens, O.; Min, M. (2018). Lock-in integration for detection of tiny bioimpedance variations. *BEC 2018: 16th biennial Baltic Electronics Conference : proceedings of the 16th biennial Baltic Electronics Conference : Tallinn University of Technology, October 8–10, Tallinn, Estonia: 2018 16th Biennial Baltic Electronics Conference (BEC), Tallinn, October 8–10*. IEEE. DOI: [10.1109/BEC.2018.8600965](https://doi.org/10.1109/BEC.2018.8600965).
- IV Priidel, E.; Annus, P.; Krivošei, A.; Rist, M.; Land, R.; Min, M.; Märtens, O. (2020). Methods for detection of bioimpedance variations in resource constrained environments. *Sensors*, 20 (5). DOI: [10.3390/s20051363](https://doi.org/10.3390/s20051363).
- V Annus, P.; Priidel, E.; Land, R.; Metshein, M.; Krivošei, A.; Min, M.; Ratasseppe, M.; Märtens, O. (2021). Automatic Detection of Real and Imaginary Parts of Electrical Impedance with Single Synchronous Demodulation Channel. In: *8th European Medical and Biological Engineering Conference (151–157)*. Springer, Cham. (IFMBE Proceedings; 80). DOI: [10.1007/978-3-030-64610-3_18](https://doi.org/10.1007/978-3-030-64610-3_18).
- VI E. Priidel, K. Pesti, M. Min, J. Ojarand and O. Martens (2021). FPGA-based 16-bit 20 MHz device for the inductive measurement of electrical bio-impedance, *2021 IEEE Int. Instrumentation and Measurement Technology Conference (I2MTC)*, Glasgow, Scotland, May 17–20, 2021, pp. 1–5. DOI: [10.1109/I2MTC50364.2021.9460073](https://doi.org/10.1109/I2MTC50364.2021.9460073)

In addition, author's other publications listed below are related to the current thesis. They cover some part of the research, contributing in frames of preliminary or supportive activities:

1. Min, Mart; Kõiv, Hip; Priidel, Eiko; Pesti, Ksenija; Annus, Paul (2019). Noninvasive Acquisition of the Aortic Blood Pressure Waveform. In: N. Nasiri (Ed.), *Wearable Devices*. London: IntechOpen, 19 pages.
2. Invention: Wearable bio-electromagnetic sensor and method of measuring physiological parameters of a body tissue; Owners: Tallinn University of Technology; Authors: Jaan Ojarand, Mart Min, Olev Märten, Raul Land, Eiko Priidel, Paul Annus; Priority number: US63/029,581 (USA), P202100015 (Estonia); Priority date: 25.05.2020
3. Invention: Method and device for quantization of the response signal differences during synchronous measurements; Owners: Tallinn University of Technology; Authors: Paul Annus, Mart Min, Raul Land, Olev Märten, Eiko Priidel, Margus Metshein; Priority number: P201700023 (Estonia), Patent EE05821B1 (EST), Pub. Date: 15.04.2020
4. Invention: Method and device for measuring complex transfer of an object; Owners: Tallinn University of Technology; Authors: Paul Annus, Raul Land, Mart Min, Olev Märten, Marek Rist, Eiko Priidel; Priority number: P201900031 (Estonia), Patent US20210190841A1 (USA); Pub. Date: 24.06.2021.

Author's Contribution to the Publications

Contribution to the papers in this thesis are:

- I. The author planned and performed the experiments. The author performed the computer simulations, processed and compared the obtained results. The author wrote the paper.
- II. The author performed the computer simulations, processed and compared simulation results.
- III. The author defined the research problem. The author performed the computer simulations, processed and compared simulation results. The author wrote the paper.
- IV. The author defined the research problem. The author performed the computer simulations, processed and compared simulation results. The author wrote the paper.
- V. The author performed the computer simulations, processed and compared simulation results.
- VI. The author defined the research problem. The author performed the computer simulations, processed and compared simulation results. The author wrote the paper.

Abbreviations

AC	Alternating Current
ADC	Analog to Digital Converter
BF	Body Floating
BIS	Bioimpedance Spectroscopy
CC	Current Carrying (electrode)
CIA	Compact Impedance Analyzer
CIC	Cascaded Integrator-Comb
CF	Cardiac Floating (electrode)
CMRR	Common-Mode Rejection Ratio
CORDIC	Coordinate Rotation Digital Computer
CW	Continuous Wave
DAC	Digital to Analog Converter
DC	Direct Current
DDS	Direct Digital Synthesis
DFT	Discrete Fourier Transform
DMA	Direct Memory Access
DSP	Digital Signal Processor
DUT	Device Under Test
EBI	Electrical Bioimpedance
ECF	Extracellular Fluid
ECG	Electrocardiography, Electrocardiogram
EEG	Electroencephalography
ENOB	Effective Number Of Bits
FFT	Fast Fourier Transform
FIR	Finite Impulse Response
FMCW	Frequency Modulated Continuous Wave
FPGA	Field-Programmable Gate Array
GPIO	General Purpose Input/Output
HPF	High Pass Filter
I2C	Inter-Integrated Circuit (bus)
IC	Integrated Circuit
ICF	Intracellular Fluid
INA	Instrumentation Amplifier
IS	Impedance Spectroscopy
IST	Impedance Spectrum-Tomography
LDO	Low-dropout regulator

LFSR	Linear Feedback Shift Register
LPF	Low Pass Filter
LSB	Least Significant Bit
LVDS	Low Voltage Differential Signaling
MCU	Micro Controller Unit
MLS	Maximum Length Sequence
MSPS	Million Samples Per Second
MUX	Multiplexer
NCO	Numerically-Controlled Oscillator
OPA	Operational Amplifier
OTA	Operational Trans-conductance Amplifier
PC	Personal Computer
PCB	Printed Circuit Board
PWM	Pulse Width Modulation
RMS	Root Mean Square
SFDR	Spurious-Free-Dynamic-Range
SMA	Sub-Miniature Version A (connector)
SNR	Signal to Noise Ratio
SPI	Serial Peripheral Interface bus
SPS	Samples Per Second
TDR	Time Domain Reflectometry
USB	Universal Serial Bus
UWB	Ultra Wide Band
VCCS	Voltage Controlled Current Source

Introduction

The Motivation for the Study

According to the World Health Organization, 15 million people suffer stroke worldwide each year. Of these, 5 million die and another 5 million are permanently disabled. Patients with head injuries need immediate care for survival. The two most common strokes – hemorrhagic and ischemic have similar symptoms but require different medical treatment. Therefore, distinguishing between them is necessary and wrong treatment can be fatal. Therapeutic yield is good within one hour after the onset of symptoms and declines rapidly during the next three hours.

The above means that the condition needs to be analyzed quickly and repeatedly monitored to apply the correct care procedures. Standard diagnostics methods for head injuries are CT (computed tomography) and MRI (magnetic resonance imaging), which lack mobility, are expensive, do not provide real-time results, use ionizing radiation and cannot be used for continuous monitoring. Ultrasound diagnostics devices provide real-time results and are portable, but ultrasound cannot penetrate the bone, making it impossible to diagnose brain damage. The detection method that has given promising simulation results is based on Ultra Wide Band (UWB) radar.

The European Society of Cardiology, the ESC, states that cardiovascular disease (CVD) accounts for over 3.8 million deaths yearly or 45% of all deaths across ESC member countries. The most common CVD, ischemic heart disease (IHD), was the leading cause, responsible for 1.7 million deaths (20% of all deaths), with stroke responsible for 970 391 deaths (11% of all deaths) [1]. The numbers are frightening and even more so, if the fact that 90% of heart attacks are preventable is considered [2]. Hypertension remains a significant public health challenge because it increases the risk for cardiovascular disease. The prevention and diagnosis of hypertension are of utmost importance. Unfortunately, the early detection of hypertension is complicated even today, and it is estimated that around 30% of the hypertensive population is unaware of their disease [3]. The World Health Organization webpage [4] states that high blood pressure (HBP) or hypertension is a “silent killer” because it has no apparent signs or symptoms to indicate that something is wrong. The best way to protect oneself is to be aware of the risks and change one’s lifestyle if necessary.

Assessments of the working of the human cardiovascular system have been one of the critical tasks of medicine. Better diagnostic means and methods and wearable devices are needed for ubiquitous early detection of cardiovascular disease.

Overview of the Thesis Work

This thesis introduces and analyzes non-invasive methods for continuous monitoring of cardio-respiratory activity parameters using electrical bioimpedance (EBI) and compact instrumentation, preferably suitable for wearable applications.

It is assumed that real-time information about minute ventilation (MV), tidal volume (TV), respiratory rate (RR), and heart rate (HR) is obtained from the curves of the electrical bioimpedance (EBI) changes. Moreover, also central aortic blood pressure (CAP) curve may be acquired from the EBI variations related to heart activity [5]–[8].

The following topics were focused on to carry out the research.

First, the feasibility of contactless monitoring with radio waves using UWB radar is investigated. A contactless method is preferred as it allows continuous monitoring without disturbing the subject and avoids potential injuries by long-term contacts with electrodes. Additionally, benefiting from good spatial resolution and radio wave partial penetration into the tissue could potentially allow the detection of tumors and hematomas.

Second, the background of electrical bioimpedance (EBI) measurement is studied, focusing on the aspects whose impact has not yet been sufficiently considered in numerous previous works. Those aspects are selecting an adequate electrical model, dependence of measurement results on the surrounding environment and selected measurement solution. Based on the analysis of named aspects, the requirements for a new impedance analyzer have been prepared.

Third, a solution for the wearable low-energy device is investigated. The main research was about minimizing hardware (HW) requirements and computational power. This solution uses contact measurement of EBI changes with Ag/AgCl electrodes. Known problems with contact electrodes as long-term instability, long transient process, inconvenient attachment to the skin and mechanical instability are discussed.

Fourth, introduction and justification of the novel compact impedance analyzer (CIA) design, including issues of the calibration and correction of the influence of the connection cables. Analysis of EBI measurement results obtained with CIA using capacitive electrodes on the left forearm, including separation of spectra of model components and presentation of cardiovascular activity detection results based on EBI changes.

Fifth, the feasibility of implementing sensors with inductive coupling for detecting cardiac activity-related signals on a forearm is investigated, including an analysis of the sensitivity of different inductive sensor designs, allowing the determination of their optimal parameters and limiting factors. In addition, a novel sensor solution with the flexible toroidal ferrite core employing additional electrodes closing the induced current loop is presented.

The research started with describing the object's model and measurement solutions, followed by the simulation of model parameter changes and analysis of obtained results.

The LabVIEW software environment was mainly used for calculations and presentation of results, PSpice software MicroCap 12 for circuit modeling and Comsol Multiphysics software package for simulation of electromagnetic field (EMF).

The results of modeling and simulations were validated with experimental ones. The bottlenecks of the solutions and the issues that need further research were identified.

The Methodology Used in the Thesis

A non-invasive method for monitoring cardio-respiratory activity parameters using electrical bioimpedance (EBI) has been studied for over a hundred years [9]–[11], and it has remained particularly relevant in recent years [12]–[14]. When an alternating current (AC) electromagnetic field (EMF) stimulation (later here – excitation) is applied to the body, the current in the organs and tissues depends on their electrical complex impedance. The changes in tissue state, e.g., when the lung fills with air or the heart fills with blood, cause the impedance changes of the corresponding body part. In addition, the expansion and contraction of blood vessels in the heart's rhythm (changes in the pulse volume) affect the impedance of the tissue. Thus, by observing the change in impedance of a given body part, some conclusions can be drawn about the state of that body part.

In order to associate the tissue properties with their impedance, it is necessary to use an electrical equivalent circuit model, or shortly, its electrical model. Many different versions have been proposed over time, but in our case, where mainly impedance changes are of interest, the classic model with two resistors and one capacitor (see section 2.1.2) has been used. However, as explained in the second chapter, the capacitor must be replaced by a constant phase element (CPE) for a more accurate result.

If the impedance is measured with electrodes, their electrical model must be considered. In addition, parasitic impedances due to the measuring instrument connected to the object must be involved. As explained in the second chapter, the electrodes' impedance and parasitic impedances significantly affect the measurement result, and their impacts are difficult to separate from the information-carrying signals. One of the aims of the present study was to minimize these impacts: firstly, by using the contactless method and secondly, by reducing parasitic impedances by developing a galvanically isolated and compact measuring instrument – the compact impedance analyzer (CIA).

Electrical impedance spectroscopy (EIS), with the frequency range covering the area where significant changes due to the object occur, allows finding the values of elements of the model [15]–[21]. Tissue models' parameters (intracellular resistance, capacitance of the cell membranes, and extracellular resistance) are then found by fitting the models and measured data of complex spectra.

As the main aim of the research was monitoring of the cardio-respiratory activity parameters, based on the changes of EBI, the highest accuracy of EBI spectra measurements was not the goal. Moreover, EBI changes over time are usually monitored on only one frequency which is better suited to the chosen solution. The criteria for selecting the frequency are mainly the sensitivity and the repeatability of measurement results.

However, the data of the whole impedance spectra are also necessary because, through these, the impedance and its changes found at a single frequency can be related to the object model and associate the change in impedance with a specific object parameter (e.g., extracellular resistivity). Unfortunately, these relationships are not unique, as several model parameters usually change simultaneously and may mask each other, as shown in subsections 4.5.1 and 5.2.3. The detailed analysis of this problem is outside the scope of the current study. However, more accurate impedance spectra measurement is still the goal since it opens up better possibilities for analysis.

Objectives of the Thesis and Research Questions

The goal of the thesis is to gain knowledge and provide recommendations for developing a sensor device for the continuous monitoring of cardio and respiratory activity parameters, including the design of wearable devices for that.

The main tasks of the thesis to be solved for the development of efficient wearable devices:

- A. To test the capabilities of UWB radar for cardiorespiratory measurement, considering the suppressing of sensitivity to movement artifacts and finding the excitation method for best spatial resolution for the detection of tumors and hematomas.
- B. To find the ways and measurement methods to optimize power consumption and computational power requirements in detecting EBI changes with non-polarizable electrodes.
- C. To develop a compact battery-powered impedance analyzer (CIA) with wireless data transmission capable of determining EBI model parameters and their changes at least in 10 MHz frequency range with a 16-bit resolution.
- D. To test the feasibility of detecting and monitoring cardiac activity-related signals on a forearm with capacitive and inductive sensors using the developed CIA.

The research questions raised in the thesis and answered on the bases of experimental and modeling results are the following:

1. What are the capabilities of UWB radar sensors, and can they be used to detect tumors and hematomas?
2. How to minimize the complexity, power consumption and computational power requirements in the case of detecting EBI changes with non-polarizable electrodes?
3. How to build a sensitive and compact battery-powered impedance analyzer (CIA) to determine EBI model parameters and their changes in a human body at least in the 10 MHz frequency range?
4. What is the SNR and accuracy of developed CIA, how to calibrate it and how to correct the influence of connection cables?
5. What are the EBI model parameters obtained from the forearm?
6. How the sensitivity of the detection of impedance changes depends on the design and other properties of sensors with inductive coupling?
7. Is radial artery blood pulsation monitoring feasible with the inductive or capacitive sensors placed on a wrist?

Contributions of the Thesis

The present work focuses on developing non-invasive sensors, including wearable devices, intended for monitoring cardio-respiratory activity parameters based on radio wave and electrical bioimpedance (EBI) measurements on the human body. The main contributions of thesis work summarized by chapters are as follows:

1. The study of the feasibility of monitoring of cardio-respiratory activity and the detection of tumors and hematomas using the UWB radar technology:
 - Comparison and analysis of the properties of known solutions.
 - Design and comparison of UWB antennas.
 - Analysis of spatial resolution of the solution.
2. The study of the background of electrical bioimpedance (EBI) measurement:
 - Introduction of the historical background of the emergence of three-element EBI equivalent circuit models with examples of transformations that highlight their non-equivalence.
 - Comparison of the influence of the constant phase element (CPE) and capacitance on impedance, including demonstration of resulting spectral errors and changes in model parameters when replacing CPE with a capacitance.
 - Explanation of the impact of stray impedances in the case of stationary and battery-powered measurement instruments along with experimental stray impedances data.
 - Determination of requirements and solutions for the impedance measurement instrumentation in the β dispersion area and for detecting impedance changes.
3. The study of the feasibility of measurement and monitoring of cardio-respiratory activity with contact electrodes method and proposed optimized but straightforward hardware design and the reduced signal processing method.
4. Presentation and justification of the design of the developed compact impedance analyzer (CIA), including:
 - Determination of required parameters of CIA and presentation of the solution.
 - Presentation and justification of the impedance measurement solution, including calibration and correction of the impact of connection cables.
 - Analysis of EBI measurement results obtained with capacitive electrodes, including separation of spectra of model components and their weight in the impedance spectrum.
 - Presentation of cardiovascular activity detection results based on EBI changes measured with capacitive electrodes on the left forearm.
5. The study of the feasibility of implementation of inductive sensors for detecting cardiac activity-related signals on a forearm, including:
 - Analysis of the sensitivity of inductive sensor designs allowing the determination of their optimal parameters and limiting factors.
 - Proof of the analysis results with practical experiments.
 - Presentation of the novel sensor solution with the flexible toroidal ferrite core employing additional electrodes closing the induced current loop.

1 Measurement with Radio Waves

Ultra Wide Band (UWB) technology is an emerging technology that has been gaining more and more popularity in recent years. Because of some unique and attractive features, UWB signals can be used for medical diagnostics, measuring properties of various materials, high-speed communication and radars. UWB technology was used exclusively in military applications before 2001, when commercial usage was allowed in USA and 2007 in the EU followed by intensive research activities. UWB signals have some unique properties compared to continuous wave signals – the ability to share frequency spectrum, ability to work in low signal-to-noise (SNR) conditions, high performance in multipath channels, superior material penetration properties, high spatial resolution, very low electromagnetic radiation, simple transceiver architecture, and finally – low energy consumption [22]. Main applications in medicine are as follows: cardiac biomechanics assessment, chest movements assessment, OSA (obstructive sleep apnoea) monitoring, soft-tissue biomechanics research, heart imaging ('Holter type' echocardiography), chest imaging, cardiac monitoring, respiratory monitoring, SIDS (sudden infant death syndrome) monitors, breast cancer and brain hematoma diagnosing and 3D imaging [23]–[25]. As UWB signals are non-ionizing, these can be used for long-term non-invasive monitoring without adverse effects. The working principle of UWB radar enables the measurement of electromagnetic impulse reflections from body tissue boundaries. The reflected signal is analyzed in the framework of the Time Domain Reflectometry theory [26]. However, Staderini states in his research that deep echo reflections from the tissues does not seem to be a realistic explanation of the phenomenon and at the moment, no hypothesis can be eventually accepted for explaining UWB medical radar operation [27]. Although numerous publications about propagation characteristics are available, these do not give reliable evidence of what is actually measured. UWB echo can also be interpreted in the frequency domain; however, not much research is done in this field in spite of being a promising method to analyze tissue properties.

1.1 Continuous Wave Radar

Continuous wave (CW) radars have been used for detecting cardio-pulmonary activities since the 1970s [28]. It is the simplest radar-based measurement method using Doppler effect and working reliably in an open environment. However, CW radar has disadvantages – the inability to measure distance and distinguish more than one person. The distance can be measured with another type of CW radar – frequency modulated continuous wave (FMCW) radar – but it still cannot measure vital signs if more than one person is present. Also, both radars have problems in environments where reflected signals are present. Radio wave reflections from room walls or furniture can lead to poor measurement accuracy or measurement failure. These problems are solved in UWB radars. UWB radar has a good spatial resolution, is insensitive to the reflected signals, can measure distance and can measure more than one person simultaneously. Compared to FMCW radar, UWB radar has better accuracy and signal-to-noise ratio [29].

1.2 Ultra Wide Band Radar

Ultra wide band radar generates short pulses, which are radiated through the antenna towards the body. The short impulse spreads transmitted energy over wide frequency band giving good material penetration and spatial resolution [30]. Electromagnetic energy propagating into and through the body is reflecting from the tissue interfaces due to the different relative dielectric constant of the organs. The reflection coefficient is determined by the following formula:

$$\Gamma = \frac{\sqrt{\epsilon_{r1}} - \sqrt{\epsilon_{r2}}}{\sqrt{\epsilon_{r1}} + \sqrt{\epsilon_{r2}}} \quad (1.1)$$

The attenuated and reflected energy from the organ boundaries is received by the antenna, and the boundary location is calculated based on the time difference between the transmitted and received signal [31]. Reflected signal attenuation values are shown in Fig. 1.1.

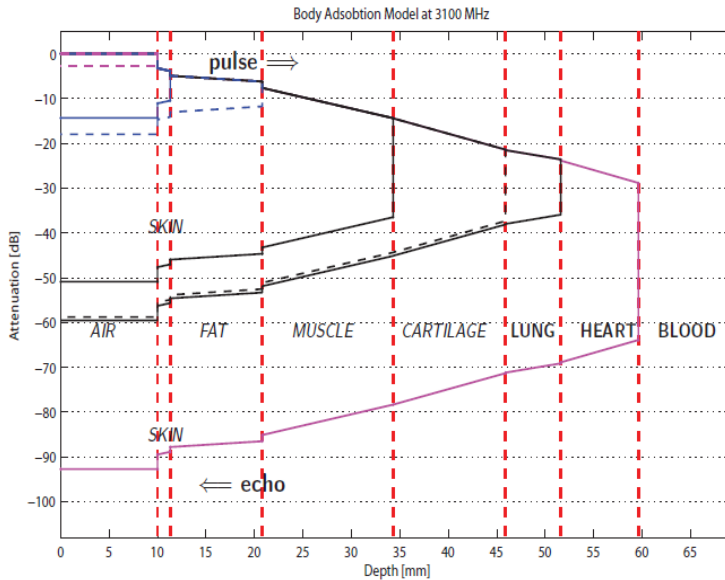


Fig. 1.1. Signal attenuation in different body tissues [27].

This effect allows relatively easy monitoring of breathing activity and heart rate, even from long distances [32]. The difference between the permittivity of brain tissue and hematoma is sufficient to detect a reflected signal from the hematoma area. UWB signals are non-ionizing, allowing continuous patient monitoring and evaluation of treatment progress. The most important reason for having the device in the intensive care unit (ICU) is that the patient would need to be moved to the radiology department as seldom as possible.

The diagnosis, based on measuring microwave scattering parameters, has been evaluated, and the first clinical tests have been conducted [33]. This method gave promising results but requires a helmet which is not a good solution in the case of head injuries and does not give any information about stroke location. Similar methods have

been used for breast cancer diagnosis and are already in clinical test phases [34]. There are numerous researches in breast cancer detection using UWB impulse radars with very promising results. The time-domain analysis makes radar imaging and reconstruction of 3D structure possible. However, detecting breast cancer is less complicated than detecting anomalies in the brain as there is no bone layer in the signal path, and antenna matching problems can be partly solved by the liquid interface between antenna array and skin. Most of the research in breast cancer and brain hematoma detection is done by modeling or based on a simulated environment because of the complexity of the real imaging system. A few teams have built a UWB imaging system for experiments with phantom models of the tissue layers or conducted tests with biological material. Good head phantoms are challenging to build as they consist of multiple layers which have to match with bone and tissue relative permittivity and conductance properties simultaneously. A few models are designed with gelatine/sugar mixture [35] and agar/NaCl/polyethylene mixture [36], but both lack skin and bone layer. The results from actual measurements are currently not as accurate as predicted in simulations showing UWB radar capability to find tumors and hematomas with sizes up to 5mm in the white matter close to the skull [37] and 30mm from deeper regions [38].

One of the challenges in UWB tomography is antenna design. Antenna properties that are not relevant in the case of narrowband radar antennas have a significant impact on signal quality in UWB radars. The largest problematics encountered in today's UWB antennas is that characterization methods were, since the beginning, meant to describe narrowband antennas. The frequency characteristics of these antennas are constant over their operational bandwidth; hence they can be fully characterized in the frequency domain. UWB antennas, on the other hand, are meant to transmit pulsed signals. Analyzing them only in the frequency domain is not enough to fully evaluate their performance, as pulse distortion is an important parameter that should be controlled [39]. Antenna dispersion, group delay, impulse response, bandwidth and impedance matching a wide frequency range, and also antenna ringing are the parameters that have to be optimized and a trade-off between them considered. In case the antenna arrays are used for tomography applications, the antenna size is also an essential property. Antenna size depends on the used maximum wavelength, but the use of higher frequencies is feasible as the signal attenuation in tissues is too high. One potential solution for antenna miniaturization is the usage of metamaterials [40].

Antenna ringing properties are of limiting factor in close-range operations – a new type of fractal antenna is showing promising results in decreasing ringing duration. Antenna design for medical applications differs from free-space operations design as there are strong reflections from the boundary of air and human skin, which means that a good body matching must be achieved [35]. Antenna crosstalk and reduction of reflections from early interfaces have a significant impact on the receiver design and have to be optimized to receiver saturation and dynamic range parameters [41]. Early interface reflections can be minimized by controlling the dielectric properties of the antenna's surrounding environment. Antenna systems where the antenna is immersed in distilled water or molded to the high dielectric permittivity ceramics are studied and finished with positive results [42].

UWB radar differs from CW radar in many aspects, but the main difference is that the UWB transmitter generates a single extremely short impulse instead of a longer duration carrier. Impulse lengths differ depending on requirements for the center frequency of the emitted spectrum. Usually, the impulse lengths are in the range of tens of picoseconds up

to a few nanoseconds. The nanosecond range is mainly used for ground penetrating radar applications. Picosecond range impulses give millimeter range spatial resolution, but their energy concentrates to the frequency range of tens of gigahertz. Such a high frequency will be attenuated in human tissue and cannot be used for medical UWB tomography.

The main research field in UWB transmitters' area is impulse generation methods. Commercial chips are not available, and the standard approach is to use specific semiconductor devices like tunneling diodes, step recovery diodes, avalanche transistors, and nonlinear transmission lines, to name a few. The aim of the research is to generate single ultra-short impulses with high repetition rate, high amplitude and low ringing properties. Avalanche transistor-based generators can achieve high amplitude, but impulse duration is relatively long, SRD diode based generators are capable of generating sub-nanosecond impulses, which are quite suitable for medical radars [43]. Nonlinear Transmission Line (NLTL) impulse formers are capable of even shorter pulses but are complex and challenging to build [44]. Another promising approach is to use silicon-germanium (SiGe) based logic gates which have become commercially available lately. The problem with these devices is low signal amplitude, so the impulse must be amplified to make it usable for medical radars. Demands for amplifier parameters are high and difficult to achieve – amplifier bandwidth is extremely wide, and impulse distortions, especially ringing, are not allowed. However, impulse generation flexibility and controllability make that kind of generator attractive and allow digital formation of impulse patterns.

Demands for radar receiver are mainly related to sensitivity, bandwidth, saturation, dynamic range and low sensitivity to the interfering signals. The usual approach in time gating receivers is based on T. E. McEwan proposed topology [45]. The reflected signal from the body gets highly attenuated, and the signal's recovery is often based on correlation.

Time gating correlation receivers [46] are a common approach in UWB radars, but better performance can be achieved with MLS sequence [47], [48]. Using SiGe-based logic chips makes it possible to design transmitters using codes with good autocorrelation properties, like Barker or Golay codes. Short chirp signals or frequency modulated continuous waves (FMCW) are also studied, giving promising results for UWB radar receivers [41].

Received signal suffers from high attenuation and unwanted reflections; therefore, signal processing algorithms must be used to compensate for motion artifacts and reflections from air-skin interfaces. Unwanted reflection methods are usually based on reference target measurements, but in medical diagnostics, the reference targets cannot be used as patients are different. One possible skin and clutter removal method is described in [49] as well as Hilbert transform and wavelet-based filtering for the received signal are usable. Two other potential skin artifact removal methods – the background subtraction and the Wiener filter are described in [50]. Signal analysis and possible 2D or 3D image reconstruction is a process of solving a classical inverse problem used for reconstructing tomographic images from a measured projection or scattering data. Several methods are simulated for the detection of intracranial hemorrhage. A confocal image processing algorithm based on delay and sum approach was proposed in [51] and the UWB synthetic aperture radar based on the time-domain global back-projection technique given in [52]. The image processing method for evaluating hemorrhage development was proposed in [53], based on the TSVD algorithm.

1.2.1 Experimental results with UWB radar and multisensory device

Three main sensory units – an electrocardiography amplifier (3-lead type), multisensory device and UWB radar – were used in the experiment. The multisensory device is designed to measure heart sounds, skin reflectivity in two wavelengths and acceleration forces in 3D space. Acceleration sensor output is an analog type and digitized by a microcontroller in the sensory board. Skin reflectivity measurement results together with acceleration information are transferred to the PC in digital form. The UWB radar and ECG output signals, together with audio channel output, are obtained in an analog form. Multisensory device based on a single board with the size of 15mm, shown in Fig. 1.2.

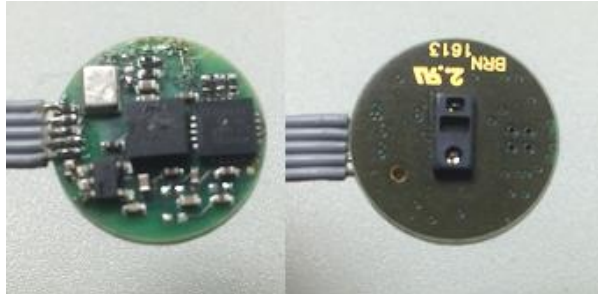


Fig. 1.2. Multisensory device's top and bottom side. The bottom side SpO2 sensor is in contact with the skin.

The basic UWB radar working principle is that electromagnetic energy propagating towards and through the body is reflecting from the tissue interfaces due to the different relative dielectric constant of the organs. Attenuated and reflected energy from the organ boundaries is received by the antenna, and boundary location is calculated based on the time difference between transmitted and received signals [43].

In this work, UWB radar, see Fig. 1.3, was developed and used for contactless cardio-respiratory monitoring. The measurement distance was 50 cm from the chest. ECG electrode stickers were used to attach the multisensory device to the chest in the position of the heart. The measurement setup is shown in Fig. 1.4.

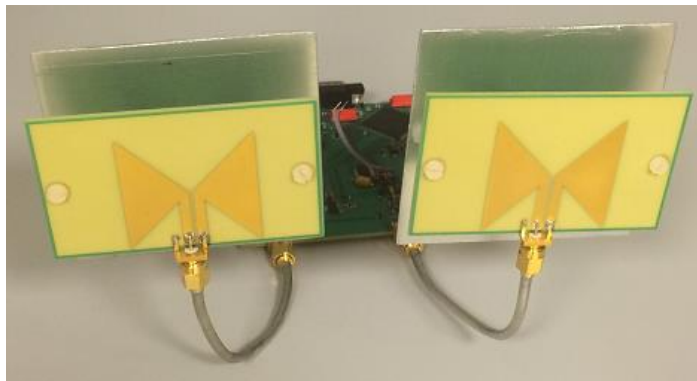


Fig. 1.3. UWB radar setup with two "Bow-Tie" type antennas is shown.

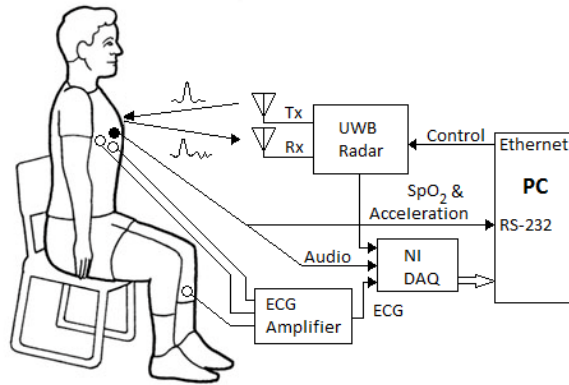


Fig. 1.4. Measurement set-up illustrating sensor positions and connections.

Antennas have a significant impact on the performance of the UWB radar, especially in the short range where antenna ringing has to be minimized. Several antennas were made, fig. 1.5, and their performance measured. Best results were obtained with a “Bow-Tie” type antenna, also used in the experiment.

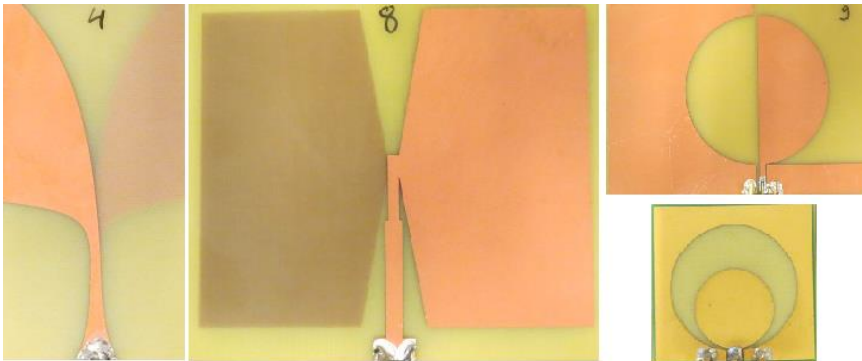


Fig. 1.5. Selection of designed UWB antennas.

The radar output signal expresses the reflected signal power from the set distance of the radar antenna. The distance can be set by adjusting the radar time gating delay. Consequently, the radar sensitivity point can be tuned to the needed distance from the antenna. The typical biomedical radar output signal is in good correlation with heartbeat and respiration activities. The sample output signal from vital sign monitoring is shown in Fig. 1.6.



Fig. 1.6. Medical radar output waveform. Measured with 12-bit ADC from a distance of 90 cm. Breath is held in the beginning, followed by one deep respiratory cycle.

As seen in Fig. 1.6, heartbeat and breathing signal is measured with a good signal-to-noise ratio.

Next, reflection measurements were conducted to evaluate radar spatial resolution and quality of distinguishing objects with different permittivity values. A two-layer head phantom was used in the experiment, mimicking skin and bone layers, and two reflective metallic targets spaced 6 cm from each other. Hematoma's permittivity is much lower than the metallic target resulting in lower response amplitude. Metallic targets were used in initial tests to verify measurement system functionality. Results from initial tests did not show expected performance – the spatial resolution was relatively poor as from a distance between targets less than 30 mm, it was impossible to distinguish targets from each other. The reason for that was too long excitation impulse from radar, but shorter impulses shifted output spectrum to higher frequencies where phantom attenuation was too high for measurements resulting very weak reflected signal. Measurement results from the reflection test are shown in Fig. 1.7.

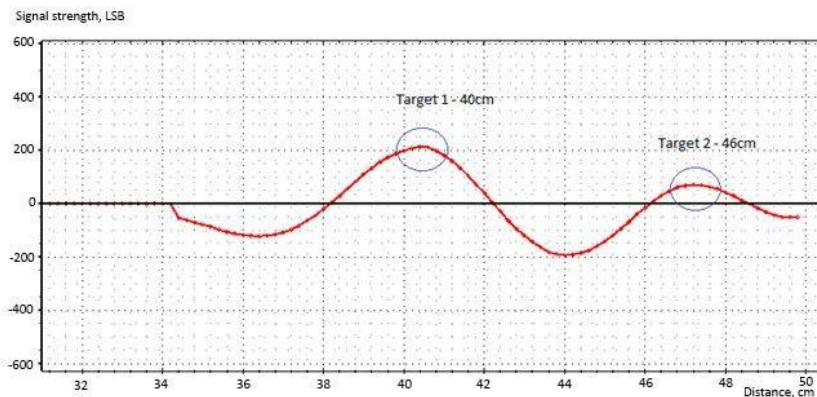


Fig. 1.7. The measured signal from two targets in phantom.

Experiment results lead to the conclusion that UWB radar can be efficiently used for cardiovascular and respiratory contactless monitoring but detecting body layer boundaries or hematomas is a challenging task. The main reason is the high attenuation of short impulse (higher frequency spectrum) required for good spatial resolution. Longer impulses with better tissue penetration lead to poor spatial resolution.

1.3 Summary of Chapter

Chapter 1 focuses on the principles of detecting changes in tissue by using radio waves. Cardio-pulmonary activity causes changes in tissue properties which are detectable with the aid of radio waves reflected or passing through the tissue. Acquired signals can be used to measure heart rate, respiratory activity or irregularities in the tissue.

Working principles of the CW, FMCW and UWB radars were discussed. Challenges in different research areas like ultra-short pulse generators, transmitters, receivers, antennas and signal processing are covered.

The work in the first chapter aimed to study the feasibility of measurement and monitoring of cardio-respiratory activity and the detection of tumors and hematomas using the UWB radar technology. For that, experiments and analysis were carried out with UWB radar and supporting sensors to test the capabilities of UWB radar for cardio-respiratory measurement and find the excitation method and antennas for the best spatial resolution for detecting tumors and hematomas.

An experimental multisensory device and UWB radar were designed to conduct measurements. Multiple antennas were designed and tested.

Performed experiments and measurement results indicated that the UWB radar could be successfully used to monitor cardio-pulmonary activity. However, the source of the signal is a mechanical movement of skin rather than a volume change of lungs or blood volume change in the heart, as widely expected. The UWB radar shows a strong signal and good signal-to-noise ratio, especially if a stationary or lying subject is monitored. Possible applications of non-invasive contactless UWB are long-term monitoring of obstructive sleep apnoea, cardiac monitoring (including severe burn victims when contact electrodes cannot be used), respiratory monitoring and sudden infant death syndrome monitoring, to name some.

Experiments related to determining boundary layers in tissue to detect hematomas were unsuccessful. Even when UWB radar could detect different layers, its spatial resolution and sensitivity for hematoma detection were insufficient. The reason for that is the very high attenuation of ultra-short impulses required for high spatial resolution.

2 Bioimpedance Sensing

The efficient monitoring of cardio-respiratory changes through electrical bioimpedance requires understanding the relationship between tissue properties and tissue impedance. An electrical equivalent circuit model according to the nature of the object (tissue, organ, cells) describes this relationship. As this relationship is not unique, prior knowledge provides a proper outcome.

In the case of employing electrodes, their influence may significantly affect the overall EBI measurement result. Electrodes part must be involved in the model and later separated from the parts of the object. Otherwise, significant measurement errors may occur. The effect of the electrodes can also be reduced with a measuring scheme (e.g., a four-electrode scheme). A more radical method to avoid this error source is a solution without electrodes (by inductive or capacitive coupling). However, both are more complex measurement schemes, and each of the contactless solutions has its weaknesses.

The third important aspect of using the EBI method often overlooked is the impedances between the body, the instrument and the environment. Their effects can also have a drastic influence on the measurement results.

As the research's main aim was monitoring cardio-respiratory activity parameters based on the changes of EBI, usually at a single frequency, high accuracy of EBI spectra measurement seems not to be a serious goal. However, the supporting data from impedance spectra are still necessary since it is required to associate the impedance change with a specific object parameter that mainly causes the impedance variation on the used frequency and set aside all other changes.

2.1 Electrical Bioimpedance

2.1.1 Electrical impedance

Electrical impedance is the ratio between voltage and current. In general, it applies both to direct current (DC) and alternating current (AC); however, in the case of using AC, other mechanisms are impeding the flow of current besides the resistance to DC. The induction of voltages in conductors is self-induced by the magnetic fields of currents (inductance), and the electrostatic storage of charge is induced by voltages between conductors (capacitance). The impedance Z caused by these two effects is called reactance X , which forms the imaginary part of complex impedance, whereas resistance R forms the real part. The use of complex numbers results in the following equation:

$$Z = R + jX = \text{Re} + j\text{Im} , \quad (2.1)$$

where j is the imaginary unit defined as $j = \sqrt{-1}$. The length $|Z|$ of the vector (also named as magnitude) and its phase angle φ can be calculated as

$$|Z| = \sqrt{R^2 + X^2} , \quad (2.2)$$

and

$$\varphi = \arctan(X / R) \quad (2.3)$$

Corresponding impedance vector $|Z|$ is shown in Fig. 2.1.

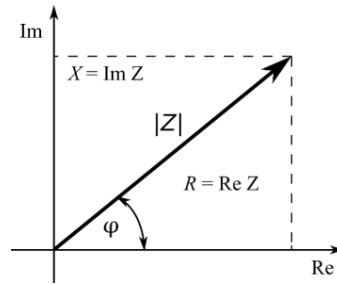


Fig. 2.1 Impedance vector and its real and imaginary parts.

In biological objects, inductances are usually very small, allowing these to be neglected in electrical models. However, at higher frequencies above about 1 MHz, it may also be necessary to consider the inductance of the connecting leads. This frequency limit also depends on the desired accuracy.

2.1.2 Electrical model of the tissue

Analyzing the electrical response caused by the electrical excitation allows one to determine the passive electrical properties of an object. In contrast to the passive case, objects can generate electricity, e.g., heart tissue (usable in electrocardiography, ECG). This so-called endogenic electricity is not a topic of the current work; however, it can influence the measurements of passive electrical properties in some cases.

Attempts to measure and interpret living tissues' electrical properties started over a hundred years ago. In 1907, Lopicque extensively investigated the use of the three-component parallel combination of resistance and capacitance, both in series with resistance to model the excitation of nerve membrane [9], Fig. 2.2b (later here as model B). As the membrane resistance is shortened at infinitely high frequencies by its capacitance's low reactive resistance, R_b is also denoted by R_∞ and the sum by $R_0 = R_b + R_m$ at very low frequencies [54].

Fricke and Morse [55] found that their measurements on suspensions of red blood cells at various frequencies could be represented with an equivalent circuit shown in Fig. 2.2a (later here as model A). R_{ext} was thought to represent the resistive properties of the suspending medium, R_{int} those of interiors of the corpuscles (cells) and C_m the capacitances of the membranes. Later, such a simplified equivalent circuit has also been widely used for biological tissues, Fig 2.2c.

However, as noted in [54], Zobel [56] has shown that spectra of certain types of two-terminal networks – of which the circuits of Fig. 2.2 are exceptional cases – can be made equivalent.

The conversion of the Model A parameters to the Model B parameters is performed using the following relationships

$$C_m(B) = \left(\frac{1+a}{a} \right)^2 C_m(A); R_m = \frac{a^2}{1+a} R_{int}; R_b = \frac{a^2}{1+a} R_{int}, \quad (2.4)$$

where $a = R_{ext}/R_{int}$. The conversion of the Model B parameters to the Model A parameters is performed using the following relationships

$$C_m(A) = \left(\frac{1}{1+b} \right)^2 C_m(B); R_{int} = (1+b)bR_m; R_{ext} = (1+b)R_m, \quad (2.5)$$

where $b = R_b/R_m$. From equations (2.4) and (2.5), it is evident that despite the equivalency of spectra, the membrane capacitances are not equal: $C_m(A) \neq C_m(B)$ and depends on a ratio of resistances.

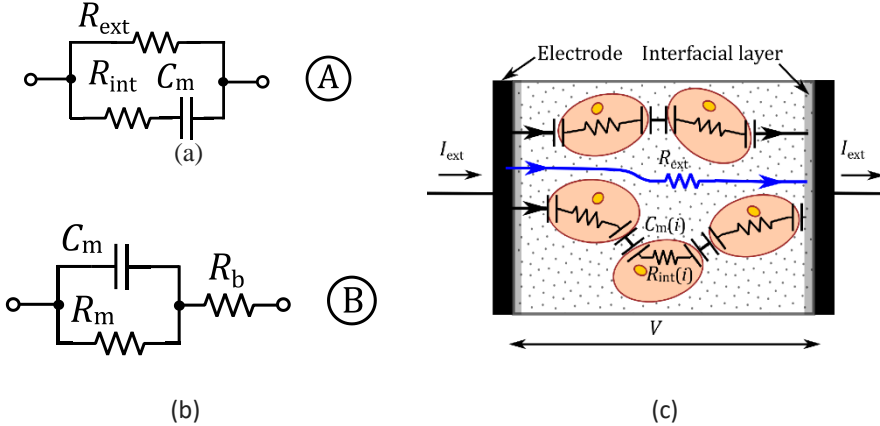


Fig. 2.2. Equivalent circuit representing the membrane capacitances C_m in series with internal resistances of cells R_{int} , where R_{ext} denotes the resistance of suspending medium (a), and an alternative circuit representing membrane capacitance C_m and resistance R_m in series with a resistance R_b (b). A variant of model A with electrodes to represent biological tissue (c).

When more components are involved, the number of circuits with equivalent spectra increases. Thus, it is apparent that the configuration of elements of such networks cannot be determined solely by impedance measurements made at terminals. Moreover, a comparison of conversion results shows that also R_∞ and R_0 remain the same for both models and do not help to distinguish them. Table 2.1 shows examples of parameter transformations for models A and B based on the identical impedance spectra. It turns out that depending on the selected model, the same parameter, capacitance of the membrane, can differ nearly ten times. A relatively small difference in membrane resistance R_m , intracellular resistance R_{int} and the resistance of the surrounding fluid R_{ext} is also questionable. Thus, the knowledge about the physiology of the object is crucial; also, intuitive ideas checked by a series of measurements in different conditions are helpful.

It has been proposed that model A is better suited for living tissue and cell suspensions [57]. Model B suits well for skin, where R_b is the deeper tissue series resistance, and the parallel combination represents the stratum corneum with an independent sweat duct in parallel. Although model B is often referred to as the Cole model, e.g., [58], [59] in his later work [60], Cole also uses model A when analyzing the solutions of the Laplace equations for the electrical resistance and capacitance of simple composite systems for understanding of the impedance of tissues.

Table 2.1 Parameters of models A and B with equivalent spectra.

Parameter	R_m	R_b	R_∞	R_0	C_m	R_{int}	R_{ext}	R_∞	R_0	C_m
Unit	Ω	Ω	Ω	Ω	F	Ω	Ω	Ω	Ω	F
Model	B	B	B	B	B	A	A	A	A	A
	50	100	100	150	10 u	300	150	100	150	1.11 u
	50	100	100	150	1 u	300	150	100	150	0.11 u
	100	50	50	150	10 u	75	150	50	150	4.44 u
	100	50	50	150	1 u	75	150	50	150	0.44 u
	100	100	100	200	10 u	200	200	100	200	2.50 u
	100	100	100	200	1 u	200	200	100	200	0.25 u

Both equivalent circuits in Fig. 2.2 are still greatly simplified. The distribution of cells in the tissue is not uniform, and their microscopic properties may be independently distributed. Thus, the measured electrical bioimpedance (EBI) data does not match well with the impedance of an equivalent circuit involving only a finite number of common lumped-constant elements. Phillipson [10] found that the capacitance of guinea pigs' muscles and liver varied about as the inverse square root of the frequency and referred to this capacitive impedance as a polarization resistance. It has been observed later that the use of distributed impedance elements, e.g., constant-phase elements (CPEs), significantly aids the process of fitting observed impedance data. Kenneth Cole introduced its influence on the impedance of cell membranes in [61], as

$$z = z_\infty + (r_0 - r_\infty) / [1 + (j\omega\tau)^\alpha], \quad (2.6)$$

where z is a complex impedance, r_0 and r_∞ the resistances at zero and infinite frequency, $\tau = (R_m C_m)^{1/\alpha}$ is the time constant of the suspension, α is a variable related to membrane impedance, and ω is the angular frequency. Using the equivalent circuit Fig 2.2(b) and considering that $z_\infty = R_\infty$, $r_0 - r_\infty = R_m$, it is possible to represent (2.6) as

$$\tilde{Z} = R_b + \frac{R_m}{1 + (j\omega)^\alpha R_m C_m} = R_b + \frac{1}{1/R_m + (j\omega)^\alpha C_m}, \quad (2.7)$$

Here the impedance of the CPE Z_{CPE} expresses as

$$\tilde{Z}_{CPE} = \frac{1}{Q(j\omega)^\alpha}, \quad (2.8)$$

where Q and α are the pseudo-capacitance and fractional-order (exponent), respectively, with $0 < \alpha < 1$ for biological tissues. In this case, CPE has an electrical characteristic between resistor ($\alpha = 0$) and capacitor ($\alpha = 1$). The impedance has a negative phase angle $\varphi = -\alpha\pi/2$, in the range $0 > \varphi > -\pi/2$, that is independent of frequency. The unit of Q is $S \cdot s^\alpha$. Many researchers have also explored the relationship between Q and so-called effective capacitance C_{eff} representing it in a specific range of α [62]–[64]. When $Q = C_{eff}$, its unit is $F \cdot s^{\alpha-1}$ [63].

While several physical explanations exist for CPE behavior, it is mainly interpreted as a distribution of time constants in biological tissues due to a statistical distribution of cell

sizes and geometry. When polarizable electrodes are used in the EBI measurement circuit, the total equivalent circuit also includes CPE related to their surface roughness and porosity [65]. In both cases, such multiple relaxation models correspond to topoelectrical circuits [66], e.g., with a ladder or self-similar tree topology [67].

The CPE model also corresponds to an equivalent complex relative permittivity $\tilde{\epsilon}(\omega)$ [68]

$$\tilde{\epsilon}(\omega) = \frac{Qd}{\epsilon_0 A (j\omega)^{1-\alpha}}, \quad (2.9)$$

where d and A are the equivalent plate distance and plate area of the capacitor and ϵ_0 is the permittivity of vacuum. However, since the equivalent dimensions do not correspond to a physical capacitor, its capacitance is also equivalent. For that reason, the analogy with the permittivity of the dielectric material is challenging to interpret. Although an approximate effective capacitance corresponding to Q can be found, it is not a capacitor. Unlike with a capacitor, whose impedance depends only on the capacitance and frequency, the impedance of Q also crucially depends on α , as shown in Fig. 2.3b. These circumstances could also explain the high relative permittivity values proposed for biological tissues [21].

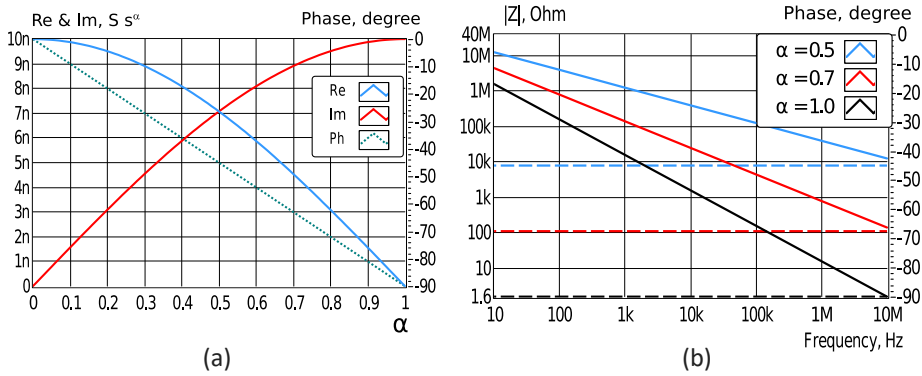


Fig. 2.3. Dependence of the Re, Im, and phase of the impedance on α for the CPE with $Q = 10 \text{ n S s}^\alpha$ (a), and its impedance magnitude and phase dependence on frequency (b). The phase data is presented with dashed lines in (b).

Fractional-order α does not change when converting models A and B with equivalent spectra, and Q changes in the same proportion as in the case of pure capacitance ($\alpha = 1$) when the ratio of resistances alters (see Table 1). However, it does not follow that the CPE could be replaced with a capacitor when fitting the values of model elements. On the contrary, if the nature of the physical object presupposes the presence of one or more CPEs, their replacement by capacitances leads to a considerable difference in the impedance spectra.

Generally, no exact algebraic solution exists for equivalent circuit parameters calculation from the experimentally obtained spectra. For this reason, mainly the complex non-linear least squares (CNLS) algorithm is employed. The method of the CNLS algorithm is to approximate (fit) the equivalent circuit parameters by the following minimization function:

$$E_f = \min \sqrt{\sum_{i=1}^n \left| \tilde{Z}_{\text{exp}}(\omega_i) - \tilde{Z}_{\text{eqv}}(\omega_i, \vec{P}) \right|^2 w(\omega_i)}, \quad (2.10)$$

where E_f is a fitting error, \tilde{Z}_{exp} experimentally obtained impedance, \tilde{Z}_{eqv} equivalent circuit impedance, both at frequency ω_i . \vec{P} is a vector of the equivalent circuit parameters (resistances, capacitances, and others), n is a number of frequencies, and $w(\omega_i)$ denotes a weighting factor for compensating differences of the impedance impact to the sum of squares at different frequencies. The minimal sum of the residual (fitting error) obtained with (2.10) depends on the number of used frequencies (except in the case of the exact match of impedances when it is zero). A normalizing fitting error by dividing the sum with a number of frequencies allows their comparison. However, the used frequency range must cover the area where the dispersion of spectra caused by circuit elements appears. Otherwise, the obtained values of elements may be significantly distorted. In the case of relative presentation of the fitting error, the difference of impedances in (2.10) is divided by $\tilde{Z}_{\text{exp}}(\omega_i)$.

Fig. 2.4 illustrates the case when the equivalent circuit A with $R_{\text{int}} = 50 \Omega$, $R_{\text{ext}} = 100 \Omega$, and CPE ($Q = 1 \mu \text{S} \cdot \text{s}^\alpha$, $\alpha = 0.6$) is substituted with a similar circuit where CPE is replaced with a capacitor ($\alpha = 1$). After CNLS fitting of initial spectra with 64 logarithmically distributed frequencies from 100 Hz to 100 MHz, new parameters are obtained: $R_{\text{int}} = 67.3 \Omega$ (+34.6 %), $R_{\text{ext}} = 92.3 \Omega$ (-7.7 %) and $C_m = 2.1 \text{ nF}$ (476 times lesser Q). It is also evident that both the magnitude and phase spectra differ considerably from the original, i.e., replacing the CPE with a capacitor cannot guarantee equivalent impedance spectra. Limiting the frequency range for fitting from the upper side to 1 MHz causes additional changes: $R_{\text{ext}} = 95.8 \Omega$, $R_{\text{int}} = 128.7 \Omega$ and $C_m = 3.5 \text{ nF}$. Reducing the effect of the capacitive chain results in a more accurate R_{ext} , but at the same time, increases the error in determining the R_{int} .

2.1.3 Electrical properties of biological tissue – dispersion regions

In 1957, Hermann Schwan proposed a definition of frequency spectrums, where vastly different phenomena appear in dielectric permittivity graphs to characterize the biomaterials: α -, β - and γ -dispersion. The mechanisms behind these phenomena rely on mechanisms specific to a certain frequency range.

α -dispersion is classically defined to appear in some mHz (millihertz) to a kHz range and is related to the appearance of the electric double layer. The electric double layer, e.g., the counter-ion layer, causes the polarization phenomenon to arise in the channel systems and on the surface of the cells [17].

However, the relatively complex permittivity and its increase are claimed not to be the reason for the capacitive properties of biological objects at low frequencies [18]. The reason for the domination of capacitive properties in measured impedance of living tissues at low frequencies is expected to be the conductive properties of liquids, i.e., water [19]. Though the living tissues are highly complex in structure and the inclusion of additional problems that appear in the form of electrode polarization apply in low-frequency measurements, the difficulties appear when giving explanations.

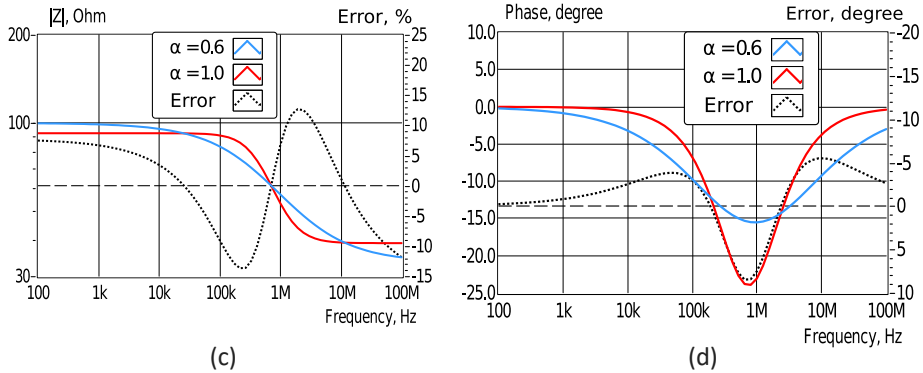
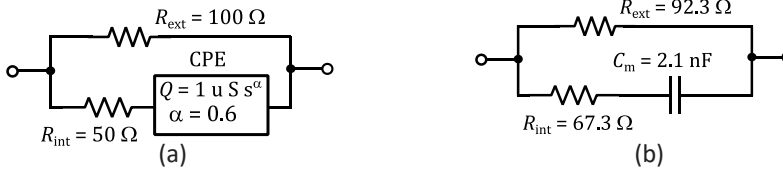


Fig. 2.4. Equivalent circuit of model A with CPE (a) and equivalent circuit of the same model with a capacitor (b) where the parameters are obtained by CNLS fitting using initial spectra of the model with CPE. The initial and fitted spectra (with $\alpha = 1$) curves are shown in (c) and (d). Dotted curves show differences in magnitude and phase of the original and fitted spectra (substitution error).

β -dispersion is claimed to apply in the range of 1kHz – 100 MHz and is generally related to the properties of cell and organelle membranes. If the biological material does not have membranes, the β -dispersion is small. The charging of the membranes depends on their different dielectric constants and electrical conductivities – arising from interfacial polarization [19]. In the case of inhomogeneous tissue, different cell membranes cancel the resistive components by parallel capacitances and resemble homogenous properties [69].

γ -dispersion appears in the highest frequency range of 0.1–100 GHz and is related to the dipolar mechanism for the entire electrolytic content. In the γ -dispersion range, the properties of biological materials are related to their water content [69]. The reorientation of water molecules phenomenologically causes it, containing both the intra- and extracellular water data [21].

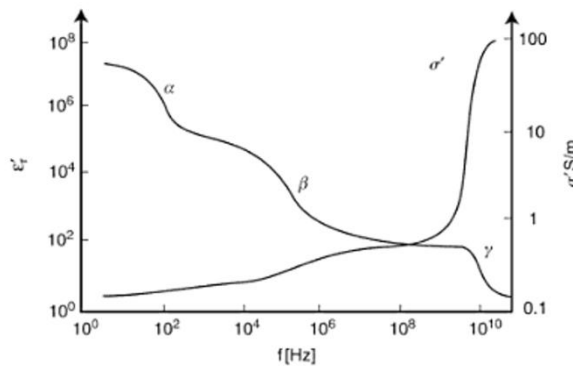


Fig. 2.5. Idealized dispersion regions of biological material (adapted from [70])

2.2 Measurement of the Electrical Bioimpedance

2.2.1 Impact of the measurement setup and environment

EBI measurement problem often overlooked is the impedances between the body, the instrument and the surrounding environment.

Typical resistance distribution of body segments without skin contribution has been found with a four-electrode technique [15] as shown in Fig. 2.6 a. In [71], the values of impedance magnitude measured on the wrist with a four-electrode technique are reported to be in the range of 20–40 Ω at frequencies up to 250 kHz.

Unfortunately, the impedance values reported in different sources vary substantially. For example, in [72], the magnitude of the wrist's impedance measured with the self-balancing half-bridge and 4-electrode technique is reported to have a baseline of 1–2 k Ω at 50 kHz.

One of the reasons for the large discrepancy in results is the structure of the general measurement setup, which, in many cases, is not mentioned at all. If the measuring instruments or the computer connected to it is powered from the mains, the ground loop impedance affects the measurement results. A simplified illustration of the situation is depicted in Fig 2.6 (b). Measurements with the compact battery-powered impedance analyzer CIA described in chapter 4 gave the impedance and capacitance values provided in Table 2. All measurements were performed against a copper sheet with dimensions 700 x 400 x 1 mm. MFLI Lock-in Amplifier from Zürich Instruments with dimensions of 28.3 x 23.2 x 10.2 cm was used as a test instrument. The capacitance C_{i-GND} was measured relative to the copper sheet on the table.

The detailed equivalent circuit is more complex and depends on both the measurement scheme and the characteristics of the device's power supplies connected to the mains. Experiments with the ZI MFLI showed that avoiding mains power increased the impedance of the parasitic circuit almost twice. However, the specific results depend on a number of factors, including mains supply circuit characteristics, dimensions of the instrument and additional shielding. The internal shield that may be left floating is shown in dark gray in Fig. 2.6b. Using the floating shield of the ZI MFLI increased the stray impedance related to C_{b-i} by around 11%.

A comprehensive analysis of the effect of parasitic capacitance to ground in impedance measurements is provided in [73]. As an example, it is shown that the magnitude of the impedance measured with a four-electrode scheme between the arms changes 22.8 Ohms at 1 MHz and the base value near 420 Ohm (i.e., 5.4%) when one foot is raised 10 cm above the floor.

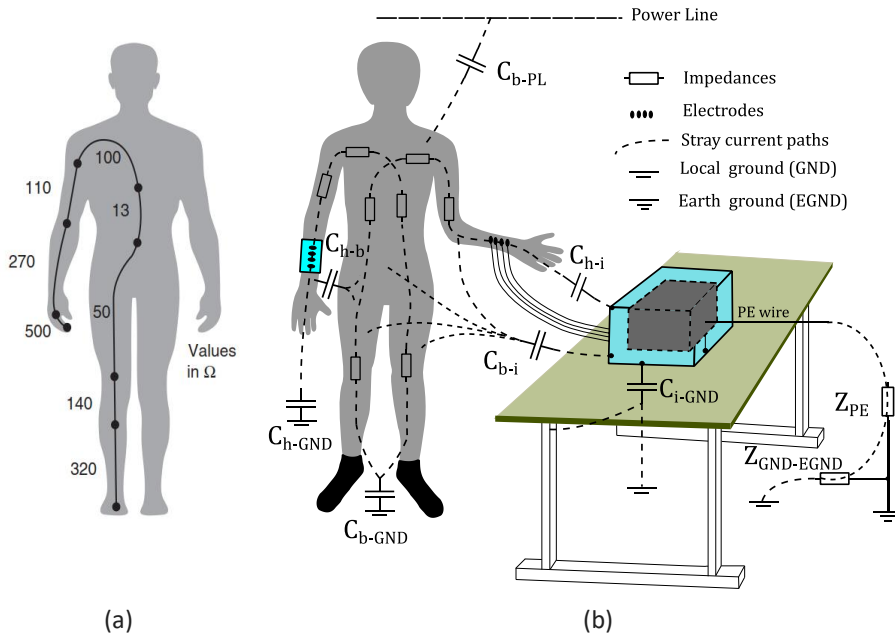


Fig. 2.6. Typical body segment resistances (a) adapted from [14] and simplified illustration of stray impedances and capacitances with the compact battery-powered instrument on a right hand and stationary instrument on a table (b). The internal floating shield of the stationary instrument is shown in dark gray.

Table 2.2 Stray impedances $|Z|$ and capacitances C at frequencies f_m .

Parameter	$ Z $ k Ω	C pF	f_m kHz	Comment
C_{b-GND}	12.9	123	100	Shoes ¹⁾
C_{b-GND}	14.8	107	100	Shoes ²⁾ , one leg raised 30 cm
C_{b-GND}	1.29	123	1000	Shoes ³⁾
C_{b-GND}	1.15	139	1000	Shoes ⁴⁾ , hands on table
C_{b-GND}	2.98	5340	10	Socks, cotton
C_{b-GND}	1.04	1540	100	Socks, cotton, isolated with 50 μ m LDPE foil
C_{b-i}	3.84	41.0	1000	ZI MFLI, distance 10 cm, \sim 230 V supply
C_{b-i}	8.66	18.4	1000	ZI MFLI, distance 10 cm, 12V battery supply
C_{b-i}	3.27	48.7	1000	ZI MFLI, distance 5 cm, \sim 230 V supply
C_{b-i}	7.28	21.8	1000	ZI MFLI, distance 5 cm, 12V battery supply
C_{i-GND}	1.02	156	1000	ZI MFLI, \sim 230 V supply
C_{i-GND}	1.67	95.0	1000	ZI MFLI, 12V battery supply
C_{h-GND}	n/a	\approx 10	1200	[74]
C_{b-PL}	n/a	3	n/a	[75]

¹⁾ - ⁴⁾ Shoes, # 45, with the sole rubber thickness of 8 mm.

The phase angle change was significant already at 100 kHz and became positive at 1.1 MHz (a false measurement result, in principle, showing inductive behavior of the capacitance). Measurements with a developed compact battery-powered analyzer gave the body to ground capacitance decrease and corresponding impedance magnitude change of by 13% at 100 kHz when one leg is raised by 30 cm. A similar 13% increase of body-to-ground capacitance appears when placing hands on the table; see cases 1) to 4) in Table 2.2.

There are several ways to reduce the impact of the ground loop, but the most effective method is to use a compact battery-powered device with wireless data transmission. However, even in a battery-powered solution, the effect of the earth (or common ground) is not eliminated. The body and its parts have impedance to ground, primarily capacitive. A stray current loop is formed, which passes through the measuring circuit, e.g., in the case of a hand-held measuring instrument, through the capacitances C_{b-GND} , C_{h-GND} and C_{h-b} . A similar issue has been extensively studied in the human body communication field (HBC) [74].

Although most capacitances between the body parts and the earth are in tens of pF, their effect at higher frequencies is still essential, considering that the variation in impedance magnitude of the impedance related to the heart activity on the wrist is less than 1%. In contrast, the capacitive reactance of the ten pF is 1.6 k Ω at 10 MHz, which is about 3 % or 53 Ω of the impedance base value.

Parasitic capacitances significantly depend on the position of the body. For example, the capacitance of a body lying in bed is about 300 pF to ground [75]. Moreover, the body of a standing person forms a quarter-wave monopole antenna that resonates between 40 and 60 MHz [76] and therefore becomes more sensitive to disturbances in this range.

There are several ways to improve the situation. First, to design the measurement circuit in a way that the effect of parasitic impedances will be minimal. To ensure that, the measuring device must be very close to the object and the device's dimensions must be as small as possible. Compensation of parasitic effects, for example, by the differential scheme, is also helpful but cumbersome to do. In order to reduce the impact of the stray current loop between the body and ground, the measurement loop must be closed in the vicinity of the body organ of interest (e.g., the heart).

Another alternative is to reduce the frequency of the excitation signal. Unfortunately, this is not always possible for several reasons. First, it is necessary to work at the frequency where the changes in the object's parameters are to the best extent. Secondly, the impedance of capacitive electrodes increases at lower frequencies. Third, with inductive excitation, the current induced in the object is related to the magnetic flux rate.

2.2.2 Impedance of electrodes

Electrodes may be classified as non-polarizable and polarizable.

Non-polarizable electrodes use the electrochemical equilibrium between a metal and its hardly soluble salt, e.g., silver/silver chloride (Ag/AgCl). This type of electrode has a relatively large value of allowed current density, a low value of charge transfer resistance R_{ct} and they are widely used in sensitive bio-potential measurements (e.g., ECG measurements). Unfortunately, these electrodes are commonly single-use parts stuck to the skin by an adhesive electrode surface [77]. This adhesive complicates improving the electrodes' positioning once the electrodes are attached and can also cause skin irritations [78].

The class of polarizing electrodes includes noble metals. They are relatively inert, as it is difficult for them to oxidize and dissolve. Thus, the current passing between the electrode and the electrolyte changes the concentration primarily of ions at the interface – the so-called interfacial double layer. The electrical characteristics of such an electrode show a high R_{ct} and significant capacitive effect [79]. However, the electrical model of the electrode-electrolyte requires the use of a CPE element for a more accurate representation shown in Fig. 2.7a. Since R_s here represents the resistance of the solution, the EBI equivalent scheme takes the form shown in Fig. 2.7b in summary.

The overall result also depends on the impedance of the instrument and stray components of impedances.

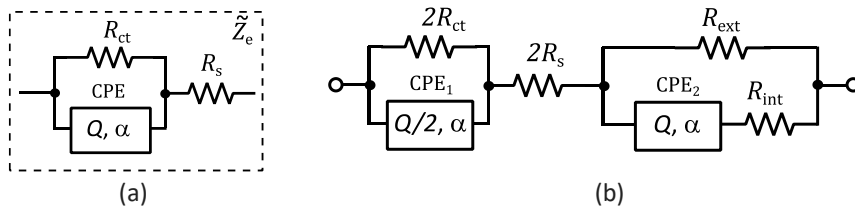


Fig. 2.7. Equivalent circuit of the polarizable electrode (a) and combined equivalent circuit for EBI measurement (b).

2.2.3 Electrode-tissue system

With ideal electrodes (impedance is close to zero) and homogeneous objects, the electrical properties of the electrode-tissue system depend on geometrical configuration. Fig. 2.8a shows two current-carrying electrodes CC connected to tissue volume. Fig. 2.8b depicts current density lines in the case of four-electrode impedance measurement. In both cases, the properties of tissue are homogeneous here.

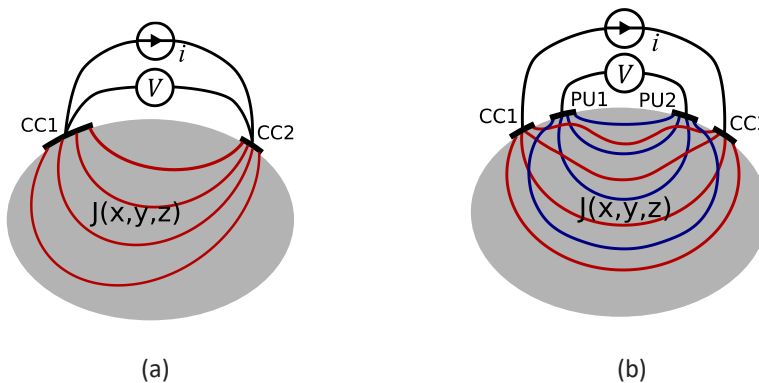


Fig. 2.8. Current i in external wire and current density J lines in the tissue volume with two current-carrying electrodes CC1 and CC2 (a) and current density lines the case of four-electrode impedance measurement, where CC1, CC2 are forming a current-carrying electrode pair and PU1, PU2 are the voltage pick-up electrode pair (b).

In a four-electrode system, the volume impedance density VID is expressed as

$$VID = \rho S = \rho \frac{\overline{J_{CC}} \overline{J_{PU}}}{\overline{I_{CC}} \overline{I_{PU}}}, \quad (2.11)$$

where S is the EBI detection sensitivity [m^{-4}], ρ the resistivity of the volume, J_{CC} the current density under CC electrodes, and J_{PU} the current density under PU electrodes [80]. As current densities decrease with distance from the electrodes, the sensitivity of impedance detection also decreases rapidly. In addition, sensitivity formation depends on the direction of current density vectors of the CC and PU electrodes. Therefore, there are also negative sensitivity areas. Since the voltage signal is not picked up from the sites of current application in the four-electrode system, the ratio of the measured voltage and current is not impedance but transfer impedance [81]. The impedance of each tissue in contributing to the measured transfer impedance can be obtained by integrating the sensitivity values of the tissue over the volume it occupied [82]. However, as shown in [83], in practice, the measurement result is susceptible to the placement of electrodes, which may cause relative changes up to $\pm 75\%$.

In a bipolar system, equation (2.11) simplifies to

$$VID = \rho S = \rho \overline{J}^2, \quad (2.12)$$

where J [$1/m^2$] is the local current density caused by a unity current passed through the electrode pair. This representation of true impedance with a more uniform sensitivity is better suited for determining EBI model parameters than a four-electrode system. The disadvantage is that impedances of all components (electrodes, skin, and inner tissues) are in series. The contribution of inner tissues remains low, especially when the impedance of electrodes is high. The advantage of a four-electrode system in cooperation with a constant current source and a high input impedance voltage measurement is the elimination of the impact of electrodes and skin impedance. However, as discussed in the following subsection, this statement is somewhat idealized.

2.2.4 Instrumentation

The choice of measurement solution is based on the task and the constraints that exist in performing that task. The detection of cardiac and respiratory signals via EBI involves the following:

- 1) The relative changes in impedance associated with cardiac work are small. For example, the results obtained from the wrist are typically less than 1% variations of static impedance [84] when detecting the changes.
- 2) As reported in the papers, the β -dispersion of EBI typically reaches 10 MHz [70].
- 3) When using electrodes, they must be suitable for long-term use; contactless solutions are preferred, therefore.
- 4) The device must be small in size for the portable/wearable solution and use the wireless data transmission.
- 5) The supply voltages are limited due to both low power supply (battery) and broadband and high-resolution signal processing.
- 6) For real-time monitoring of heart signals, the signal recording and processing must be fast enough.

- 7) The detection of small EBI changes is greatly influenced by the parasitic impedances associated with the body.
- 8) The requirements for the accuracy of the measurements depend on the task. If the aim is only to detect changes in impedance, the device's design may be more straightforward, reducing the power consumption and dimensions.

When measuring the impedance, a voltage source (low output impedance) and a current source (high output impedance) can both be used for generating the excitation signal. The current source is considered to have the advantage of reducing the influence of electrode impedance (typically in a four-electrode measurement scheme, accompanied by high input resistance voltage measurement). However, for the present task, the use of the voltage source is preferred due to the following circumstances:

- 1) Building a high-impedance current generator in the 10 MHz range is complicated. In most cases, the current generator parameters start to deteriorate from 1 MHz or below, so the current must be measured. As the voltage is measured differentially to achieve a better common mode rejection ratio (CMMR), the current generator must also have a differential output that increases the complexity of the current generator and its measurement circuits [85].
- 2) The current generator must increase the voltage to ensure constant current at higher impedances, but the supply voltages (maximum $\pm 5V$ in the present case) exclude this option.
- 3) Due to the high output resistance of the current source, the time constant of the response signal development is considerable. However, this is unsuitable when measurement channels need to be switched quickly or measuring impedance spectra with changing frequencies.
- 4) Coaxial cables with 50-ohm characteristic impedance are commonly used to connect the object at MHz range, the best match of which is guaranteed for the voltage source with 50-ohm output resistance.
- 5) Due to safety requirements, the applied current must be strictly limited. Since the practical current generator is typically based on operational amplifiers; in the event of a fault, the supply voltage is applied to the object and exceeds the limit set by the IEC 60601-1 standard (10 μA for DC).

In addition to the current generator considerations discussed above, alternative solutions can help measure impedance changes in an extensive range. One solution used in the impedance analyzer described in Chapter 4 is to adjust the excitation voltage adaptively using digital feedback.

In four-electrode measurement, the input impedance of the amplifier measuring the potential difference of the voltage measuring electrodes needs to be high across the bandwidth to ensure near-zero current through these electrodes. In practice, this is not the case, leading to a potential drop across the interface impedance of the voltage measurement input and thus to measurement errors. One of the factors also limiting the input impedance of voltage measurement input at higher frequencies is the impedance of the connecting cables. In addition, the high input resistance accompanies a higher thermal noise, which leads to a decrease in the SNR of measurements.

The four-electrode measurement scheme is not well suited for the impedance measurement in the β -dispersion range. First, the complexity of the measurement scheme increases, but the association of the results with the electrical model will become more

uncertain due to the complex relationships (see Section 2.2.3). Second, more electrodes are needed, contrary to the condition of compactness and long-term comfortable use. However, in cases where changes in lower frequencies (below 100 kHz) mainly related to the resistive part of the impedance are of interest, a four-electrode circuit may be suitable.

2.3 Summary of Chapter

The chapter discusses the main factors that hinder the reliable measurement of bioimpedance and its changes in the human body.

The first part of the chapter describes the historical background of EBI measurements and the problems related to the electrical model. The knowledge about the physiology of the object is crucial for selecting its equivalent circuit model. The configuration of networks cannot be determined solely by impedance measurements made at terminals. Commonly used three-element EBI models with two different configurations have equivalent spectra. Although this ambiguity is known, current work also reveals that the same parameter (cell membrane capacitance) obtains significantly different values when changing models. When more components are involved, the number of circuits with equivalent spectra increases. Thus, using a minimum number of model elements is reasonable. However, the distribution of cells in the tissue is not uniform, and their microscopic properties may be independently distributed. Thus, EBI data does not match well with the impedance of an equivalent circuit involving only a finite number of common lumped elements. The use of elements representing distributed impedance, CPEs, significantly aids the process of fitting observed impedance data. CPE replacement with a capacitor results in significant spectral errors and changes in other model parameters.

The second part of the chapter focuses on the impact of the measurement setup and environment. EBI measurement problem often overlooked is the impedances between the body, the instrument and the surrounding environment. Typical situations with stationary and battery-powered measurement instruments are illustrated along with stray impedances data. The impact of stray current loops on the measurement results is discussed, and suggestions for improving the situation are proposed. Next, the properties of an electrode-tissue system with two and four-electrode configurations are discussed. It is concluded that a two-electrode system suits better for determining EBI model parameters than a four-electrode system. Finally, requirements and solutions for the impedance measurement instrumentation in the β dispersion area and for detecting impedance changes are discussed. Although EBI changes can also be detected at lower frequencies with more straightforward solutions, it is impossible to determine which model parameters caused the changes.

3 Detection of Bioimpedance Variations in Resource Constrained Environments

3.1 Basic Configurations for Impedance Measurements

As a standard, electrical impedance is measured by using two-, three- or four-electrode systems. The three-electrode system is mainly used in electro-chemical experiments with liquids and is usually not used for bioimpedance measurement applications. In the case of a two-electrode system, the voltage is measured across the whole measurement tract, including the impedance of the sample under test and the impedances of both electrodes. The measured impedance, in that case, deviates from the real impedance of the object due to the added impedances of the electrodes. In practice, often, a two-electrode system is preferred due to its robustness and is qualitatively usable if the impedances of the electrodes are significantly lower than the impedance of the object of interest.

The electrode system improving the described problem is the four-electrode system. In a four-electrode system, separate leads for the application of current and measuring the voltage allow for minimizing the influence of electrode impedances. As a result, mainly the voltage drop on the object of interest is measured. The controversy of the four-electrode system is emphasized and realized in the scientific literature – arising from the difference in location of the actual exciting and measuring electrode positions on the object of interest. So, to be precise, the result of the 4-electrode measurement is not unambiguous since the sensitivity to impedance change depends significantly on electrode positioning. Four-electrode system improves the measurement quality and decreases motion artifacts but does not eliminate two-electrode system problems as was described in the previous chapter in sections 2.2.3 and 2.2.4. It also introduces additional technical challenges and complexity. In the case of a four-electrode system, the emergence of sensitivity field is more complex due to the usage of different electrodes for excitation and measurement. In such a case, the sign in front of the sensitivity can be either positive or negative, or even zero depending on the emergence of the fields to each other [86].

3.2 Cardiorespiratory Activity Monitoring

Several impedance-based methods are available in material characterization and clinical medicine: bioelectrical impedance analysis (BIA), impedance plethysmography (IPG), electrical impedance spectroscopy (EIS) and electrical impedance tomography (EIT).

The bioimpedance measurement-based methods for detecting cardiorespiratory induced volume changes in biological objects are classically gathered under the name of IPG [87]. Depending on which cardiovascular process is detected, the method is named either as impedance pneumography (IP) (in respiratory activity monitoring) or impedance cardiography (ICG) (in cardiac activity monitoring).

The circulation of blood in the human body, caused by the heart rhythms, is making the impedance of the body vary. When considering a cylinder-like idealization of the artery with cross-section A (Fig. 3.1), the flow of pulsating blood periodically expands the walls of the vessel, increasing the area of the cross-section by ΔA , and thus also the blood volume (pulse volume).

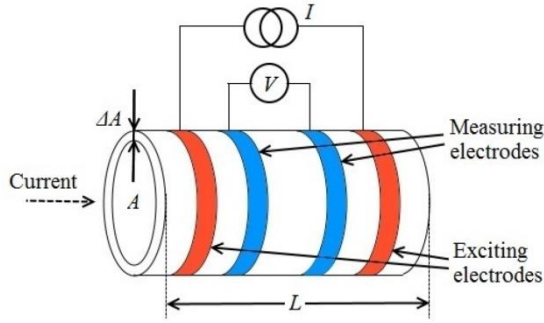


Fig 3.1. Four-electrode impedance measurement of the idealized cylinder-like body (from [88]).

The conductivity of blood (0.703 S/m at 100 kHz) is about twice better than the one of the muscle (0.362 S/m at 100 kHz) or of the blood vessel wall (0.319 S/m at 100 kHz) and more than 30 times better than of the bone (0.021 S/m at 100 kHz) [89]. The impedance of a blood vessel can be calculated [90] according to:

$$\Delta Z = \frac{Z_b Z}{Z_b + Z} - Z = -\frac{Z^2}{Z + Z_b} \quad (3.1)$$

where Z_b is the impedance of the blood, ΔZ is the additional impedance that arises from the expansion of the blood vessel during the arrival of the pulse wave and Z is the impedance of the original volume A . The volume of the arising ΔZ can be calculated according to [90]:

$$\Delta V = -\frac{\rho_b L^2}{Z^2} \quad (3.2)$$

Relying on that expression, a number of hemodynamic parameters can be evaluated. It is more straightforward in the case of the wrist by concentrating on the radial and ulna arteries and more complicated in the classical approach by focusing on the location of the heart in the thoracic cavity. A technique for estimating the hemodynamic parameters in the thorax in measured bioimpedance signal is called ICG – representing the heart rate and its variation, cardiac output, stroke volume and respective time intervals like left ventricular ejection time, pre-ejection period [91], [92].

Similarly, the whole thorax must be set between the electrodes to determine the respiratory activity data. The classical method IP can be used to determine changes in lung gas volume and in lung water as well as respiratory rate [86]. During inhalation, the impedance of the thorax increases as the increasing volume of the lungs increases the lengths of conductive paths. During exhalation, the length of conductive paths decreases, and the measured value of impedance decreases due to the reduced amount of air in the lungs.

However, the human body, including the cardiorespiratory system, constitutes a complex system, i.e., cardiac activity physically affects the lungs and vice versa – inhalation and exhalation apply pressure on the heart [93].

3.2.1 The origin of the bioimpedance signal

When considering the human body, the anatomical structure and buildup have been a subject of research for thousands of years – first signs of studies have been found in artifacts of the times of Ancient Egypt (like Edwin Smith Papyrus from 1600 BC [94]). The biological objects are of highly complex and inhomogeneous structure, consisting of layers and zones of different conductivity. However, the electrical methods have consciously been applied much later, for example, studies that started in the year 1965 at the University of Minnesota for developing the methodology for measuring cardiac output (CO) on the astronauts for the Apollo Moon mission [95]. However, regardless of decades of studies of different scales up to today, so far, no gold standard method exists for estimating the stroke volume and cardiac output [18].

Assumedly, the reason for that is the controversy concerning the origin of the measured signal, or more specifically, the origin of the human anatomy-related patterns carried by the signal. Even more, in the case of cardiorespiratory monitoring – which is the main frame of the current thesis – the interest is in the majority focused on the periodic changes in the volume of interest (ΔA in Fig. 3.1) and not so much on the static value (A in Fig. 3.1).

Intuitively, it is reasonable to expect that the increase of non-invasively measured impedance of the thorax increases when the volume of the lungs increases during the inhalation process and vice versa. Similarly, it is reasonable to expect that with the increase of the volume of blood and, as a result, the diameter of arteries, the impedance of the vessel decreases and vice versa. However, when considering the whole entity of the human body and applying the non-invasive approach with surface electrodes, the presence of different organs and layers are inevitable. I.e., starting from the skin with its high environmental and physiological status, time-varying properties, etc., and considering the wide variety of different layers, the exact sensitivity distribution in the body is uncertain.

The question of sensitivity distribution and the contribution of the pulsating volume of blood in the aorta and arteries in the case of whole thorax-related impedance measurements has been an intensive subject of discussion in the scientific literature. The question is almost always intertwined with the positions of exciting and measuring electrodes attached to the skin surface for impedance signal monitoring.

The topic has been raised and extensively discussed in the frames of detecting the cardiac output (CO) through applying the impedance cardiography (ICG) monitoring technique. Specifically, the finite element modeling has revealed that in the case of classical ICG monitoring spot electrode placement strategy (for extensive discussion on ICG monitoring, refer to [96]), the contribution of the aorta is close to 1% [95]. The aorta, with its task to distribute the pulsating oxygen-rich blood to the whole circulatory system, which is the leading destination of ICG, cannot be the primary source with such a low contribution. On the other hand, the contribution of the upper thorax, where the skeletal muscle dominates, is reported to contribute about 60% of the impedance change [95]. The same has been reported by Kauppinen et al. in [97], highlighting the dependence of the described phenomenon on the choice, number and location of electrodes.

In the case of IP, the question of linearity has been raised – being directly related to the electrode locations on the surface of the thorax. By locating the electrodes either too low or too high in relation to, for example, the xiphisternal joint, the effect of inhaled and exhaled air volume in the measured value of impedance deteriorates [98].

3.2.2 Central aortic pressure of blood – detection and methods

The method for determining BP on the upper arm (brachial) is known to everyone, being a routine procedure in medical examinations. However, this method determines peripheral blood pressure, representing an estimation of an average of the pressure waves that propagate away from the heart. The method gives information on the general pressure level but lacks preciseness due to the distance from the heart. The central aortic pressure (CAP) of blood, measured in the aorta, is declared to reflect much more precisely the “actual” pressure of blood, i.e., the central blood pressure (CBP) [99].

The clinically accepted and widely used method for the determination of CAP is coronary angiography. The method includes cardiac catheterization, during which the pressure sensor is inserted through the arteries into the aortic arc, while the concurrently taken X-ray images help to position the sensor and monitor the possible blockages in blood flow [100]. Due to its invasiveness, the procedure can lead to complications, requires highly experienced medical personnel and is costly.

Currently, the only accepted noninvasive approach to CAP is the applanation tonometry, during which the pressure sensor is pressed against the location of the radial artery in the wrist and the pressure waveform gathered. After that, the gathered pressure waveform is analyzed mathematically/empirically to obtain a generalized transfer function (TF) for the information of the aortic pressure waveform [101]. The most known tonometry device is SphygmoCor (AtCor Medical Pty Ltd, Sidney, Australia). However, novel miniature devices have been developed and commercialized today like A-PULSE CASPro® (HealthStats International Pte. Ltd., Singapore) and PulsePen® (DiaTecne s.r.l., Milano, Italia). The common drawback of the devices utilizing the same principle of measurement by using the pressure sensor against the radial artery is the uncertainty of measurements. To achieve persistent measurement results, the pressure sensor must physically precisely match the location of the artery.

A promising and widely intriguing method for determining the CAP of blood is the measurement of EBI. Specifically, the EBI waveform of the wrist on top of the radial artery’s location is measured using the four-electrode measuring system (Fig. 3.2) and gathered for consequent transfer function based on the estimation of CAP of blood.

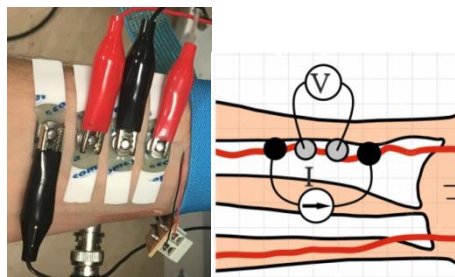


Fig. 3.2. Placement of electrodes on top of the location of radial artery (a) to measure the EBI with four electrode system (b) for estimating the CAP of blood (from [102]).

The bottleneck of this method is developing a true and reliable transfer function capable of being adapted to a real-life situation and considering the possible limitations and conditions of anatomical variability. The development of such TF has already been a task for a decade, resulting in promising results [103], [104]. In the presence of such TF, the implementation of wearable apparatus for ubiquitous and unobtrusive monitoring of CAP of blood would result in a proper step against hypertension – a “silent killer”.

3.3 Methods and a Device for Bioimpedance-based Cardiovascular Activity Monitoring

The basics of electrical bioimpedance monitoring is the excitation of the object by a small current or voltage at single or multiple frequencies and measuring the responsive signal that appears on the object as a result of the applied excitation [105]. As in the case of bioimpedance measurements, the target object is living, and safety standards apply (IEC 60601-1), defining the maximum allowable patient currents for normal and fault conditions. Classically, the frequency range or excitation signal for bioimpedance measurement based cardiorespiratory monitoring applications falls into the frequency range of 20–100 kHz.

The generation of excitation signal can be implemented in various ways, classically by using an oscillation circuit [106] or in more novel ways through the digital-analog-converter (DAC) [107]. The oscillating signal (voltage, typically) is transduced to a suitable current by using voltage-controlled-current-source (VCCS) [108], [109], implemented today in complementary metal-oxide-semiconductor (CMOS) technology.

The other essential portion of the impedance monitoring apparatus is the measurement circuitry. The presence of several topologies is a fact, and the improvement of these schemes has been a serious topic for several decades by many impedance measurement research groups.

The development of instrumentation for electrical bioimpedance based cardiorespiratory activity monitoring has its specifics. The volume changes caused by the inhalation and exhalation and pulsating blood in the heart and arteries are essentially different – largely already because of the conductivity of matter of the changing volume, e.g., air versus blood. Secondly, the variability of the volume itself is the main interest in cardiorespiratory monitoring applications and not the static volume of the matter. The complexity, energy consumption and, finally, the price with the physical dimensions are influenced mainly by the design of the apparatus.

As the current thesis focuses partly on monitoring cardiac activity, the following discussion targets the blood circulatory system of a man, using the better conductivity of the pulsating matter in the form of blood as a prerequisite. The non-invasive monitoring of cardiac activity presumes the usage of surface electrodes attached to the skin. However, as largely known, the human body is very mobile – causing the movement of the skin surface or body organs and zones related to the electrodes. Such phenomenon is named motion artifacts and can have even an amplitude up to 30 times larger than the change of impedance caused by the pulsation of blood in arteries [110]. It has been stated in [18] that “around 85% of the problems in EBI measurement can be associated with the electrodes”. The amplifier's dynamic range in the analog front end of the impedance measurement device must be large enough to cope with massive peaks in the measured signal. This, in turn, requires complex instrumentation and heavy computing power.

When detecting the impedance signal from the wrist in a laboratory environment, the electrodes can be attached to the skin surface as in figure 3.3a.

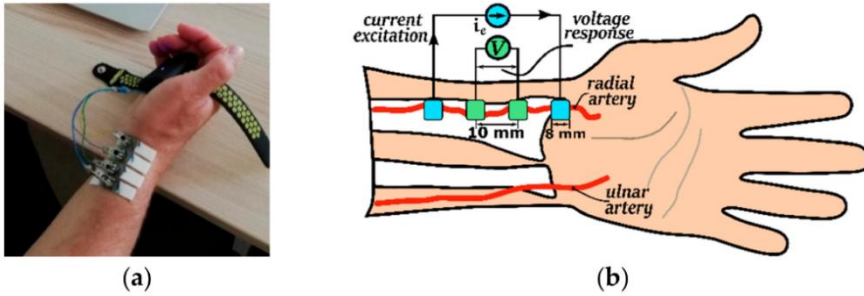


Fig. 3.3. Electrode placement on the skin (a) and respective EBI measurement principle (b) (from [111]).

A common strategy is to attach the electrodes in a straight line so that exciting electrodes are at the edges and measuring electrodes in the middle (Fig. 3.3b). However, several modified electrode placement strategies exist, including focused impedance measurement solutions, that have shown promising results [102], [112].

In the case of impedance measurements on the wrist, the main modulation on the measured signal can be expectedly be caused by the pulsating blood flow, being remarkably low in amplitude (Fig. 3.4). But, as already mentioned, the friction and movement in an electrode-skin interface is a source of distortions, possibly masking the small pulsating blood flow-induced biomodulation completely. A device for detecting such changes must have a wide dynamic range; otherwise, the saturation chance of the measurement channel is likely.

A large part of the measurement circuitry design considerations relies on the questions of the complexity of the instrumentation. Very generally, classically, the solution is to detect the total value of impedance – the static value of the impedance (A in Fig. 3.1) and change the value of the impedance (ΔA in Fig. 3.1). Commonly used classical solution to measure complex impedance is to digitize response voltage directly so-called “brute force” method and calculate impedance vector length and phase angle in software. For this, the highest possible resolution analog-to-digital converters are needed, requiring high computational power, needing complex design and possessing high power consumption [111]. Clearly, it is not a suitable way for battery-powered wearable devices. Another commonly used solution to determine the length and phase of the resulting impedance vector is using two analog synchronous demodulation channels. The measured voltage signal is multiplied in the analog domain with an in-phase reference signal and with quadrature, 90 degrees shifted, reference signal resulting real and imaginary components of the complex response voltage. As a result of this synchronous demodulation operation, the correlation between excitation and response waveforms is then digitized and further processing is carried on digitally. Relatively slow multibit analog-to-digital converters (ADC) can be used (Fig. 3.4).

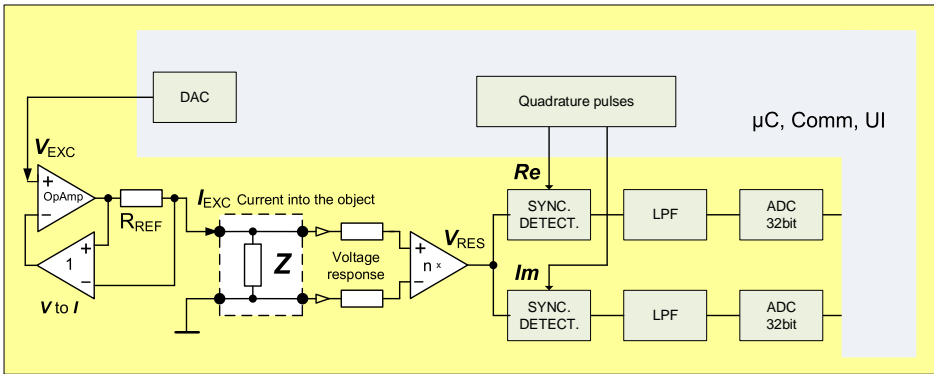


Fig. 3.4. The main components of the “brute force” device use high-resolution ADCs to detect the EBI [111].

The sampling rate typically varies between a few hundred and a thousand samples per second. However, the required number of bits is relatively high, preferably over 20, due to a minimal modulation depth.

Current work proposed four novel solutions to reduce the complexity and power consumption, focusing on the changing part of the impedance only [111], [113]–[115]. The experimentation has shown that non-invasively measured impedance shows slightly capacitive behavior [114]. The same applies to the whole impedance vector, including the variation on top of the impedance signal caused by the pulsating flow of blood (Fig. 3.5). The varying part of the EBI has a slightly different phase than the static part since the impedance of the changing or pulsating quantity (such as blood, for example) can be different from the average impedance of all the tissues in the measurement path.

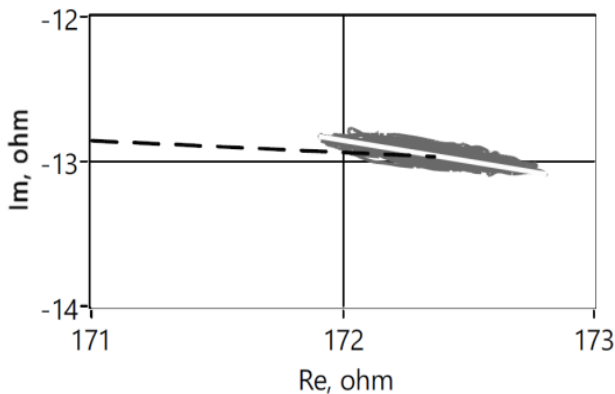


Fig. 3.5. Measured vector of EBI in the complex plane, showing the biomodulation caused by the pulsating flow of blood (from [114]).

Experimental measurements have shown the practicability of the proposed idea of focusing only on the changing part of impedance [111]. Experiments on a single volunteer revealed over the 500 times smaller magnitude of the changing part of impedance than the static part of impedance, and the static part does not contain the information about the cardiorespiratory activity. Measurements indicated that the phase angle of the impedance vector is typically less than 4 degrees in the case of excitation signal frequency

of 120 kHz, and the real part of the impedance can be taken approximately equal to impedance magnitude without introducing significant errors. The maximum error introduced by discarding the imaginary part of the response can be found as the ratio of the modulus of the complex response signal to the real part. The estimated measurement error introduced by sampling only ReV, in that case, is approximately 0.24% [111]. This relation considerably simplifies the realization of the device.

The first proposed solution to reduce complexity and power requirements – “differential sampling” – eliminates impedance base value, allowing low-resolution ADC. In this method, two adjacent samples are taken synchronously to the excitation. Then the difference between said samples will be calculated in the analog domain and digitized later with the aid of ADC. Essentially, we are differentiating the signals during the proposed sampling, i.e., calculating a magnitude difference per sampling interval, and therefore the follow-up integration is required to restore the modulation part. Two adjacent similar samples can be considered as having essentially the same value since the excitation signal frequency (from kHz to MHz range) is very high compared to the speed of the change of the signal caused by the biomodulation with less than 100 Hz frequency spectrum, and also of the typical motion caused artifacts (up to 10 Hz range, maximally). From the nature of the derivative, it also follows that the actual difference between samples does not depend on the magnitude of the signal itself but only on the speed of signal change. Therefore, large but slow artifacts have roughly the same level of impact as tiny but fast variations caused by noise. The method is more deeply described in [113] and patent EE05821B1 issued on 15.Apr.2020 [116].

The second proposed solution is a further development of the differential sampling method – a lock-in integrator used to differentiate the peak detector. The base component of the signal is rejected, giving a better dynamic range for the information-carrying variable component of the bioimpedance due to the apparent differentiation. Sampling in the previous solution is ideal with infinitely short pulses. Real samplers do obviously require some time to take the sample and do have aperture errors. On the other side, short samples do ignore a large part of the incoming signal and limit the achievable signal-to-noise ratio (SNR). Lock-in integrator is free of those shortcomings as infinitely short samples are replaced with half-period or multiple full-period integrals instead. The method is based on the phenomenon that the slope of the linear function is equal to its derivative, and therefore the integral taken synchronously over the full period of the excitation signal is linearly related to the derivative of the modulating signal. The original modulating signal can be restored later with an integrator. A clear benefit of the proposed synchronous integration method is that the base value of the impedance is automatically excluded from the detection result. Therefore, the dynamic requirements for the following ADC circuit can be considerably relaxed. The method is in more detail described in [114].

The third proposed solution is based on a synchronous detector, but analog derivation is used over the modulation frequency range of interest instead of having an analog low pass filter at 0.1 Hz [111]. While the low pass filter has an inherently long settling time, in seconds, as it has also been described in several other publications describing similar items, the derivative approach settles in milliseconds. It is crucial when wearable implementation is used during everyday activity instead of static sitting or lying position. The significant difference is in the block of dZ/dt . The device uses an AVR ATXMEGA microcontroller, together with BLE 4.0. ADC is CPU internal, rather noisy low-quality 10-bit ADC instead of high quality external high-resolution ADC (Fig. 3.6).

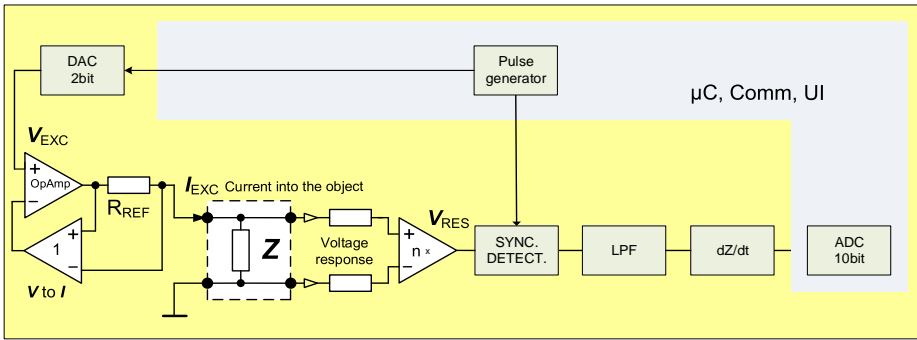


Fig. 3.6. Simplified schematic of the EBI measurement device using filtering for derivation [111].

The quality of the solution is visible in (Fig. 3.7), representing the actual waveform acquired on top of the radial artery without additional filtering or processing. It is a pretty clear and good-quality signal.

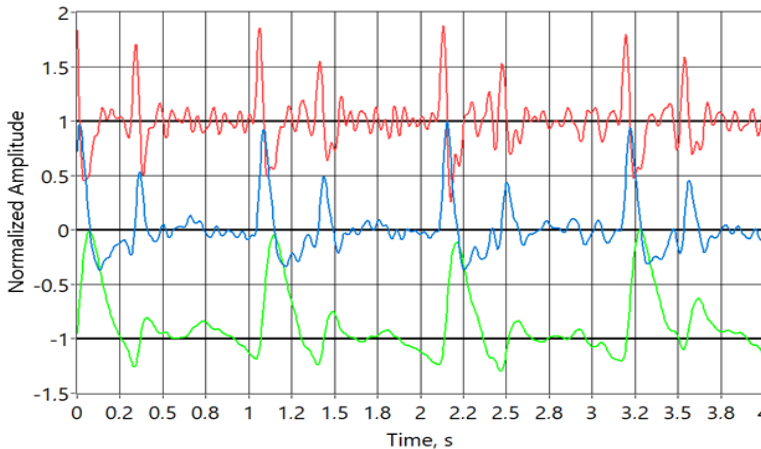


Fig. 3.7. Bioimpedance signal, acquired with derivative technology. All curves are normalized. The blue curve in the middle is the actual signal from the device, i.e., the first derivative of the bioimpedance signal, the upper red curve is the second derivative of the bioimpedance signal, and the lower green curve is integral of the incoming signal, which is also the actual bioimpedance signal [111].

dZ/dt , in this case, is achieved with simple high pass filtering, with high corner frequency, so that in the frequency range of the bioimpedance modulation caused by the beating heart, the frequency response is rising 20 dB/dec, which is effectively equal to the mathematical derivative dZ/dt . The presented derivative detector was able to resolve impedance changes as small as 4 m Ω (ADC resolution 1 m Ω /LSB), which is in the range of 1% of impedance change caused by cardiac activity. The blue curve of Figure 3.7 represents the derivative signal caused by an impedance change of approximately 300 m Ω . A picture of the demonstrator device is visible in (Fig. 3.8).

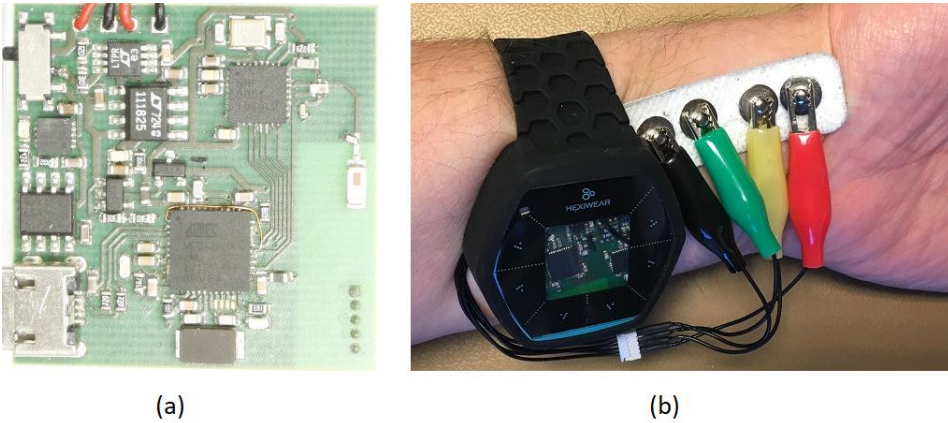


Fig. 3.8. Image of the 10-Bit derivative bioimpedance acquisition system prototype (a) and implementation in a watch (b).

The proposed derivative detector has several advantages compared to the so-called “Brute Force” and “Direct Carrier Compensation” (DCC) method – it uses simpler hardware, has lower power consumption and requires less computational power.

The fourth solution is based on quadrature synchronous demodulation but uses only one measurement channel and a single ADC to measure complex impedance. The proposed method uses a sliding phase difference between the excitation signal and the synchronous demodulator reference signal.

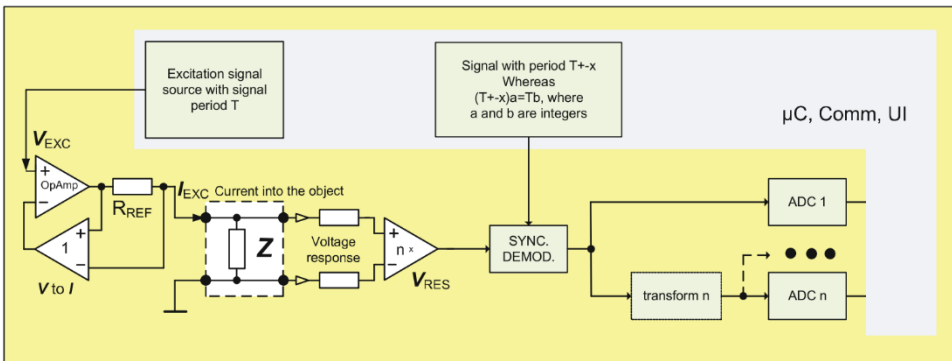


Fig. 3.8. Block diagram for EBI measurement unit using single synchronous demodulation channel.

The sliding phase is achieved by using slightly different frequencies in reference and excitation signal oscillators which causes a known phenomenon called beating. Frequencies have to be selected so that the excitation signal and the reference signal phases coincide at the beginning and the end of a measurement period. From the maximums and zeros of the low-frequency beating signal, the complex transfer values can be determined. A detailed description of the method is described in [115] and the patent US20210190841A1 was issued on June 24th, 2021 [116].

3.4 Summary of Chapter

In this chapter, application areas of bioimpedance measurement like cardiorespiratory activity monitoring and assessment of central aortic pressure of blood were covered, followed by a summary of the methods and a device description for bioimpedance based cardiovascular activity monitoring. The research was mainly focused on the wearable low-energy device. Most of the work was conducted on minimizing hardware (HW) requirements and computational power.

Based on research, two patents were issued covering the measurement methods. Proposed methods allowed to design of simple analog front ends for pervasive EBI acquisition with enhanced protection against artifacts. The requirements for the ADC used after detection circuitry can be substantially relaxed using the differentiation principle. Differentiation implies improvement in the dynamic range of the valid signal at the input of ADC, as the variations can be more than 500 times smaller than the whole measured value. Results show that the microcontroller's internal 10-bit analog-to-digital converter (ADC) is enough to achieve the signal quality, comparable to one of the more complicated "brute force" devices.

Four novel methods for impedance measurement with wearable devices are described with the following conclusions:

- It is beneficial to calculate differences between time adjacent synchronous samples before quantization takes place (Differential Sampling Method)
- It is beneficial to replace short sampling instances with larger integrative intervals, thereby optimizing signal to noise ratio (Synchronous Integration Method)
- Derivative processing reduces considerably impact of slow but high-magnitude disturbances and artifacts on the quantization process
- Dynamic range requirement can be reduced drastically – high-resolution ADC can be replaced with 8-bit ADC
- The novel proposed demodulation method allows using detuned oscillators to measure complex impedance by a single demodulation channel

4 Compact Impedance Analyzer (CIA)

4.1 Introduction

The reason for developing a wearable impedance spectroscopy analyzer was facing specific but serious measurement problems when using commercially available instruments. The main issue is the size of the measurement device, which leads to interfering capacitive coupling between the object, instrument and the surrounding environment. Even with the battery-powered option, bulky devices have a capacitance range of 50–100 pF to the body. Because of body movements, the change in capacitance will create measurement artifacts with a magnitude up to ten times the measured signal itself. In such a situation, stable detection of both cardiac and pulmonary activities is problematic. The aim set up was to design a measurement instrument that is wearable, battery-powered and small to minimize the device's capacitance between the device and the human body. Another shortcoming with existing devices is too limited frequency range. The required frequency range for using inductive and capacitive electrodes is 10 to 20 MHz. At the same time, somewhat suitable commercially available instruments, e.g., the box form-factor Lock-in Amplifier MFLI of Zürich Instruments, ranges to 5 MHz. The wireless data channel is also required as a wired connection creates ground loops and increases the noise level, which must be avoided to acquire the low-level signals from inductive and capacitive electrodes.

The developed wearable impedance analyzer requires the following features to acquire signals from capacitive or inductive electrodes:

- Single-ended and balanced output for excitation signal with output current up to 50 mA
- Configurable embedded front-end amplifiers for current and voltage input.
- Measurement bandwidth from 1 kHz to 10 MHz.
- Accuracy with measurement uncertainty better than 1%.
- Wireless communication at least 1 MB/s.
- Low noise power supply and battery management capability.
- Modest current consumption for battery operation, ensuring the interval between recharges minimum of 30 min.
- Local digital signal processing capabilities to reduce the amount of transferred data.
- Software for controlling and configuring the device.
- Small size to reduce parasitic capacitances, preferably less than 10 pF.

4.1.1 Commercially available analyzers

There are several commercially available medium-size analyzers in the market:

- Zürich Instruments AG, Switzerland – MFLI Impedance Analyzer.
- PalmSens BV, Netherlands – PalmSens 4.
- Ivium Technologies BV, Netherlands – CompactStat.

The MFLI from Zürich Instruments is a professional and expensive analyzer. It is a medium-size instrument (23 x 23 x 10 cm), but has up to 150 pF of stray capacitances as experimentally measured. It is very accurate (0.05%) and covers the higher frequency

range from 500 kHz to 5 MHz, providing excitation current up to 10 mA and having a 16-bit 60 MSPS digitizer (ADC) of measurement signals. PalmSens4 is a much smaller instrument, it sizes 16 x 10 x 3.5 cm and could be used as a wearable device, but its bandwidth is limited to 1 MHz (100 kHz to achieve higher accuracy). CompactStat is the biggest one sizing 26 x 25 x 12 cm, and its impedance analysis bandwidth is limited to 3MHz.

Other wearable analyzers of small size and cheap custom design are available, but all these lack measurement bandwidth and accuracy.

4.2 Developed Wearable Impedance Analyzer

The basic architecture and electronic components were selected during requirement analysis and searching for available components. The following main technical parameters and conditions were defined:

- Size 70 x 45 mm (restricted by available battery sizes).
- 16-bit ADC and DAC, sample rate at least 80 MSPS.
- ADC and DAC with differential LVDS interface to achieve the best suppression of interferences and other disturbances and the lowest noise performance.
- FPGA has to be used for local signal processing; an FPGA size of at least 16000 Logic Elements is required.
- Microprocessor with a WiFi interface to handle the wireless communication with the host system.
- Power source with 3.7 V and 2000 mA/h capacity rechargeable LiPo battery
- Analog front-end and excitation signal amplifier with the maximum current consumption of 100 mA.
- Analog electronics supply voltage +/- 4.8V (defined by the required output swing).
- Ultra-low jitter clock source required.

The impedance analyzer consists of two units to minimize footprint – a digital board and an analog front-end/excitation board. The Digital part consists of a microprocessor, FPGA, ADC, DAC, a clock source and a power supply/battery management unit. The analog part consists of a low-noise voltage converter, excitation signal amplifier, analog front-end amplifiers and signal multiplexers (Fig. 4.1).

The 32-bit MCU controls the digital board. The tasks for the processor are as follows: analyzing the configuration and system control, communications, and low-speed signal processing. FPGA's main tasks are data exchange with analog-to-digital (AD) and digital-to-analog (DA) converters and digital signal processing (DSP). The analyzer is accessible through the local access point and the web page as well as through a TCP connection to the host system. Measurements data is exchanged between the analyzer and host PC with the aid of the LabVIEW application through the TCP connection.

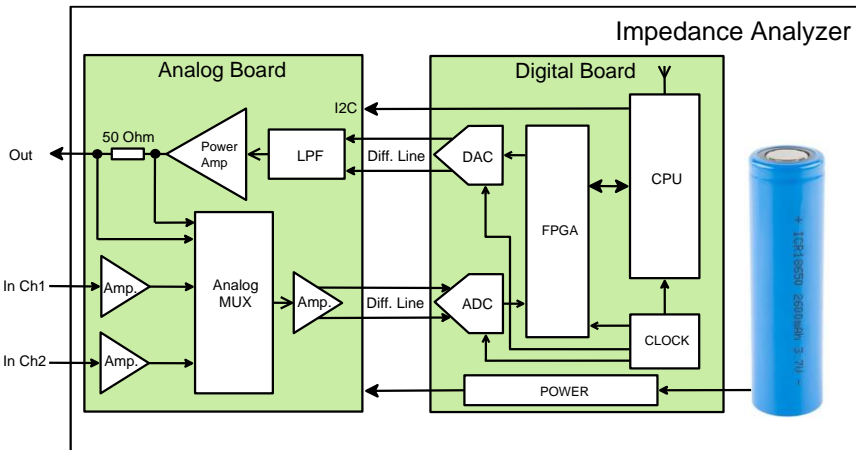


Fig. 4.1. Structure of the impedance analyzer.

WiFi bandwidth is too small to transfer raw data from the AD converter, so the raw data is filtered and down-sampled. Down-sampled real and imaginary parts of signals are converted to magnitude and phase information. MCU configures the ultra-low jitter clock generator, and the clock signal is delivered to ADC, DAC and FPGA. Balanced lines are fed between the boards to minimize the noise of analog signals. LVDS pairs also connect ADC and DAC interfaces to FPGA. The power management unit is responsible for the supply voltages and battery management – low voltage shutdown and charging.

The analog board consists of the front-end amplifiers, excitation signal driver, multiplexers, anti-alias filters and voltage converters for analog electronics. MCU controls the board through the I2C interface, and the MUXs are controlled directly by FPGA through the GPIO for high-speed multiplexing.

4.2.1 The digital board of the analyzer

The digital board is built on Espressif ESP8265 microcontroller, core is based on the Tensilica L106 32-bit RISC processor running at 80 MHz. The microprocessor is in a small 32-pin QFN package and includes WiFi b/g/n transceiver. The processor selection depends on communication interfaces, small packages, low current consumption, and embedded program flash memory. MCU has two serial interfaces for hardware control, one RS232 interface for serial-to-USB converter and GPIO pins for power control. Communication between the MCU and FPGA occurs through the I2S interface. It is a bi-directional synchronous serial interface with word alignment. The MCU I2S controller has direct memory access (DMA) capability, and a data transfer between FPGA and MCU creates minimal load to MCU.

There are double input buffers in MCU – while one buffer is transmitted through the WiFi interface, the FPGA fills the second buffer. In case of gaps in WiFi transmission, the FPGA has a long FIFO, which is used to handle the WiFi transmission gaps. In the case of FPGA, the FIFO overrun data will be lost, and the overrun condition will be signaled to MCU. The I2S controller is connected to a high-speed streaming data FIFO buffer, and a memory-mapped register bank is for configuration and control from the FPGA side. The I2C bus is used for clock generator configuration and analog board control purposes. RS232 interface is used for a USB connection and firmware downloading. Another option is to update the firmware through the WiFi connection. Block schematic of the digital board is shown in Fig. 4.2.

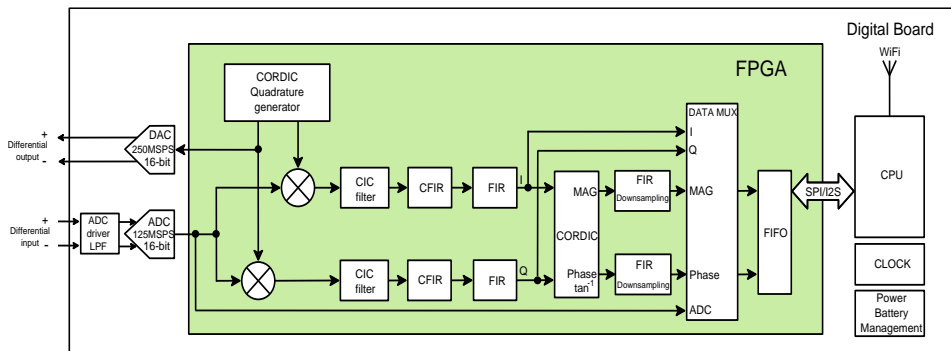


Fig. 4.2. Structure of the digital board.

The main tasks for FPGA are signal processing, excitation signal generation, data buffering and being a communication interface to MCU. The type of the FPGA is the Intel MAX10 series M16SAU169. It is embedded with flash FPGA in BGA with 169 pins package. FPGA selection is based on chip size and minimal external components requirements. There are 16000 Logic Elements in FPGA, and current FPGA resource utilization is 55%. The current design is capable of running at a 200 MHz clock frequency.

The Clock Generator is based on SiliconLabs Si549 ultra-low jitter programmable crystal oscillator. The oscillator frequency can be programmed from 200 kHz to 800 MHz. High-speed precision ADCs require a very low jitter to achieve a high SNR ratio. Si549 oscillator jitter is only 90 fs, but low jitter devices' power consumption is also high – 200 mW for the Si549. Renesas 1:4 LVDS fanout buffer shares the clock signal between the FPGA, ADC and DAC, which increases the jitter by 34 fs. As a result, the total clock jitter is approximately 0.12 ps. According to the ADC datasheet, the 0.12 ps jitter results in an SNR ratio of about 77 dBc at 80 MSPS. Further jitter reduction is not reasonable as SNR improvement is minimal compared to the increased oscillator and fanout buffer power requirements.

The digitizer ADC is based on Analog Devices AD9265 converter. ADC resolution is 16-bit, the maximum sampling frequency is 125 MSPS, and the analog input bandwidth is 650 MHz. The Signal-to-Noise Ratio (SNR) is 79dBFS, Spurious-Free-Dynamic-Range (SFDR) is 88 dBc, and Effective Number of Bits (ENOB) achieves 12.8 bits. The selection of ADC is a trade-off of power consumption and speed. As the impedance analyzer is designed as a wearable battery-powered device, the selection of ADCs is limited to 80 MSPS speeds. The power consumption of the selected ADC is 310 mW. Entirely differential ultra-low noise ADC driver ADA4930 drives the ADC input differentially. The ADA4930 has a -3 dB bandwidth at 1.35 GHz at the gain of 1 and a slew rate of 3400 V/us. This is sufficient performance to drive 16-bit ADC at speeds of 125 MSPS. The ADC input is filtered by third-order LC anti-alias filter with a cut-off frequency of 30 MHz. The ADC input driver is configured to accept differential or single-ended bipolar signals in the range of +/- 1V. With an internal reference voltage source, the LSB value for the AD9265 converter is 15 μ V.

DAC converter is from Maxim Inc, MAX5891; it has a 16-bit resolution and a sampling rate of 600 MSPS. Power consumption is 300 mW at full speed. Although such a high speed is unnecessary for our application, the selection was based on power consumption at the sampling rates used in the analyzer – 80 to 200 MSPS, reducing the power consumption to 130–170 mW. The DAC has a current output from 2 to 20 mA, and its Spurious-Free-Dynamic-Range (SFDR) is 90 dBc.

The ADC and DAC converters require several independently regulated voltages for low noise operation. The DAC converter requires five different power sources for analog, digital and interface parts: 1.2 V, 1.8 V and 3.3 V, and the ADC converter needs three supply voltages: 1.8 V and 3.3 V. All regulators are based on low-dropout linear regulators (LDO) while switching regulators are avoided for the best noise performance. The realization of the CIA digital board is shown in Fig. 4.3.

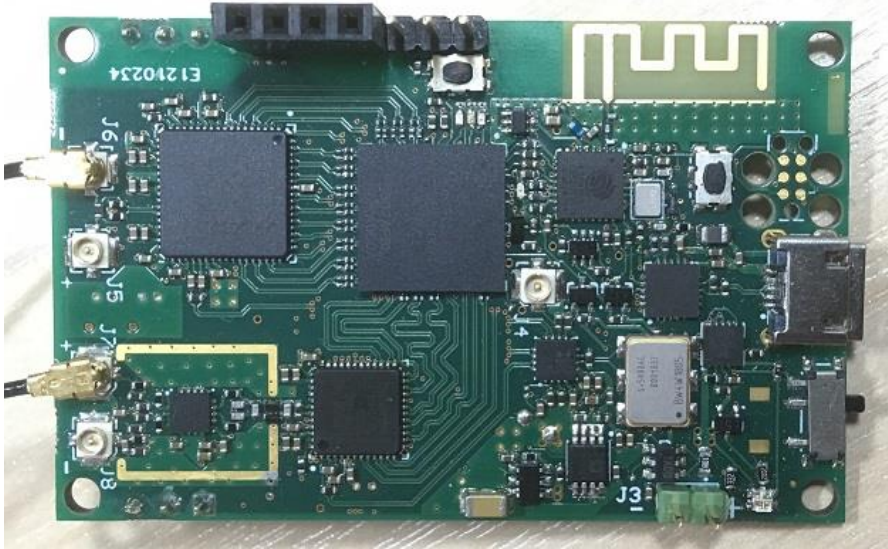


Fig. 4.3. Compact Impedance Analyzer digital board.

4.2.2 The analog board of the analyzer

The main functionality of the analog board is the conversion and amplification of input signals to the input range of the AD converter and amplifying the DA converter's output current to meet the specifications for the excitation signal. The analog board also includes a DC offset regulator and power supplies for the excitation and front-end amplifiers. Block schematic of the analog board is shown in Fig. 4.4. Feedback circuitry of the op-amps of the input signal path is shown in a general configuration. The inputs may be configured as trans-impedance (TIA) or voltage amplifiers according to the measurement need.

A DC-offset regulator can compensate for the high baseline level of the input signal if it drives amplifiers to saturation. MCU adjusts the offset voltage and can be switched off if not needed.

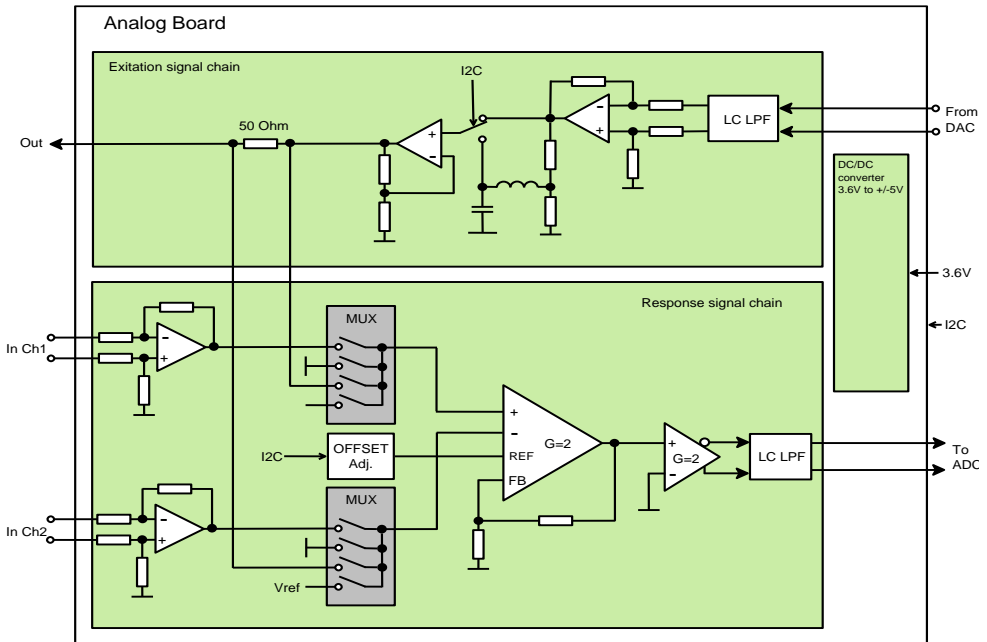


Fig. 4.4. Structure of the analog board.

There are separate voltage converters for input signal path amplifiers and excitation signal power amplifiers. Separation is necessary to provide enough current to the excitation amplifier and reduce the noise level caused by crosstalk between input/output paths through the supply lines. As the power supply for the impedance analyzer is 3.7V LiPo battery voltage, it has to be boosted up to the 5 V level and the -5 V has to be converted from this. At least +/-4.5 V power voltages are needed for operational amplifiers and power amplifiers to meet specified requirements.

The voltage conversion has two stages. First, the 3.7V is converted to the 5 V by Texas Instruments LM2775 switched capacitor voltage doubler. The LM2775 operates at a switching frequency of 2 MHz and provides a 200 mA current with an efficiency of 75 %. The next step is to convert +5 V to -5V by voltage inverter. Texas Instruments flying capacitor voltage inverter LM27761 is used for that purpose. The LM27761 also operates at 2 MHz and provides a 250 mA current with an efficiency of 90%. Inductor-based boost converters are avoided to achieve lower noise levels. The first converter for +5V restricts the total current to 200 mA, which leads to a maximum load for +/- 5V rails of 80 to 90 mA when current consumption is very high for the specified efficiencies. Further, both power rails are regulated by low noise 120 mV dropout LDO regulators to +/-4.8 V. Current limitation of 90 mA sets restrictions to high-speed op-amp selection.

4.2.3 Input signal path

The frontend input signal amplifiers are based on Analog Devices ADA4817 op-amps. The ADA4817 is a 1 GHz op-amp that can provide a 2Vpp output swing at 200 MHz. Its current consumption is 19 mA, input resistance 500 GΩ, and input capacitance 1.3 pF. This op-amp can be used in trans-impedance amplifier (TIA) configuration, meeting the design requirements. The input stage can be configured as TIA by a voltage amplifier or differential amplifier for mounting required resistors onto the PCB. The output signal of

the input amplifiers is fed to the multiplexers. Analog multiplexers are configured by software through the FPGA. Multiplexers used in the analog board are AD8184 from Analog Devices. The AD8184 is a 700 MHz bandwidth 4-to-1 multiplexer with a power consumption of 4.5 mA. One input from both multiplexers is connected to the excitation signal path current as a shunt for excitation signal measurements current amplitude by configuring the multiplexers to measure:

- U_{in} of channel 1.
- U_{in} of channel 2.
- U differential between channel 1 and channel 2.
- Excitation amplifier output voltage.
- Excitation voltage (after the shunt resistor).
- Excitation current (voltage on shunt resistor over shunt resistance).

Outputs of multiplexers are fed to the differential amplifier AD8130 from Analog Devices. The AD8130 has a bandwidth of 270 MHz and current consumption of 10 mA. Differential amplifier gain is set to 2. Differential ADC driver ADA4950 converts the single-ended output of the differential amplifier to balanced output from Analog Devices. The bandwidth of ADA4950 is 750 MHz, its current consumption is 10 mA, and amplifier gain is set to 2. The total quiescent current consumption for the input signal path is 67 mA, and with the input signal being present, it still meets the total current consumption limit of 90 mA.

4.2.4 Excitation signal path

The DA converter supports a 2mA to 20mA full-scale output current range at the requirements for impedance analyzer excitation of +/-3 V output swing and +/-50 mA output current limits. The excitation signal power amplifier has to be used to meet specified parameters. The differential output of the DA converter has to be converted to single-ended output using a suitable power amplifier with differential input THS3215 from Texas Instruments. The differential to Single-Ended DAC Output Amplifier THS3215 has 270 MHz bandwidth and can supply 140 mA current while the quiescent current is 30 mA. As the excitation path power supply is limited to 90 mA, the total current of 60 mA is available from the excitation output. The output does not provide a rail-to-rail swing hence the output voltage headroom from the power supply is 1.5 V limiting the maximum output swing to +/- 3.3 V. Output impedance at 40 mA current is 0.05 Ohm. In the input of the power amplifier, a third-order Butterworth anti-alias filter is used with a cut-off frequency of 35 MHz. The THS3215 consists of two parts – the preamplifier and power stage. Power stage input can be internally switched to preamplifier or external input. That feature allows using an additional external filter and voltage divider to change the cut-off frequency and output voltage. Using the external filter and voltage divider makes it possible to use the excitation output for lower signal levels still using the full dynamic range of the DA converter. The realization of the CIA digital board is shown in Fig. 4.5.



Fig. 4.5 Compact Impedance Analyzer analog board.

4.2.5 Digital signal processing in the FPGA

The first task of the FPGA is to generate an excitation signal feeding DA converter. Excitation signals can be locally generated or received from MCU. Signals of different types can be generated – sinusoidal single or multi-frequency, meander, triangle, binary pattern and frequency sweep of a sinusoidal signal. Signal generation is based on a numerically-controlled oscillator (NCO) and CORDIC engine (for COordinate Rotation Digital Computer) for quadrature signal generation. The Cordic method is used as it is a better alternative to the table-based sinusoidal signal generation, easily implemented in FPGA, fast and requires little FPGA resources (no multipliers needed).

The second task is down-sampling, magnitude/phase calculations and buffering of the input signal. Demodulation requires multiplying the input signal with the quadrature excitation signal as real and imaginary components of the complex signal are

$$\text{Re}(V) = |V| \sin(\varphi); \text{Im}(V) = |V| \cos(\varphi) \quad (4.1)$$

Multiplication is performed with the same speed as the sample rate, limited by AD converter speed in the analyzer, which is 80 MSPS. As changes in biological origin signals are relatively slow, the required bandwidth is usually less than 5 kHz, allowing down-sampling of the real and imaginary components to the sample rate of 10 kSPS. Down-sampling requires limiting the signal spectrum to half the sampling rate to avoid aliasing. Filter length to limit frequency range to 5 kHz at a sampling rate of 80 MSPS is exceptionally high and cannot be implemented as a single filter. For example, the FIR filter with a passband of 5 kHz and stopband of 10kHz with attenuation of 96 dB requires a 70000-tap filter. It is clearly impossible to build a described filter with available FPGA resources. The solution is to downsample in multiple stages, gradually decreasing the sample rate, easing the anti-alias filter requirements. The designed filter is split into four stages where the most extended filter is the size of 250-tap. As the sampling rate is only

250 kSPS for a 250-tap filter, there is time to calculate response sequentially using only one multiplier.

The second task is demodulation, filtering, down-sampling, magnitude/phase calculation and buffering of the input signal. The signal path of the incoming data is shown in Fig. 4.6.

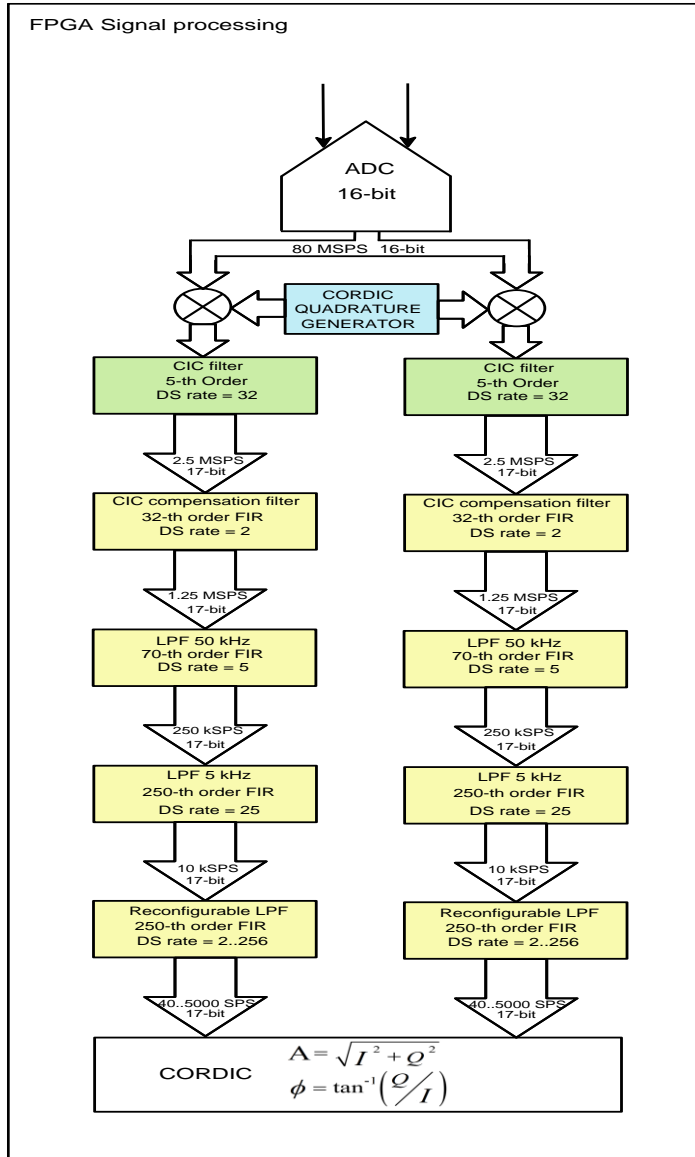


Fig. 4.6. Signal path in the FPGA.

However, as the first stage of the down-sampling filter runs at full speed of 80 MSPS and the FPGA's maximum clock is 200 MHz, there is not enough time to calculate the response in two clock cycles as the multiplier resource in FPGA is limited. Therefore, the first down-sampling filter is the cascaded integrator-comb (CIC) filter, invented by

Eugene B. Hogenauer, which is not using multipliers but uses only addition and subtraction. The CIC filter has a down-sampling rate of 32, resulting in a sample rate of 2.5 MSPS. Conventional FIR filter can handle such sample rate if filter order is relatively low. The downside of the CIC filter is high-speed frequency roll-off, which starts immediately from 0 Hz. If a flat frequency response is required in the passband, a special compensation filter has to be used. In the current design, a 32-tap CFIR compensation filter is used to achieve 0.1 dB flatness in the 250 kHz passband. The sample rate is reduced by 2 (1.25 MSPS), and the stopband starts at 600 kHz. The frequency characteristic of the CIC filter is shown in Fig. 4.7.

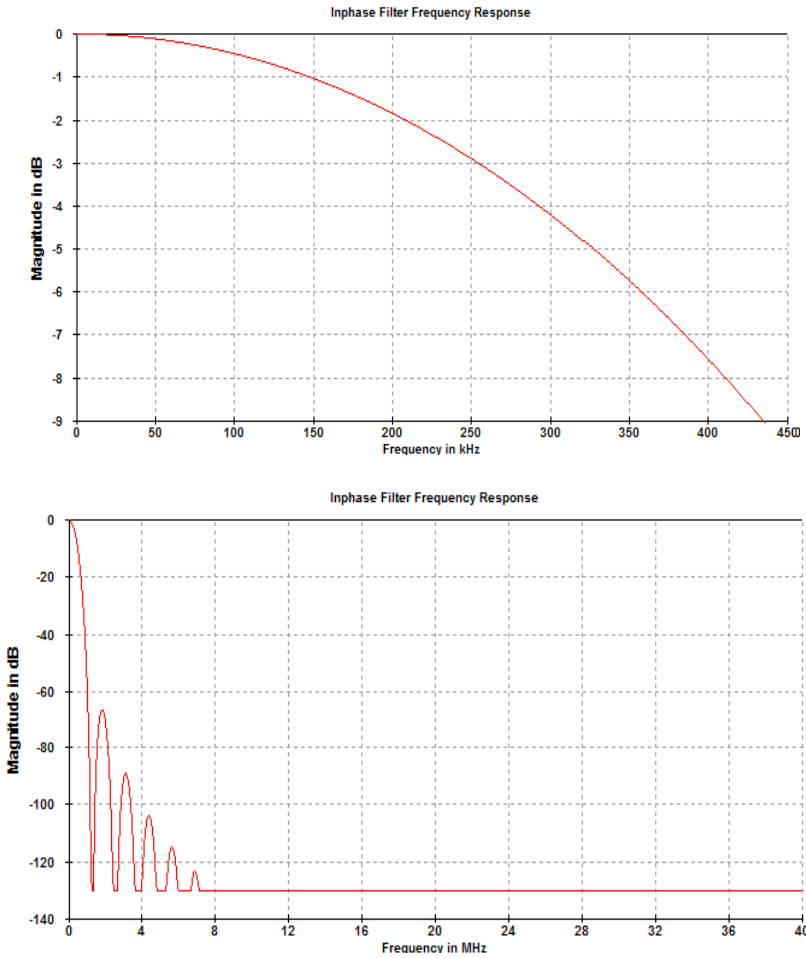


Fig. 4.7. The frequency characteristic of the CIC filter in the full frequency range and a zoomed roll-off from 0Hz to 450 kHz.

As seen in Fig. 4.8, the specific frequency response of the CFIR compensating filter (blue) applied to the CIC filter (red) results in flat frequency response in the range of 0 Hz to 250 kHz with stopband attenuation of 96 dB (black).

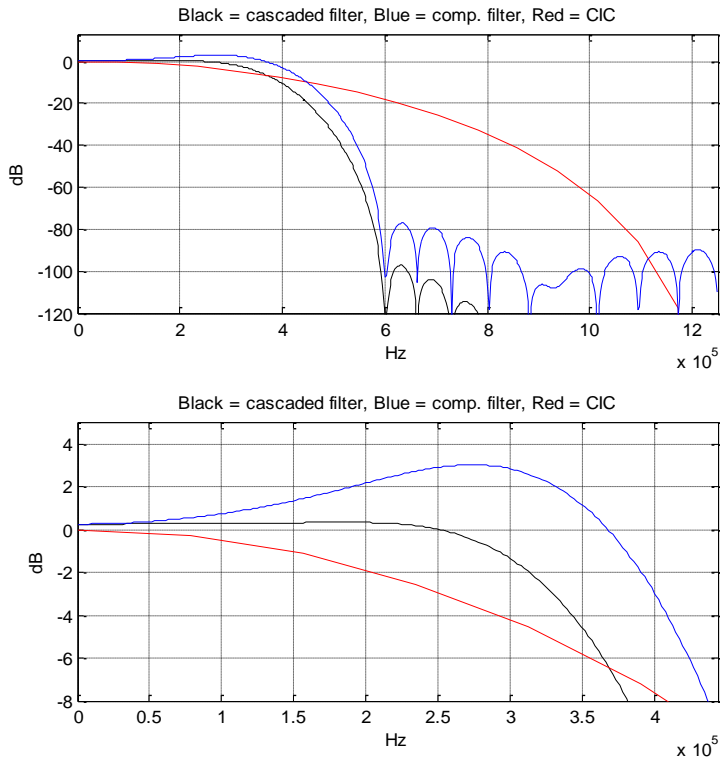


Fig. 4.8. The frequency characteristic of the compensation filter and the resulting frequency response.

The third downsampling filter has a rate of 5 (250 kSPS), stopband starts at 125 kHz, as seen in Fig. 4.9.

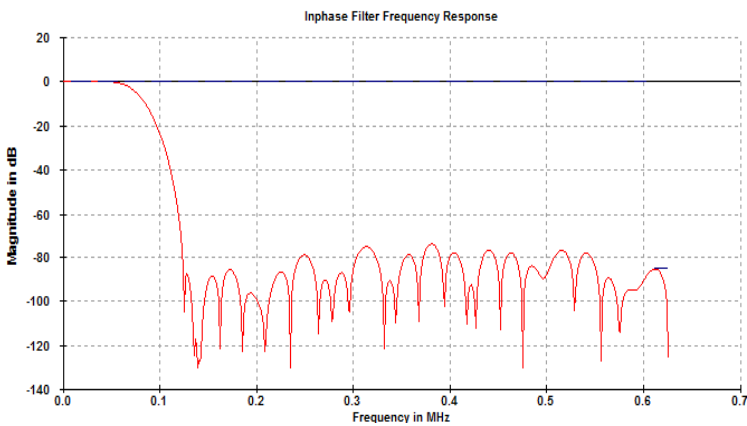


Fig. 4.9. Frequency response of the third down-sampling filter.

The fourth down-sampling filter has a downsampling rate of 25 (10 kSPS), stopband starts at 5 kHz, as seen in Fig. 4.10.

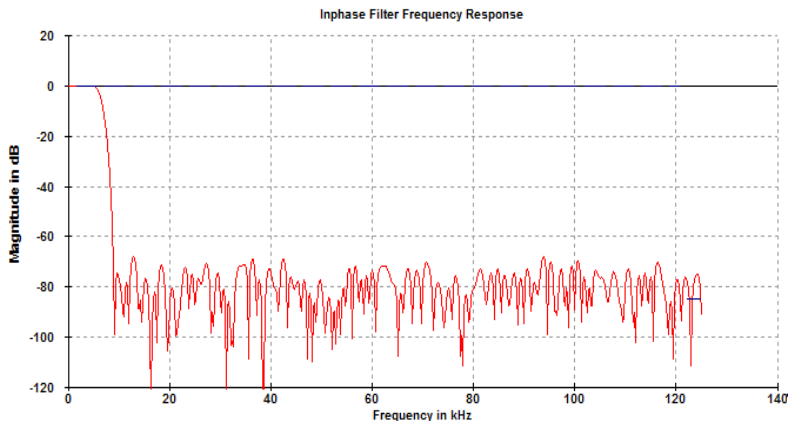


Fig. 4.10. Frequency response of the fourth down-sampling filter.

The last down-sampler is reconfigurable, allowing adjusting the output sample rate from 40 to 5000 SPS. The complex signal's real and imaginary components can be transmitted through the data multiplexer directly to the MCU, or the magnitude and phase information can be calculated. Data multiplexer can also select a signal directly from the ADC converter, allowing real raw data from the ADC. The data rate from the ADC is too high to be streamed continuously – an interface between the FPGA and the WiFi bandwidth doesn't allow continuous streaming. The maximum continuous data packet from the ADC is limited by FPGA's FIFO buffer size, which is 16 kWords. Calculations of magnitude and phase are realized with the CORDIC engine in a vectoring mode.

4.3 Performance of Digital Board

Noise measurements are made to evaluate the quality of the signal generation DAC and the ADC with the input driver. Measurements are conducted without an analog board and based on the direct balanced connection between the DAC output and ADC driver input. First, the quality of the DAC signal generation was verified. The FFT analysis of the CORDIC output shows that 1 MHz digital sinewave has an SNR ratio of 97.5 dB, which is in good agreement with 16-bit sinewave, as seen in Fig. 4.11.

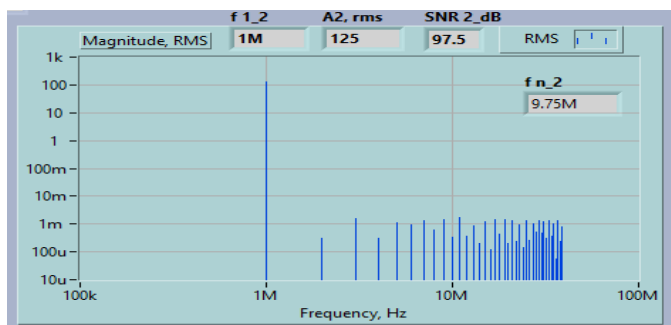


Fig. 4.11. SFDR analysis of the CORDIC digital output.

ADC Spurious-Free-Dynamic-Range (SFDR) measured at frequency 1 MHz was 86.5 dBc. Datasheet of the ADC AD9265 specifies 88 dBc SFDR at 2.4 MHz. The 86.5 dBc result, shown in Fig. 4.12, is in good agreement with the specification, with some signal degradation introduced by the signal source (DAC MAX5891) and ADC driver (ADA4930). The measured 1 MHz sinewaves were analyzed similarly.

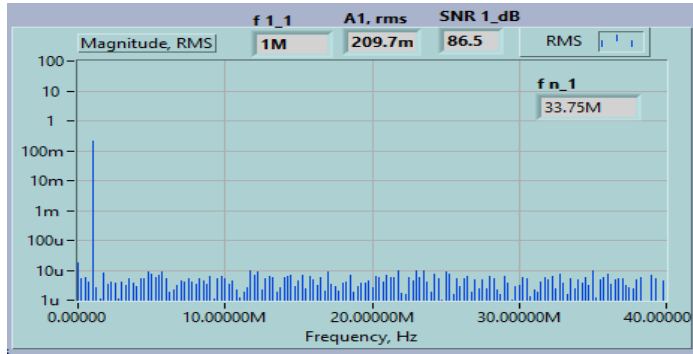


Fig. 4.12. SFDR analysis of the acquired signal from ADC.

Finally, the ADC noise was measured while ADC driver input was shorted. Noise with the amplitude of 168 μVpp (11 LSB) and 36.8 μV RMS was measured (Fig.4.13), which matches the ADC specifications.

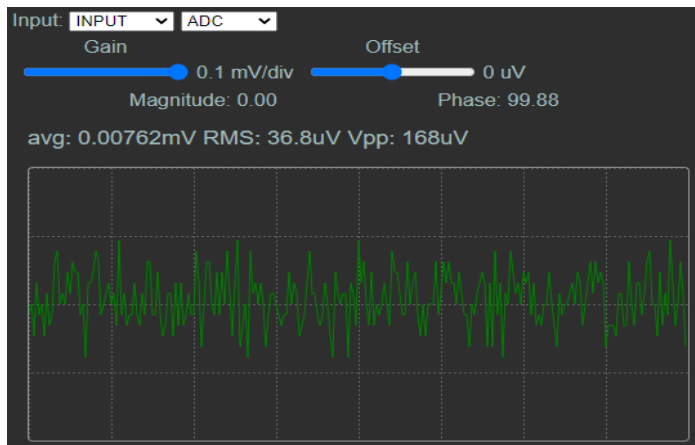


Fig. 4.13. Output noise from the ADC converter.

Datasheet of the ADC AD9265 specifies the input-referred noise as 2.17 LSB (33.1 μV), compared to measured 36.8 μV – it is a fully satisfying result. Peak-to-peak noise levels also match the datasheet, as seen from the grounded input histogram in Fig. 4.14, where the peak noise ranges from 11 to 12 LSB, which is approximately 168 μV as measured (see Fig. 4.13).

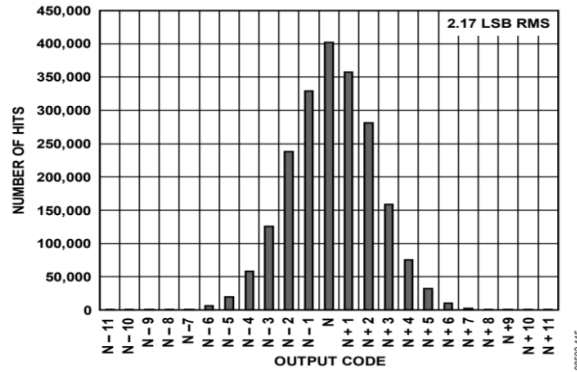


Figure 15. AD9265-80 Grounded Input Histogram

Fig. 4.14. Output noise histogram.

Those measurements confirm that the hardware design of the digital board works as specified and that noise levels meet the manufacturer's specifications.

4.4 Measurement Part Instrumentation

The measuring device, a compact impedance analyzer (CIA), was developed based on both the purpose and the factors described in the previous chapter. The composition and basic parameters of the CIA are described in section 4.2.

The CIA has two identical measurement channels that can be used for both separate and differential measurements. According to the commands selected from the control program, the channels and the operating mode are selected through the high-speed multiplexers of the analog module. Fig. 4.15 shows a structural diagram of one measuring channel. Excitation voltage V_{exc} came from the low output impedance buffer of the 16-bit D/A converter and passed via inverting buffer B for recording.

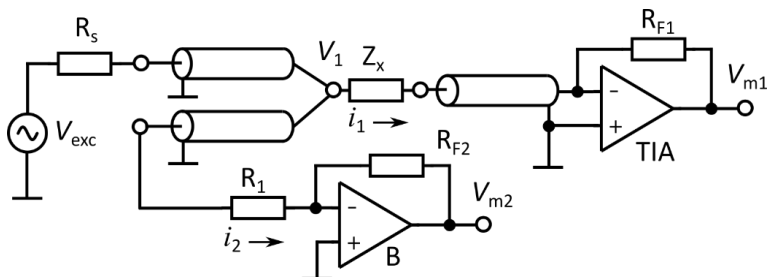


Fig. 4.15. Structural diagram of the CIA measurement channel.

Fig. 4.16 on the next page gives a more detailed circuit diagram of one measuring channel. R_s is a $50\ \Omega$ precision resistor matching the output with the output cable connected to the object under test Z_x . The components C_{co1} , L_{co1} and R_{co1} are the capacitance, inductance, and resistance of the output cable. C_{co1} , L_{co1} and R_{co3} represent the same parameters of the input cable. The current through the object is converted to a voltage by a trans-impedance amplifier TIA with a transmission factor equal to the

resistance R_{F1} . Voltages V_{m1} and V_{m2} are transmitted through a multiplexer, a differential voltage amplifier, and matching circuits to the input of a 16-bit A / D converter.

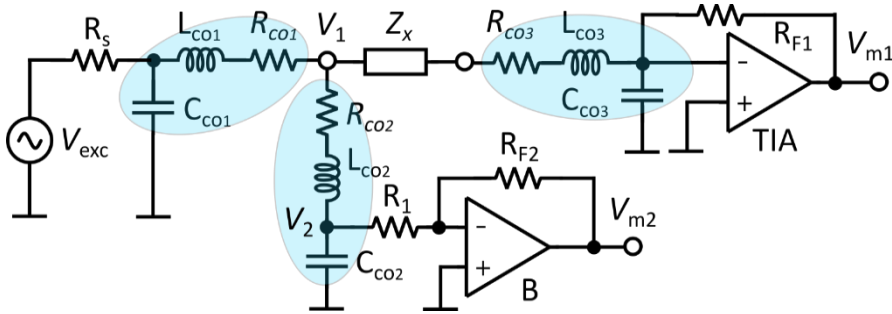


Fig. 4.16 Structural diagram of the CIA measurement channel.

4.4.1 Initial calibration and corrections

The initial calibration sets the impedance measurement scale for the CIA base solution channels. Other corrections relate to specific measurement schemes and interconnection cables.

INITIAL CALIBRATION. Three consecutive measurements are performed for the initial calibration by recording the readings obtained with short-circuit, open-circuit and reference resistor. Then, the complex form calibration factor K is calculated over the used frequency range $i = 1$ to n , where n is a number of frequency points.

$$K(i) = \frac{\tilde{Z}_{et}(i)}{1} = \frac{1/(\tilde{Z}_m(i) - \tilde{Z}_{sh}(i)) + 1/\tilde{Z}_{op}(i)}{\tilde{Z}_{et}(i)}, \quad (4.2)$$

where Z_m is measured impedance, and Z_{sh} , Z_{open} , Z_{et} , the short circuit, open circuit, and etalon resistor impedances. The short-circuit (zero impedance) and etalon resistors used for the initial calibration were connected to the CIA through a minimum-sized adapter. Their impedance spectra were measured in advance with the most accurate measuring instrument available, in the current case, a Keysight E4990A Impedance Analyzer.

Since connection cables are usually required for the actual measurement, some associated capacitance C_{co3} is always present at the TIA input. For an ideal TIA, this does not affect because the voltage at the input is zero. However, in practice, it slightly alters the transfer coefficient at higher frequencies as the TIA open-loop gain decreases. Therefore, a 10-pF capacitor can be included in the adapter corresponding to 10–12 cm cable length. This solution is helpful if the calculational correction of the impact of connection cables is used. However, if the effect of the cables is corrected together with the initial calibration as described below, no additional capacitor is required.

CORRECTION OF THE IMPACT OF CONNECTION CABLES. Two options were studied to correct the impact of cables:

- 1) Calculated compensation for the effects of cables.
- 2) Compensation in the process of the initial calibration.

In the case of calculated compensation, the effect of the capacitance of the input cable is small and compensated during the initial calibration. The effect of L_{co3} and R_{co3} is easily correctable by subtracting their impedance from the measurement result. However, the resistance R_{co3} increases at higher frequencies due to the skin effect. The inductance of the coaxial cable L_{co3} depends on more parameters than the inductance of the straight wire (e.g., the distance of the screen and grounding points). These dependencies make it more challenging to determine the effect of a cable. Fig. 4.17 illustrates the influence of the skin effect and variation of the inductance of the 10 cm length Hirose U.FL-LP-068HF ($d = 1.13\text{mm}$) coaxial cable measured with a Keysight E4990A Impedance Analyzer.

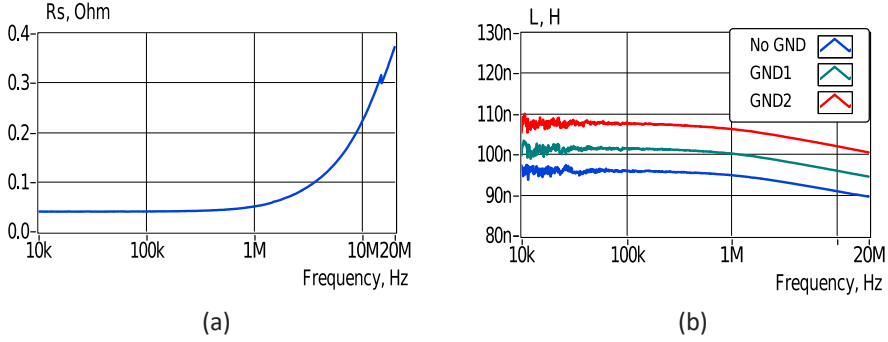


Fig. 4.17 Frequency dependence of the series resistance of the 10 cm length Hirose U.FL LP 068HF coaxial cable (a) and its inductance variation on grounding connection (b).

Correcting the effect of the output cable is more complicated because R_s and C_{co1} form a frequency-dependent voltage divider, which also depends on the impedance of the rest of the circuit, including Z_x .

Denoting the sum of the inductance L_{co2} of the excitation voltage measuring cable and the frequency-dependent loss resistance R_{co2} with impedance Z_1

$$\tilde{Z}_1 = j\omega L_{co2} + R_{co2}(\omega) \quad (4.3)$$

and the capacitance C_{co2} of the same cable and input resistor R_1 , with the impedance Z_2 , which is expressed as their parallel connection:

$$\tilde{Z}_2 = \frac{1}{1/R_1 + 1/\tilde{Z}_{C_{co2}}} = \frac{1}{1/R_1 + j\omega C_{co2}} \quad (4.4)$$

where $Z_{C_{co2}}$ is the impedance of the capacitance C_{co2} of the voltage V_1 measurement cable. Due to the voltage drop across the cable impedance Z_1 , $V_2 < V_1$. The classical voltage divider formula finds the voltage division factor $K_D = V_2 / V_1$ through the impedances Z_1 and Z_2 as

$$K_D = \frac{\tilde{Z}_2}{\tilde{Z}_1 + \tilde{Z}_2} \quad (4.5)$$

To find the voltage V_1 on the object to be measured, the input voltage V_2 of the buffer amplifier is multiplied by the correction coefficient $K_{co2} = 1 / K_D$. Using (4.3), (4.4), and (4.5), K_{co2} expresses as:

$$K_{co2} = \tilde{Z}_1 \left(\frac{1}{R_1} + \frac{1}{\tilde{Z}_{C-co2}} \right) + 1 = (R_{co2}(\omega) + j\omega L_{co2}) \left(\frac{1}{R_1} + j\omega C_{co2} \right) + 1 \quad (4.6)$$

Multiplying the members of the equation, we get:

$$K_{co2} = \left(\frac{R_{co2}(\omega) + j\omega L_{co2}}{R_1} - R_{co2}(\omega) j\omega C_{co2} - \omega^2 L_{co2} C_{co2} \right) + 1 \quad (4.7)$$

The correction coefficient K_{co2} does not depend on the impedance of the object Z_x and the impedance of the input cable. The influence of the excitation cable impedance does not require an additional correction because K_{co2} has already corrected the relation of V_1 and V_2 . Experiments with R-C test circuits prove the validity of the proposed initial calibration and cable influence correction methods illustrated in the following section.

The disadvantage of the described computational method is the complexity of determining the parameters of the cables. As an alternative, compensation of the impact of cables in the initial calibration process was also tested. In this case, the initial calibration according to (4.2) was performed with the cables used in the following measurements. The tests with shorter (10–15 cm) cables showed that the results were approximately equivalent to those obtained by the computational correction method.

The results obtained with two compensation methods for the impact of connection cables are presented in the following section.

4.4.2 Resolution and accuracy

NOISE AND DISTORTIONS IN THE MEASUREMENT CHANNEL. One of the characteristic parameters of the developed CIA is the spectral composition of the generated excitation signal and the measured response signal, which characterizes the signal-to-noise ratio (SNR) of the measurement channel.

Fig. 4.18 shows the magnitude spectra of the excitation signal and the measured response signal. The ratio of the main harmonic component of the signal to the levels caused by noise and non-linear distortion gives 94.1 dB at the output of the DA converter at 625 kHz and 75.6 dB for the measured response. In Fig. 4.19, the spectra of the response signal at 6.25 MHz and 10 MHz are shown.

ACCURACY OF THE IMPEDANCE MEASUREMENT. The impedance of precision resistors and R-C circuits was measured to evaluate the accuracy of results obtained with CIA. These results were compared with the results obtained with Keysight E4990A Impedance Analyzer. In addition, the measured impedance of the R-C circuits was also compared with the results obtained with Zürich Instrument MFLI Lock-in Amplifier. In all cases, the instruments were pre-calibrated and measurements were not taken within the first 10 minutes after the instrument was turned on.

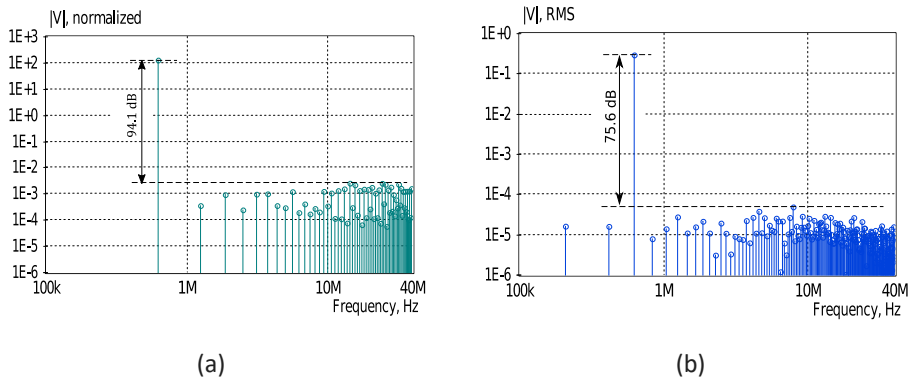


Fig. 4.18 Magnitude spectra of the excitation signal (a) and measured response signal (b), both at the frequency of 625 kHz.

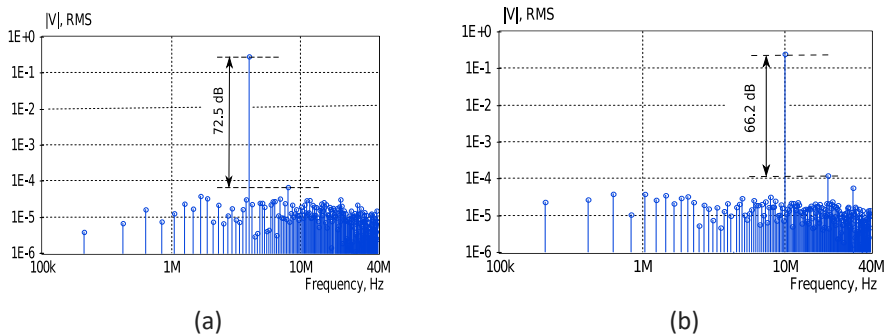
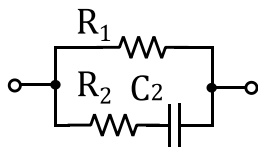


Fig. 4.19 Magnitude spectra of the measured response signal at 4 MHz (a) and 10 MHz (b).

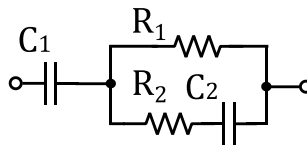
Two test circuits, 1C-2R and 2C-2R, with corresponding magnitude and phase spectra shown in Fig. 4.20, were used for experiments. The capacitances and resistances of the test circuit's elements were specified by measurements made with Keysight E4990A.

Measurement errors are found as the differences between the spectra of the test circuit and spectra measured with Keysight E4990A and CIA. Since the differences in the spectra found also include the E4990A measurement error, obtained differences do not indicate actual values. However, it is assumed that the E4990A results are more than three times more accurate. Fig. 4.21 shows the results with computational correction of the impact of cables (notation "Cab_Corr") and during the process of the initial calibration (notation "Cab_Cal") in the frequency range up to 10 MHz. 2C-2R ZI and 2C-2R ZI stand for Zurich Instrument MFLI results up to 5MHz, which is its highest operating frequency.

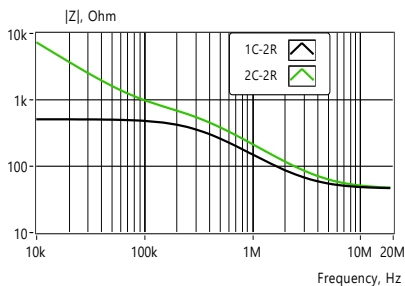
In Fig. 4.22 are shown measurement errors obtained with the same test samples as in the previous test but in the frequency range up to 20 MHz and without Zurich Instrument MFLI results.



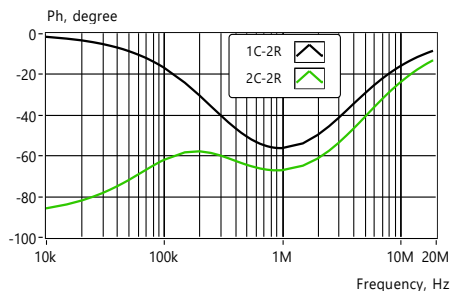
(a)



(b)

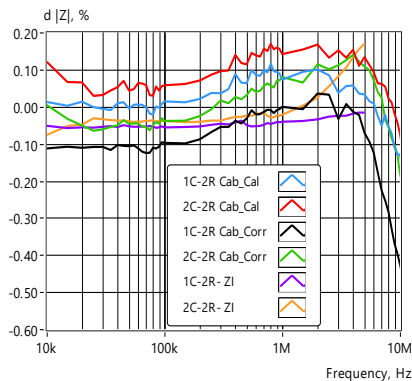


(c)

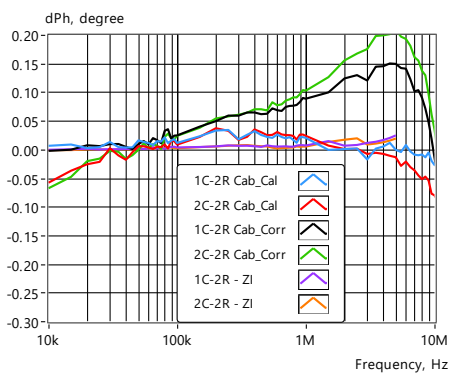


(d)

Fig. 4.20 Impedance magnitude (c) and phase (d) spectra of the 1C-2R (a) and 2C-2R (b) test circuits. Capacitances of C_1 and C_2 are 2.21 nF and 981 pF, resistances of R_1 and R_2 are 49.9 Ω and 500 Ω .



(a)



(b)

Fig. 4.21 Differences of the impedance magnitude (a) and phase (b) with a 1C-2R and 2C-2R test circuits using computational correction of the impact of cables (notation Cab_corr) and during the process of the initial calibration (notation Cab_Cal). 2C-2R ZI and 2C-2R ZI denote Zurich Instrument MFLI results.

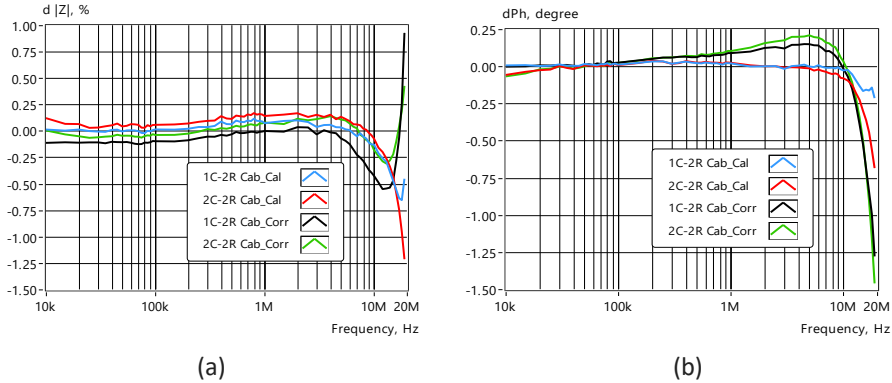


Fig. 4.22 Differences of the impedance magnitude (a) and phase (b) with a 1C-2R and 2C-2R test circuits using computational correction of the impact of cables (notation Cab_corr) and during the process of the initial calibration (notation Cab_Cal).

In Fig. 4.23 are shown standard deviation (STD) of magnitude (a) and phase errors obtained with the same 1C-2R and 2C-2R test circuits during 100 measurements.

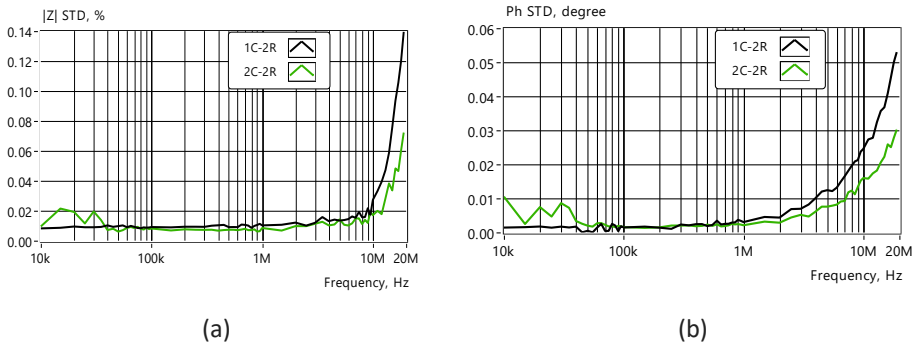


Fig. 4.23 STD of magnitude (a) and phase errors (b) obtained with the same 1C-2R and 2C-2R test circuits shown in Fig. 4.20 during 100 measurements.

4.5 Experimental Measurements of Bioimpedance

4.5.1 Capacitive electrodes

As discussed in the bioimpedance introduction in chapter 2, a two-electrode system suits better for determining EBI model parameters where investigation of the β dispersion area requires measurements of at least up to 10 MHz. In the case of using electrodes with a galvanic connection, several other parameters related to the properties of the interfacial double-layer are added to the model (see section 2.2.2). In addition, the double-layer properties depend significantly on the skin surface conditions (e.g., sweat). The use of non-polarizable electrodes is an alternative that also provides lesser series impedance. However, their surface area is limited, limiting the depth of the current distribution; impedance also depends on the skin surface conditions and attachment to the skin.

The alternative is using large-area capacitive electrodes. In the subsequent experiments, flexible bracelets (Fig. 4.24b) with a thin insulating layer of polyurethane (PUR varnish ECS 71, from ECS Cleaning Solutions GmbH, Germany) were used. The electrodes were positioned on the forearm at a distance of 4 cm, as shown in Fig. 4.24a. The surface area of the electrode is 145 x 18 mm and the thickness of the PUR layer is around 10–20 nm. Obtained parameters are presented in Table 4.1.



Fig. 4.24 Measurement of the forearm impedance at a distance of 4 cm (a) and used flexible capacitive electrode (b).

Since the capacitive electrodes were selected to determine the model’s parameters, the equivalent electrical circuit looks as shown in Fig. 4.23. C_e denotes the total capacitance of two capacitive electrodes and C_s the total distributed stray capacitance between the analyzer’s common (GND) and object. R_{ext1} , R_{int1} , and CPE_1 represent the impedance of the internal part of the tissue, and R_{ext2} , R_{sk} , CPE_2 represent the impedance of the outer part – the skin. The values of resistances R_{ext2} , R_{sk} are doubled, and Q_2 , C_e are divided by two due to the double appearance in the circuit.

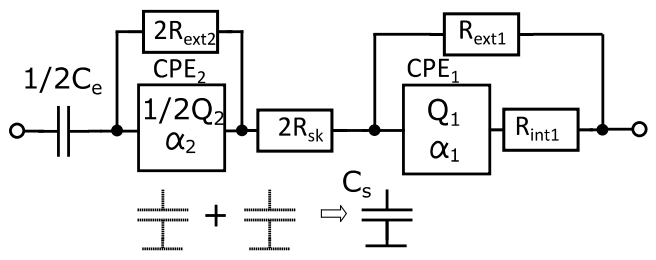


Fig. 4.23 Electrical equivalent circuit of the enhanced EBI model. C_e denotes the total capacitance of two capacitive electrodes and C_s the total distributed stray capacitance between the analyzer’s common (GND) and object. R_{ext1} , R_{int1} , and CPE_1 represent the impedance of the internal part of the tissue, and R_{ext2} , R_{sk} , CPE_2 represent the impedance of the outer part – the skin. The values of resistances R_{ext2} , R_{sk} are doubled, and Q_2 , C_e are divided by two due to the double appearance in the circuit.

There are several options for counting the influence of the distributed stray capacitance C_s . Experiments show that connecting it to the equivalent circuit’s middle point gives the value corresponding to the measured one, 8 pF. Measurement of the stray capacitance C_s with Keysight E4990A is accomplished with the CIA placed on the forearm

phantom. CNLS fitting of the equivalent circuit parameters was conducted on a cohort of 6 subjects (Female: 3 and Male: 3) aged 16 to 80 years.

Table 4.1. Parameters of the equivalent circuit elements.

#	$\frac{1}{2} C_e$	R_{ext1}	R_{int1}	Q_1	α_1	$2R_{ext2}$	$2R_{sk}$	$\frac{1}{2} Q_2$	α_2	Error	R_{ext1}/R_{int1}	Comment
	F	Ω	Ω	$S \cdot s^\alpha$	-	Ω	Ω	$S \cdot s^\alpha$	-	%	%	
1	4.10n	77.9	95.4	151n	0.58	9.70k	4.90	102n	0.81	0.080	18.3	
2	8.00n	42.1	56.9	60.8n	0.66	5.10k	4.40	118n	0.80	0.099	26.1	
3	6.98n	41.3	60.2	11.6n	0.74	13.0k	10.5	68.3n	0.79	0.097	31.2	
4	7.41n	39.5	62.6	14.5n	0.74	8.00k	5.60	50.3n	0.83	0.101	37.0	
5	2.74n	54.1	99.3	19.5n	0.70	20.1k	6.00	21.2n	0.86	0.095	45.5	
6	6.05n	48.1	201	0.66n	0.88	8.10	7.80	50.1n	0.83	0.171	76.0	
1 - 6	5.88n	50.5	95.9	18.1n	0.72	9.32k	6.5	68.3n	0.82	0.11	55.8	Mean values

Measured impedance spectra used for fitting of parameters presented in Table 4.1 are shown in Fig. 4.25.

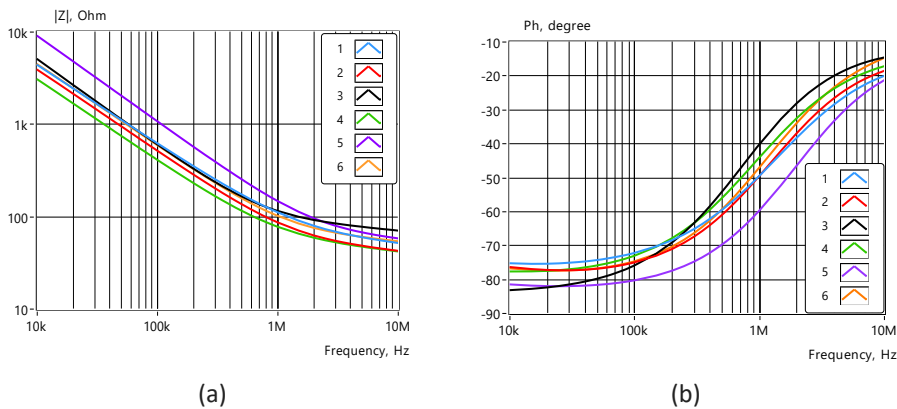


Fig. 4.25 Spectra of the impedance magnitude (a) and phase (b). Numbers are related to persons as in Table 4.1.

The relative magnitude of the impedance of equivalent circuit components shown in Fig. 4.26 characterizes their weight in a sum at different frequencies. We can draw several valuable conclusions based on the proportion of impedance components, e.g., both resistive components of the inner part of a tissue (under the skin) manifest more at higher frequencies, and their influence becomes equal at some point. In addition, the proportion of extracellular resistance continues to increase, but the proportion of intracellular resistance declines with the increase in frequency. The effect of CPE1 only increases at frequencies above 2 MHz, and the influence of the extracellular resistance of the skin becomes considerable only below 100 kHz. Despite its relatively low value (< 10 pF), the influence of stray capacitance increases significantly above 1 MHz and reaches around 2% at 10MHz. Considering that the changes in the impedance magnitude caused by cardiovascular activity are below 1 %, the need to keep the value of stray capacitance constant becomes clear. Fixing the CIA on the arm solves that task.

Once the parameters of the equivalent circuit components are found, they can be used to separate the spectra of the parts of the model. Fig. 4.27 illustrates the impact of the electrode's impedance, and Fig. 4.28 shows the impact of the skin impedance. In both cases, also the spectra of the internal part of the object are shown.

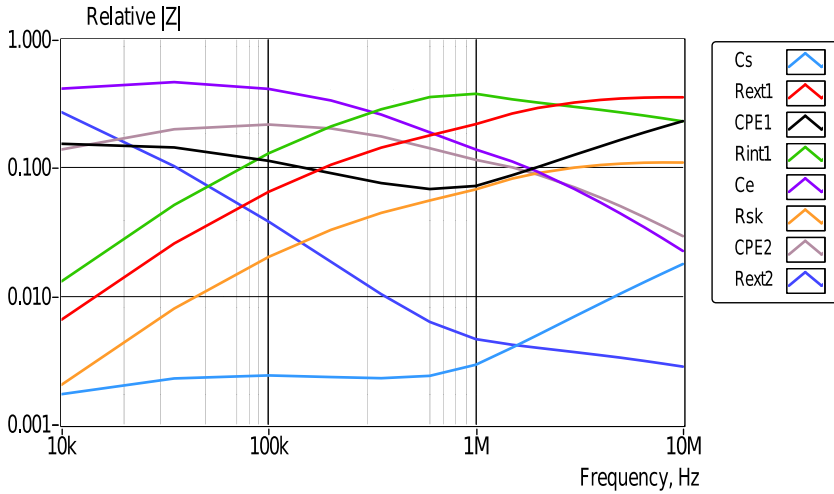


Fig. 4.26 The relative weight of every single component of the equivalent circuit of impedance is given in Fig. 4.23.

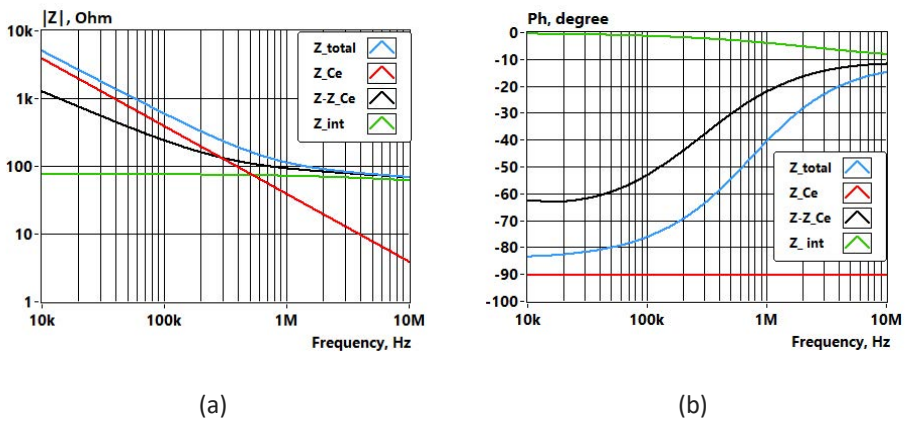


Fig. 4.27 Spectra of the impedance magnitude (a) and phase (b) where Z_{total} denotes total spectra, Z_{Ce} the spectra of electrodes, $Z-Z_{Ce}$ the difference of total and electrode spectra, Z_{int} the spectra of the internal part located under the skin.

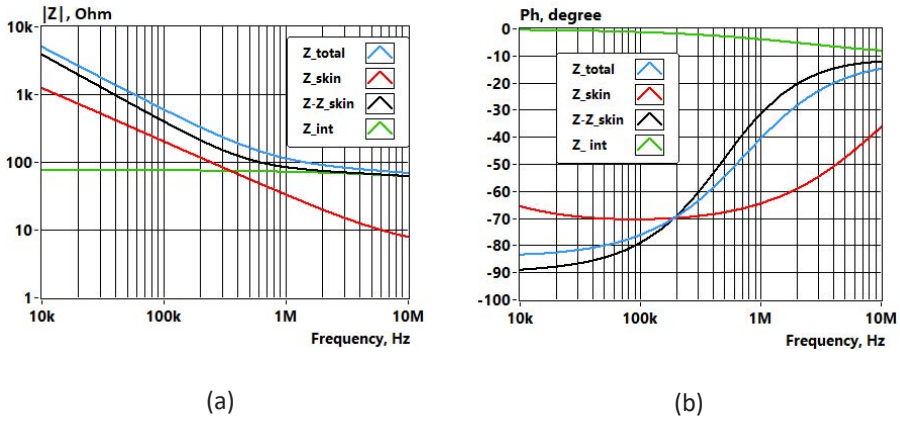


Fig. 4.28 Spectra of the impedance magnitude (a) and phase (b) where Z_{total} denotes total spectra, Z_{skin} the spectra of the skin, $Z-Z_{skin}$ the difference between total and skin spectra, Z_{int} the spectra of the internal part located under the skin.

In Fig. 4.29, the spectra of the internal part are zoomed out for better visualization. Based on the presented result, it can be concluded that the changes in the impedance amplitude and phase of the tissue under the skin are relatively small below 100 kHz and increase significantly at frequencies above 1 MHz. It can also be concluded that the increase in impedance magnitude at lower frequencies is mainly due to the effect of skin impedance.

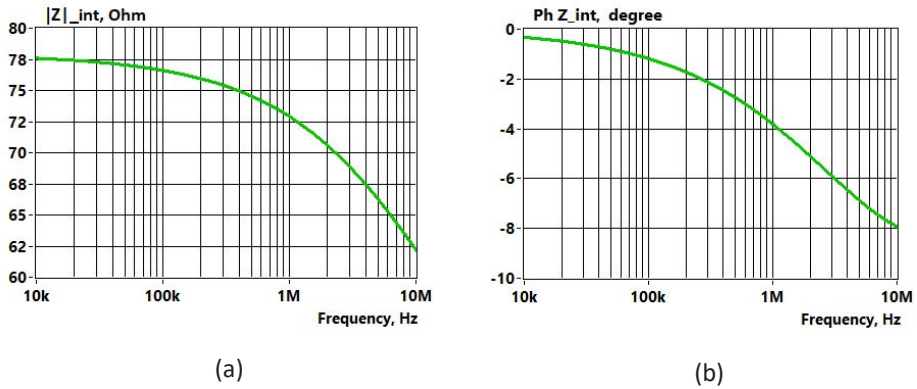


Fig. 4.29 Spectra of the impedance magnitude (a) and phase (b) of the internal part of the forearm tissue located under the skin.

Fig. 4.30 shows the changes in impedance magnitude and phase due to cardio-vascular activity obtained with capacitive electrodes from the left forearm.

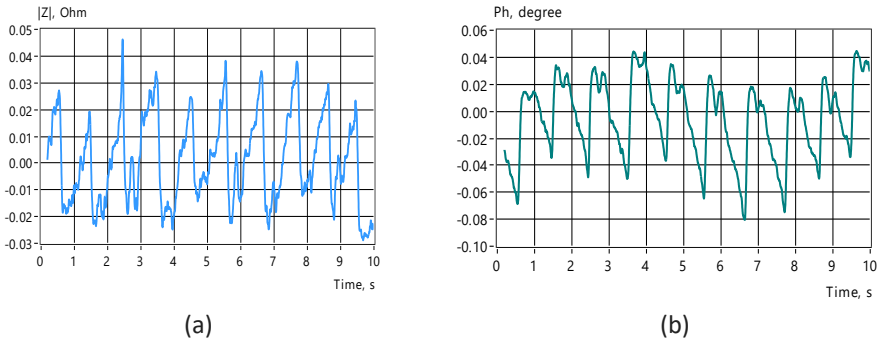


Fig. 4.30 Change of magnitude (a) and phase (b) of the EBI caused by the influence of cardiovascular activity on the left forearm. The results were obtained with capacitive electrodes discussed in section 4.5.1 at a distance of 2cm. The excitation voltage was 50 mV and the frequency 2.5 MHz. The mean value of the impedance was 45.2Ω and phase -37.3° .

4.5.2 Excitation voltage control via digital feedback

Voltage excitation was used to avoid the weaknesses of the current generator described in Chapter 2. However, the disadvantage of using a voltage source is the decrease of the current at higher impedances, reducing the SNR. Excitation voltage was adjusted adaptively using digital feedback to avoid the current decrease. As illustrated in Fig. 4.31, the current remains almost constant in a wide range of impedance. It is limited only by the maximum value of the excitation voltage, similarly to the current source. The advantage of the voltage source is its more straightforward design providing good accuracy, as illustrated in Fig. 21–23.

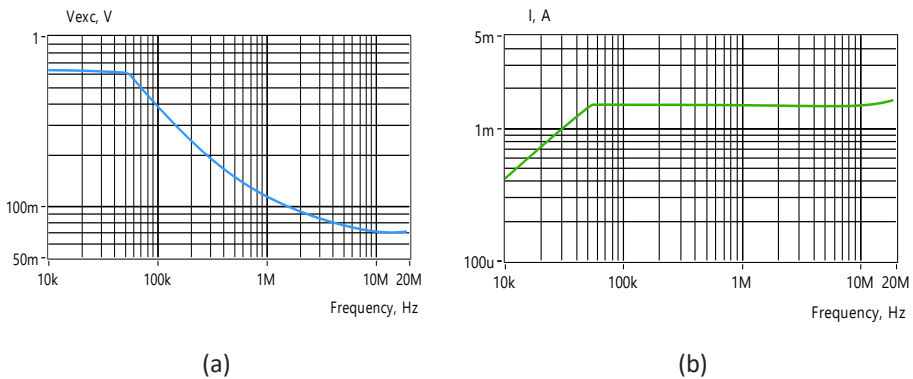


Fig. 4.31 Change of excitation voltage adapted via digital feedback (a) and corresponding current in (b) in a left forearm. The results were obtained with capacitive electrodes discussed in section 4.5.1.

4.6 Summary of Chapter

The chapter focuses on developing a compact impedance analyzer (CIA) suitable for measuring body bioimpedance parameters based on the requirements analyzed in the second chapter and provides the results of experimental EBI measurements accompanied with the fitting of model parameters and investigating their weight in the spectrum.

The first part of the chapter describes and justifies the CIA's hardware design. The following main technical parameters and conditions were defined: 16-bit ADC and DAC resolution with a sample rate of 80 MSPS, WiFi interface for data communication to the host system, and dimensions of 70 x 45 x 20 mm. The impedance analyzer consists of a digital board and an analog front-end/excitation board. The digital part consists of FPGA, a microprocessor, and a power supply/battery management unit. The analog part consists of an excitation signal amplifier, analog front-end amplifiers and signal multiplexers of a low-noise voltage converter. Measurements data is exchanged between the analyzer and host PC with the aid of the LabVIEW application through the TCP connection.

The second part of the chapter describes and justifies the CIA's measurement instrumentation design. Two methods for initial calibration and correction of the influence of connection cables are introduced and tested; as can be seen from the comparison, the compensation of the effect of short cables with the initial calibration gives similar or better results than the computational correction in the 10 MHz frequency range. Therefore, the first method was used in the experiments described in this work. Adapting the excitation voltage level via digital feedback implemented in the CIA improves accuracy at lower frequencies where the impedance increases. However, as the CIA has only a fixed measuring range and limited supply voltages, it cannot compete with more advanced measuring instruments where the input and output ranges can be changed and adapted. To further reduce errors at higher frequencies, using more complex equivalent circuits for the error correction may help. However, for longer connection cables, it is better (but also more cumbersome) to use active front-end interfaces to connect electrodes or inductive sensors to the measurement unit. Nevertheless, the measurement accuracy of developed CIA remains relatively high up to 10 MHz and can be considered exemplary for such a compact impedance analyzer.

The third part of the chapter presents and analyzes the results of experimental bioimpedance measurements on a forearm with flexible capacitive electrodes. Fitted parameters of the model allowed separation of the spectra for different model elements. It is shown that β dispersion of the internal part (tissue) appears mainly in the frequency range between 100 kHz to 10 MHz. Analyzing the weight of model elements in the impedance spectrum allows drawing conclusions about the sensitivity to changes of model element parameters at different frequencies. E.g., both resistive components of the inner part of a tissue (under the skin) manifest more at higher frequencies, and their influence becomes equal near 2 MHz. Finally, a change of magnitude and phase of the EBI caused by the impact of cardiovascular activity on the left forearm is illustrated. The detected signals change below 0.1 % of the base value, making their practical use questionable considering the immobility condition during the experiment.

5 Magnetic Induction Based Measurement of Electrical Bioimpedance Variations

5.1 Introduction

Electrical bioimpedance (EBI) is the electrical impedance of biological matter, describing living biological materials (cells, tissues, organs) and physiological processes such as breathing, contractions of the heart and flowing of blood (hemodynamics). In summary, electrical bioimpedance allows measuring and analyzing the cardiopulmonary and cardiovascular dynamics, which are the most necessary physiological processes for medical diagnostics of human health. Unfortunately, achieving reliable electrical contact between the body and electronic measuring equipment, especially in the conditions of movement of the human body, has become a factor causing uncertainty.

5.1.1 The rationale for the investigation of electromagnetic induction methods

In most known devices, the electrodes having a galvanic (ohmic) contact with the body are usually used to measure bioimpedance. Although such electrodes allow tiny impedance variations to be measured, they cannot be used effectively for long-term measurements and trend monitoring, as reliable galvanic contact is difficult to maintain due to motion artifacts and the aging of electrode surfaces. A solution that would be essentially not so sensitive to movements and aging of contacts between the body and measuring device is needed.

Fortunately, the impedance of the tissues can be measured not only by electrically conductive electrodes placed on the body but also by using the non-contact mode coupling [117], enabling not only cardiovascular but also respiratory monitoring [118]. Both capacitive and inductive coupling, but mainly the inductive electromagnetic connection between the body and the electronic measuring device, demonstrate their perspectives on avoiding serious electrode problems and reducing artifacts [119]–[121].

5.1.2 Methods of the Inductive coupling

Inductive coupling is a known technique [117], [118], [122], [123], which has found well-established use in magnetic induction tomography [124]. However, the known devices use either solenoidal or planar coils to create the magnetic field. Unfortunately, neither solenoid nor planar coil can generate the magnetic field inside the body or body parts (hand, leg, neck etc.) so that the induced current is directed along the body part (a blood vessel, for example). As a result, the informative potential of the magnetic induction method remains not fully used when solenoids or planar coils are applied.

GRADIOMETER. The gradiometer with multiple coils, primarily used in Magnetic Induction Tomography (MIT), increases the sensitivity to impedance changes [125]–[129]. In a typical gradiometer design, two differential sensor coils on both sides of the excitation coil suppress its signal. However, there are several disadvantages in the case of detection of impedance changes on a wrist. First, the design is larger and more complex, and since the excitation coil moved away from the sensor coils, a much higher current is required to obtain the same magnetic field in the wrist (Fig. 5.3b). Second, the induced voltages in the two sensing coils are unequal because of the different separation from the hand, which significantly reduces the suppression efficiency. Third, although the dynamic range increases by amplification of the lesser residual signal, it does not increase the SNR of the

transformed impedance change. Gradiometer solutions are not studied in more detail in this work.

SOLENOIDAL COIL. An electromagnetic circuit is an electromagnet (solenoid) with a magnetic or non-magnetic core (e.g., air or human body), along with which a linear coil of wire is wound and through which an alternating magnetizing current passes to create a magnetic flux around the circular magnetic or non-magnetic core (Fig. 5.1). As a result, this magnetic flux induces an electromotive force which generates the induced electrical current flowing circularly nearby the circular magnetic core.

It is known that, for example, in the case of a solenoid placed around a finger or an arm, the highest density of the electromagnetic field is on the surface of the finger or the arm, respectively, wherein the electromotive force generated inside the finger or arm, such as a blood vessel, is local and marginal. The density B of the magnetic flux Φ_m generated by the magnetizing current i_m weakens rapidly moving from near the surface towards the center (Fig. 5.2). It does not allow the induction of an electrical current with the intensity and direction required for vascular diagnostics.

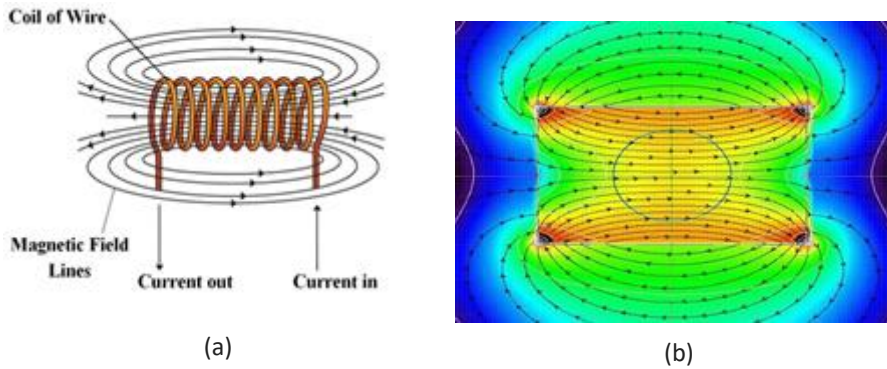


Fig. 5.1 Magnetic induction with solenoid: (a) – construction and created magnetic field, (b) – distribution of the magnetic field.

Nevertheless, solenoids have found widespread use in magnetic impedance tomography (MIT), see [128], [130].

PLANAR COIL. The magnetizing electric current in the planar winding (Fig. 5.3a) causes a magnetic flux, which generates an eddy current just below the planar coil, which weakens when increasing the object's distance [131]. If the measuring point is moved away from the center of the coil along the coil x-axis, then the strength of the field H will decrease as the distance d is increased. The field strength is related to the coil's radius (or area), and it remains almost constant up to a certain distance and then falls rapidly (see Fig. 5.3b). For shorter distances ($d \ll a$), the field strength can be found with the following equation [132]:

$$H = \frac{i N a^2}{2\sqrt{(a^2 + d^2)^3}}, \quad (5.1)$$

where i is a current, N number of windings, and a is the radius of the coil and d is the distance from it in the x-axis direction.

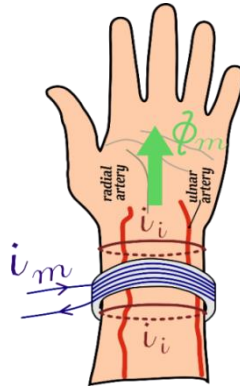


Fig. 5.2 The vortex-like circular induced current i_i flows near the surface of the wrist, balancing the effect of magnetizing current i_m . The induced current i_i enables the impedance measurement close to the surface of a round object. In the case of an arm or wrist, we mainly measure the average impedance of the skin and subcutaneous tissues. Only a small portion of the induced current flows inside the arm being too small to give an informative response.

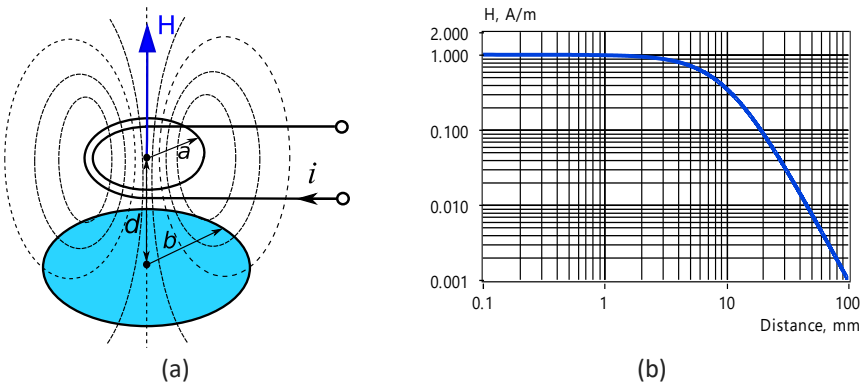


Fig. 5.3 Planar coil at a distance from d from the eddy current loops shown in blue (a) and the strength of the magnetic field (b) when the current in the coil is 40 mA, the number of windings is 2, and the radius of the coil a and secondary loop are 10 mm.

Inductive coupling to eddy current loop in the body comes up with magnetic flux Φ which density B depends on the surface area A it passes, $B = \Phi/A$, and permeability (magnetic conductivity) of the medium μ .

$$B = \mu H = \mu_0 \mu_r H, \tag{5.2}$$

where μ_0 is the magnetic field constant ($\mu_0 = 4\pi \times 10^{-6}$ V s/A m) and μ_r is relative permeability that shows how many times it is greater than or less than μ_0 . Permeability of the body is near μ_0 ($\mu = \mu_0$). However, the coil may employ a core with significantly higher permeability (μ_r typically in the range of 20–2000) which allows concentrating magnetic flux into the core.

The conductor's loop inductance L of the coil depends upon the permeability of the space that the flux flows through and the geometry of the loop (e.g., number of turns N).

Two nearby loops influence each other by partial flux (coupling flux) ψ_{21} . The magnitude of the coupling flux depends upon the geometric dimensions of both conductor loops, their positions to one another and the magnetic properties of the medium (e.g., permeability). The coupling of two loops is characterized by mutual inductance M as shown in Fig. 5.4. Coupling flux ψ_{21} also depends on the angle between loop planes as it is maximal when loops are parallel and minimal when loops are perpendicular.

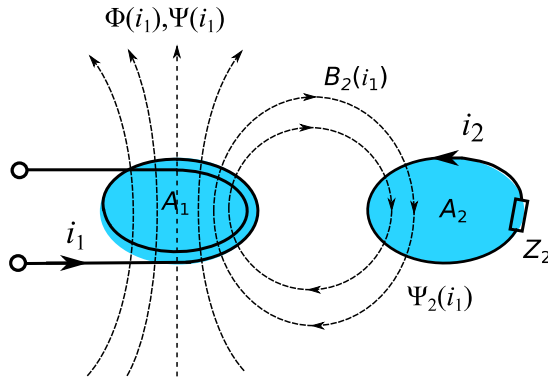


Fig. 5.4 Mutual inductance M_{21} by coupling two loops via partial coupling flux ψ_2 .

Similarly, there is also mutual inductance M_{12} . Its dimension and unit are the same as for inductance.

$$M = M_{12} = M_{21} \quad (5.3)$$

Mutual inductance is a quantitative description of the flux coupling of two conductor loops. The coupling coefficient k allows making a qualitative prediction about the coupling of the conductor loops without their geometric dimensions (this information is contained in inductances).

$$k = \frac{M}{\sqrt{L_1 L_2}} \quad (5.4)$$

Coupling factor k is always in the range of 0 to 1. Thus, one denotes the total coupling when both loops have the same magnetic flux Φ . Assuming a homogeneous magnetic field, the coupling factor k between two loops centered on a common x -axis can be calculated [132]:

$$k(d) \approx \frac{a^2 b^2}{\sqrt{(a^2 + b^2)} \left(\sqrt{(a^2 + d^2)} \right)^3} \quad (5.5)$$

The shape of coupling factor k graphs shown in Fig. 5.5a has substantial similarity to magnetic field strength H in Fig. 5.3b. The radius of the excitation coil a is the same (10 mm) and the smaller radius b of the eddy current loop varied from 1 to 5 mm.

The so-called skin effect of the induced current penetration depth has also been considered a factor influencing the results. The depth of penetration decreases with increasing frequency f and increasing conductivity σ and magnetic permeability μ . The standard depth of penetration δ is defined as the depth at which eddy current intensity drops to $1/e$ (about 37%) of their surface density [133]:

$$\delta \approx 1 / \sqrt{\pi f \mu \sigma} \quad (5.6)$$

Fig. 5.5b illustrates the electromagnetic field penetration depth inside the living tissue. Since the penetration depth is above 20 cm at 10 MHz, this influence has a low impact on the human body below 10 MHz.

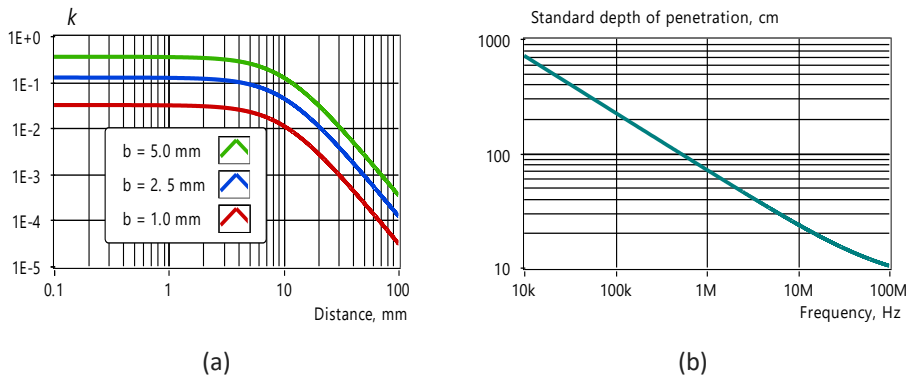


Fig. 5.5 Changes of coupling factor k between two loops centered on a common x-axis of the coil with eddy current loop shown in Fig. 5.3 in the case of changing its radius b (a) and electromagnetic field penetration depth δ inside the living tissue (b).

Fig. 5.5a illustrated the change of coupling factor k in a simplified case when two circular loops centered on a common x-axis and radius b of the secondary loop varied from 1 to 5 mm, and k degrades almost proportionally. The reason is that magnetic flux Φ density B depends on the surface area A it passes, $B = \Phi/A$ and the surface area is proportional to the radius b . In addition, the coupling factor decreases sharply when the distance increases by more than 5 mm. Since the tissue dimensions are spatial, these results are approximate but still show that the induced currents remain weak due to a small coupling factor in the small loop area, such as a wrist artery.

The magnetic flux concentration to the space of interest could increase the excitation current and simplify the measurement of its response. Magnetic flux concentration in the desired area depends on the shape of the excitation coil and the magnetic permeability of the environment.

Fig. 5.6 illustrates the placement of the planar coils on the wrist.

The use of planar coils has the following disadvantages:

- 1) Since the magnetic field travels in two directions (Fig. 5.3a), the coupling in the desired direction decreases and the results are affected by objects located in the unwanted direction.

- 2) The planar coil has a significant capacitance to the surface of the arm. The capacitance of the coil shown in Fig. 5.7a is 17.1 pF (measurements were carried out with a Keysight E4990A, simulating the hand surface with a copper foil). Such a significant capacitance results in a parasitic capacitive current loop, significantly affecting the measurement results.

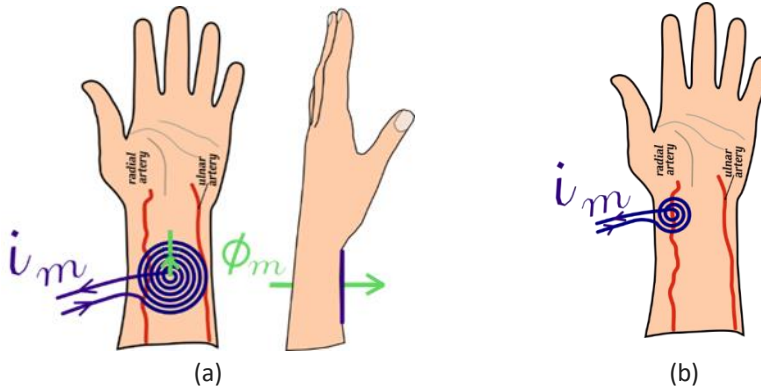


Fig. 5.6 The magnetizing electric current i_m causes a magnetic flux Φ_m of density directed perpendicular to the coil into the wrist tissue. This magnetic flux creates an eddy current in the wrist just below the planar coil, which weakens rapidly toward the depth of the wrist.

The effect of the opposite magnetic field can be reduced by ferrite in this direction (Fig.5.7b). However, this also increases the self-capacitance of the coil nearly four times since the relative permittivity ϵ_r of manganese-zinc ferrites such as PC200 is around 90 (see section 5.1.4 for more detail).

Two methods have been tested to reduce the influence of parasitic capacitance:

1) Moving the winding away from the surface of the hand, e.g., with a U-shaped magnetic circuit or a rod-shaped magnetic circuit, Fig. 5.8.

2) Excitation of the coil with a differential circuit, which ensures the compensation of capacitive currents in the symmetrical design. This approach has been applied in all experiments with inductive excitation.

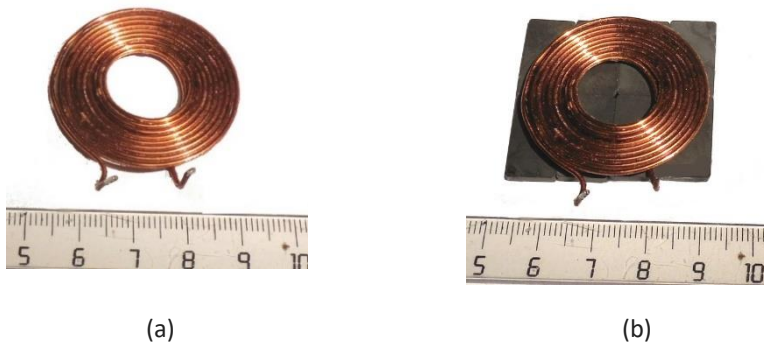


Fig. 5.7 A planar coil with 10 windings (a) and planar coil with a PC200 2 mm ferrite on the backside (b).

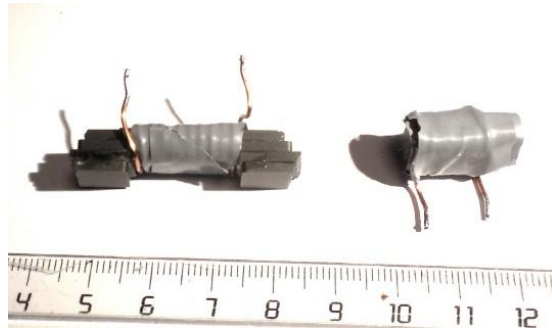


Fig. 5.8 Sensor coils with the U-shaped and short rod ($l = 18 \text{ mm}$) ferrite cores, composed of 2 mm PC 200 plates.

TOROIDAL COIL. An alternative for the concentration of magnetic flux in the desired direction is using a circular (toroidal) magnetic core. A current passing a spiral coil wound around it creates a magnetic flux along with the core (Fig. 5.9a). As a result, an electromotive force perpendicularly to its opening is created. This phenomenon was invented in 1831 by English physicist Michael Faraday, who discovered that a changing magnetic field induces a voltage in a nearby wire (Faraday's law of induction).

The induced electric current i_i flows mainly through the blood vessels (radial and ulnar arteries in the present (Fig. 5.10a) due to both the magnetic field's directing and the electrical conductivity of blood being several times higher than in the surrounding living tissues. However, the situation in Fig. 5.9a and Fig. 5.10a is idealized: the induced current i_i can flow in a predetermined manner only when the electrical circuit is closed; otherwise, uncertainty arises. Moreover, low relative permeability and uneven distribution of windings on the core also lead to magnetic field scattering and uneven distribution in the opening of the toroid.

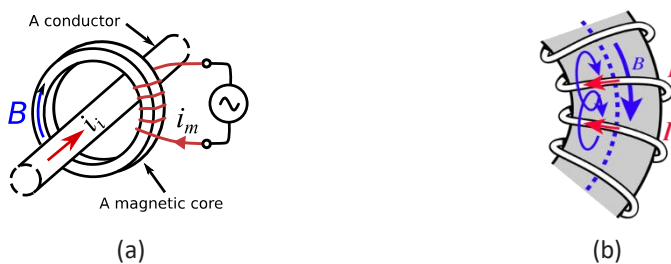


Fig. 5.9 A toroid: alternating electrical current i_m creates a magnetic flux with the density B in the closed magnetic core, which in turn induces electrical current i_i in the electrical conductor passing through the opening of the toroidal core.

The magnetic toroidal core may be a flexible magnetic material, e.g., IRL02 from TDK Corporation. In photography, Fig. 5.10b incomplete toroidal core (open core) sensor consisting of flexible magnetic core 2 and coil 4 is illustrated.

The process is reversible, i.e., the current in the conductor induces a voltage in the coil. However, the voltage, current and impedance relationships do not follow the formulas of an ideal toroidal transformer for several reasons discussed in the following sections.

5.1.3 Impact of magnetic cores

The permeability of magnetic cores is limited to the frequency range required. The relative permeability μ_r of flexible IRL02 is around 25. As the number of turns N is in the range of 3 to 10, the coil covers only a short part of the toroidal core. As a result, the effect of magnetic field concentration decays fast in the region beyond the coil. As the following experiments have shown, the closed state of the toroid is therefore not very relevant, and the magnetic field is concentrated near the coil. Unfortunately, stretching the winding does not have a positive effect either since it decreases magnetic field coupling between them (see Fig. 5.9b). Both a low μ_r and uneven distribution of windings on the core lead to magnetic field scattering, which in turn is reflected in a lower coupling factor k between the excitation coil and conducting material in the opening of the toroid.

The relative permeability of U-shaped and short rod ferrite cores made of PC200 ferrite from TDK Corporation, shown in Fig. 5.8, is 640. However, due to an open magnetic circuit, the effective permeability of the sensor is nearly 40 times lower, as discussed below.

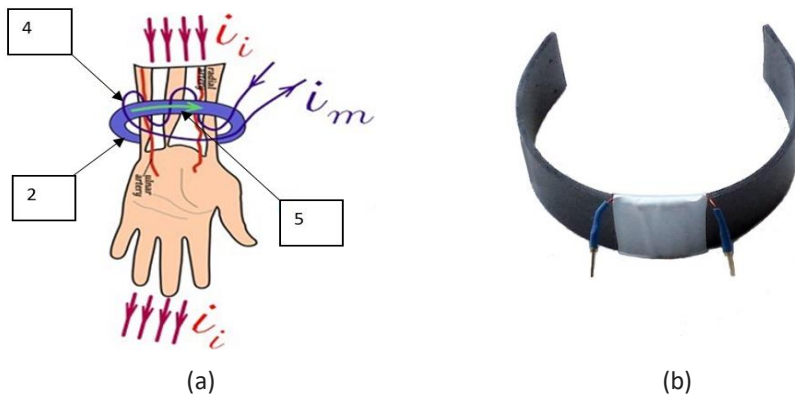


Fig. 5.10 Toroidal electromagnetic sensor on the wrist (a). In core 2, a magnetizing current i_m passing through the winding (coil) 4 generates a magnetic flux 5, which induces an induced electric current i_i , the value of which depends on the electrical resistance in the direction of the arm. Incomplete (open) toroidal core sensor consisting of flexible magnetic core and coil (b).

The effective permeability is dependent on multiple factors: the relative permeability, length and diameter of the core, as well as the size and position of the coil. The analytical derivation of the relationship between the two permeability is cumbersome. In the case of rod ferrite, an approximation from measurement results for the effective permeability μ_e is [134]

$$\mu_e = \frac{\mu_r}{1 + D_f(\mu_r - 1)}, \quad (5.7)$$

where the demagnetization factor D_f depends on the core length-to-diameter ratio in the range of from 2 to 20

$$D_f = 0.37R^{-1.44} \quad (5.8)$$

It follows that a core with a high permeability can perform similarly to a material with moderate permeability, depending on the core length/diameter ratio. Since the given equations do not consider the length of the coil and its position, a more exact value can be obtained experimentally.

The inductance of the sensor with a U-shaped PC200 ferrite core with $\mu_r = 640$ and $N = 10$ is around $5 \mu\text{H}$. A similar air wound coil has an inductance of $0.31 \mu\text{H}$, so the effective permeability $\mu_e = 5/0.31 = 16.2$, i.e., around 40 times less. The positive effect is that tolerance for permeability also decreases.

In addition to the above, ferrite cores are also associated with losses, which increase with frequency. At the same time, however, the wire resistance is reduced because the number of turns decreases proportionally to the effective permeability. The wire resistance consists of ohmic resistance and resistance due to the skin effect that increases with frequency. Both wire resistance components can be calculated and found by measuring the loss resistance of the air-wound coil. Measuring the loss resistance of the same coil with ferrite core also allows the determination of loss resistance caused by it.

Conversion of the series resistance R_s of the coil to equivalent parallel resistance R_p bases on the equality of impedances

$$R_s + j\omega L = \frac{R_p j\omega L}{R_p + j\omega L} \quad (5.9)$$

From here, equivalent parallel resistance R_{pe} reveals as

$$R_{pe} = \text{Re} \left(\frac{(\omega L)^2 - j\omega L}{R_s} \right) \approx \frac{(\omega L)^2}{R_s} \quad (5.10)$$

The loss resistance caused by the ferrite core R_{lp} is a difference of measured total loss resistance R_{lt} and loss resistance of air coil R_{ls} converted to its parallel equivalent R_{lsp} with (5.10)

$$R_{lp} = \frac{R_{lt} R_{lsp}}{R_{lsp} - R_{lt}} \quad (5.11)$$

5.2 Excitation and Acquisition of the Response via Inductive Coupling

For a non-contact solution with inductive excitation, detecting impedance changes in the excitation signal side would be desirable.

5.2.1 Impedance transformation via inductive coupling

In the present application, the inductive coupling can be viewed as a transformer, where the impedance of the secondary side is manifested in a single-coil eddy current loop, Fig. 5.11.

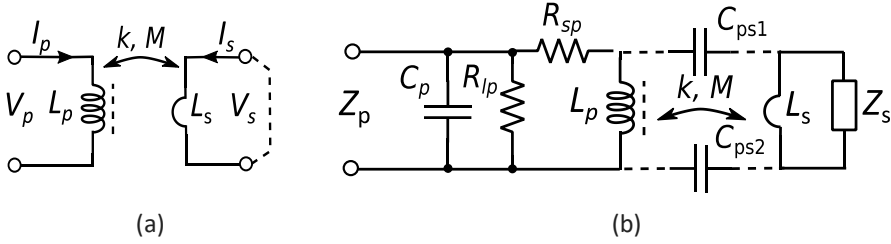


Fig. 5.11 The inductive coupling as a transformer with a single turn secondary winding (a) where L_p and L_s are inductances of the primary and secondary sides. More detailed equivalent circuit (b), where R_{sp} and R_{lp} are the series and parallel loss resistances, Z_s the impedance connected to the secondary winding, C_p the capacitance in parallel with the primary coil, and C_{ps1} , C_{ps2} stray capacitances between primary and secondary windings.

The coupling coefficient k allows making a qualitative prediction about the coupling of the conductor loops without their geometric dimensions, and according to (5.4), it is related to mutual inductance M as

$$M = k\sqrt{L_p L_s} \quad (5.12)$$

Omitting the influence of capacitances C_p , C_{ps1} , C_{ps2} , and parallel loss resistance R_{lp} , the effect of the impedance Z_s in the secondary winding circuit on the primary impedance Z_p^* can be expressed as [135]

$$\tilde{Z}_p^* = R_{sp} + j\omega L_p + \frac{\omega^2 M^2}{j\omega L_s + \tilde{Z}_s} = R_{sp} + j\omega L_p + \frac{\omega^2 k^2 L_p L_s}{j\omega L_s + \tilde{Z}_s}, \quad (5.13)$$

where L_p and L_s are the inductances of the primary and secondary windings, respectively, R_{sp} is the resistance of primary winding, and Z_s is the impedance connected to the secondary winding. Here the transformed part of the impedance is in series presentation. When the influence of parallel components, the capacitance C_p and loss resistance R_{lp} are involved too, Z_p expresses

$$\tilde{Z}_p = \frac{1}{\frac{1}{\tilde{Z}_p^*} + \frac{1}{R_{lp}} + j\omega C_p} \quad (5.14)$$

The effect of stray capacitances C_{ps1} and C_{ps2} has not been considered here. However, these capacitances may significantly influence the Z_p , as discussed in the following subsection. In a simplified approach, their effect expresses as a capacitance added to C_p .

The capacitance between the windings determines the C_p unless a capacitor is added to produce the parallel resonance in the employed frequency range. The capacitance between the windings can be affected by the dielectric constant of the ferrite core, which can be high in manganese-zinc ferrites such as PC200. Measurement of the capacitance with Keysight E4990A between copper films bonded to a 2 mm thick PC200 ferrite plate showed a capacitance increase of 90 times at 1 MHz, i.e., $\epsilon_r \approx 90$. One way to reduce the

impact of high permittivity is to have an insulating layer between the coil and the core. The 0.5 mm thick insulation reduced the effect of the core almost 16 times. Another solution is using nickel-zinc ferrites as K1 from TDK Corporation, which gave $\epsilon_r \approx 10$. However, the permeability of K1-type ferrite is around ten times lower than that of PC200.

5.2.2 Finding mutual inductance and coupling factor

Expressing Z_p would first require knowing the value of mutual inductance M or k . The so-called self and leakage inductance test can be used to find it. Here inductance measured at a winding when another winding is shorted is called the leakage inductance.

Describing the coupled windings according to Fig. 5.11a, the primary and secondary voltages V_p and V_s are expressed:

$$\tilde{V}_p = j\omega (I_p L_p + M I_s); \quad \tilde{V}_s = j\omega (I_s L_s + M I_p) \quad (5.15)$$

In the case of a shorted secondary circuit ($V_s = 0$), the current and voltage on the primary side can be calculated by the relationships:

$$\tilde{I}_p = -\frac{M \tilde{I}_s}{L_s}; \quad \tilde{V}_p = j\omega I_p (L_p - \frac{M^2}{L_s}) \quad (5.16)$$

Then, in the case of a shorted secondary circuit, the inductance of the primary side equals:

$$L_{sh} = L_p - \frac{M^2}{L_s} \quad (5.17)$$

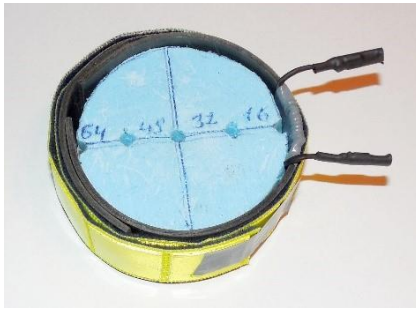
From here, the mutual inductance M and the coupling factor k based on equation (5.12) are expressed:

$$M = \sqrt{L_s (L_p - L_{sh})} \quad (5.18)$$

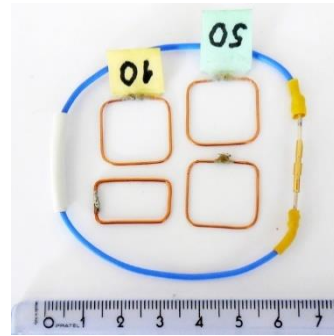
$$k = \sqrt{1 - \frac{L_{sh}}{L_p}} \quad (5.19)$$

The following describes the test results with different sensor configurations. Inductances were measured with a Keysight E4990A; the distance of the sensors from the short turn was changed with a 0.05 mm resolution 3D coordinate table (except for the sensor with toroidal core, where the positions of the short turn were determined with holes in the foam).

Experiment 1. The results with a coil employing a toroidal core (Fig. 5.12a) and a long short-circuit loop shown in Fig. 5.12b are presented in Fig 5.14a.



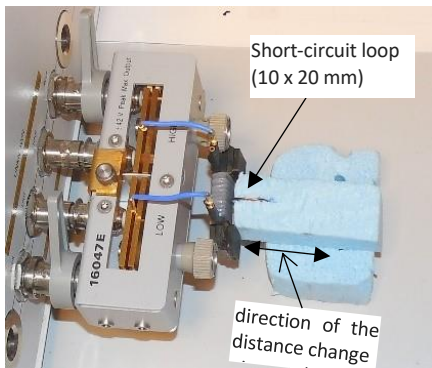
(a)



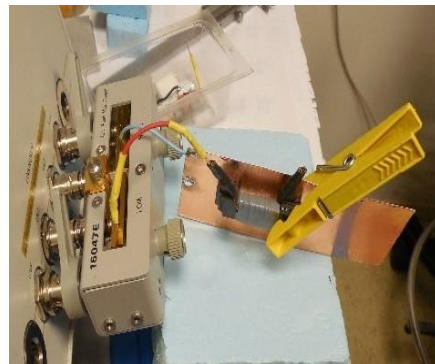
(b)

Fig. 5.12 Sensor with toroidal flexible ferrite IRL02, $d_{max} = 64$ mm, width 32 mm, $L_p = 5.91 \mu H$, $N = 10$ (a) and coupling loops (b). The diameter of the longer loop is 65mm. Smaller loop dimensions are 10 x 20 mm and 18 x 18 mm. 0.1 % precision resistors may also be added into loops.

Experiment 2. The results with a coil employing a toroidal U-shape core (Fig. 5.13a) and a smaller shorting loop shown in Fig. 5.12b are presented in Fig 5.14. The measurement results presented for U-shaped and rod-sensors are obtained with a shorting loop placed in parallel with the end part of cores.



(a)



(b)

Fig. 5.13 Sensor with U-shaped PC200 ferrite, length 36 mm, width 10 mm, $L_p = 5.60 \mu H$ (a) and test setup for measurement of the coupling capacitance using a copper foil. The number of windings $N = 10$.

The measurement illustrated in Fig. 5.13b gives stray capacitance C_{ps} 10.5 pF for the U-shaped core, 17.1 pF for the planar coil and 3.0 pF for the rods with a coil placed 1 mm from the edge.

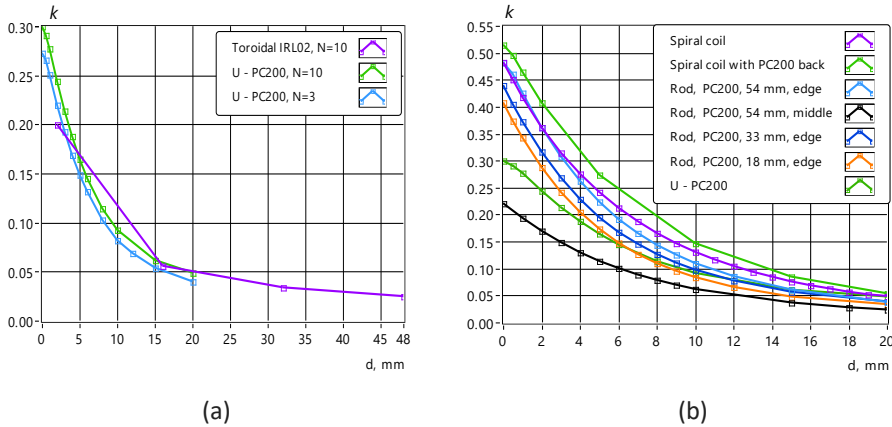


Fig. 5.14 Dependence of the coupling factor k on a distance for the sensor with the toroidal core employing IRL02 ferrite and U-shaped sensors employing PC200 ferrite with $N = 10$ and $N = 3$ (a) and for the different sensors with $N = 10$ (b). All sensors in (b), except the first spiral coil, employ PC200 ferrite. Rods have lengths of 54, 33 and 18 mm, windings placed near the edge at a distance of 1 mm or in the middle.

CONCLUSIONS from the results presented in Fig. 5.14:

- 1) Coupling factor k of the sensor with toroidal core decays similarly to U-shaped sensor, indicating that it differs significantly from the idealized toroidal transformer. Both a low μ_r and uneven distribution of windings on the core lead to magnetic field scattering. As a result, the magnetic flux density concentrates near the coil and does not depend much on distal parts of the core, i.e., the closing of the core has a marginal effect. The experiment showed that shortening the core by half decreases the sensor's inductance by only 1%.
- 2) The difference in coupling factors of U-shaped coils with 10 and 3 windings is below 11%.
- 3) The highest coupling factors are obtained with the spiral coil backed with a ferrite and longer rods when the coil is placed near the edge. Placing the same long rod coil in the middle part drops k over two times.

Since the obtained coupling factors depend on dimensions and angles of primary and secondary loops, they are indicative and only suitable for a relative comparison of sensors. In addition, the accuracy of the self and leakage inductance test in a situation with one secondary turn is limited.

5.2.3 Impedance transformation and sensitivity

In an ideal transformer, the impedance is transformed by the square of the winding ratio. Considering that the number of secondary windings is one, the transformed ideal primary impedance $Z_{pi} = N^2 Z_s$. In the case when coupling factor $k < 1$, loss resistances and capacitive elements are involved, the impedance transformation depends on the more complex relationships (5.12)–(5.14).

Moreover, when a relative change of the primary impedance dZ_p/dZ_s is of interest, the influence of N is not straightforward, especially when considering the impact of separate components of the secondary impedance (R_{int} , R_{ext} , Q , α). Increasing N increases both the transformed secondary impedance and impedance of the primary winding in (5.13), thus

compensating for relative changes. Furthermore, the impact of C_p is higher since it affects the primary side directly, but the low coupling factor k weakens the influence of secondary impedance significantly.

The relative transferred impedance changes analysis is based on (5.14). A 1% change is given to the different secondary impedance Z_s components, and the corresponding change in primary side impedance Z_p in ppm is calculated as a normalized sensitivity $S_n = dZ_p/dZ_s$. In addition, the influence of the change of the capacitance C_p may be involved, and the simultaneous changes in values of two chosen components are possible.

The base values of Z_s components are optional. However, the following examples use the average values of the previously found forearm tissue's three-element model (see Table 4.1): $R_{int} = 84 \Omega$, $R_{ext} = 49.4 \Omega$, $Q = 38.4 \text{ S}\cdot\text{s}^{-1}$, $\alpha = 0.72$. The loss resistances R_{sp} and R_p are found with measurements and relationships (5.9)–(5.11). The inductance L_p and the sensor's self-capacitance are measured with Keysight E4990A Impedance Analyzer.

Fig. 5.15 illustrates the relative change of the primary impedance magnitude and phase when R_{int} decreases by 1% from its base value for U-shaped sensor with $N = 10$, $L_p = 5.74 \mu\text{H}$, $C_p = 2.2 \text{ pF}$ in the frequency range 1 to 10 MHz. The relative change of $|Z_p|$ and phase increases with frequency and k up to 100 ppm and $6 \text{ E-}3^\circ$. However, at $k = 0.3$, only 8.6 ppm and $6 \text{ E-}4^\circ$ remain.

When R_{ext} decreases by 1 % in similar conditions and $k = 0.3$, the relative change of $|Z_p| = 13.6 \text{ ppm}$ and -0.003° at 10 MHz.

Fig. 5.16 illustrates the relative change of the primary impedance magnitude and phase when Q decreases by 1 %. In this case, the maximum relative change of $|Z_p|$ varies in the range of 10 ppm to -40 ppm and is zero at a frequency around 5.7 MHz. The phase change reaches $6 \text{ E-}3^\circ$ at 10 MHz. At $k = 0.3$, the phase change decreases to $5.3 \text{ E-}4^\circ$.

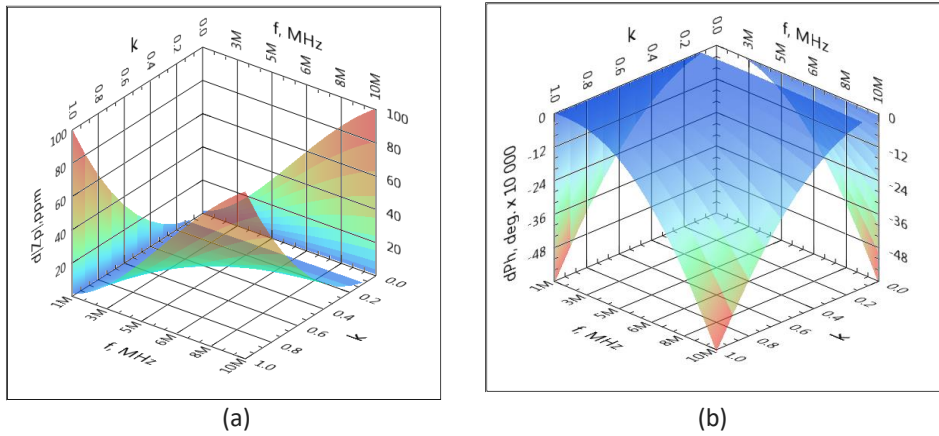


Fig. 5.15 Normalized relative change of the primary impedance $d|Z_p|$ (a) and phase dPh_p of the U-shaped sensor with $N = 10$ in the case of 1% change of the secondary impedance element R_{int} with a base value of 84Ω . 2D projections of 3D plots provide additional information.

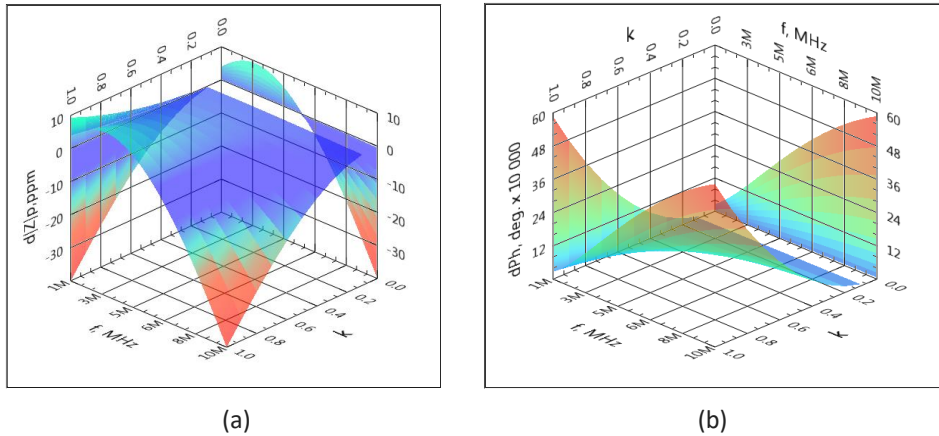


Fig. 5.16 Normalized relative change of the primary impedance $d|Z_p|$ (a) and phase dPh_p of the U-shaped sensor with $N = 10$ in the case of 1% change of the secondary impedance element Q with a base value of 38.4 S s^{-1} and $\alpha = 0.72$. 2D projections of 3D plots provide additional information.

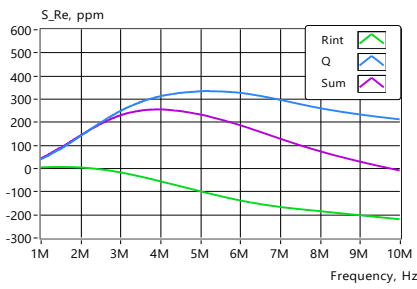
Magnitude, Re and Im changes are in ppm and phase changes in degrees multiplied by $1 \text{ E}4$. In Table 5.1, normalized sensitivity $S_n = dZ_p/dZ_s$ is shown at the highest frequency of 10 MHz for some typical situations. Maximum sensitivity typically corresponds to the highest frequency, except for Re for R_{ext} and Q , where it is located at frequencies between 2.7 MHz to 3.6 MHz for the sensors with ten windings and between 4.5 MHz to 5.2 MHz for the sensors with three windings.

Table 5.1. Normalized sensitivity S_n in ppm, and degrees multiplied by 10000 at 10 MHz against changes of secondary impedance components R_{int} , R_{ext} and Q values for the U-shaped sensors with 10 and 3 windings.

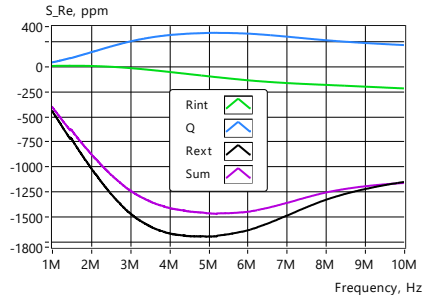
Conditions	R_{int}				R_{ext}				Q			
	$S_{ Z }$	S_{Ph}	S_{Re}	S_{Im}	$S_{ Z }$	S_{Ph}	S_{Re}	S_{Im}	$S_{ Z }$	S_{Ph}	S_{Re}	S_{Im}
U-10w, $k = 0.3$	8.6	5.9	87	7.2	14	29	380	20	4.3	5.3	65	5.5
U-3w, $k = 0.3$	9.1	5.2	221	8.7	8.7	29	1150	11	3.3	5.3	211	3.7
U-10w, $k = 0.5$	24.0	16.1	221	20.0	36.1	81	2110	56	11.6	14.7	365	15.3
U-3w, $k = 0.5$	25.4	14.3	482	24.1	22.4	79	2510	30	8.9	14.6	460	10.3

Analysis of the results indicates that the real part of the impedance's sensitivity is significantly higher compared to other presentations. However, since the result depends on the confluence of several components in practice, no definitive conclusions can be drawn from these results. Fig. 5.17 shows examples of the interaction of two and three elements of the model with $k = 0.3$.

The impact of the 0.5 pF C_p change is illustrated in Fig. 5.18. It almost completely masks the effect of R_{int} and significantly affects the effect of R_{ext} , with zero sensitivity at some frequency.

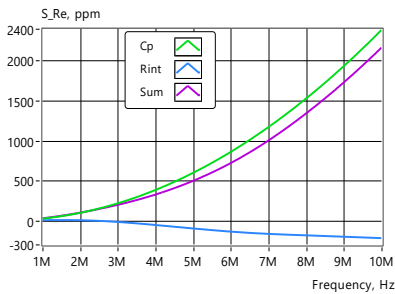


(a)

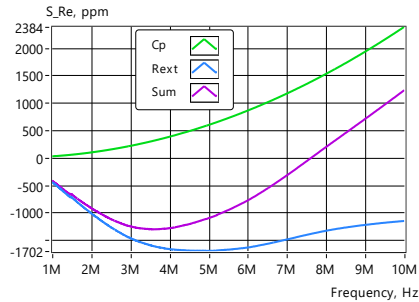


(b)

Fig. 5.17 The dependence of normalized sensitivity based on impedance real component change of U-shaped sensor with $N = 3$ in the case of changes of two model elements, R_{int} and Q (a) and three elements, R_{int} , R_{ext} , and Q (b). All model elements changed by 1% from their base values in the same decaying direction.



(a)



(b)

Fig. 5.18 The dependence of normalized sensitivity based on impedance real component change of U-shaped sensor with $N = 3$ in the case of changes of elements, C_p and R_{int} (a) and C_p , R_{ext} (b). C_p changed by 0.5 pF and R_{int} , R_{ext} by 1% from their base values in the same decaying direction.

The sensitivity also depends on the base value of the secondary side impedance. Fig. 5.19 illustrates that dependence for the 1% change of the secondary resistance R_s . Since the sensitivity decreases almost linearly with the increase of base value, it is evident that the model elements with lower impedance magnitude dominate in the total result. There are no other model components involved in this case for clarity.

Considering that the resolution of the 16-bit A/D converter corresponds to 15.26 ppm of the full scale and at least 20 points are required for the waveform presentation, 300 ppm is the limit of sensor sensitivity. Because of the lower effective resolution of the A/D converter and additional noises in the measurement circuitry, the sensitivity limit rises around four times, i.e., to 1200 ppm. Only a few values in the Table 5.1 meet this requirement. The given estimate assumes that the base value of the response signal is close to the $\frac{1}{2}$ of the full scale of the A / D converter and its peak values are near it.

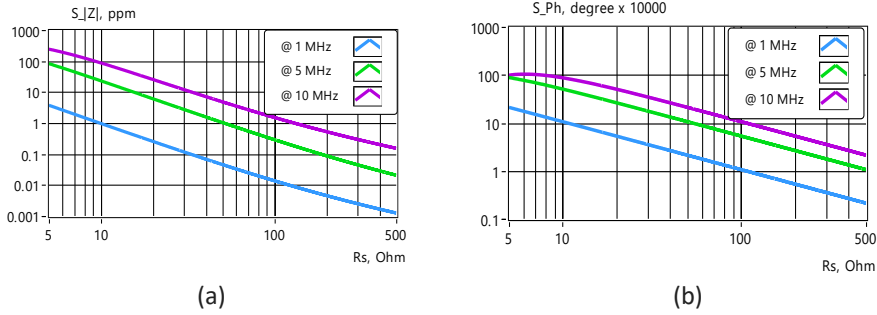


Fig. 5.19 The dependence of normalized impedance magnitude (a) and phase (b) sensitivity on the base value of secondary resistance R_s employing a U-shaped sensor with $N = 3$, in the case of R_s 1% changes at frequencies 1 MHz, 5 MHz and 10 MHz.

CONCLUSIONS from the sensitivity analysis using the base values of model elements given at the beginning of the section:

- 1) The changes in the model elements have the highest impact on the real part of the input impedance. However, it is unsuitable for directly detecting changes since only the waveform's amplitude and phase are directly observable.
- 2) The lower number of turns of the sensor gives the higher sensitivity in the real part. However, the trackable differences in amplitude and phase are slight and sometimes with opposite signs.
- 3) The effect of R_{ext} is significantly higher than other elements of the model (mainly caused by its lower base value).
- 4) A relatively small change in the input capacitance C_p significantly affects the overall result.
- 5) As a rule, the sensitivity increases with frequency, but the model components' combined effect can also be maximal and zero at intermediate frequencies.

There are several possibilities for increasing sensitivity. First, using resonance. In this case, the reactive resistances are equal and compensating, leaving a real component with increased detection sensitivity. Second, by difference measurement as discussed in chapter 3. However, it is much more complicated here because of the need for high-frequency base value compensation in real-time. The gradiometer method provides a similar effect by suppressing the excitation signal on the sensing input. However, although the dynamic range increases when amplifying lesser residual signals, it does not increase the SNR of the transformed impedance change.

Other possibilities are using the amplitude modulation detector circuitry or processing a modulation after down-conversion. However, these are quite different approaches that have not been investigated in the present work.

5.2.4 Detection of the impedance change with a resonance circuit

In resonance, the reactive resistances are equal and compensating, leaving a real component with increased detection sensitivity, as discussed in the previous section.

In resonance, the real component also equals the magnitude of the impedance that depends on a quality factor Q_r

$$Q_r = \frac{R_p}{Z_0}; Z_0 = \sqrt{\frac{L_p}{C_p}}, \quad (5.20)$$

where L_p is the coil's inductance, C_p is the capacitance, and R_p is the resistance in parallel. In an initial condition (without the secondary side's influence), a C_p 's capacitance is a sum of the self-capacitance of the coil C_{pL} , the capacitance of the added capacitor C_c , and R_p is a total parallel loss resistance representing the losses of the coil, core and added capacitor. Fig. 5.20 and Fig. 5.21 show the magnitude curves and Q_r values of the resonant circuits obtained experimentally with two U-shaped sensors used in previous non-resonance experiments. The sources of losses and their conversion method to equivalent parallel loss resistance are the same as discussed in the previous section, except for the added capacitor losses that are relevant above several MHz.

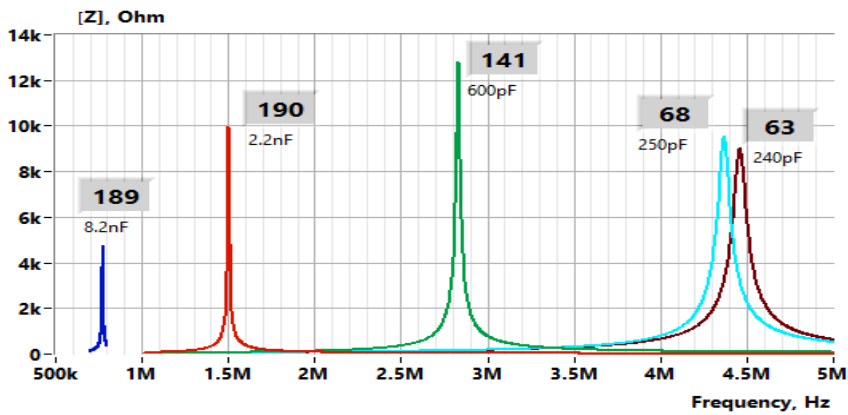


Fig. 5.20 Impedances, Q_r factors (in greyed boxes) with corresponding capacitances of six resonant circuits. The coil has 10 windings with a PC200 ferrite core.

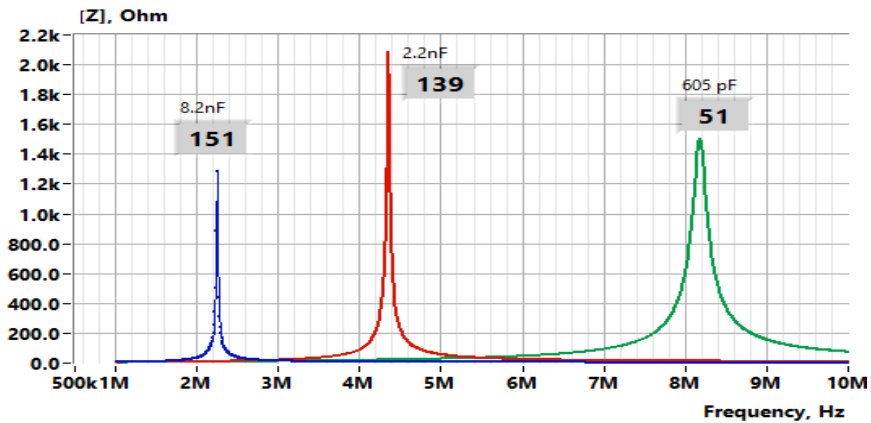


Fig. 5.21 Impedances, Q_r factors (in greyed boxes) with corresponding capacitances of three resonant circuits. The coil has 3 windings with a PC200 ferrite core.

The 0.8 mm copper wire and capacitors with the highest available Q factor (Murata GCM, GRM, GRT series) are used, except 240 pF in Fig. 5.20. PC200 ferrite provides low losses up to 10 MHz.

It is evident that the largest impedances of the resonance do not coincide with the most significant Q_r factors. This is because the equivalent parallel loss resistance determines the magnitude of the impedance, but the Q_r factor also depends on the ratio of L and C. In addition, the transformation of a serial loss resistance into an equivalent parallel loss resistance according to (5.10) and (5.11) depends on the inductance and frequency.

The transformed impedance reduces the initial impedance when the sensor is placed near the body. Firstly, because of transformed impedance, which reduces the parallel resistance of the resonant circuit and changes the reactive part that also slightly shifts resonance frequency. Intuitively, a higher initial impedance of the resonant circuit can be expected to provide higher sensitivity, but in practice, the situation is more complex. An important factor is the effect of stray capacitance between the body and the coil, which significantly affects the frequency of resonance.

Fig. 5.22a illustrates the dependence of the normalized sensitivity on R_{int} , R_{ext} and Q for the resonance sensors with 10 and 3 windings. Fig. 5.22b shows the dependence of the normalized sensitivity on the change of the C_p by 0.1 pF and its summary change with R_{ext} for the resonance sensors with 3 and 1 windings. Base values of components are the same as in previous examples without resonance; C_p values are 605 pF, 2.2 nF and 10 nF for sensors with 10, 3, and 1 windings, respectively.

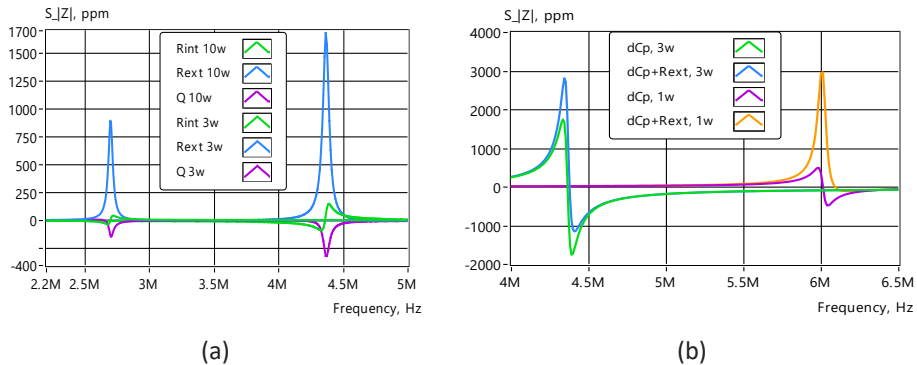


Fig. 5.22 The dependence of the normalized sensitivity on R_{int} , R_{ext} , and Q for the resonance sensors with 10 and 3 windings (a) and the change of the C_p by 0.1 pF and its summary change with R_{ext} for the resonance sensors with 3 and 1 windings (b).

CONCLUSIONS from the sensitivity analysis with resonance sensors:

- 1) The normalized sensitivity based on the impedance magnitude changes is similar to real part changes of non-resonance sensors.
- 2) A relatively small change in the input capacitance C_p affects the overall result more than in the case of non-resonance sensors. The sensitivity dependence may also have zero sensitivity at a frequency close to maximal sensitivity. Moreover, the frequency of zero phases may not match the frequency of maximal sensitivity. As a result, minimizing the impact of stray capacitance below 0.2 pF is crucial. Otherwise, the obtained impedance changes may depend mainly on stray capacitance, and following the frequency of maximum sensitivity is complicated.

5.3 Experimental Results with U-shaped and Rod Sensors

5.3.1 Detection of the impedance change with a U-shaped sensor

Experiment 3. The sensitivity test results employing a U-shaped ferrite core (Fig. 5.8a) and 18×18 mm coupling loops shown in Fig. 5.12b are presented in Table 5.2. The coupling loop in the plane of one end of the U-shaped sensor with the exchange of 50Ω and 10Ω resistors provides an 80% change in the secondary resistance R_s . Such a more significant change was necessary because otherwise, unwanted factors would have exceeded the accuracy of measuring changes in primary side impedance. The main factors influencing the measurement accuracy here are the accuracy of the dimensions and arrangement of the coupling loops, the accuracy of the measuring instrument (E4990A) in the given range, as well as the temperature drift of the sensor impedance. The temperature drift of the PC200 ferrite permeability is around 0.1% per degree. The inductivities of sensors are $5.19 \mu\text{H}$, 527 nH and 83 nH for $N = 10$, $N = 3$ and $N = 1$, respectively.

Table 5.2 Measured and calculated primary impedance magnitude and phase changes at 3MHz and 10 MHz on secondary resistance R_s change from 50Ω to 10Ω (80 %).

	$d Z_p , \%$		$d Ph_p , \text{degree}$		k
	3 MHz	10 MHz	3 MHz	10 MHz	
Measured, $N = 10$	-0.081	-0.56	-0.40	-1.40	0.274
Calculated, $N = 10$	-0.043	-0.58	-0.27	-0.90	
Measured, $N = 3$	-0.060	-0.67	-0.31	-0.94	0.267
Calculated, $N = 3$	-0.040	-0.45	-0.25	-0.77	
Measured, $N = 1$	0.001	-0.61	-0.26	-0.74	0.242
Calculated, $N = 1$	-0.035	-0.35	-0.20	-0.63	

Despite the 80% change of the secondary resistance, its transferred impedance change is reliably detectable only at 10 MHz. However, the change in impedance magnitude normalized to 1% remains small: 44–84 ppm, which is below the analyzer's sensitivity limit.

Experiment 4. A parallel resonant circuit with a coil employing a toroidal U-shape core (Fig. 5.8a) and 18×18 mm coupling loops shown in Fig. 5.12b are presented in Table 5.3. The capacitor C_p is added for resonance at frequency f_r . The coupling loop in the plane of one end of the U-shaped sensor with the exchange of resistors 50Ω to 10Ω or 100Ω to 50Ω provides an 80 % or 50 % change in the secondary resistance R_s .

In the resonance situation, the impedance change transformed to the primary side is around 60 times larger for the R_s change from 50Ω to 10Ω , resulting in 5600 ppm normalized sensitivity for the sensor with $N = 3$. R_s change from 100Ω to 50Ω provides normalized sensitivity of 1500 ppm.

The differences in measured and calculated sensitivities are caused by inaccuracies in determinations of parameters L_p , L_s , k , R_{sp} , R_{lp} , C_p (see Fig. 5.11) and measurement errors. The slightly lower sensitivity of a single-coil sensor is due to higher core losses at 5.5 MHz and the lower coupling factor because it did not form a complete turn. However, significantly lower sensitivity to parasitic capacities remains a positive feature, as the fixed capacitance is almost five times higher than with three winding sensors. Increasing the capacitance with a coil of just over one turn would probably give the best result.

Table 5.3 Measured and calculated primary impedance magnitude changes at resonance frequency on secondary resistance R_s change from 50 Ω to 10 Ω (80 %) and from 100 Ω to 50 Ω (50%).

	$d Z_p , \%$		C_p, nF	f_r, MHz	k
	$dR_s (50-10)$	$dR_s (100-50)$			
Measured, $N = 10$	-39.2	-6.17	0.60	2.855	0.274
Calculated, $N = 10$	-39.2	-8.08			
Measured, $N = 3$	-45.2	-12.2	2.20	4.624	0.267
Calculated, $N = 3$	-45.5	-10.5			
Measured, $N = 1$	-34.9	-7.76	10.00	5.507	0.242
Calculated, $N = 1$	-34.4	-6.67			

As all differences are minor, the agreement between the calculations and the measurements can be considered good.

5.3.2 Experimental pulse sensing results with a rod-shaped sensor

Given the factors discussed in the previous subsection, the changes in the signal amplitude caused by cardiac activity were detected employing developed CIA with a PC200 ferrite core sensor with a coil of 1.8 (not full 2) turns. The 54 mm long rod core was chosen for the high coupling factor (see Fig. 5.14b) and the convenience of locating the artery on the left wrist. Windings were placed 2 mm from the sensor's edge to minimize the stray capacitance's impact, slightly decreasing the coupling factor ($k = 0.37$). The coil with $L_p = 197 \text{ nH}$ and the capacitor with $C_p = 10 \text{ nF}$ forms a parallel resonant circuit with $Q = 110$ and the magnitude of the impedance $|Z| = 488 \Omega$ at the resonant frequency of 3.5058 MHz in the initial condition. Fig. 5.23 illustrates the measured magnitude and phase curves at different secondary resistance R_s in an $18 \times 18 \text{ mm}$ test loop.

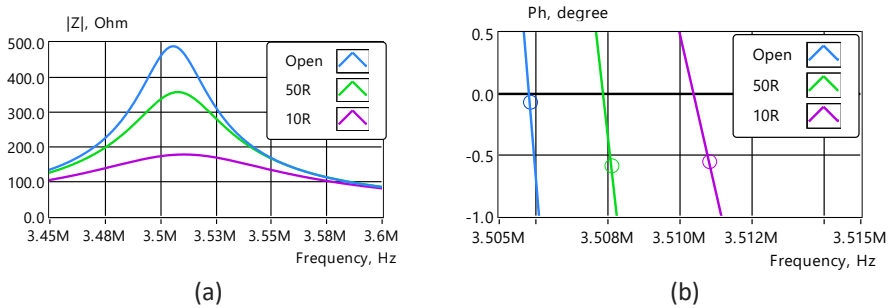


Fig. 5.23 Magnitude (a) and phase (b) changes of the rod-shaped sensor impedance with two windings for the open secondary loop and 50 Ω , 10 Ω secondary resistance R_s . Phase curves are zoomed out near zero phase crossing, where the circles denote the phases at frequencies corresponding to the maximum impedance magnitude.

The measured $d|Z_p|$ is 50.4%, which is higher in comparison with other cases provided in Table 5.3. However, the coupling factor k of the sensor with a long rod is also higher. The measurement results also indicate that the impedance magnitudes maxima do not coincide with a zero phase and the differences depend on the value of the secondary resistance. The phase difference described arises from the asymmetry of the loss resistance in the capacitance and inductance parts of the resonant circuit. Due to this

situation, it becomes difficult to monitor the impedance maxima (because it cannot be decided based on phase zero). Another related fact is that a change in the secondary circuit impedance produces a change in phase that depends on which side of the phase zero it is. In practice, the situation is even more complex since the secondary impedance is not purely resistive.

Fig. 5.24 to Fig. 5.26 illustrate the results obtained with a rod-shaped sensor. The sensor coil was excited with a 0.4 V signal at the expected resonance frequency, and the change of the response current was monitored. The current (minimal at resonance) was amplified and converted to voltage with a TIA (as shown in Fig. 4.16) and digitized with a 16-bit A/D converter of the CIA. The shape of the current waveform is mirrored in comparison with the impedance change. It can be converted to impedance, but as the relationship between the excitation voltage and the response current depends significantly on the actual coupling factor of the inductive sensor, it is still applicable only for the presentation of relative changes. As explained in the previous sections, the real coupling factor depends on many hard-to-determine variables. However, it is not necessary when only relative changes and the shape of the curve are of interest.

Fig. 5.24 illustrates unfiltered response current magnitude and phase changes caused by the cardiac activity of the artery on the left wrist. The steps in Fig. 5.24a correspond to LSB of the 16-bit A/D converter. Around 50% of the full-scale is in use in the current case.

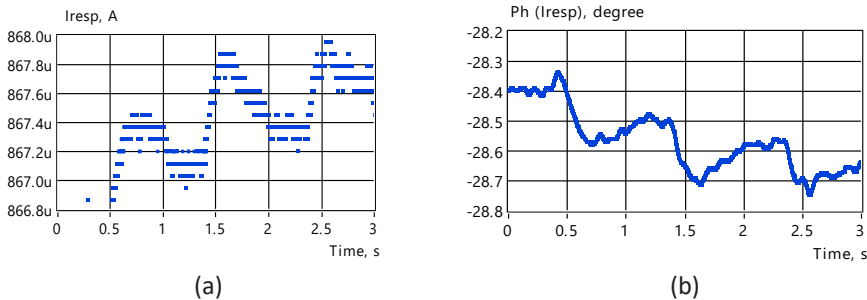


Fig. 5.24 Raw magnitude (a) and phase (b) changes of the response current caused by the cardiac activity of the artery on the left wrist obtained with the rod-shaped sensor.

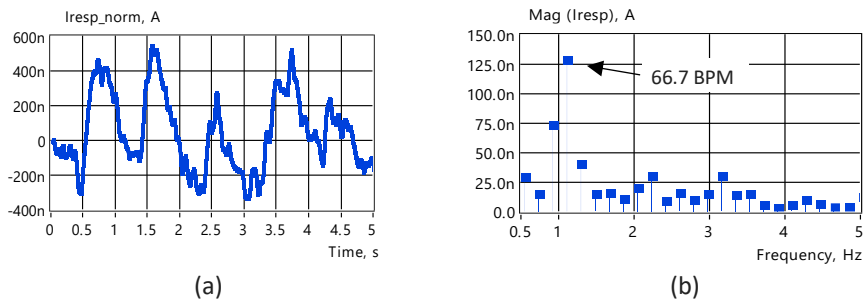


Fig. 5.25 Filtered and normalized magnitude (a) of the response current shown in Fig. 5.24a and its magnitude spectrum (b).

Fig. 5.25a shows the normalized and filtered by 8-point half-width moving-average FIR filter curve of the same signal and Fig. 5.25b shows its magnitude spectrum. The peak value in the spectrum corresponds to the pulse rate of 66.7 beats per minute (BPM). Fig. 5.26a shows the normalized and filtered curve of changes caused by the cardiac activity of the artery on the left wrist, and Fig. 5.26b shows its magnitude spectrum obtained in the second experiment.

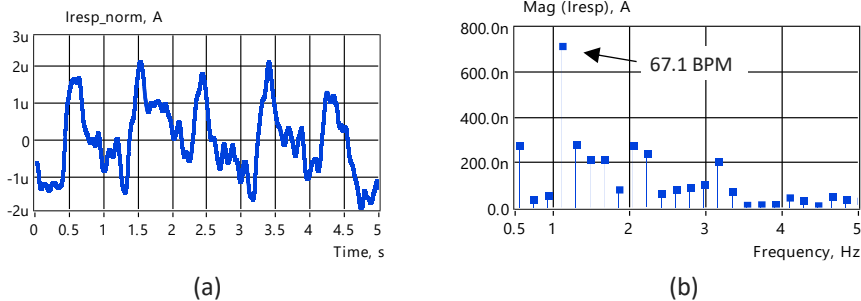


Fig. 5.26 Filtered and normalized magnitude (a) of the response current and its magnitude spectrum (b) caused by the cardiac activity of the artery on the left wrist.

In the second experiment, the mean value of the response current was 1.02 mA, which corresponds to 70 % of the full scale; also, its relative change is around three times higher. The peak value in the spectrum corresponds to the pulse rate of 67.1 BPM.

CONCLUSIONS. Experiments have proved that cardiac activity-related signals are detectable with an induction sensor near the artery on the left wrist. However, the signals were obtained only at one of the carefully searched locations of the sensor when finding the appropriate measurement frequency with an accuracy of near 1 kHz at the same time. As the signals found were also noisy and close to the sensitivity limit, the possibility of practical use of such a solution remains highly questionable.

Even when using resonance, the significant baseline value of the measured signal, which was around 1 mA in the described experiment, remains a problem because the amplitude of the change was only 8–30 LSB of the A/D converter. Increasing the initial impedance of the resonant circuit reduces the baseline value, which allows an increase in the sensitivity and improves the SNR related to A/D conversion. For example, choosing a 3-winding sensor with a C_p capacitance of 2.2 nF (see Fig. 5.21) would give a nearly four-fold lower current value and a possibility to increase the signal's absolute change by increasing the TIA gain four times. However, such a solution for increasing sensitivity has several drawbacks. The overall SNR remains almost the same but most likely decreases due to higher signal source (resonant circuit) resistance and TIA gain. Secondly, a higher Q factor of the resonant circuit complicates following the impedance maximum. However, the most significant disadvantage is the almost 5-fold lower C_p value, which makes the sensor too sensitive to changes in stray capacitances. Thus, it remains unclear whether the signal's changes are related to inductive coupling or changes in capacitances.

5.4 Toroidal Sensor with a Closing Loop of the Induced Current

5.4.1 Measurement strategy

Fig 5.27 illustrates the measurement strategy with a toroidal sensor introduced in sections 5.1.2 and 5.1.3. Two additional electrodes close the induced current loop and are also used for current measurement.

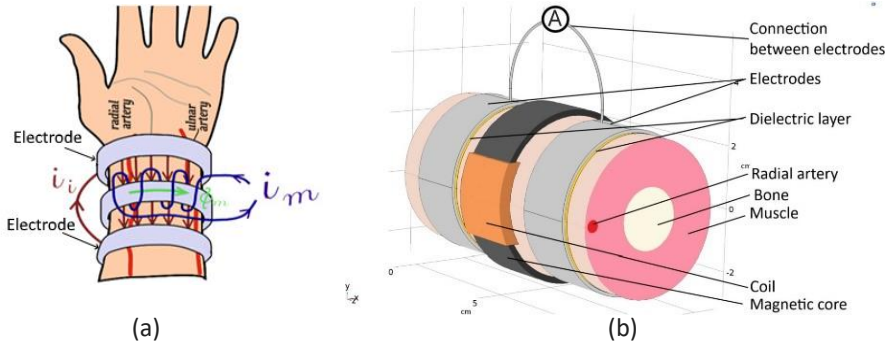


Fig. 5.27 The induced current i_i closed by a wire connecting the additionally introduced electrodes (a) and a model used for computer simulation (b).

It is assumed that in this situation, the induced current flows mainly through the radial artery, as illustrated with FEM modeling results in Fig. 5.28.

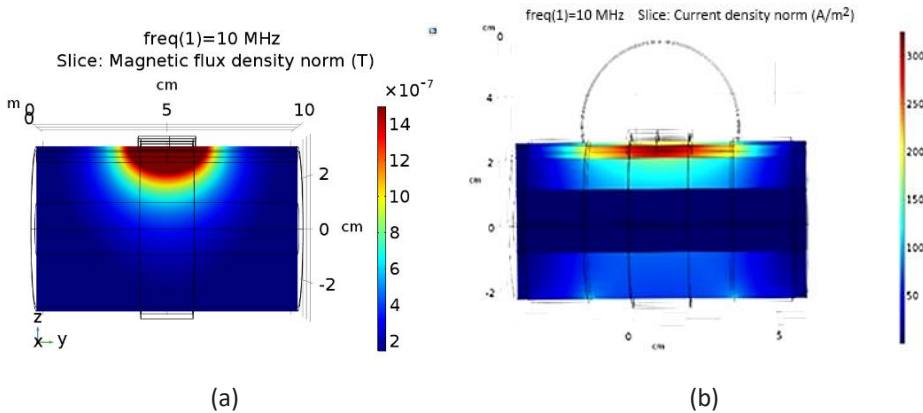


Fig. 5.28 Simulation results: (a) - distribution of the magnetic flux density and (b) – distribution of the induced current density; the highest current density is inside the blood vessel (radial artery).

Fig 5.29 shows an experimental measurement setup.

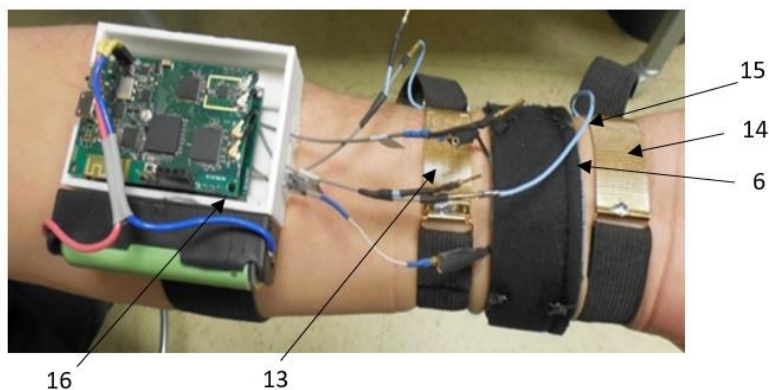


Fig. 5.29 A photograph of the experimental measurement setup containing the following components: 6 – toroidal magnetic system, 13 and 15 – electrodes for closing the induced current loop, 15 – the closing wire, 16 – CIA containing measurement, signal processing and data communication components.

5.4.2 Experimental results obtained with the local closing loop method

The following are the results obtained by measuring the induced current with electrodes, as illustrated in Fig. 5.27 and Fig. 5.29. In Fig. 5.30, the normalized waveform of the response current corresponding to cardiac activity is shown for the closed toroidal core with a cross-section of 2×30 mm. The coil is excited differentially, providing double maximum amplitude at the same supply voltage and reducing stray capacitance influence between the body and CIA.

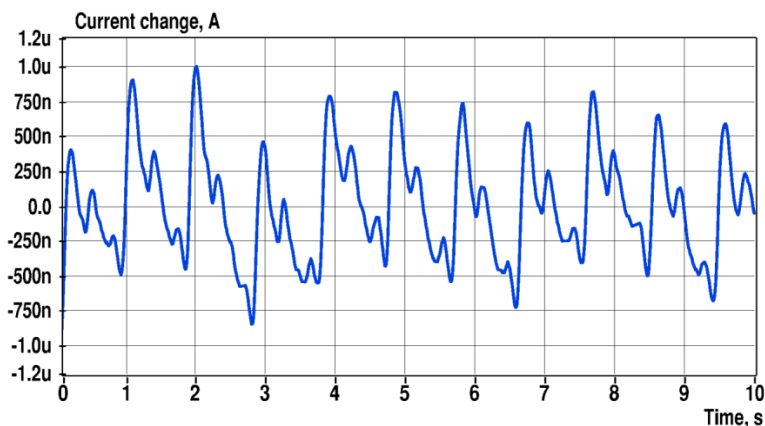


Fig. 5.30 Response current change corresponding to cardiac activity. Core: toroidal flexible TDK Flex IRL02, 2 mm thick and 30 mm wide, closed ring. The number of coil windings $N = 10$, the diameter of wire $d = 0.5$ mm, winding width 12 mm, inductance $5.68 \mu\text{H}$. Differential excitation voltage $V_{exc_d} = 2$ V, $I_{exc} = 23.1$ mA at frequency 4 MHz. Mean value of measured response current in the forearm: $927 \mu\text{A}$.

The shape of the current waveform is mirrored in comparison with the impedance change. However, its conversion to the impedance is not necessary when only relative changes and the shape of the curve are of interest (see explanation in section 5.1.9). Fig. 5.32 shows the waveform of the response current with a modified core cross-section of the sensor's core; it is two times narrower and two times thicker. The mean value of the response current increased, but its change remained almost the same, i.e., the relative sensitivity of the sensor decreased.

Fig. 5.33 shows the waveform of the response current detected with a shortened to 1/3 of the full-length core depicted in Fig. 5.31. The cross-section dimensions are the same as in the previous case. The relative sensitivity of the sensor is the lowest.

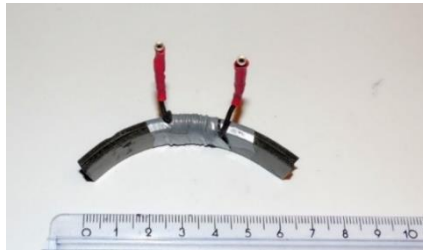


Fig. 5.31 Shortened to 1/3 of the full-length ferrite core with a coil.

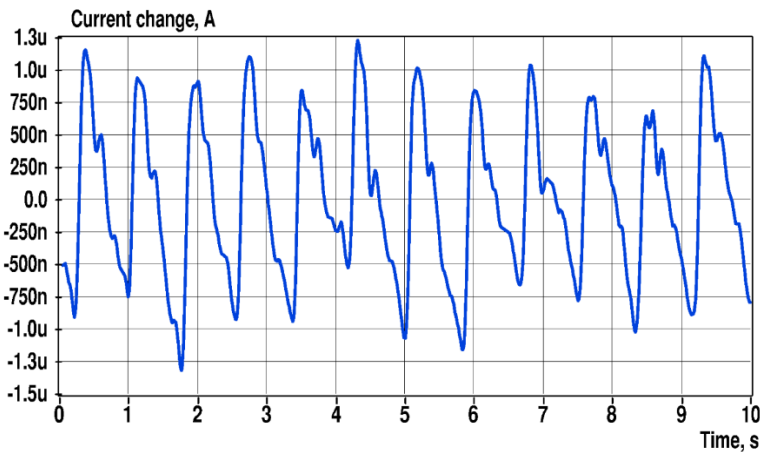


Fig. 5.32 Response current change corresponding to cardiac activity. Core: toroidal flexible TDK Flex IRL02, 4 mm thick and 15 mm wide, closed ring. The number of coil windings 10, the diameter of wire $d = 0.5$ mm, winding width 12 mm, inductance $4.46 \mu\text{H}$. Differential excitation voltage $V_{\text{exc}_d} = 2$ V, frequency 4 MHz. Mean value of measured response current in the wrist: 1.74 mA.

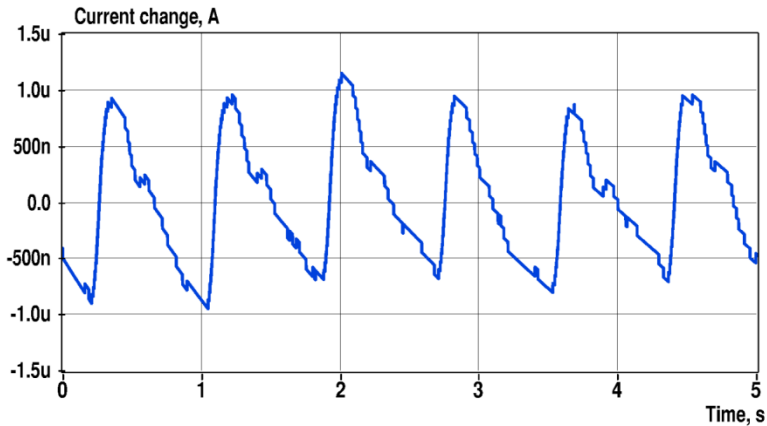


Fig. 5.33 Response current change corresponding to cardiac activity Core: toroidal flexible TDK Flex IRL02, 4 mm thick and 15 mm wide, shortened to 7 cm (see Fig. 5.31). The number of coil windings 10, the diameter of wire $d = 0.5$ mm, winding width 12 mm, inductance $4.33 \mu\text{H}$. Differential excitation voltage $V_{\text{exc}_d} = 2$ V, frequency 4 MHz. Mean value of measured response current in the wrist: 1.5 mA.

CONCLUSIONS. Experiments have proved that an induction sensor with an additional current closing loop detects cardiac activity-related signals on a forearm. The advantage in comparison with the reflected impedance change detection is lesser dependence on the positioning of the sensor and no need for searching for a sensitivity maximum. Experiments also proved that closing the ferrite core is not required since the magnetic flux density concentrates near and does not depend considerably on distal parts of the core. However, the signals were still close to the sensitivity limit, and the sensor had large dimensions. Moreover, there is a relatively large capacitance of around 16 pF between the coil and forearm (measured against the copper foil of 40 x 70 mm with E4990A). The differential excitation of the coil reduces the influence of capacitive coupling. However, the asymmetry of the design (CIA location on one side of the sensor) decreases its efficiency. Thus, the influence of capacitive coupling remains unclear and needs further investigation.

5.5 Summary of Chapter

The chapter focuses on magnetic induction-based measurement of electrical bioimpedance variations.

The first part of the chapter describes different methods and types of inductive sensors, including sensors with solenoidal, planar and toroidal coils and the fundamental relationships determining the parameters of inductive coupling in the case of interaction with a body. The dependences of the coupling factor on the distance and surface area of the secondary eddy current loop are illustrated. The magnetic flux concentration to the space of interest could increase the excitation current and simplify the measurement of its response. The impact of magnetic cores and their parameters, such as effective permeability and permittivity, are discussed and illustrated.

The second part of the chapter focuses on analyzing impedance transformation via inductive coupling. Experimentally measured coupling factors and their dependence on a

distance are compared for different sensor designs. It is found that the coupling factor of the sensor with toroidal core decays similarly to the U-shaped sensor, indicating that it differs significantly from the idealized toroidal transformer. It is also shown that in the case of a similar sensor design, the inductive coupling factor does not depend considerably on the number of windings. Next, the comprehensive analysis of the normalized sensitivity of different sensors in the non-resonant and resonant operating modes is given, and the following conclusions are drawn:

- 1) The impedance magnitude and phase changes detection sensitivity are significantly higher in resonant mode (over 60 times in given conditions) than in the non-resonant mode of operation.
- 2) The sensitivity of impedance change detection does not depend considerably on the number of windings N of the sensor coil.
- 3) A relatively small change (below one pF) in the input capacitance C_p significantly affects the overall result since it affects the primary side directly, but the low inductive coupling factor weakens the influence of secondary impedance by the squared rule.
- 4) As the sensitivity does not depend considerably on N , setting it to 1 or 2 reduces the influence of C_p change since its base value increases. However, this also causes a lower initial maximum magnitude of the impedance, increasing the base value of the detected signal (current in the case of voltage excitation) and limiting the measurement sensitivity.
- 5) The initial value of the sensitivity depends on serial and parallel loss resistances and the initial magnitude of the secondary impedance. It increases almost proportionally when this initial value decreases, thus, suppressing the influence of changes in model elements with higher impedance.

The third part of the chapter provides the results of the experimental measurements with different U-shaped and rod sensors and their comparison with calculated values showing their good matching. Experiments with the rod sensor having two windings have proved that cardiac activity-related signals are detectable with such an induction sensor near the artery on the left wrist. However, the signals were obtained only at one of the carefully searched locations of the sensor when finding the appropriate measurement frequency with an accuracy of near 1 kHz at the same time. As the signals found were also noisy and close to the sensitivity limit, the possibility of practical use of such a solution remains highly questionable. The sensitivity can be increased to some extent with more windings; however, minimization of the capacitive coupling becomes crucial in this case, and no good solution has been found for that during current research work.

The fourth part of the chapter presents a novel solution of the induction sensor with the flexible ferrite toroidal core employing additional electrodes closing the loop of induced current. Experiments proved that such a sensor detects cardiac activity-related signals on a forearm. An advantage in comparison with the reflected impedance change detection is lesser dependence on the positioning of the sensor and no need for searching for a sensitivity maximum. However, the signals were still close to the sensitivity limit, and the sensor had large dimensions. Moreover, there is a relatively large capacitance (around 16 pF) between the coil and forearm. The differential excitation of the coil reduces the influence of capacitive coupling. However, the asymmetry of the design (CIA location on one side of the sensor) decreases its efficiency. Thus, the influence of capacitive coupling remains unclear and needs further investigation.

6 Conclusions

The current thesis focused on the methods and solutions for detecting the changes in body tissue state using electromagnetic interaction. The highest interest and practical application was the observation of activities of the cardiovascular system. The changes in tissue properties caused by cardio-pulmonary activity are tiny. Therefore, reliable results may be obtained only with proper methods, a carefully designed measurement setup and a good relationship between the tissue and its electrical equivalent circuit model.

Methods covered are based on electromagnetic waves, resistive, capacitive, and inductive coupling. Based on the results of the work, the following conclusions were drawn:

1. UWB radar is proved to be helpful for contactless long-term cardio-pulmonary activity monitoring with good results in well-prepared rooms for that purpose, e.g., in the hospital ward. Examples of the use of UWB radar are long-term monitoring of obstructive sleep apnoea, cardiac monitoring (including severe burns when contact electrodes cannot be used), respiratory monitoring and sudden infant death syndrome monitoring. Experiments on the determination of boundary layers in tissue to detect hematomas were unsuccessful because of the high attenuation of ultra-short impulses required for high spatial resolution.
2. The study of the background of electrical bioimpedance (EBI) measurement on the human body reveals that considering the dependence of measurement results on selecting an adequate electrical model, the surrounding environment and selected measurement solution are insufficient in many previous works. A compact battery-powered wireless analyzer capable of the highest possible resolution and accuracy impedance measurement in the 10 MHz range is required to determine EBI model parameters in the β -dispersion area. Moreover, a two-electrode measurement scheme with a voltage excitation has essential advantages compared to a four-electrode method employing current-source excitation. However, in the cases where only the EBI changes at lower frequencies (below 100 kHz) mainly related to the resistive part of the impedance are of interest, a four-electrode circuit with a current excitation allows for building simpler and low-power devices.
3. Developed enhanced patent-pending measurement solution for monitoring EBI changes on a wrist with Ag/AgCl electrodes at 120 kHz demonstrates a wearable low-energy device with minimized hardware requirements and computational power to the lowest level. The method uses the running differences of the response signal in that the output signal is the derivative as the measure of EBI change. Integration of the derivative also provides the original EBI signal change waveform.
4. Tests and practical experiments prove that the developed compact impedance analyzer (CIA) shows exceptional performance comparable with high-end commercial ones with significantly larger dimensions, complexity and price and allows minimization of the influence of the stray capacitance. The experiments with large capacitive electrodes employing the CIA allowed determining the forearm model parameters and evaluating their weight at different frequencies. Analysis of the measurement results shows that the effect of the cell membrane capacitances of the forearm tissue is considerable only at

frequencies above 100 kHz, and extracellular and intracellular conductivities mask it; thus, the possibility of monitoring its changes remains questionable.

Experiments also show that the impedance changes related to cardiovascular activity measured between large capacitive electrodes on a wrist remain below 0.1%. Although the pulse rate is obtainable, the signal is near the sensitivity limit of the 16-bit analyzer and still influenced by motion artifacts mostly related to changes in stray capacitances above 1 MHz, while below 1 MHz, the sensitivity of such sensors is insufficient due to the increased impedance of capacitive electrodes. Increased sensitivity will not improve the situation, as it does not reduce the impact of artifacts.

5. The analysis of properties of different designs of inductive sensors and experiments employing the developed CIA allowed determining the feasibility of using magnetic coupling for monitoring cardio-vascular activity on the forearm. Sensors with magnetic cores were mainly considered assuming minimization of dimensions of sensors and the possibility of concentration of the magnetic flux in the desired location. The analysis that matches well with experimental data allows finding optimal parameters of sensors for better sensitivity and determining the influence of model elements on the total results.

Only the sensors working in the resonant mode provided sufficient sensitivity for detecting transformed to primary side impedance magnitude and phase changes. However, the signals were obtained only at one of the carefully searched locations of the sensor when finding the appropriate measurement frequency with an accuracy of near 1 kHz at the same time. The sensitivity can be increased to some extent with more windings; however, minimization of the capacitive coupling becomes crucial in this case.

Also, a novel solution of the induction sensor with the flexible ferrite toroidal core employing additional electrodes closing the loop of induced current was designed. However, the signals were also close to the sensitivity limit, and the sensor had large dimensions. Moreover, there is a relatively large capacitance (around 16 pF) between the coil and forearm. While partly compensated by differential excitation, its influence is still unclear.

6.1 General Conclusions and Directions for Further Research

Impedance changes are reasonable to measure where they occur – for example, heart-related changes in a circuit loop passing the heart area rather than on a forearm or wrist.

Too tiny relative changes in the impedance of body parts away from the chest and factors disturbing the measurements, mainly the influence of stray capacitances and movement of the body and its inner parts, make it questionable to monitor the cardiovascular activity by changes of EBI waveform reliably. Respiratory-related EBI changes are probably undetectable in the forearm, as not observed in the case of the minimized influence of stray capacitances.

Two main factors limiting the efficiency of sensors with inductive coupling are: 1) a low coupling factor with inner tissue layers and blood vessels and 2) the influence of stray capacitances. Addressing these bottlenecks, for example, by efficient sensor shielding, could be the subject of further research.

References

- [1] A. Timmis *et al.*, “European Society of Cardiology: Cardiovascular Disease Statistics 2017,” *European Heart Journal*, vol. 39, no. 7, pp. 508–579, Feb. 2018, doi: 10.1093/eurheartj/ehx628.
- [2] H. C. McGill, C. A. McMahan, and S. S. Gidding, “Preventing Heart Disease in the 21st Century: Implications of the Pathobiological Determinants of Atherosclerosis in Youth (PDAY) Study,” *Circulation*, vol. 117, no. 9, pp. 1216–1227, Mar. 2008, doi: 10.1161/CIRCULATIONAHA.107.717033.
- [3] A. V. Chobanian *et al.*, “Seventh Report of the Joint National Committee on Prevention, Detection, Evaluation, and Treatment of High Blood Pressure,” *Hypertension*, vol. 42, no. 6, pp. 1206–1252, Dec. 2003, doi: 10.1161/01.HYP.0000107251.49515.c2.
- [4] WHO, “Hypertension,” Aug. 25, 2021. <https://www.who.int/news-room/factsheets/detail/hypertension> (accessed Dec. 01, 2021).
- [5] H. Kõiv, M. Rist, and M. Min, “Development of bioimpedance sensing device for wearable monitoring of the aortic blood pressure curve,” *tm - Technisches Messen*, vol. 85, Mar. 2018, doi: 10.1515/teme-2017-0113.
- [6] B. Ibrahim, V. Nathan, and R. Jafari, *Exploration and validation of alternate sensing methods for wearable continuous pulse transit time measurement using optical and bioimpedance modalities*, vol. 2017. 2017, p. 2055. doi: 10.1109/EMBC.2017.8037256.
- [7] M. Min, H. Kõiv, E. Priidel, K. Pesti, and P. Annus, “Noninvasive Acquisition of the Aortic Blood Pressure Waveform,” in *Wearable Devices - the Big Wave of Innovation*, N. Nasiri, Ed. IntechOpen, 2019. doi: 10.5772/intechopen.86065.
- [8] B. Ibrahim and R. Jafari, “Cuffless Blood Pressure Monitoring from an Array of Wrist Bio-Impedance Sensors Using Subject-Specific Regression Models: Proof of Concept,” *IEEE Trans. Biomed. Circuits Syst.*, vol. 13, no. 6, pp. 1723–1735, Dec. 2019, doi: 10.1109/TBCAS.2019.2946661.
- [9] L. Lapicque, “Recherches quantitatives sur l’excitation électrique des nerfs traitée comme une polarisation,” *J. Physiol. Pathol. Gen.*, vol. 9, pp. 620–635, 1907.
- [10] M. Philippson, “Les lois de la résistance électrique des tissus vivants,” *Bull. Cl. Sci. Acad. Roy. Belgique*, vol. 7, pp. 387–403, 1921.
- [11] H. Fricke, “A Mathematical Treatment of the Electric Conductivity and Capacity of Disperse Systems ii. The Capacity of a Suspension of Conducting Spheroids Surrounded by a Non-Conducting Membrane for a Current of Low Frequency,” *Phys. Rev.*, vol. 26, no. 5, pp. 678–681, Nov. 1925, doi: 10.1103/PhysRev.26.678.
- [12] N. De Pinho Ferreira, C. Gehin, and B. Massot, “A Review of Methods for Non-Invasive Heart Rate Measurement on Wrist,” *IRBM*, vol. 42, no. 1, pp. 4–18, Feb. 2021, doi: 10.1016/j.irbm.2020.04.001.
- [13] G. Y. Jang *et al.*, “Noninvasive, simultaneous, and continuous measurements of stroke volume and tidal volume using EIT: feasibility study of animal experiments,” *Sci Rep*, vol. 10, no. 1, p. 11242, Dec. 2020, doi: 10.1038/s41598-020-68139-3.
- [14] G. Anand, Y. Yu, A. Lowe, and A. Kalra, “Bioimpedance analysis as a tool for hemodynamic monitoring: overview, methods and challenges,” *Physiol. Meas.*, vol. 42, no. 3, p. 03TR01, Mar. 2021, doi: 10.1088/1361-6579/abe80e.

- [15] S. Grimnes and Ø. G. Martinsen, *Bioimpedance and Bioelectricity Basics - 3rd Edition*. 2014. [Online]. Available: <https://www.elsevier.com/books/bioimpedance-and-bioelectricity-basics/grimnes/978-0-12-411470-8>
- [16] M. Min, T. Parve, and U. F. Pliquett, "Impedance Detection," in *Encyclopedia of Microfluidics and Nanofluidics*, D. Li, Ed. New York, NY: Springer New York, 2015, pp. 1338–1361. doi: 10.1007/978-1-4614-5491-5_1783.
- [17] K. R. Foster and H. P. Schwan, "Dielectric Properties of Tissues and Biological Materials: a Critical Review," *Crit Rev Biomed Eng*, vol. 17, no. 1, pp. 25–104, 1989.
- [18] S. Grimnes and Ø. G. Martinsen, *Bioimpedance and Bioelectricity Basics - 3rd Edition*. 2014. Accessed: Mar. 19, 2019. [Online]. Available: <https://www.elsevier.com/books/bioimpedance-and-bioelectricity-basics/grimnes/978-0-12-411470-8>
- [19] W. Kuang and S. O. Nelson, "Low-frequency dielectric properties of biological tissues: a review with some new insights," *Trans. ASAE (USA)*, vol. 41, no. 1, pp. 173–184, 1998.
- [20] R. Pethig and D. B. Kell, "The Passive Electrical Properties of Biological Systems: Their Significance in Physiology, Biophysics and Biotechnology," *Physics in Medicine & Biology*, vol. 32, no. 8, p. 933, 1987, doi: 10.1088/0031-9155/32/8/001.
- [21] C. Gabriel, S. Gabriel, and E. Corthout, "The Dielectric Properties of Biological Tissues: I. Literature Survey," *Physics in Medicine & Biology*, vol. 41, no. 11, p. 2231, 1996, doi: 10.1088/0031-9155/41/11/001.
- [22] F. Nekoogar, *Ultra-wideband communications: fundamentals and applications*. Upper Saddle River, NJ: Prentice Hall Professional Technical Reference, 2006.
- [23] P. Tupin, "UWB Radar in Health Monitoring Products," presented at the ITU WORKSHOP on SHORT RANGE DEVICES (SRDs) AND ULTRA WIDE BAND (UWB), Geneva, Switzerland, Jun. 03, 2014. [Online]. Available: <https://www.itu.int/en/ITU-R/study-groups/workshops/RWP1B-SRD-UWB-14/Presentations/UWB%20Radar%20in%20Health%20Monitoring%20Products.pdf>
- [24] C. N. Paulson, J. T. Chang, C. E. Romero, J. Watson, F. J. Pearce, and N. Levin, "Ultra-wideband radar methods and techniques of medical sensing and imaging," Boston, MA, Nov. 2005, p. 60070L. doi: 10.1117/12.630004.
- [25] E. M. Staderini, "UWB radars in medicine," *IEEE Aerosp. Electron. Syst. Mag.*, vol. 17, no. 1, pp. 13–18, Jan. 2002, doi: 10.1109/62.978359.
- [26] S. Azevedo and T. E. McEwan, "Micropower impulse radar," *Science and Technology Review*, Jan. 1996, [Online]. Available: <https://www.osti.gov/biblio/269435>
- [27] G. Varotto and E. M. Staderini, "On the UWB medical radars working principles," *IJWBCS*, vol. 2, no. 2, p. 83, 2011, doi: 10.1504/IJWBCS.2011.044600.
- [28] J. C. Lin, "Noninvasive microwave measurement of respiration," *Proc. IEEE*, vol. 63, no. 10, pp. 1530–1530, 1975, doi: 10.1109/PROC.1975.9992.
- [29] D. Wang, S. Yoo, and S. H. Cho, "Experimental Comparison of IR-UWB Radar and FMCW Radar for Vital Signs," *Sensors*, vol. 20, no. 22, p. 6695, Nov. 2020, doi: 10.3390/s20226695.
- [30] T. Kaiser and F. Zheng, *Ultra wideband systems with MIMO*. Chichester, West Sussex, U.K. ; Hoboken, NJ: Wiley, 2010.
- [31] I. Oppermann, Ed., *UWB theory and applications*, Reprinted. Chichester: Wiley, 2006.
- [32] I. Y. Immovreev, S. Samkov, and Teh-Ho Tao, "Short-distance ultra wideband radars," *IEEE Aerosp. Electron. Syst. Mag.*, vol. 20, no. 6, pp. 9–14, Jun. 2005, doi: 10.1109/MAES.2005.1453804.

- [33] M. Persson *et al.*, "Microwave-Based Stroke Diagnosis Making Global Prehospital Thrombolytic Treatment Possible," *IEEE Trans. Biomed. Eng.*, vol. 61, no. 11, pp. 2806–2817, Nov. 2014, doi: 10.1109/TBME.2014.2330554.
- [34] T. Henriksson *et al.*, "Clinical trials of a multistatic UWB radar for breast imaging," in *2011 Loughborough Antennas & Propagation Conference*, Loughborough, United Kingdom, Nov. 2011, pp. 1–4. doi: 10.1109/LAPC.2011.6114004.
- [35] X. Li, *Body matched antennas for microwave medical applications*. Karlsruhe: KIT Scientific Publishing, 2014.
- [36] T. Onishi and S. Uebayashi, "Biological tissue-equivalent phantoms usable in broadband frequency range," *NTT DoCoMo Tech. J.*, vol. 7, no. 4, pp. 61–65, 2006.
- [37] H. Zhang, B. Flynn, A. T. Erdogan, and T. Arslan, "Microwave imaging for brain tumour detection using an UWB Vivaldi Antenna array," in *2012 Loughborough Antennas & Propagation Conference (LAPC)*, Loughborough, Leicestershire, United Kingdom, Nov. 2012, pp. 1–4. doi: 10.1109/LAPC.2012.6402964.
- [38] M. Jalilvand, E. Pancera, X. Li, T. Zwick, and W. Wiesbeck, "Hemorrhagic stroke detection via adaptive UWB medical imaging radar," in *2011 8th European Radar Conference*, 2011, pp. 317–320.
- [39] G. Quintero Díaz De León, "Analysis and Design of Ultra-Wideband Antennas in the Spectral and Temporal Domains," 2010, doi: 10.5075/EPFL-THESIS-4719.
- [40] Md. Islam, M. Islam, M. Faruque, Md. Samsuzzaman, N. Misran, and H. Arshad, "Microwave Imaging Sensor Using Compact Metamaterial UWB Antenna with a High Correlation Factor," *Materials*, vol. 8, no. 8, pp. 4631–4651, Jul. 2015, doi: 10.3390/ma8084631.
- [41] X. Z. Raimundo, *FMCW Signals for Radar Imaging and Channel Sounding*. Durham University, 2015. [Online]. Available: <https://books.google.ee/books?id=liOrvwEACAAJ>
- [42] M. A. Alzabidi, M. A. Aldhaeabi, and I. Elshafiey, "Optimization of UWB Vivaldi Antenna for Tumor Detection," in *2013 1st International Conference on Artificial Intelligence, Modelling and Simulation*, Kota Kinabalu, Malaysia, Dec. 2013, pp. 81–86. doi: 10.1109/AIMS.2013.20.
- [43] P. P. M. J. and J. Machac, "Universal Generator of Ultra-Wideband Pulses," *Radioengineering*, vol. 17, Jan. 2008.
- [44] J. Zhou, Q. Lu, F. Liu, and Y. Li, "A Novel Picosecond Pulse Generation Circuit Based on SRD and NLTTL," *PLoS ONE*, vol. 11, no. 2, p. e0149645, Feb. 2016, doi: 10.1371/journal.pone.0149645.
- [45] T. E. McEwan, "Ultra-wideband receiver," 5,345,471, Sep. 1994
- [46] L. Liu, X. Xia, S. Ye, J. Shao, and G. Fang, "Development of a Novel, Compact, Balanced, Micropower Impulse Radar for Nondestructive Applications," *IEEE Sensors J.*, vol. 15, no. 2, pp. 855–863, Feb. 2015, doi: 10.1109/JSEN.2014.2356510.
- [47] J. Sachs *et al.*, "Ultra-wideband pseudo-noise sensors and their application in medical engineering, non-destructive testing and for search and rescue," *Information technology and electrical engineering - devices and systems, materials and technologies for the future*, vol. 54, 2009, p. Session 2.1, Nov. 2009.
- [48] J. Sachs, P. Peyerl, and R. Zetik, "Stimulation of UWB-Sensors: Pulse or Maximum Sequence?" 2003.
- [49] Z. Haoyu, "Microwave imaging for ultra-wideband antenna based cancer detection," PhD Thesis, Edinburgh, 2015.

- [50] A. Lazaro, D. Girbau, and R. Villarino, "SIMULATED AND EXPERIMENTAL INVESTIGATION OF MICROWAVE IMAGING USING UWB," *PIER*, vol. 94, pp. 263–280, 2009, doi: 10.2528/PIER09061004.
- [51] A. T. Mobashsher and A. Abbosh, "Microwave imaging system to provide portable-low-powered medical facility for the detection of intracranial hemorrhage," in *2014 1st Australian Microwave Symposium (AMS)*, Melbourne, Australia, Jun. 2014, pp. 23–24. doi: 10.1109/AUSMS.2014.7017347.
- [52] D. Oloumi, P. Boulanger, A. Kordzadeh, and K. Rambabu, "Breast tumor detection using UWB circular-SAR tomographic microwave imaging," in *2015 37th Annual International Conference of the IEEE Engineering in Medicine and Biology Society (EMBC)*, Milan, Aug. 2015, pp. 7063–7066. doi: 10.1109/EMBC.2015.7320019.
- [53] R. Scapatucci, O. M. Bucci, I. Catapano, and L. Crocco, "Differential Microwave Imaging for Brain Stroke Followup," *International Journal of Antennas and Propagation*, vol. 2014, pp. 1–11, 2014, doi: 10.1155/2014/312528.
- [54] K. S. Cole, "Electric impedance of suspensions of spheres," *Journal of General Physiology*, vol. 12, no. 1, pp. 29–36, Sep. 1928, doi: 10.1085/jgp.12.1.29.
- [55] H. Fricke and S. Morse, "The electric resistance and capacity of blood for frequencies between 800 and 4(1/2) million cycles," *J Gen Physiol*, vol. 9, no. 2, pp. 153–167, Nov. 1925, doi: 10.1085/jgp.9.2.153.
- [56] O. J. Zobel, "Theory and design of uniform and composite electric wave-filters," *The Bell System Technical Journal*, vol. 2, no. 1, pp. 1–46, 1923, doi: 10.1002/j.1538-7305.1923.tb00001.x.
- [57] S. Grimnes and Ø. G. Martinsen, "Bioimpedance," in *Wiley Encyclopedia of Biomedical Engineering*, John Wiley & Sons, Ltd, 2006, pp. 438–447. doi: <https://doi.org/10.1002/9780471740360.ebs0128>.
- [58] D. Ayllon, F. Seoane, and R. Gil-Pita, "Cole Equation and Parameter Estimation from Electrical Bioimpedance Spectroscopy Measurements - A Comparative Study," in *Conference proceedings : ... Annual International Conference of the IEEE Engineering in Medicine and Biology Society. IEEE Engineering in Medicine and Biology Society. Conference*, Jul. 2009, vol. 2009, pp. 3779–82. doi: 10.1109/IEMBS.2009.5334494.
- [59] T. J. Freeborn and S. Critcher, "Cole-Impedance Model Representations of Right-Side Segmental Arm, Leg, and Full-Body Bioimpedances of Healthy Adults: Comparison of Fractional-Order," *Fractal and Fractional*, vol. 5, no. 1, 2021, doi: 10.3390/fractalfract5010013.
- [60] K. S. Cole, "Analogue solution for electrical capacity of membrane-covered cubes in cubic array at high concentration.," *Proc Natl Acad Sci U S A*, vol. 73, no. 11, pp. 4003–4006, Nov. 1976, doi: 10.1073/pnas.73.11.4003.
- [61] K. S. Cole, "Permeability and impermeability of cell membranes for ions," *Cold Spring Harbor Symposia on Quantitative Biology*, vol. 8, pp. 110–122, 1940.
- [62] C. H. Hsu and F. Mansfeld, "Technical Note: Concerning the Conversion of the Constant Phase Element Parameter Y_0 into a Capacitance," *Corrosion*, vol. 57, no. 9, pp. 747–748, Sep. 2001, doi: 10.5006/1.3280607.
- [63] M. E. Orazem *et al.*, "Dielectric Properties of Materials Showing Constant-Phase-Element (CPE) Impedance Response," *Journal of The Electrochemical Society*, vol. 160, no. 6, pp. C215–C225, 2013, doi: 10.1149/2.033306jes.
- [64] Chang Byoung-Yong, "Conversion of a Constant Phase Element to an Equivalent Capacitor," *J. Electrochem. Sci. Technol*, vol. 11, no. 3, pp. 318–321, 2020, doi: 10.33961/jecst.2020.00815.

- [65] J. Huang and J. Zhang, "Theory of Impedance Response of Porous Electrodes: Simplifications, Inhomogeneities, Non-Stationarities and Applications," *Journal of The Electrochemical Society*, vol. 163, no. 9, pp. A1983–A2000, 2016, doi: 10.1149/2.0901609jes.
- [66] C. H. Lee *et al.*, "Topoelectrical Circuits," *Communications Physics*, vol. 1, no. 1, p. 39, Jul. 2018, doi: 10.1038/s42005-018-0035-2.
- [67] A. S. Elwakil, A. Allagui, and C. Psychalinos, "On The Equivalent Impedance of Two-Impedance Self-Similar Ladder Networks," *IEEE Transactions on Circuits and Systems II: Express Briefs*, vol. 68, no. 7, pp. 2685–2689, 2021, doi: 10.1109/TCSII.2021.3057961.
- [68] S. Holm, T. Holm, and Ø. G. Martinsen, "Simple circuit equivalents for the constant phase element.," *PLoS One*, vol. 16, no. 3, p. e0248786, 2021, doi: 10.1371/journal.pone.0248786.
- [69] R. Pethig and D. B. Kell, "The Passive Electrical Properties of Biological Systems: Their Significance in Physiology, Biophysics and Biotechnology," *Phys. Med. Biol.*, vol. 32, no. 8, p. 933, 1987, doi: 10.1088/0031-9155/32/8/001.
- [70] H. P. Schwan, "Biological effects of non-ionizing radiations: Cellular properties and interactions," *Ann Biomed Eng*, vol. 16, no. 3, pp. 245–263, May 1988, doi: 10.1007/BF02368002.
- [71] R. Kusche and M. Ryschka, "Multi-Frequency Impedance Myography: The PhaseX Effect," *IEEE Sensors J.*, vol. 21, no. 3, pp. 3791–3798, Feb. 2021, doi: 10.1109/JSEN.2020.3022899.
- [72] Y. Liu, X. Qiao, G. Li, and L. Lin, "An improved device for bioimpedance deviation measurements based on 4-electrode half bridge," *Review of Scientific Instruments*, vol. 87, no. 10, p. 105107, Oct. 2016, doi: 10.1063/1.4963658.
- [73] C. Aliau-Bonet and M. Quílez-Figuerola, "Effects of stray capacitance to ground in impedance measurements," in *Bioimpedance and Spectroscopy*, Elsevier, 2021, pp. 51–77. doi: 10.1016/B978-0-12-818614-5.00012-6.
- [74] Y. Tseng, C. Su, and Y. Ho, "Evaluation and Verification of Channel Transmission Characteristics of Human Body for Optimizing Data Transmission Rate in Electrostatic-Coupling Intra Body Communication System: A Comparative Analysis," *PLoS ONE*, vol. 11, no. 2, p. e0148964, Feb. 2016, doi: 10.1371/journal.pone.0148964.
- [75] C. Metting van Rijn, A. Peper, and C. Grimbergen, "High quality recording of bioelectric events. Part 1. Interference reduction, theory and practice," *Medical & biological engineering & computing*, vol. 28, pp. 389–97, Oct. 1990, doi: 10.1007/BF02441961.
- [76] B. Kibret, A. K. Teshome, and D. T. H. Lai, "Characterizing the Human Body as a Monopole Antenna," *IEEE Transactions on Antennas and Propagation*, vol. 63, no. 10, pp. 4384–4392, 2015, doi: 10.1109/TAP.2015.2456955.
- [77] R. Kusche, S. Kaufmann, and M. Ryschka, "Dry electrodes for bioimpedance measurements—design, characterization and comparison," *Biomed. Phys. Eng. Express*, vol. 5, no. 1, p. 015001, Nov. 2018, doi: 10.1088/2057-1976/aaea59.
- [78] J.-Y. Baek, J.-H. An, J.-M. Choi, K.-S. Park, and S.-H. Lee, "Flexible polymeric dry electrodes for the long-term monitoring of ECG," *Sensors and Actuators A: Physical*, vol. 143, no. 2, pp. 423–429, May 2008, doi: 10.1016/j.sna.2007.11.019.
- [79] J. D. Bronzino, Ed., *The biomedical engineering handbook*, 2nd ed. Boca Raton, FL: CRC Press, 2000.

- [80] C. Canali *et al.*, “An impedance method for spatial sensing of 3D cell constructs – towards applications in tissue engineering,” *Analyst*, vol. 140, no. 17, pp. 6079–6088, 2015, doi: 10.1039/C5AN00987A.
- [81] F. F. Kuo, *Network Analysis and Synthesis*, 2nd ed. Wiley, 1962. [Online]. Available: <https://books.google.ee/books?id=wKNrAAAAMAAJ>
- [82] S. B. Rutkove, A. Pacheck, and B. Sanchez, “Sensitivity distribution simulations of surface electrode configurations for electrical impedance myography,” *Muscle & Nerve*, vol. 56, no. 5, pp. 887–895, 2017, doi: <https://doi.org/10.1002/mus.25561>.
- [83] B. Sanchez, A. Pacheck, and S. B. Rutkove, “Guidelines to electrode positioning for human and animal electrical impedance myography research,” *Scientific Reports*, vol. 6, no. 1, p. 32615, Sep. 2016, doi: 10.1038/srep32615.
- [84] K. Pesti, “Modelling and Simulation of Arterial Blood Pulsation via Bioimpedance,” Tallinn University of Technology, 2021. doi: 10.23658/TALTECH.34/2021.
- [85] V. Sirtoli, K. Morcelles, J. Gomez, and P. Bertemes-Filho, “Design and Evaluation of an Electrical Bioimpedance Device Based on DIBS for Myography during Isotonic Exercises,” *Journal of Low Power Electronics and Applications*, vol. 8, no. 4, 2018, doi: 10.3390/jlpea8040050.
- [86] V.-P. Seppä, “Development and Clinical Application of Impedance Pneumography Technique,” Tampere University of Technology, Tampere, 2014.
- [87] A. Grenvik, S. Ballou, E. McGinley, J. E. Millen, W. L. Cooley, and P. Safar, “Impedance Pneumography: Comparison between Chest Impedance Changes and Respiratory Volumes in 11 Healthy Volunteers,” *Chest*, vol. 62, no. 4, pp. 439–443, Oct. 1972, doi: 10.1378/chest.62.4.439.
- [88] M. Metshein, “Wearable Solutions for Monitoring Cardiorespiratory Activity.,” Tallinn University of Technology, 2018. Accessed: Mar. 22, 2019. [Online]. Available: <https://digi.lib.ttu.ee/i/?9961>
- [89] D. Andreuccetti, R. Fossi, and C. Petrucci, “An Internet Resource for the Calculation of the Dielectric Properties of Body Tissues in the Frequency Range 10 Hz - 100 GHz.” 1997.
- [90] J. Nyboer, M. M. Kreider, and L. Hannapel, “Electrical Impedance Plethysmography: A Physical and Physiologic Approach to Peripheral Vascular Study,” *Circulation*, vol. 2, no. 6, pp. 811–821, Dec. 1950, doi: 10.1161/01.CIR.2.6.811.
- [91] H. Yazdanian, A. Mahnam, M. Edrisi, and M. A. Esfahani, “Design and Implementation of a Portable Impedance Cardiography System for Noninvasive Stroke Volume Monitoring,” *J Med Signals Sens*, vol. 6, no. 1, pp. 47–56, 2016.
- [92] T. K. Bera, “Bioelectrical Impedance Methods for Noninvasive Health Monitoring: A Review,” *Journal of Medical Engineering*, vol. 2014, pp. 1–28, 2014, doi: 10.1155/2014/381251.
- [93] A. Krivošei, “Model Based Method for Adaptive Decomposition of the Thoracic Bioimpedance Variations into Cardiac and Respiratory Components,” Tallinn University of Technology, Tallinn, 2009. Accessed: Nov. 07, 2017. [Online]. Available: <https://digi.lib.ttu.ee/i/?447>
- [94] J. P. Allen and D. T. Mininberg, *The Art of Medicine in Ancient Egypt*. 2005.
- [95] R. P. Patterson, “Impedance Cardiography: What is the Source of the Signal?,” *J. Phys.: Conf. Ser.*, vol. 224, no. 1, p. 012118, 2010, doi: 10.1088/1742-6596/224/1/012118.
- [96] J. Vedru, “Electrical Impedance Methods for the Measurement of Stroke Volume in Man: State of Art,” in *Acta et commentationes Universitatis Tartuensis*, 1994, pp. 110–129.

- [97] P. K. Kauppinen, J. A. Hyttinen, and J. A. Malmivuo, "Sensitivity Distributions of Impedance Cardiography Using Band and Spot Electrodes Analyzed by a Three-Dimensional Computer Model," *Annals of Biomedical Engineering*, vol. 26, no. 4, pp. 694–702, Jul. 1998, doi: 10.1114/1.44.
- [98] V.-P. Seppä, J. Hyttinen, M. Uitto, W. Chrapek, and J. Viik, "Novel electrode configuration for highly linear impedance pneumography," *Biomed Tech (Berl)*, vol. 58, no. 1, pp. 35–38, Feb. 2013, doi: 10.1515/bmt-2012-0068.
- [99] C. M. McEniery, J. R. Cockcroft, M. J. Roman, S. S. Franklin, and I. B. Wilkinson, "Central blood pressure: current evidence and clinical importance," *Eur Heart J*, vol. 35, no. 26, pp. 1719–1725, Jul. 2014, doi: 10.1093/eurheartj/eh565.
- [100] O. Aquilina, V. Grech, H. Felice, J. Debono, and A. Fenech, "Normal adult coronary angiography," *Images Paediatr Cardiol*, vol. 8, no. 2, pp. 1–16, 2006.
- [101] M. F. O'Rourke, "Method for ascertaining the pressure pulse and related parameters in the ascending aorta from the contour of the pressure pulse in the peripheral arteries," US5265011A, Nov. 23, 1993 Accessed: Jun. 15, 2021. [Online]. Available: <https://patents.google.com/patent/US5265011A/en>
- [102] K. Pesti, M. Metshein, P. Annus, H. Kõiv, and M. Min, "Electrode Placement Strategies for the Measurement of Radial Artery Bioimpedance: Simulations and Experiments," *IEEE Transactions on Instrumentation and Measurement*, pp. 1–1, 2020, doi: 10.1109/TIM.2020.3011784.
- [103] M. Min, P. Annus, H. Kõiv, A. Krivošei, T. Uuetoa, and J. Lamp, "Bioimpedance sensing - a viable alternative for tonometry in non-invasive assessment of central aortic pressure," in *2017 IEEE International Symposium on Medical Measurements and Applications (MeMeA)*, May 2017, pp. 373–378. doi: 10.1109/MeMeA.2017.7985905.
- [104] A. Krivošei, J. Lamp, M. Min, T. Uuetoa, H. Uuetoa, and P. Annus, "Non-invasive Method for the Aortic Blood Pressure Waveform Estimation Using the Measured Radial EBI," *J. Phys.: Conf. Ser.*, vol. 434, no. 1, p. 012048, 2013, doi: 10.1088/1742-6596/434/1/012048.
- [105] A. S. Tucker, R. M. Fox, and R. J. Sadleir, "Biocompatible, High Precision, Wideband, Improved Howland Current Source With Lead-Lag Compensation," *IEEE Transactions on Biomedical Circuits and Systems*, vol. 7, no. 1, pp. 63–70, Feb. 2013, doi: 10.1109/TBCAS.2012.2199114.
- [106] M. Etemadi, P. Chung, J. A. Heller, J. A. Liu, L. Rand, and S. Roy, "Towards BirthAlert—A Clinical Device Intended for Early Preterm Birth Detection," *IEEE Transactions on Biomedical Engineering*, vol. 60, no. 12, pp. 3484–3493, Dec. 2013, doi: 10.1109/TBME.2013.2272601.
- [107] J. E. Sanders *et al.*, "A Bioimpedance Analysis Platform for Amputee Residual Limb Assessment," *IEEE Transactions on Biomedical Engineering*, vol. 63, no. 8, pp. 1760–1770, Aug. 2016, doi: 10.1109/TBME.2015.2502060.
- [108] T. R. Qureshi, C. Chatwin, and W. Wang, "Bio-impedance Excitation System: A Comparison of Voltage Source and Current Source Designs," *APCBEE Procedia*, vol. 7, no. Supplement C, pp. 42–47, Jan. 2013, doi: 10.1016/j.apcbee.2013.08.010.
- [109] P. Bertemes-Filho, V. C. Vincence, M. S. Santos, and I. X. Zanatta, "Low power current sources for bioimpedance measurements: A comparison between Howland and integrated CMOS OTA circuits," *Journal of Electrical Bioimpedance*, vol. 3, no. 1, pp. 66–73, Oct. 2012, doi: 10.5617/jeb.380.

- [110] M. Metshein, "Alternatives of Measurement of Electrical Bioimpedance of the Body with the Aim to Determine the Cardiac and Respiratory Activity," in *2014 14th Biennial Baltic Electronic Conference (BEC)*, Oct. 2014, pp. 197–200. doi: 10.1109/BEC.2014.7320590.
- [111] E. Priidel *et al.*, "Methods for Detection of Bioimpedance Variations in Resource Constrained Environments," *Sensors*, vol. 20, no. 5, Art. no. 5, Jan. 2020, doi: 10.3390/s20051363.
- [112] K. S. Rabbani, "Focused Impedance Method (FIM) and Pigeon Hole Imaging (PHI) as two potentially low cost and simple modalities for different diagnostic applications," in *7th International Conference on Appropriate Healthcare Technologies for Developing Countries*, Sep. 2012, pp. 1–6. doi: 10.1049/cp.2012.1454.
- [113] P. Annus, R. Land, E. Priidel, M. Metshein, M. Min, and O. Märtens, "Quantization of the response signal differences for the electrical bioimpedance measurement," in *EMBECE & NBC 2017*, Singapore, 2017, pp. 290–293.
- [114] E. Priidel, P. Annus, M. Metshein, R. Land, O. Märtens, and M. Min, "Lock-in integration for detection of tiny bioimpedance variations," in *2018 16th Biennial Baltic Electronics Conference (BEC)*, Oct. 2018, pp. 1–4. doi: 10.1109/BEC.2018.8600965.
- [115] P. Annus *et al.*, "Automatic Detection of Real and Imaginary Parts of Electrical Impedance with Single Synchronous Demodulation Channel," in *8th European Medical and Biological Engineering Conference*, Cham, 2021, pp. 151–157.
- [116] P. Annus, M. Min, R. Land, O. Märtens, E. Priidel, and M. Metshein, "Method and device for quantization of the response signal differences during synchronous measurement," EE05821B1, Apr. 15, 2020
- [117] P. P. Tarjan and R. McFee, "Electrodeless Measurements of the Effective Resistivity of the Human Torso and Head by Magnetic Induction," *IEEE Trans. Biomed. Eng.*, vol. BME-15, no. 4, pp. 266–278, Oct. 1968, doi: 10.1109/TBME.1968.4502577.
- [118] D. Teichmann, J. Foussier, and S. Leonhardt, "Respiration monitoring based on magnetic induction using a single coil," in *2010 Biomedical Circuits and Systems Conference (BioCAS)*, Paphos, Cyprus, Nov. 2010, pp. 37–40. doi: 10.1109/BIOCAS.2010.5709565.
- [119] H. Saner, S. E. J. Knobel, N. Schuetz, and T. Nef, "Contact-free sensor signals as a new digital biomarker for cardiovascular disease: chances and challenges," *European Heart Journal - Digital Health*, vol. 1, no. 1, pp. 30–39, Nov. 2020, doi: 10.1093/ehjdh/ztaa006.
- [120] W. G. Kubicek, R. P. Patterson, and D. A. Witsoe, "IMPEDANCE CARDIOGRAPHY AS A NONINVASIVE METHOD OF MONITORING CARDIAC FUNCTION AND OTHER PARAMETERS OF THE CARDIOVASCULAR SYSTEM," *Ann NY Acad Sci*, vol. 170, no. 2 International, pp. 724–732, Jul. 1970, doi: 10.1111/j.1749-6632.1970.tb17735.x.
- [121] D. Naranjo-Hernández, J. Reina-Tosina, and M. Min, "Fundamentals, Recent Advances, and Future Challenges in Bioimpedance Devices for Healthcare Applications," *Journal of Sensors*, vol. 2019, pp. 1–42, Jul. 2019, doi: 10.1155/2019/9210258.
- [122] J. Sun *et al.*, "An experimental study of pulse wave measurements with magnetic induction phase shift method," *Technol Health Care*, vol. 26, no. S1, pp. 157–167, 2018, doi: 10.3233/THC-174526.

- [123] J. Ojarand, S. Pille, M. Min, R. Land, and J. Oleitšuk, "Magnetic Induction Sensor for the Respiration Monitoring.," Jun. 2015.
- [124] L. Ma and M. Soleimani, "Magnetic induction tomography methods and applications: a review," *Measurement Science and Technology*, vol. 28, no. 7, p. 072001, Jun. 2017, doi: 10.1088/1361-6501/aa7107.
- [125] P. P. Tarjan and R. McFee, "Electrodeless Measurements of the Effective Resistivity of the Human Torso and Head by Magnetic Induction," *IRE transactions on medical electronics*, vol. BME-15, no. 4, pp. 266–278, Oct. 1968, doi: 10.1109/TBME.1968.4502577.
- [126] H. Scharfetter, R. Casanas, and J. Rosell, "Biological tissue characterization by magnetic induction spectroscopy (MIS): requirements and limitations," *IEEE Transactions on Biomedical Engineering*, vol. 50, no. 7, pp. 870–880, 2003, doi: 10.1109/TBME.2003.813533.
- [127] J. Xiang, Y. Dong, M. Zhang, and Y. Li, "Design of a Magnetic Induction Tomography System by Gradiometer Coils for Conductive Fluid Imaging," *IEEE Access*, vol. 7, pp. 56733–56744, 2019, doi: 10.1109/ACCESS.2019.2914377.
- [128] R. Chen, J. Huang, B. Li, J. Wang, and H. Wang, "Technologies for magnetic induction tomography sensors and image reconstruction in medical assisted diagnosis: A review," *Review of Scientific Instruments*, vol. 91, no. 9, p. 091501, Sep. 2020, doi: 10.1063/1.5143895.
- [129] M. Steffen and S. Leonhardt, "Non-Contact Monitoring of Heart and Lung Activity by Magnetic Induction Measurement," *ACTA Polytechnica*, vol. 48, no. 3, Jan. 2008, doi: DOI: <https://doi.org/10.14311/1021>.
- [130] F. N. Adiputri, E. N. Prasetyani, Rohmadi, A. Saputra, I. Muttakin, and W. P. Taruno, "Simulation of Magnetic Induction Tomography Sensor with 8-Coils Solenoid and Planar," in *2017 5th International Conference on Instrumentation, Communications, Information Technology, and Biomedical Engineering (ICICI-BME)*, Bandung, Nov. 2017, pp. 1–5. doi: 10.1109/ICICI-BME.2017.8537753.
- [131] R. R. Robaina, H. T. Alvarado, and J. A. Plaza, "Planar coil-based differential electromagnetic sensor with null-offset," *Sensors and Actuators A: Physical*, vol. 164, no. 1–2, pp. 15–21, Nov. 2010, doi: 10.1016/j.sna.2010.09.008.
- [132] K. Finkenzerler, *Fundamentals and applications in contactless smart cards, radio frequency identification and near-field communication*, 3rd ed. Chichester, West Sussex ; Hoboken, NJ: Wiley, 2010.
- [133] H. A. Wheeler, "Formulas for the Skin Effect," *Proceedings of the IRE*, vol. 30, no. 9, pp. 412–424, 1942, doi: 10.1109/JRPROC.1942.232015.
- [134] R. Pettengill, H. Garland, and J. Meindl, "Receiving antenna design for miniature receivers," *IEEE Transactions on Antennas and Propagation*, vol. 25, no. 4, pp. 528–530, 1977, doi: 10.1109/TAP.1977.1141631.
- [135] D. Teichmann, A. Kuhn, S. Leonhardt, and M. Walter, "The MAIN Shirt: A Textile-Integrated Magnetic Induction Sensor Array," *Sensors*, vol. 14, no. 1, pp. 1039–1056, Jan. 2014, doi: 10.3390/s140101039.

Acknowledgements

The journey to finish my doctoral studies took much longer than I had expected, and it has been a constant struggle to find the balance between work, personal life, hobbies and studies. My passion for designing and building devices and verifying theoretical results with experiments also took its toll. I am happy that my studies brought me together with so many talented scientists whose support and belief in me made it possible to finish the thesis.

I would like to express my sincere appreciation to my supervisor Professor Emeritus Mart Min, whose tremendous expertise, consistent demanding supervision and support led to finishing the thesis. His enthusiastic, confident and optimistic mentoring was much more than I could expect.

I would also like to express my gratitude to my co-supervisor, Dr. Jaan Ojarand, whose support and advice exceeded the level one can expect. He is a very skillful experimenter whose broad knowledge of different technology fields is impressive, and I learned a lot from his thoroughness and practical skills.

My utmost thanks go to Dr. Paul Annus, my supervisor for the first years of studies. His broad experience in electronics and signal processing influenced my approaches a lot. Without his help and encouragement I would have terminated my studies mid-way. Thank you for the endless ideas, suggestions and advice, as well as for the historical and philosophical background.

I also thank my co-supervisor, Dr. Ants Koel, from the first years of my studies – for the ideas, motivation, and support in every possible way; I appreciate this a lot.

I would like to thank Professor Olev Märtens for support, guidance, advice and educational discussions, as well as Dr. Raul Land for interesting technical discussions and advice.

I appreciate the support from Prof. Toomas Rang and Prof. Yannick Le Moullec; without your support, my studies would have terminated mid-way.

I also like to thank my colleagues and friends who helped me in that journey, in alphabetical order – Rauno Gordon, Madis Kerner, Hip Kõiv, Alar Leibak, Margus Metshein and Marek Rist.

Of all those who have helped me, I owe my wife, Jaana, the greatest debt of gratitude. She bore the weight and extra responsibility of raising our three daughters and running a busy household while I studied. Likewise, I am indebted to my daughters, Elisabet, Emma and Mona, who saw their father at home much less than they should have.

This work has been supported financially by the following entities:

- MOBERA20 “Event Driven Artificial Intelligence Hardware for Biomedical Sensors”
- TAR16013 (EXCITE) (TK148) “Estonian Centre of Excellence in ICT Research”
- LIEEE20036 “Collaboration Agreement: Non-Invasive Measurement of the Cardiovascular System in a Clinical Environment”
- Estonian Research Council, grant EAG34
- Estonian Research Council, grant IUT1911

Abstract

Detection of Changes in Tissue State with the Aid of Electromagnetic Interaction

The thesis focused on the methods and solutions for detecting the changes in body tissue state using electromagnetic interaction. The highest interest and practical application was the observation of activities of the cardiovascular and respiratory systems. The changes in tissue electrical properties caused by cardio-pulmonary activity are tiny. The presence of external disturbances, movement of body parts and the influence of parasitic circuit elements make measurements even more complicated. Therefore, reliable results may be obtained only with proper methods, a carefully designed measurement setup, and a good relationship between the tissue and its electrical equivalent circuit model. Methods covered are based on electromagnetic waves, resistive, capacitive, and inductive coupling. The thesis introduces analysis, simulation, and experimental results obtained with developed devices and sensors in five chapters.

First, the feasibility of contactless monitoring with radio waves using UWB radar is investigated. A contactless method allows continuous monitoring without disturbing the subject and avoids potential injuries by long-term contacts with electrodes. Additionally, benefiting from good spatial resolution and radio wave partial penetration into the tissue was expected to allow the detection of tumors and hematomas. UWB radar is proved helpful for contactless long-term cardio-pulmonary activity monitoring with good results in stationary conditions, e.g., in the hospital ward. However, experiments on the determination of boundary layers in tissue to detect hematomas were unsuccessful because of the high attenuation of ultra-short impulses required for high spatial resolution.

Second, the study of the background of electrical bioimpedance (EBI) measurement on the human body revealed that the dependence of measurement results on an adequate electrical model, the influence of the surrounding environment, and the selected measurement solution is not sufficiently taken into account in many cases. Analysis of named factors shows that a compact battery-powered wireless analyzer capable of the high-resolution and accurate impedance measurement in the 10 MHz range is required to determine EBI model parameters in the β dispersion area. Moreover, a two-electrode measurement scheme with a voltage excitation has essential advantages compared to a four-electrode method employing current-source excitation. However, in the cases where only the EBI changes at lower frequencies (below 100 kHz) mainly related to the resistive part of the impedance are of interest, a four-electrode circuit with a current excitation has its own benefits.

Third, the enhanced patent-pending measurement solution is introduced for monitoring EBI changes on a wrist with Ag/AgCl electrodes at 120 kHz, demonstrating a wearable low-energy device with minimized hardware requirements and computational power to the lowest level. The method uses the running differences of the response signal in that the output signal is the derivative as the measure of EBI change. Integration of the derivative also provides the original EBI signal change waveform.

Fourth, the design of a developed novel compact FPGA-based impedance analyzer (CIA) is introduced, including issues of the calibration and correction of the influence of the connection cables. Battery-powered 16-bit CIA with up to 200 MSPS A/D and D/A sampling rate and WiFi communication provides the magnitude measurement error below $\pm 0.5\%$ and phase error below ± 0.2 degrees in the 10 MHz range at 80 MSPS.

The small dimensions (70 x 45 x 20 mm) reduced the effect of parasitic capacitance and increased the accuracy of EBI spectral measurements on the body. The analysis of EBI spectra measured with two capacitive electrodes allowed separating the spectra of the model elements and analyzing the weight of these elements in the impedance spectrum to determine the sensitivity to changes in the parameters of the model element at different frequencies. Finally, an example of the change in EBI amplitude and phase due to cardiac output from the left arm is provided.

Fifth, the feasibility of using inductively coupled sensors to detect heart-related signals in the forearm is investigated, including a sensitivity analysis of the different inductive sensor designs to determine their optimal parameters and limiting factors. The analysis results are confirmed by experiments showing good agreement between the results. In addition, a novel sensor solution is introduced with a flexible toroidal ferrite core that uses additional electrodes to close the induced current loop.

The overall conclusion is that too small relative changes in impedance in the body away from the chest and interfering factors, mainly parasitic capacitances, the movement of the body and its internal parts, call into question the reliable monitoring of activities of the cardiovascular system through EBI changes. Respiratory-related EBI changes are probably undetectable in the forearm, as not observed in the case of the minimized influence of stray capacitances.

The main factors limiting the efficiency of inductively coupled sensors are the low coupling factor with internal tissue layers and blood vessels and the substantial effect of parasitic capacitances. Addressing these bottlenecks, for example, by efficient shielding that does not violate inductive coupling, could be the subject of further research.

Lühikokkuvõte

Koe seisundi muutuste detekteerimine elektromagnetilise vastastikmõju abil

Doktoritöö keskendub meetoditele ja lahendustele, mis kasutavad kudede seisundi muutuste tuvastamiseks elektromagnetilist vastastikmõju. Suurimat tähelepanu pälvis praktilisi rakendusi arvestades südame-veresoonkonna ja hingamiselundite tegevuse jälgimine. Kardiopulmonaarsest protsessidest põhjustatud muutused kudede elektrilistes omadustes on väikesed ning välised häiresignaalid, kehaosade liikumine ja parasiitahelate elementide mõju muudavad mõõtmise veelgi keerulisemaks. Seetõttu on usaldusväärseid tulemusi võimalik saada ainult sobivate meetodite, hoolikalt kavandatud mõõteseadme ning koe omaduste ja selle elektrilise mudeli võimalikult täpse vastavuse korral. Käsitletavad meetodid põhinevad elektromagnetlainete vastastikmõjul ning sensori takistuslikul, mahtuvuslikul ja induktiivsel sidestamisel kudedega. Doktoritöö käsitleb väljatöötatud seadmete ja andurite omaduste ning nendega saadud katsetulemuste analüüsi ja simulatsioone viies peatükis.

Esiteks uuritakse südametöö ja hingamise kontaktivaba seire teostatavust üli-laiaribalise (UWB) radari abil. Kontaktivaba meetod võimaldab pidevat jälgimist ilma objekti häirimata ja väldib võimalikke vigastusi pikaajalisel kokkupuutel elektroodidega. Lisaks eeldati, et hea ruumiline eraldusvõime ja raadiolainete osaline läbitungimine kudedesse võimaldavad kasvajate ja hematoomide tuvastamist. UWB radar on osutunud kasulikuks kontaktivabal pikaajalisel kardiopulmonaarse aktiivsuse jälgimisel, mis annab häid tulemusi statsionaarses kasutuses, nt. haigla palatis. Koe üleminekukihtide määramise katsed hematoomide tuvastamiseks ebaõnnestusid suure ruumilise eraldusvõime jaoks vajalike üli-lühikeste impulsside suure sumbumise tõttu.

Teiseks, inimkeha elektrilise bioimpedantsi (EBI) mõõtmise tuntud lahenduste uurimisel selgus, et mõõtmistulemuste sõltuvust kasutatud elektrilisest mudelist, mõõteskeemist ja ümbritseva keskkonna mõjust ei ole paljudel juhtudel piisavalt arvesse võetud. Nimetatud tegurite analüüsi põhjal järeldatakse, et EBI mudeli parameetrite määramiseks β dispersiooni piirkonnas on vaja 10 MHz sagedusribas töötavat kompaktselt juhtmevaba andmesideühendusega akutoitel analüsaatorit, mis on võimeline mõõtma impedantsi suure eraldusvõime ja täpsusega. Pingeallikaga ergutussignaali ja kahe elektroodiga mõõteskeemil on 10 MHz sagedusribas olulised eelised võrreldes nelja elektroodi meetodiga, mis kasutab vooluallikaga ergutussignaali. Kuid juhul kui huvi pakub vaid EBI muutus madalamatel sagedustel (alla 100 kHz), mis on seotud peamiselt impedantsi takistusosaga, võib nelja elektroodiga ja vooluallika ergutusega lahendus olla sobivam.

Kolmandaks esitletakse patenteeritud mõõtelahendust EBI muutuste jälgimiseks sagedusel 120 kHz, kasutades randmele kinnitatud Ag/AgCl elektroode. Mõõtelahenduse tulemuseks on kantav vähese energiatarbega seade, millel on madalaimad nõuded riistvarale ja arvutusvõimsusele. Meetod kasutab vastussignaali jooksvaid erinevusi, kusjuures väljundsignaaliks on EBI muutuse tuletis. Tuletise integreerimine annab ka algse EBI signaali muutumise lainekuju.

Neljandaks esitletakse uudse kompaktse FPGA-põhise impedantsi analüsaatori (CIA) ülesehitust, sealhulgas kalibreerimise ja ühenduskaablite mõju korrigeerimise lahendusi. Akutoitega, 16-bitise resolutsiooniga ja WiFi andmesidega CIA, A/D ja D/A võendamissagedusega kuni 200 MHz tagab impedantsi amplituudi mõõtmise vea

alla $\pm 0,5\%$ ja faasi vea alla $\pm 0,2$ kraadi kuni 10 MHz sagedusribas ja 80 MHz võendamissageduse juures. Väikesed mõõtmed (70x45x20 mm) vähendasid parasiitmahtuvuse mõju ja suurendasid EBI spektrite mõõtmise täpsust kehal. Kahe mahtuvusliku elektrodiga mõõdetud EBI spektrite analüüs võimaldas eraldada mudeli elementide spektrid ning nende elementide kaalu impedantsi spektris ja määrata tundlikkuse mudeli elemendi parameetrite muutustele erinevatel sagedustel. Lõpuks on esitatud vasakult käsivarrelt mõõdetud südametööst põhjustatud EBI amplituudi ja faasi muutuse näide.

Viiendaks uuritakse induktiivse sidestusega andurite rakendamise teostatavust südametegevusega seotud signaalide tuvastamiseks käsivarrel, sealhulgas esitatakse erinevate induktiivsete andurite konstruktsioonide tundlikkuse analüüs, mis võimaldab määrata nende optimaalsed parameetrid ja piiravad tegurid. Analüüsi tulemused kinnitatakse katsetega, mis näitavad tulemuste head kokkulangevust. Lisaks esitletakse uudset andurilahendust painduva toroidaalse ferriitsüdamikuga, mis kasutab täiendavaid elektroode indutseeritud vooluahela sulgemiseks.

Üldine järeldus on, et liiga väikesed suhtelised muutused rindkerest eemal asuvate kehaosade impedantsis ja mõõtmist segavad tegurid, peamiselt keha ning selle siseosade liikumise ja parasiitmahtuvuse mõju, muudavad südame-veresoonekonna süsteemi usaldusväärse jälgimise EBI muutuste abil küsitavaks. Hingamisega seotud impedantsi muutused ei ole tõenäoliselt käsivarrel tuvastatavad, sest neid ei olnud parasiitmahtuvuste mõju minimeerimisel enam näha.

Induktiivse sidestusega andurite efektiivsust piiravateks teguriteks on väike sidestustegur sisemiste koekihtide ja veresoontega ning parasiitmahtuvuste suur mõju. Nende kitsaskohtade kõrvaldamine, näiteks tõhusa ekraniseerimise abil, mis ei riku induktiivset sidestust, võiks olla edasiste uuringute objektiks.

Appendix 1

Publication I

Priidel, E.; Land, R.; Sinivee, V.; Annus, P.; Min, M. (2017). Comparative Measurement of Cardiac Cycle by Means of Different Sensors. *IEEE Conference Proceedings, Lithuania, Palanga, 19-21 June, 2017: 21st International Conference ELECTRONICS 2017, Palanga, Lithuania from 19th to 21st June, 2017*. Palanga: IEEE Conference Publications, 1–5. DOI: 10.1109/ELECTRONICS.2017.7995221.

Comparative Measurement of Cardiac Cycle by Means of Different Sensors

Eiko Priidel¹, Raul Land¹, Veljo Sinivee², Paul Annus¹, Mart Min¹

¹*J. Seebeck Dept. of Electronics, Tallinn University of Technology,
Ehitajate tee 5, 19086 Tallinn, Estonia*

²*Department of Physics, Tallinn University of Technology,
Ehitajate tee 5, 19086 Tallinn, Estonia*

Abstract—Ultra wideband (UWB) signals for medical diagnostics have been in research focus for decades. UWB medical radar is promising technology for breast cancer detection, brain hematoma diagnosis and vital sign monitoring. It is contactless and emits only low-power non-ionizing radiation. One of the promising applications is cardiac monitoring. While the cardiac cycles can be clearly seen in the UWB radar response, the propagation path of the vital biological information into the radar signal is still debatable. Commonly three major physiological effects are considered as a source of the signal – blood perfusion of the skin, skin movement and echoes from heart wall. Multisensory approach is introduced to assess the impact of the different contributors. ballistocardiographic, phonocardiographic and optical reflection signals are recorded from the surface of the skin on chest, together with reference electrocardiography signal between two hands. Custom built UWB cardiograph was used. Recorded signals were analysed, and the results suggest that the proposed approach is viable for making assessments for the origin of the cardiac component in the UWB radar signal. Results are in agreement with findings in recent publications on the topic, where different approach was utilized.

Index Terms—Ultra wideband radar, medical radar, cardiography, ballistocardiography, bioimpedance.

I. INTRODUCTION

UWB (Ultra Wide Band) technology is an emerging technology which has been gaining more and more popularity in recent years. Because of some unique and attractive features UWB signals can be used for medical diagnostics, measuring properties of various materials, high speed communication and radars. UWB technology was used exclusively in military applications before 2001 when commercial usage was allowed in USA and 2007 in EU followed by intensive research activities. UWB signals have some unique properties compared to continuous wave signals – ability to share frequency spectrum, ability to work in low SNR conditions, high performance in multipath channels, superior material penetration properties, high spatial resolution, very low electromagnetic radiation, simple

transceiver architecture and low energy consumption [1]. Main applications in medicine are as follows: cardiac biomechanics assessment, chest movements assessment, OSA (obstructive sleep apnea) monitors, soft-tissue biomechanics research, heart imaging ('Holter type' echocardiography), chest imaging, cardiac monitoring, respiratory monitoring, SIDS (sudden infant death syndrome) monitors, breast cancer and brain hematoma diagnosis and 3D imaging [2]–[4]. As UWB signals are non-ionizing they can be used for long term non-invasive monitoring without adverse effects. UWB radar working principle is to generate ultrashort impulses and send into the body in which electromagnetic impulse propagates and reflects back due to different dielectric permittivity of body tissues. Reflected signal is analysed in the framework of the Time Domain Reflectometry theory [5]. However Staderini states in his research that deep echo reflections from the tissues does not seem to be a realistic explanation of the phenomenon and at the moment no hypothesis can be eventually accepted for explaining UWB medical radar operation [6]. Recent studies suggest that main source of the signal is movement of the chest in range of few hundred micrometers [7], 0.1 mm up to 0.5 mm in [8] and 0.1 mm in [9]. According to the [9], transmitted radar energy will probably not reach to the heart and no reflected signal from the heart and lungs can be detected. But in contrary, experiments in [10] are showing reflections from inner organs and reflected signal from lung boundaries was measured. Furthermore, reflected signal from heart wall was received and used for time-laps imaging of heartbeats [11]. Basic UWB radar working principle is that electromagnetic energy propagating towards and through the body is reflecting back from the tissue interfaces due to the different relative dielectric constant of the organs. Attenuated and reflected energy from the organ boundaries is received by the antenna and boundary location is calculated based on time difference of transmitted and received signal [12].

Only few studies are available where multisensory signals are measured together with UWB radar and analysis of possible signal sources conducted [13]. By author's knowledge blood perfusion, ballistocardiography (BCG) - mechanical skin movement measurements and phonocardiography (PCG) – sound and murmurs made by the heart are not conducted together with UWB radar.

Manuscript received 28 December, 2016; accepted 28 March, 2017.

This research was supported by Estonian Research Council grant IUT1911 and the European Regional Development Fund in frames of the Estonian Centre of Research Excellence EXCITE. The work was partly financed also through the European Research Area project H2020-WIDESPREAD-2014-2-668995-Cognitive Electronics.

Relations between impedance cardiography and seismocardiography (SCG) are assessed in [14]. In impedance cardiography (ICG) initial understanding was that source of the signal is the heart and the aorta but turned out to be very unlikely [15]. Bioimpedance measurement channel will be included to the data acquisition in the next phase to analyse also relations between UWB radar output and bioimpedance signal.

One method to analyse reasons for the radar output and the physical source of it is to measure timing between the different physiological cardiac processes and radar output signal to find correlations with radar response. Input to the analysis have to be simultaneously time-synchronized measurements of the different sensors outputs. In the current experiment chest skin displacement, blood perfusion, hearth sound, electrocardiography and UWB radar response were measured.

II. DEVICES AND PROPERTIES

Three main sensory units – electrocardiography amplifier (3-lead type), multisensory device and UWB radar – were used in the experiment. Radar sensor is custom made UWB radar with SRD pulse former and time-gating receiver which is the most common type in case of discrete component design. Alternative solution is an integrated circuit based radar as was used in heartbeat and breathing studies in [9] and [10]. Multisensory device is designed to measure heart sounds, skin reflectivity in two wavelengths and acceleration forces in 3D space. Acceleration sensor output is analog type and is digitized by microcontroller in sensory board. Skin reflectivity measurement results together with acceleration information is transferred to the PC in digital form. UWB radar and ECG output signals together with audio channel output are in analog form. All measurement data is received and processed by computer with Intel® Core™ i7 processor, running Windows 10. Measurement results in digital form are received through the RS-232 interface and analog signals through the National Instrument's DAQ device NI USB-6363. Power sources for all sensor devices were Agilent power supply type E3631A. National Instruments LabVIEW software was used for data acquisition and processing.

III. OVERVIEW OF THE SENSORY DEVICE AND THE RADAR

Multisensory device is based on Microchip 8-bit microcontroller PIC 16LF1769 which is configuring sensor chips, processing pulse density modulation (PDM) microphone output signal and controlling measurement timing. Sensor used for skin reflectivity measurement is Maxim MAX30100 SpO2 pulse oximetry sensor. Sensor is using 660nm red and 880nm infrared light for reflectivity measurement. Analog to digital conversion is built in to the chip with ADC resolution of 14 bit. Device is accessed through the I2C bus and has measurement time of 30 ms. Oximetry channel update rate is 33 Hz which is sufficient for perfusion measurement.

Heart sound is picked up by digital microphone from Knowles SPH1668LM4H-1. Microphone working in performance mode with sensitivity of -29 dBFS and SNR of 65.5 dB(A). Microphone output is PDM modulated discrete

signal with a bit rate of 3 Mbit/s. Digital signal is filtered with CIC and FIR filters, downsampled and converted to the analog form with microcontroller DAC converter. Final sampling rate for audio channel is 8 kHz. Audio signal is finally measured by National Instruments DAQ card.

Skin movement is measured with STMicroelectronics LIS-344 3-axis accelerometer. All three axes are measured separately by microcontroller ADC converter with a resolution of 10 bit. Accelerometer chip measurement range is +/- 2g and sensitivity 0.66 V/g. This gives theoretical resolution with 10 bit ADC converter 0.00064g/LSB. Sensor cut-off frequency is adjusted to 500 Hz. Measurement results are transferred to the PC in digital form through the RS-232 interface. Skin displacement is calculated from acceleration data by double integration method taking in account the sensor offset.

Multisensory device is designed in 4-layer FR4 PCB round shape board with the size of 15 mm in diameter. Board can be fitted to the standard ECG electrode sticker and attached to the chest in a standard way. Outlook of the multisensory board is shown in Fig. 1.

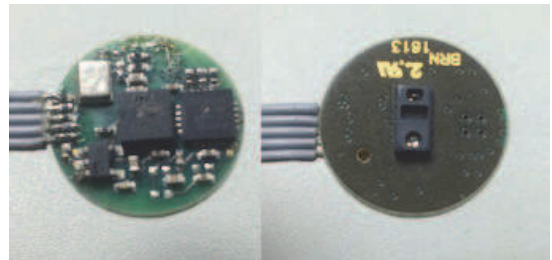


Fig. 1. Multisensory device top and bottom side. Bottom side SpO2 sensor is in contact with the skin.

Radar prototype used in experiment is based on impulse former with step recovery diode (SRD). SRD based impulse formers are fast, less than 100 ps, and can output relatively high voltage, up to 20 V, impulses [16]. Radar receiver is time gating type which frontend is based on Schottky diode sampling unit. Experiments with the prototype showed spatial resolution of 30 mm and minimal measurement distance of 400 mm. The spatial resolution is in expected range in relation to the output impulse length. SRD diode based impulse generator was capable of generating 400 ps length pulse with the amplitude of 7 V. Rise time in current design is approximately 200 ps as discrete components parasitic properties do not allow to decrease the impulse length much further. Output signal spectrum peak was in the range of 3 GHz to 4 GHz. Pulse repetition rate can be configured from 30 ns up to 100 us.

Radar control hardware is based on Texas Instruments ARM Cortex M4 microprocessor and Altera Cyclone III FPGA device. Radar raw data can be transferred to the PC through the Ethernet network interface and radar operational parameters can be adjusted through the web based user interface. Radar software is based on Free-RTOS operating system. Raw data can be processed locally with the FPGA and ARM microprocessor and output the result in analog form for easy monitoring.

Radar antenna configuration is bi-static. Antenna

properties which are not relevant in case of narrowband radar antennas have big impact on signal quality in UWB radars. Antenna dispersion, group delay, impulse response, bandwidth, impedance matching in wide frequency range and antenna ringing are the parameters what have to be optimized and tradeoff between them considered. Antenna ringing properties are also limiting factor in close range operations as transmitter antenna overloads receiver because of crosstalk.

A wideband antenna with unidirectional radiation pattern is usually required for medical radar applications. Antenna used in experiment was “Bow-Tie” type, this antenna exhibits unidirectional radiation pattern with enhanced bandwidth, reduced back radiation, and low cross polarization in the operational band [17]. Outlook of the “Bow-Tie” antennas is shown in Fig. 2.

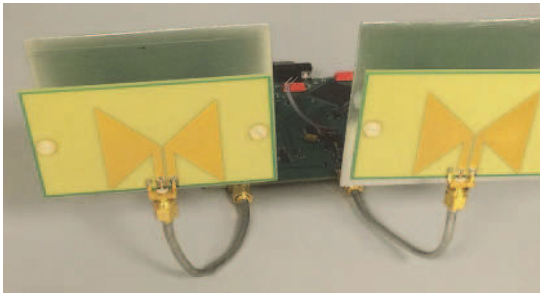


Fig. 2. UWB radar setup with two “Bow-Tie” type antennas shown.

Radar output signal is expressing reflected signal power from the set distance from the radar antenna. Distance can be set by adjusting radar time gating delay. Consequently, radar sensitivity point can be tuned to the needed distance from the antenna. Typical biomedical radar output signal is in good correlation with heartbeat and respiration activities. Sample output signal from vital sign monitoring is shown in Fig. 3 which is in good match with output signal measured from radar output in [7].

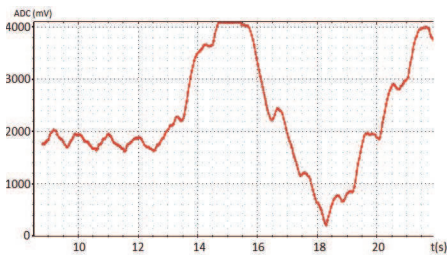


Fig. 3. Medical radar output waveform. Measured with 12-bit ADC from the distance of 90 cm. Breath is hold in the beginning followed by one deep respiratory cycle.

IV. METHODS AND THE MEASUREMENT SETUP

The experiment was conducted in indoor laboratory environment. Anechoic chamber was not used.

Electrocardiography reference signal was measured with custom built 3 Lead ECG System (Einthoven's Triangle) amplifier. Design is based on INA121 differential amplifier from Texas Instruments. Output signal was fed into the NI

DAQ card together with audio channel from multisensory device and radar output. ECG signal is used as reference and as indication of the beginning of the cardiac cycle. Subject was sitting in the chair in normal sitting position. Radar was installed to the wooden table in front of the subject at the height of the heart. Measurement distance was 50 cm from the chest. Multisensory device was attached by ECG electrode sticker to the chest approximately on the location of the heart. Measurement setup is shown in Fig. 4.

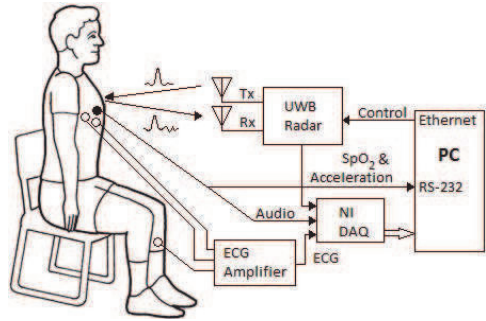


Fig. 4. Graphical presentation of measurement setup.

Measurement cycle was made when subject was holding the breath after brief inhaling. Timing accuracy and measurement channels synchronization were verified separately before the experiment.

V. MEASUREMENT RESULTS

The aim of the experiment was to measure different physiological processes which are considered as possible sources of UWB radar output signal. Measurements are synchronized with ECG and recorded together with UWB radar output. Putting all the measurements to the same timeline makes it possible to analyse time differences between radar output and physical processes to find or reject possible radar signal sources.

ECG signal was recorded as reference synchronization signal for rest of the channels. Recorded signal is typical ECG with slight 50 Hz noise as seen in Fig. 5.

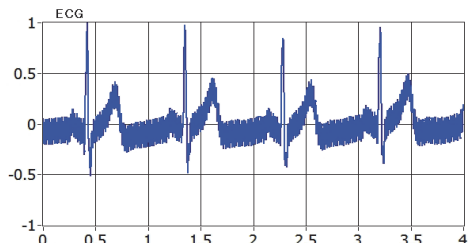


Fig. 5. Normalized ECG reference signal. Time in seconds in x-axis.

Heart sound and murmurs recorded by microphone were clearly audible. As seen from the Fig. 6 artioventricular valves closing at the beginning of systole and aortic valve closing at the beginning of the diastole are clearly detectable. Phonocardiography signals provide additional information about the time of minimal and maximal ventricular volume which is important criteria in interpreting radar signal. Ventricular volume is related to the amount of

blood in the heart and can be a source for radar output signal.

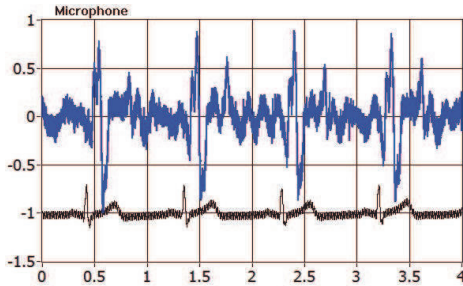


Fig. 6. Normalized PCG signal from digital microphone. Filtered and sampled with the rate of 8 kS. Time in seconds in x-axis. ECG signal in bottom is shown as a reference.

Strong radar signal with very little motion artefacts was picked up during measurement. Signal is in good correlation with ECG as seen in Fig. 7, indicating that radar response is originated from the physiological cardiac processes. As stated earlier origin of the signal is not well understood and it can be signal reflection from body internal tissue layers, skin reflection changes due to perfusion, skin displacement or secondary effects like changes in radar antenna coupling or matching.

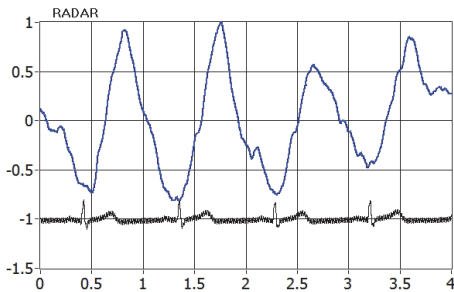


Fig. 7. Normalized UWB radar output signal. Time in seconds in x-axis. ECG signal in bottom is shown as a reference.

Acceleration sensor output signal is measured by 3-axis accelerometer and acceleration into the direction of the radar antenna is extracted. Measured output is shown in Fig. 8.

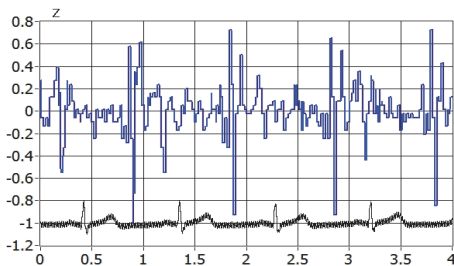


Fig. 8. Normalized acceleration sensor output. Time in seconds in x-axis. ECG signal in bottom is shown as a reference.

As one of the probable cause of the radar output is skin displacement, velocity and displacement values are calculated based on acceleration measurement. First integration of acceleration signal representing the speed of movement of the skin is shown in Fig. 9.

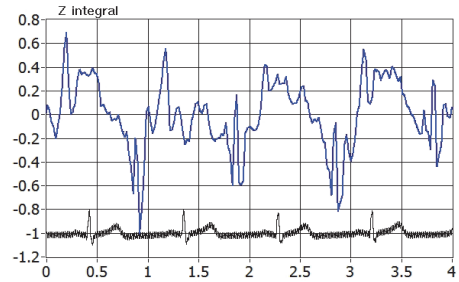


Fig. 9. Normalized velocity of the skin movement. Time in seconds in x-axis. ECG signal in bottom is shown as a reference.

Second integration of the acceleration sensor representing displacement of the skin is shown in Fig. 10.

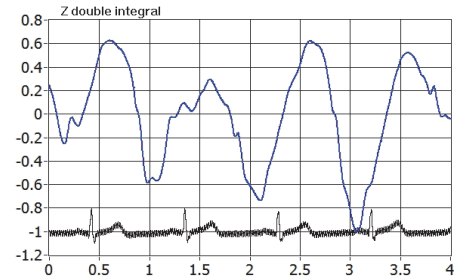


Fig. 10. Calculated displacement of the skin. Time in seconds in x-axis. ECG signal in bottom is shown as a reference.

Radar output signal is in correlation with skin displacement signal and in slightly different phase. Reasons behind this are not analysed yet. One possible reason can be that displacement of the skin is not the source of the reflected signal or there are other processes with significant impact to the radar signal – in current measurements radar output reaches its maximum at the same time with the aortic valve closing.

Radar antenna matching was one suspected reason for radar output signal. Matching depends on skin dielectrical properties which are related to the amount of blood in skin capillaries. To measure blood perfusion of the skin SpO2 sensor was used which gives output of the reflectivity of the skin in wavelengths 660 nm red and 880 nm. Signal amplitude measured on chest is very small and can be considered as noise. Further studies need to be done to verify unexpectedly weak signal. As seen in Fig. 11 amplitude of the IR channel signal is approximately 10 LSB-s which is 0.12 % change in reflectivity.

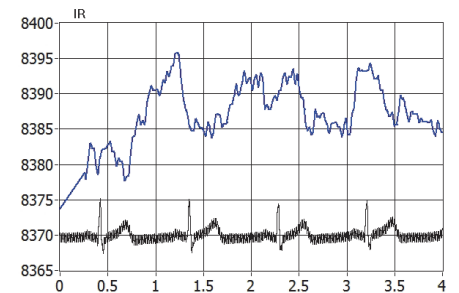


Fig. 11. Reflectivity signal in IR channel measured by 14-bit ADC. ADC output in LSB-s on y axis and time in seconds on x axis.

Reflectivity change measured by the same sensor from the fingertip is in the range of 400LSB-s which is 4.5 % change in reflectivity. Possible reasons behind very weak response can be that amount of blood does not change as much as in fingertip or coupling between skin and sensor is not sufficient. Based on current measurement results it is unlikely that radar output signal is generated because of coupling changes between chest skin and antennas.

VI. CONCLUSIONS

UWB radars can be used for heartbeat and breathing activity as radar output signal correlates well with ECG and respiratory cycle. Still there is dispute about the origins of the radar output signal. Several studies have been conducted to investigate feasibility of using UWB radars in cardiorespiratory monitoring of the patients but only few studies are focused to understand UWB radar working principles [10]. Latest studies indicate that skin displacement is considered to be the main contributor of the signal [13] in contrary to the earlier explanation where signal reflection from the body's inner layer boundaries was the main source. However, few recent investigations are claiming successful reception of the reflected signals from inner organ layer boundaries [10], [11]. Different hypothesis are considered to explain the source of the signal and these hypotheses are still under dispute. In current study few physiological processes were measured together with UWB radar output to provide data to understand possible signal origins. Measurements in current work are supporting also the hypothesis that signal origin is from air/skin interface, but there is slight mismatch in signal phase compared to the skin movement. Better match in phase was achieved with heart ventricular volume but signal power is not in match with inner layer reflections. This anomaly needs further study to be explained. Experiment also shows that radar with better spatial resolution is needed to distinguish reflections from inner layers as these reflections tend to be superimposed with radar transmitter and skin reflected signals which makes their detection more complicated. Current study does not support hypothesis that radar output signal is originated from changes in antenna matching. Changes in antenna matching are suspected to originate from blood perfusions in skin [6] but measurements in current work are showing extremely small changes in blood amount in skin layer. Those surprisingly small changes have to be verified to eliminate possible measurement or methodology errors like SpO2 sensor coupling, while measurement with different wavelength is also considered.

VII. CONCLUSIONS

Multisensor vital signs measurement hardware and software was developed and built. Experiment was conducted to evaluate functionality of the measurement setup and quality of the data. ECG, PCG, BCG, blood perfusion and UWB radar signals were recorded simultaneously. Measurement of skin movement through the double integration of acceleration sensor data is feasible -

preliminary analysis shows that UWB radar output signal is in good correlation with chest skin movement although slightly off the phase. Measurement results from blood perfusion are indicating that it does not affect antenna coupling and therefore is not the source of radar output. Results are in agreement with findings in recent publications on the topic, where different approach was utilized [13]. Further analysis is needed to explain slight phase shift between the radar output and skin displacement.

REFERENCES

- [1] F. Nekoogar, *Ultra-Wideband Communications: Fundamentals and Applications*. Prentice Hall, 2005.
- [2] J. Paul Tupin, "UWB radar in health monitoring products", *ITU Workshop on Short Range Devices and Ultra Wide Band*, Geneva, 2014.
- [3] C. N. Paulson, J. T. Chang, C. E. Romero, J. Watson, F. J. Pearce, N. Levin, "Ultra-wideband radar methods and techniques of medical sensing and imaging", in *Proc. Smart Medical and Biomedical Sensor Technology III (SPIE)*, 2005. Online. [Available]: <http://dx.doi.org/10.1117/12.630004>
- [4] E. M. Staderini, "UWB radars in medicine", *IEEE Aerospace and Electronic Systems Magazine*, vol. 17, no. 1, pp. 13–18, 2002. Online. [Available]: <http://dx.doi.org/10.1109/62.978359>
- [5] T. E. McEwan, S. Azevedo, "Microwave impulse radar", *Science & Technology Review*, 1996.
- [6] G. Varotto, E. M. Staderini, "On the UWB medical radars working principles", *Ultra Wideband Communications and Systems*, vol. 2, no. 2, 2011. Online. [Available]: <https://doi.org/10.1504/IJWBSCS.2011.044600>
- [7] T. Sakamoto, R. Imasaka, H. Taki, T. Sato, M. Yoshioka, K. Inoue, T. Fukuda, H. Sakai, "Accurate heartbeat monitoring using ultra-wideband radar", *IEICE Electronics Express*, vol. 12, no. 3, pp. 1–7, 2015. Online. [Available]: <https://doi.org/10.1587/ele.12.20141197>
- [8] K. Naishadham, J. E. Piou, L. Ren, A. E. Fathy, "Estimation of cardiopulmonary parameters from ultra wideband radar measurements using the state space method", *IEEE Trans. Biomedical Circuits and Systems*, vol. 10, no. 6, pp. 1037–1046, 2016. Online. [Available]: <https://doi.org/10.1109/TBCAS.2015.2510652>
- [9] Hui-Sup Cho, Young-Jin Park, Hong-Kun Lyu, Jin-Ho Cho, "Novel heart rate detection method using UWB impulse radar", *J Sign Process Syst.*, vol. 87, no. 2, pp. 229–239, 2016. Online. [Available]: <https://doi.org/10.1007/s11265-016-1177-7>
- [10] E. Pittella, S. Pisa, M. Cavagnaro, "Breath activity monitoring with wearable uwb radars: measurement and analysis of the pulses reflected by the human body", *IEEE Trans. Biomedical Engineering*, vol. 63, no. 7, pp. 1447–1454, 2016. Online. [Available]: <https://doi.org/10.1109/TBME.2015.2496208>
- [11] S. Brovold, T. Berger, Y. Paichard, O. Aardal, T. S. Lande, S. E. Hamran, "Time-lapse imaging of human heartbeats using UWB radar", *IEEE Biomedical Circuits and Systems Conf. (BioCAS)*, 2013. Online. [Available]: <https://doi.org/10.1109/BioCAS.2013.6679659>
- [12] I. Oppermann, M. Haamalain, J. Iinatti, *UWB Theory and Applications*. John Wiley & Sons Ltd, 2004.
- [13] O. Aardal, Y. Paichard, S. Brovold, T. Berger, T. S. Lande, S. E. Hamran, "Physical working principles of medical radar", *IEEE Trans. Biomedical Engineering*, vol. 60, no. 4, pp. 1142–1149, 2013. Online. [Available]: <https://doi.org/10.1109/TBME.2012.2228263>
- [14] S. Sadauskas, A. Naudziunas, A. Unikauskas, L. Gargasas, R. Ruseckas, V. Jurkonis, R. Jurkoniene, "Comparison of non-invasive methods – impedance cardiography and 2-dimensional transthoracic echocardiography applied for diagnostics of pulmonary artery hypertension", *Elektronika ir elektrotechnika*, vol. 9, 2010.
- [15] R. Patterson, "Impedance cardiography: What is the source of the signal?", *Int. Conf. on Electrical Bioimpedance*, 2010, pp. 1–4.
- [16] Y. W. Yeap, "Ultra wideband signal generation", *Microwave Journal*, 2005.
- [17] G. Bindu, *et al.*, "Wideband bow-tie antenna with coplanarstripline feed", *Microwave and Optical Technology Letters*, vol. 42, no. 3, 2004. Online. [Available]: <https://doi.org/10.1002/mop.20258>

Appendix 2

Publication II

Annus, P.; Land, R.; Priidel, E.; Metshein, M.; Min, M.; Märtens, O. (2017). Quantization of the response signal differences for the electrical bioimpedance measurement. *EMBEC & NBC 2017: European Medical and Biological Engineering Conference (EMBEC) and the Nordic-Baltic Conference on Biomedical Engineering and Medical Physics (NBC)*. Ed. Eskola H., Väisänen O., Viik J., Hyttinen J. Springer, 290–293. (IFMBE Proceedings; 65). DOI: 10.1007/978-981-10-5122-7_73.

Quantization of the response signal differences for the electrical bioimpedance measurement

P. Annus¹, R. Land¹, E. Priidel¹, M. Metshein¹, M. Min¹ and O. Märtens¹

¹ Tallinn University of Technology/ Thomas Johann Seebeck Department of Electronics, Tallinn, Estonia

Abstract—Solutions for practical implementation of the electrical bioimpedance acquisition typically need to be optimized and adapted for the task at hand. One of the most challenging measurement tasks is impedance plethysmography, the test that measures tiny changes in electrical conductivity, related to changes in biological volumes. These changes depend on the underlying biological processes, measurement locations, and added random artefacts. Changes in the acquired impedance due to the cardiac activity can easily be 0.1% and lower. In modern devices, the digitalization of the data acquisition results is almost mandatory, and it places heavy demand on the used analog-to-digital converters. Only few levels are left from 16-bit converter for the direct digitalization of the impedance plethysmography signal, given that the useful signal is only around thousandth of the full impedance scale, and that some margin must be left. Several solutions have been proposed, such as a direct compensation of the carrier of the response signal in order to emphasize tiny variations of it, or in the case of analog preprocessing capacitive coupling helps to separate static component of the impedance. A novel solution for the direct digitalization of the response signal is proposed. Differences between adjacent analog samples taken synchronously to the carrier are quantized instead of the full value. Essentially derivative of the response signal is digitized in this case. Number of the required quantizing levels is reduced significantly. Solution is easily embeddable and customizable.

Keywords— Bioimpedance, biomodulation, quantization, digitizing, demodulation.

I. INTRODUCTION

Noninvasive acquisition of the medically relevant data of biological origin is crucial in everyday medical praxis for reducing risks and costs, and it is unavoidable if the pervasive monitoring outside of the medical institution is required. Observation of the electromagnetic phenomena emanating from the functioning of living tissues, or related to their properties, is one of the most used noninvasive monitoring methods today [1]. Non-invasive electrical bioimpedance (EBI) measurement aids to gather information of the biological origin as well, among the multitude of other modalities [2]. From characterization of the body composition up to the real-time adjustment of the pacing algorithms. The needed information may be contained in the slowly varying impedance between the electrodes, as it is in the first case, or in relatively fast

changes of it as in the second case. Information contained in bioimpedance is typically twofold: long term slow variations and spectral content of the so called base impedance, which characterizes steady state of different larger cell groups, and short term fluctuations on top of it, which can be related to certain faster biological processes of interest, such as breathing, heart beating, digestion etc. EBI based plethysmography aims to determine the change of tissue volumes in the body. Two volumes of general interest for the long term pervasive monitoring are the cardiac stroke volume and the respiratory minute volume. Non-invasive estimation of those is generally considered highly valuable for medical purposes, for evaluation of the recreational activities, and during active training. EBI is probably the most promising carrier of the desired information. First publications date back to the 1930s, and the method has been successfully exploited in different areas [1]. Some improvements are required for EBI measurements to be used pervasively. A lean, efficient, and easily embeddable solution is proposed in the current paper.

II. STATE OF THE ART

Typical impedance plethysmography device consists of an excitation current source, generating the signal in the frequency range of few Hz to several hundred kHz, an electrode system for the injection of the strictly controlled and limited current (1 to 4 mA due to safety constraints) into the body, and a unit for measurement of the response voltage. Last but not least, analog or digital, often mixed, signal processing solution (Figure 1) is required. If injected sinusoidal current is considered as being with unity magnitude and zero phase shift, then the response voltage's magnitude is directly proportional to the measured impedance magnitude, and phase angle between the voltage and current gives the phase of impedance vector.

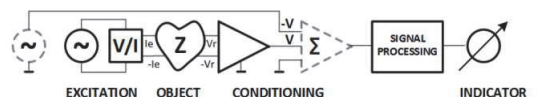


Fig. 1 Simplified EBI measurement system with optional direct carrier compensation circuitry in dashed grey

Both the cardiac stroke and the respiratory movement of the lung cause changes in the measured EBI values over the thorax area. Said EBI values are comprised of relatively large but static, and less informative base impedance Z , and of the tiny deviations $\Delta Z(t)$ on top of it (Figure 2).

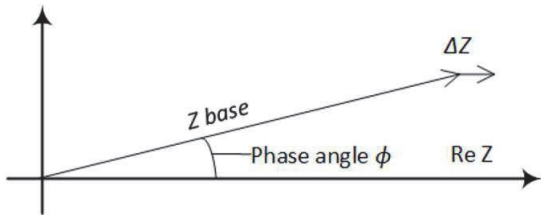


Fig. 2 Simplified illustration of the biomodulation of the body impedance

Most of the desired information is typically considered as being in the change of the magnitude of Z , and phase modulation is often disregarded, as the angle ϕ is small. Respiratory signal is certainly easier to measure, as being considerably larger, cardiac component, on the other hand, can be as low as 0.1% or lower compared to the base value. This rough estimation is based on the acquired data during number of in house experiments, and depend heavily on measurement conditions, such as placement of the electrodes. Practical placement of electrodes is often dictated by requirements not related directly to optimal measurement.

After initial conditioning of the response signal it is often directly multiplied with the carrier, and then low pass filtered. A result of this synchronous demodulation operation, correlation between excitation and response waveforms, is then digitized and further processing is carried on digitally. Relatively slow multibit analog-to-digital converters (ADC) can be used. The sampling rate varies typically between few hundred to thousand samples per second. Required number of bits is however quite high, ideally over 20, due to a very small depth of the modulation. Alternatively, the preconditioned response can be synchronously sampled and digitized directly. This requires, however, much faster converters. Even though certain amount of under sampling can be used, it results in decreased signal-to-noise ratio and is not desirable, therefore. Requirements to the ADC can be relaxed when so called direct carrier compensation is used [3] (Figure 1). In Fig. 1, the excitation oscillator generates differential sinusoidal voltage. The excitation voltage is thereafter converted into current and injected into the biological object Z . The response voltage has variable amplitude and phase due to the biomodulation. The measurement system includes another greyed-out oscillator to generate the compensating voltage opposite in sign and equal in average magnitude to the response from the object. The compensator then effectively

suppresses the carrier using amplitude and phase estimates. Practical in house experiments suggest that the carrier can be suppressed roughly by 100 times. Over that limit, both higher harmonics of the response signal and added noise make further improvement impractical. Improved dynamics has added cost of more complicated circuitry, and cumbersome adjustment of the magnitude and phase of the compensating signal. As soon as the artefacts step in, the results deteriorate quickly. Unfortunately, large, compared to the cardiac signal, disturbances caused by movement artifacts are often present.

An alternative method has been presented for multifrequency impedance measurement systems [4]. When sampling synchronously with the excitation signal, it is possible both, to minimize the complexity of the calculations and to introduce a digital-to-analog feedback for the enhancement of the resolution by digitizing only the small variations between the current sample and the previously converted one (Figure 3).

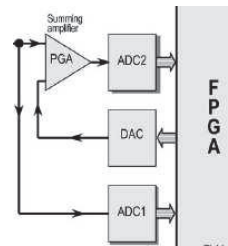


Fig. 3 Fragment of the feedback compensation principle [4]

Similar logic is in use behind the well-known pipelined or subranging ADC [5]. First introduction of the concept may be disputable, but [6] bears many of the important aspects, and is generally recognized as the first patent on differential pulse code modulation (DPCM) or delta modulation (Figure 4).

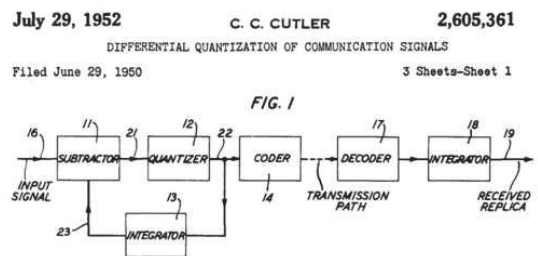


Fig. 4 Picture from the DPCM patent by Cutler [6]

Common to many implementations of it, is integration of the quantization result, which is then fed back to the input of the conversion circuitry and subtracted from the current sample to be acquired, therefore the circuit tries to minimize the difference between the integral and the actual signal. Restoration of the original signal is therefore quite straight forward requiring essentially another integrator. Pipeline structure uses feed forward techniques instead, and the calculated difference (delta) between the first conversion result and the actual input signal is amplified and further converted. Proposed approach bears marks from many of these concepts, but also differs in some important aspects.

III. PROPOSED SOLUTION

Proposed solution builds on several assumptions. First of all, it relies on the ease of synchronous sampling of the sinusoidal excitation in the lock-in impedance measurement system described in several previous papers, such as [4].

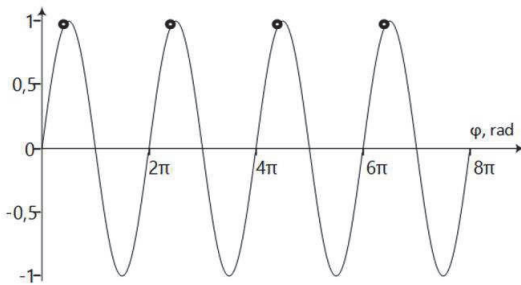


Fig. 5 Synchronous sampling of a sinusoidal response. Placement of samples in time (dark circles) coincides with maximums of the excitation signal. They are shifted to the left by phase angle of the impedance under the test (compared to the locations of the response signal maximums). Vertical axis shows normalized magnitude of the response voltage, and horizontal axis the phase of the response signal.

All of the samples (Figure 5) can be directly converted with suitably high speed ADC, with or without the following feedback compensation. Since the high speed ADC's have typically only limited number of bits, it can result in high quantization errors for the modest magnitude modulation (Figure 6). It is obvious that the results should be improved considerably.

Second assumption is that the sampling can be implemented outside of the ordinary ADC. In fact, two samplers will be employed, and two time adjacent samples will be taken synchronously to the excitation. Then the difference between said samples will be calculated in analog domain, and digitized later by the aid of ADC (Figure 7).

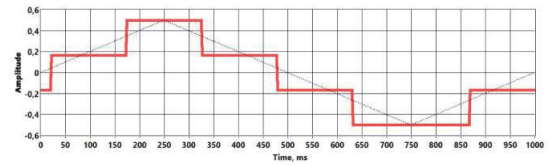


Fig. 6 A carrier of 1 V amplitude is modulated by 0.1 mV and 1 Hz triangle wave. Normalized results after synchronous conversion are depicted as follows: a narrow dashed black line is of ideal converter with infinite number of bits, and the bold red line corresponds to an ordinary ADC with 16-bit resolution

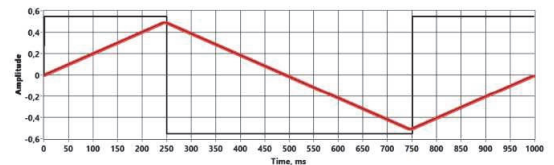


Fig. 7 The same signal as in previous figure (Fig. 6) sampled sequentially in time. A narrow black line square wave (normalized to unity magnitude) represents the calculated differences between adjacent samples, a bold red is normalized result of the 12-bit conversion of the differences integrated digitally afterwards

It is quite clear from the picture in Fig. 7 that, essentially, we are differentiating the signals during the proposed sampling, i.e. we are calculating a magnitude difference per one sampling interval, and therefore the follow up integration restores the original modulation part. In real life situations, obviously certain amount of noise is present as well. It improves somewhat the direct sampling result due to dithering (Figure 8), but the proposed sampling handles large additive noise as well (Figure 9).

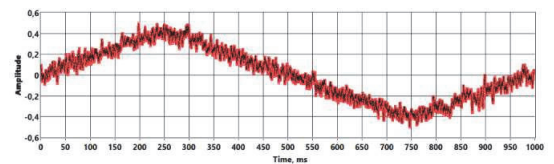


Fig. 8 The same signals and processing procedures as in Fig. 6, but with 0.1 mV noise added; all of the curves are normalized for better readability

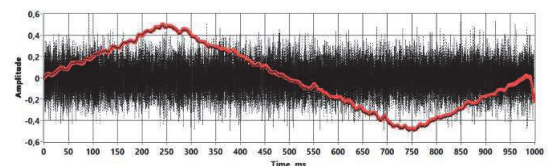


Fig. 9 The same signals and processing as in Fig. 7, but with 0.1 mV noise added; all of the curves are normalized for better readability

Obviously, the differential sampling solution performs still better, even if only 12-bit converter is used instead of 16 bit one. The 12-bit resolution was chosen for comparison, as typical microcontrollers and digital signal processors (DSP) usually have such ADCs incorporated. In reality, if carefully adapted to the measurement task, even single-bit conversion can be considered in certain cases.

Logic behind these results is pretty straight forward: two adjacent similar samples can be considered as having essentially the same value since the excitation signal frequency (from kHz to MHz range) is very high compared to the speed of the change of the signal caused by the biomodulation with less than 100 Hz frequency spectrum, and also of the typical motion caused artefacts (up to 1kHz range, maximally). From the nature of the derivative follows also that the actual difference between samples does not depend on the magnitude of the signal itself, but only on the speed of its changing. Therefore, large but slow artefacts have roughly the same level impact as tiny but fast variations caused by omnipresent noise. It is believed that replacing the integrating feedback loop, typical to DPCM, with feed forward circuitry (in proposed solution), enhances the stability of the solution. Later signal processing can be as simple as in described cases, where simple numerical integration and follow up moving average filtering was used.

Different sampling circuits can be considered, from ordinary analog switches to purpose-made silicon. As an example, the fast Sample-and-Hold (SH) circuit DS1843 from Maxim Integrated was tested with good results. If the excitation frequency is too high compared to the ADC speed, or the speed of the sampling circuits, or the power resources are limited, then it is reasonable to use undersampling.

It is worth noting that synchronous sampling described in [4], together with proposed additions performs also synchronous demodulation function in analog domain, and therefore simplifies later signal processing tasks, and saves power. It is essential for the intended usage area of the proposed solution, i.e., in the wearable pervasive diagnostic devices.

IV. CONCLUSIONS

Novel approach is proposed, whereas sampling is detached from the analog-to-digital conversion, and the difference of two consecutive samples in time, synchronously to the excitation signal, is sent to be converted instead of direct sampling of the response. The developed new method for the sampling of the EBI response signal enables to minimize the impact of the large base value of the bioimpedance together

with large but bandlimited artefacts to the resolution and accuracy of the digitalization process. It is achieved by placing simple sample-and-hold circuits in front of the ADC. More bits are left for direct digitalization of the biological modulation on top of the bioimpedance signal, and still the required ADC may have overall less bits than previous solutions required. It enables savings both in cost and in energy. Introduced principle can easily be adapted for construction of the task oriented application specific integrated circuits (ASIC). The concept has been positively evaluated with computer experiments in the LabVIEW environment.

ACKNOWLEDGMENT

The research supported by Estonian Research Council grant IUT1911 and European Regional Development Fund in frames of the Estonian ICT Center EXCITE. Partly also by the EU project H2020- 2014-2-668995-Cognitive Electronics.

CONFLICT OF INTEREST

The authors declare that they have no conflict of interest.

REFERENCES

1. Malmivuo J, Plonsey R (1995) *Bioelectromagnetism - Principles and Applications of Bioelectric and Biomagnetic Fields*, Oxford University Press, New York
2. Grimnes S, Martinsen Ø G (2014) *Bioimpedance and Bioelectricity Basics*. Academic, San Diego
3. Annus P, Lamp J, Min M et al. (2005) Design of a Bioimpedance Measurement System Using Direct Carrier Compensation, Proc. of ECCTD'05, Cork, Ireland. IEEE Publ, pp 23–26
4. Min M, Parve T et al. (2007) Synchronous Sampling and Demodulation in an Instrument for Multifrequency Bioimpedance Measurement. *IEEE Trans I&M*, 56 (4), 1365–1372
5. Kester W, Analog Devices, inc (2005) *Data conversion handbook*. Elsevier ; Newnes, Amsterdam ; Boston
6. Cutler C (1950) *Differential Quantization of Communication Signals*. U.S. Patent 2,605,361

Enter the information of the corresponding author:

Author: Paul Annus
 Institute: Tallinn University of Technology/ Thomas Johann Seebeck
 Department of Electronics
 Street: Ehitajate tee 5
 City: Tallinn
 Country: Estonia
 Email: paul.annus@ttu.ee

Appendix 3

Publication III

Priidel, E.; Annus, P.; Metshein, M.; Land, R.; Märtens, O.; Min, M. (2018). Lock-in integration for detection of tiny bioimpedance variations. *BEC 2018: 16th biennial Baltic Electronics Conference: proceedings of the 16th biennial Baltic Electronics Conference: Tallinn University of Technology, October 8-10, Tallinn, Estonia: 2018 16th Biennial Baltic Electronics Conference (BEC), Tallinn, October 8-10*. IEEE. DOI: 10.1109/BEC.2018.8600965.

Lock-in integration for detection of tiny bioimpedance variations

Eiko Priidel, Paul Annus, Margus Metshein, Raul Land, Olev Märtens, Mart Min
Thomas Johann Seebeck Department of Electronics
Tallinn University of Technology
Tallinn, Estonia
paul.annus@ttu.ee

Abstract—It is often desirable to detect tiny variations on top of larger static base value. Synchronous or lock-in measurement related problems are discussed in the current paper, and new solution is proposed for detection of bioimpedance variations. Proposed method is believed to be simpler, and more robust compared to known solutions. In the heart of the method is lock-in integrator, used as differentiating peak detector. The base component of the signal is rejected, giving better dynamic range for the information carrying variable component of the bioimpedance due to the apparent differentiation. Reduction of the additive off band signals and noise is considered as well.

Keywords—*bioimpedance, dynamic range, synchronous measurement, lock-in detection*

I. INTRODUCTION

European Society of Cardiology, the ESC, states that Cardiovascular disease (CVD) has accounted for over 3.8 million deaths each year, or 45% of all deaths across ESC member countries. Most common CVD the ischemic heart disease (IHD) was the leading cause, responsible for 1.7 million deaths (20% of all deaths) with stroke responsible for 970 391 deaths (11% of all deaths) [1]. The numbers are frightening. Even more so, if the fact that 90% of heart attacks are preventable is considered [2]. Hypertension remains an important public health challenge because it increases the risk for cardiovascular disease. Clearly the prevention and diagnosis of the hypertension is of utmost importance. Unfortunately, the early detection of the hypertension is complicated even today, and it is estimated, that around 30% of the hypertensive population is unaware of their disease [3]. The American Heart Association webpage [4] states that the high blood pressure (HBP) or hypertension is a “silent killer”, because it has no obvious signs or symptoms to indicate that something’s wrong. The best ways to protect yourself are being aware of the risks and making changes that matter.

Classical, widely used, HBP detection method is the upper arm (brachial) peripheral blood pressure measurement. It is not flawless though. The biggest criticism is that it is considered less informative than required, and the central pressure in the aorta (CAP) near the output of the left ventricle of the heart is the only true source of the information [5]. Today’s „gold

standard“ measurement device is still invasive pressure sensor inserted into the aortic arch [6]. Procedure is complicated, requires hospital surroundings, is costly, and carries added risk to the health. Noninvasive preemptive assessment of the CAP, and associated indices is vital. Brachial cuff based sphygmomanometer is not a reliable tool, but there is known tonometry device SphygmoCor [7], which has been in use for the diagnostic practice in Mayo Clinic (Rochester, MN, USA) and in many other hospitals around the world for several years already [8]. Credible measurements with SphygmoCor require supine rest conditions with the hand laid in the fixed position.

It has been shown however that electrical bioimpedance (EBI) sensing over radial artery can be very promising competitive solution [9]. It is less operator dependent method, and has been validated against the “golden standard” invasive procedure in the East-Tallinn Central Hospital (ITK), Estonia, in the frames of ongoing research project. It has also been validated against the SphygmoCor device in the clinical experiments carried out in the ITK. The earliest papers that suggested the viability of the EBI based central aortic pressure assessment were circulated already in 1980’s [10]. Herscovici and Roller proposed attachment of four conductive Velcro electrodes to the regular blood pressure cuff, and use impedance plethysmography for determination of the mean arterial pressure. The algorithm showed a good correlation between direct and indirect measurements. In 1994, Rudolf A. Hatschek patented a blood pressure measuring device and method, which allows to make measurements in a non-invasive manner [11]. He explains that the blood pressure can be determined relatively accurately by obtaining two different values: volume, as a variable that changes periodically over time in the rhythm of the pulse beat, and a pulse wave velocity. Among other proposed possibilities as light waves, ultrasonic waves and magnetic/electrical induction, the author suggests also configuring the device so that it determines changing blood volume in the measuring region of a body part with EBI. J. Sola et al. presented in 2011 a pilot study, where they provided first experimental evidence that electrical impedance tomography (EIT) is capable of measuring pressure pulses directly within the descending aorta. Their research measures impedance on thorax, not on arm or wrist, but the study supports, nevertheless, the idea of central aortic pressure

assessment with bioimpedance [12]. Numerous researchers have had promising preliminary results, and many scholars have showed practical improvements on the EBI based assessment of the aortic pressure curve. Notably however number of corresponding devices for the clinical practice is still not significant, which suggests that probably both the method and device need further research and development. Current paper discusses device improvement by using novel peak detection method for EBI acquisition.

Main problem in the EBI measurement is that small changes are often lost in large basal quantities. It may pose a serious challenge for the examiner, if those changes are of interest, and they often are. It requires wide dynamic diapason from the measurement apparatus in case of the direct measurement. Secondly abrupt changes in contact impedance, motion caused artifacts etc. may saturate the measurement channel for long periods, and cause slow wandering afterwards.

Several methods have been proposed to overcome these difficulties. The clinical device Circmon, used during the ITK experiments, employs one of them - the direct carrier compensation (DCC) [13]. Creation of simpler, more robust devices has been attempted. Sample by sample compensation method [14] is also one of the viable alternatives. In contrast to the previous methods the feed forward compensation is less prone to long lasting transients due to its finite impulse response (FIR) nature. Quantization of the response signal differences was proposed for the bioimpedance measurement [15], as method of choice. Essentially differences between adjacent analog samples were processed, and then digitized (Fig. 1). Such samples were taken synchronously to the excitation signal thereby accomplishing synchronous demodulation together with basal value elimination from the demodulated signal. Solution proposed here can be viewed as an evolution of the later method.

II. BIOMODULATION OF THE RADIAL EBI

In its simpler form the impedance is calculated as complex ratio between the voltage on the object and the current through that object under investigation [16]. This general description allows excitation with voltage and measurement of the resulting current or current excitation together with voltage measurement. In fact, excitation with arbitrary source with simultaneous measurement of the voltage and current is

possible. However current excitation is usually preferred in case of the bioimpedance measurement for several reasons. It allows minimization of the impact of the electrode impedances, sometimes much larger than the impedance of the actual object. Most importantly however it ensures the safety of the object under investigation. It is due to the hard limitation of the current through the biological tissue. In case of single frequency sinusoidal excitation signals the calculations can also be simplified. If we take the magnitude of the applied known sinusoidal current as unity and consider it having zero beginning phase then the complex division can be omitted. Therefore the impedance of the system under investigation will essentially directly determine the magnitude and the phase of the response voltage (Fig. 2). Impedance of the biological object shows typically capacitive behavior within measurement range from some kilohertz to some hundred kilohertz. Same applies also for the EBI measurement on the radial artery (Fig. 3). The result shows slightly capacitive behavior of the impedance vector and tiny variation on top of it due to the biomodulation of the impedance signal. The varying part of the EBI has slightly different phase, than the basal, since the impedance of the changing or pulsating quantity (such as blood for example) can be different from the average impedance of all of the tissues in the measurement path. Signal on Fig. 3 was acquired with Zurich Instruments AG HF2LI 50 MHz Lock-in Amplifier together with HF2TA Current Amplifier. Measurement was conducted on single frequency 120 kHz. Electrodes used on the wrist are depicted on Fig. 4. It is ordinary FR4 printed circuit board with gold plated electrodes. Phase angle of the base impedance is around -4 degrees. Phase angle of the modulating signal caused by blood pulsation is slightly higher ca -16 degrees, and the magnitude is roughly 200 times smaller than the, much less informative, value of the base impedance. The ratio is clearly unfavorable, and requires good dynamic diapason from the measurement system. It is challenging when designing truly wearable data acquisition solutions. Few conclusions can be drawn from this (and numerous other) measurement results. First of all, the phase angle is small, and secondly the modulation is mostly in the change of the magnitude of the vector, which would suggest that phase detector could be omitted in wearable indicator without large errors. Main idea of the improved, compared to the solution on Fig. 1, envelope detector is discussed in the following part.

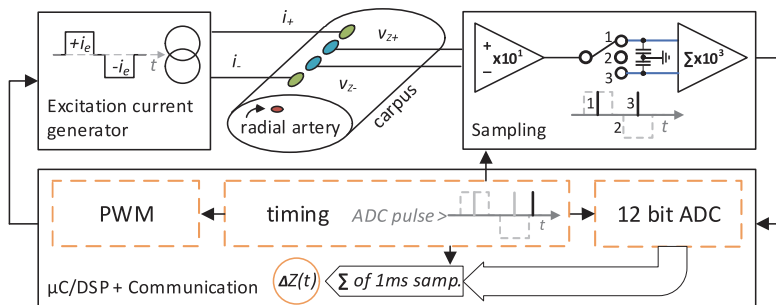


Fig. 2. Block diagram of the EBI measurement unit using digitalization of the differences between adjacent analog samples.

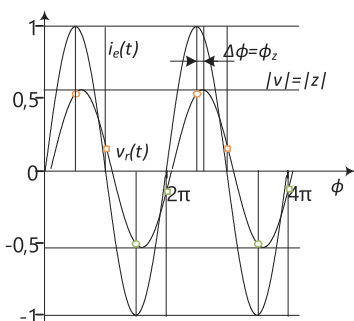


Fig. 2. Unity magnitude excitation current with zero beginning phase, and voltage response with its magnitude, and phase shift. Magnitude of the current and voltage in relative units on vertical axis, and phase on the horizontal axis. Dots represent the values of the quadrature samples.

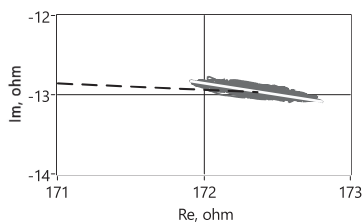


Fig. 3. Measured EBI vector on the complex plain. Bio-modulation is shown with gray smeared line. Black dashed line shows the vector of the base impedance.

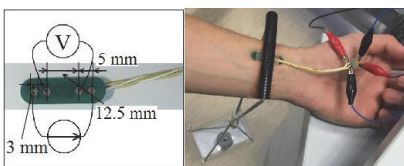


Fig. 4. Electrodes used during data acquisition on the wrist.

III. PROPOSED MEASUREMENT SOLUTION

Novel synchronously integrating envelope detector is proposed. Sampling in the previous solution is ideally with infinitely short pulses. Real samplers do obviously require some time to take the sample, and do have aperture errors. From the other side short samples do ignore large part of the incoming signal and limit the achievable signal to noise ratio (SNR). That in turn brought up the idea to investigate the performance of the system, when infinitely short samples are replaced with half period integrals instead. The basic principle can be seen on Fig. 5. Modulation with linear ramp is considered for simplicity of the discussion. That simplification seems to be valid, if we consider slow biomodulation (few Hz),

and compare it with relatively fast excitation (120 kHz excitation) signal.

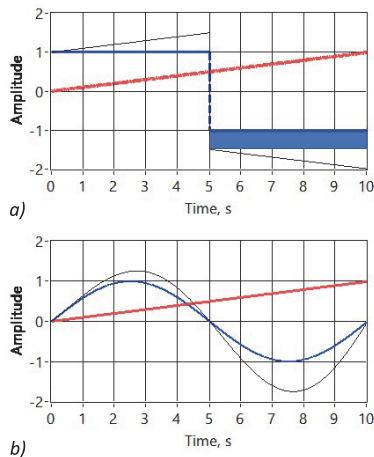


Fig. 5. Synchronously integrating AM detection, when the carrier is square wave a), and when the carrier is sinusoidal b). Carrier is modulated in both cases with linearly growing ramp. Unmodulated carrier is wider blue line, modulated carrier is narrow black line, and modulating signal wide red.

The idea is clearly visible in case of the square wave carrier. Without modulation the net integral over the full carrier period is zero, with modulation however one of the half periods is larger than other. Change in the area is depicted as dark rectangle on the Fig. 5 a), and therefore the resulting integral (area) is not zero anymore. Clearly the area depends on two things: period of the carrier (known and can be considered constant), and on the slope of the modulating signal. Slope of the linear function is equal to its derivative, and therefore the integral taken synchronously over the full period (or number of them in a row) of the excitation signal is linearly related to the derivative of the modulating signal. With some simple mathematics it can be shown that the statement is also valid for the sinusoidal excitation. It is also clear that the original modulating signal can be restored later with integrator. Clear benefit of the proposed synchronous integration method is that the base value of the impedance is automatically excluded from the detection result, and therefore the dynamic requirements for the following ADC circuit can be considerably relaxed. There is however also unfortunate side effect, as with ordinary peak detection as well: detector is sensitive to all signals. Therefore unwanted additive components or noise can destroy the measurement entirely. Pre-filtering of the acquired signal becomes mandatory. In addition to that the filter should be tuned exactly to the excitation signal. Even tiny phase variations will be unacceptable, not to mention frequency errors. While typical RLC filter cannot handle that there is a solution – synchronous lock-in filtering. In its different forms it has been around for many decades [17]. Essentially it is a lock-in demodulator (multiplier) with low pass filter followed by an additional lock-in multiplication.

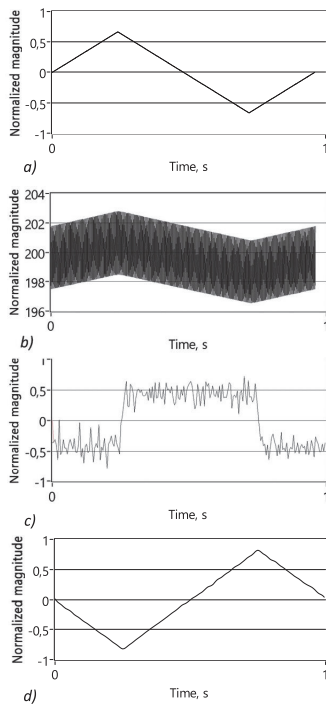


Fig. 6. Modulating signal a), signal after lock-in detector b), synchronously integrated signal c), signal after final integration d).

Besides serving as the narrow band pass filter it enables also detection of the base impedance value, which could serve as indicator for the quality of the electrode attachment. Realization can have many different forms, such as solutions proposed by O. Märtens [18] for example. Proposed system has been successfully simulated in LabView environment (Fig. 6). Sinusoidal carrier is modulated with triangular waveform, and small noise is added. As a result, the carrier is roughly 200 times bigger than the modulation on top of it. Square wave signal is used for lock-in filtering and synchronous integration. It enables usage of ordinary switches instead of multipliers. Due to simple first order RC filter used, the lock-in demodulator output still has small residue from carrier. Lock-in integration gives the derivative of the original modulating signal together with some noise, and 180 degrees shifted result is shown after the final integration.

IV. CONCLUSION

Novel lock-in integration for detection of tiny bioimpedance variations has been proposed and simulated. When applied together with lock-in filtering it enables design of simple analog front ends for bioimpedance acquisition with enhanced protection against artefacts. Requirements for the ADC used after detection can be substantially relaxed. Actual prototype is currently being built and tested.

ACKNOWLEDGMENT

This research was supported by Estonian Research Council grant IUT1911 and the European Regional Development Fund in frames of the Estonian Center of Research Excellence EXCITE. The work was partly financed also through the European Research Area project H2020-WIDESPREAD-2014-2-668995-Cognitive Electronics and H2020-2016-FET-JPC-Convergence.

REFERENCES

- [1] Atlas Writing Group *et al.*, "European Society of Cardiology: Cardiovascular Disease Statistics 2017," *Eur. Heart J.*, vol. 39, no. 7, pp. 508–579, Feb. 2018.
- [2] H. C. McGill, C. A. McMahan, and S. S. Gidding, "Preventing Heart Disease in the 21st Century: Implications of the Pathobiological Determinants of Atherosclerosis in Youth (PDAY) Study," *Circulation*, vol. 117, no. 9, pp. 1216–1227, Mar. 2008.
- [3] A. V. Chobanian *et al.*, "Seventh Report of the Joint National Committee on Prevention, Detection, Evaluation, and Treatment of High Blood Pressure," *Hypertension*, vol. 42, no. 6, pp. 1206–1252, Dec. 2003.
- [4] "American Heart Association - Building healthier lives, free of cardiovascular diseases and stroke." [Online]. Available: <http://www.heart.org/HEARTORG/>. [Accessed: 10-Jun-2018].
- [5] C. M. McEniery, J. R. Cockcroft, M. J. Roman, S. S. Franklin, and I. B. Wilkinson, "Central blood pressure: current evidence and clinical importance," *Eur. Heart J.*, vol. 35, no. 26, pp. 1719–1725, Jul. 2014.
- [6] E. O. Lau *et al.*, "Prediction of aortic augmentation index using radial pulse transmission-wave analysis," *J. Hypertens.*, vol. 24, no. 4, pp. 723–730, Apr. 2006.
- [7] "AtCor Medical | Central Arterial Pressure Waveform Analysis."
- [8] M. R. Nelson, J. Stepanek, M. Cevette, M. Covalciuc, R. T. Hurst, and A. J. Tajik, "Noninvasive Measurement of Central Vascular Pressures With Arterial Tonometry: Clinical Revival of the Pulse Pressure Waveform?," *Mayo Clin. Proc.*, vol. 85, no. 5, pp. 460–472, May 2010.
- [9] M. Min, P. Annus, H. Koiv, A. Krivosei, T. Uuetoa, and J. Lamp, "Bioimpedance sensing - a viable alternative for tonometry in non-invasive assessment of central aortic pressure," 2017, pp. 373–378.
- [10] H. Herscovici and D. H. Roller, "Noninvasive Determination of Central Blood Pressure by Impedance Plethysmography," *IEEE Trans. Biomed. Eng.*, vol. BME-33, no. 6, pp. 617–625, Jun. 1986.
- [11] R. Hatschek, "Blood pressure measuring device and method," US5309916A, 1994.
- [12] J. Solà, A. Adler, A. Santos, G. Tusman, F. S. Sipmann, and S. H. Bohm, "Non-invasive monitoring of central blood pressure by electrical impedance tomography: first experimental evidence," *Med. Biol. Eng. Comput.*, vol. 49, no. 4, pp. 409–415, Apr. 2011.
- [13] P. Annus, J. Lamp, M. Min, and T. Paavle, "Design of a bioimpedance measurement system using direct carrier compensation," 2005, vol. 3, pp. 23–26.
- [14] M. Min, T. Parve, A. Ronk, P. Annus, and T. Paavle, "Synchronous Sampling and Demodulation in an Instrument for Multifrequency Bioimpedance Measurement," *IEEE Trans. Instrum. Meas.*, vol. 56, no. 4, pp. 1365–1372, Aug. 2007.
- [15] P. Annus, R. Land, E. Püridel, M. Metshein, M. Min, and O. Märtens, "Quantization of the response signal differences for the electrical bioimpedance measurement," in *EMBECC & NBC 2017*, vol. 65, H. Eskola, O. Väisänen, J. Viik, and J. Hyttinen, Eds. Singapore: Springer Singapore, 2018, pp. 290–293.
- [16] S. Grimnes, *Bioimpedance and bioelectricity basics*. Boston, MA: Elsevier, 2014.
- [17] M. L. Meade, *Lock-in Amplifiers: Principles and Applications*. P. Peregrinus, 1983.
- [18] O. Martens, "Precise synchronous detectors with improved dynamic reserve," *IEEE Trans. Instrum. Meas.*, vol. 49, no. 5, pp. 1046–1049, Oct. 2000.

Appendix 4

Publication IV

Annus, P.; Priidel, E.; Land, R.; Metshein, M.; Krivošei, A.; Min, M.; Ratassepp, M.; Märtens, O. (2021). Automatic Detection of Real and Imaginary Parts of Electrical Impedance with Single Synchronous Demodulation Channel. In: 8th European Medical and Biological Engineering Conference (151–157). Springer, Cham. (IFMBE Proceedings; 80). DOI: 10.1007/978-3-030-64610-3_18.



Automatic Detection of Real and Imaginary Parts of Electrical Impedance with Single Synchronous Demodulation Channel

Paul Annus^(✉) , Eiko Priidel, Raul Land, Margus Metshein, Andrei Krivošei, Mart Min, Madis Ratassepp, and Olev Märtens

Tallinn University of Technology, 19086 Tallinn, Estonia

paul.annus@ttu.ee

Abstract. Measurement of a voltage response caused by a current excitation signal sent to a biological system under study, i.e. measurement of electrical bioimpedance, is typically using analog or digital lock-in detection. Such a detector consists multiplying unit together with following low pass filter. Result of such a multiplication is typically acquired in-phase with excitation signal, and in quadrature with it. Later the actual bioimpedance vector can be calculated with its magnitude and phase. It can be viewed as performing correlation between excitation and response signals in two positions: with zero shift and 90° shift. It requires two identical channels, the exact identity of which is hard to achieve. Method for automatic single-channel detection is proposed, analyzed and tested in the lab for the acquisition of the electrical bioimpedance signal at the radial artery. The proposed method is useful when wearable low power acquisition of the electrical bioimpedance is required. It simplifies circuitry significantly, by thereby increasing reliability and lowering power consumption.

Keywords: Lock-in detection · Electrical bioimpedance · Correlation in analog domain

1 Introduction

Electrical impedance or simply impedance is defined by Oliver Heaviside as an opposition of a matter to a sinusoidal excitation current [1]. At first glance it may seem to be rather restrictive to the waveform of the excitation signal, since the sinusoidal current is explicitly mentioned. The ideas of Gauss, Fourier and many others do however expand the indefinitely, as signals can be composed of a number of sinusoidal components. The second thing that may not be immediately obvious is, that impedance is defined in the frequency domain. Indeed: the sinusoidal signal is fully characterized by its frequency and magnitude. The starting phase is a rather relative concept but can be mentioned here as well. After important work by Arthur Edwin Kennelly, and Charles Proteus Steinmetz the impedance is mathematically defined as the complex ratio of the complex voltage to the complex current:

$$\dot{Z} = \dot{V}/\dot{I} \text{ or more precisely } \dot{Z}(\omega) = \dot{V}(\omega)/\dot{I}(\omega) \quad (1)$$

Since the times of the Heaviside and Kennelly the concept of the impedance has been extensively studied by many others, applied in scientific research and even more importantly used to advance measurement technology and industry. Due to its frequency dependence it is customary to refer to impedance spectroscopy in many cases [2]. Many applications lie in electrochemistry, physical chemistry, and physics, but it can be applied also to study and characterize a living tissue, and ultimately human beings. In the latter case it is called an electrical bioimpedance (EBI) [3]. While the applications are slow to emerge, there are already several areas where EBI measurement is a must, such as a body composition analysis that characterizes relationships between fat, bone, water and muscle content in the human body. The EBI, in this case, is changing very slowly, and there is ample of time to calculate the average value of it. It is entirely a different story when fast modulations caused by the biological processes, such as breathing, heart beating, or digestion are studied in real-time. In this case the EBI can be viewed as comprising of two parts:

$$\dot{Z}_{EBI}(\omega) = \dot{Z}_{Base\ EBI}(\omega) + \Delta\dot{Z}_{EBI}(\omega) \quad (2)$$

Whereas $\dot{Z}_{Base\ EBI}(\omega)$ is so-called base or basal value and $\Delta\dot{Z}_{EBI}(\omega)$ is changing part or modulation of the base value caused by the biological processes. Two problems are introduced here. First is that the impact of the processes under inspection can be very small, such as in the case of the acquisition of the cardiac signal. Second and equally severe problem is that there are many other signals acting simultaneously, and potentially corrupting the readout entirely, such as it is the case of motion artefacts. It is unfortunately complemented with one of the biggest issues of the EBI acquisition, namely the quality of the electrodes and their attachment. It is estimated that up to around 85% of the problems in EBI measurement can be associated with the electrodes [3]. Issues are caused both by the actual coupling of the electrodes and by parasitic coupling of the body to outside targets. Perhaps it is not surprising then that it did lead to the statement that “impedance surprises” [4]. Also, safety issues must be considered, generally leading to excitation with the current source with very strict limits. Added on top of that the EBI acquisition device should be small to be easily attached to the body and conservative when energy consumption is considered.

Some devices exist, which satisfy discussed requirements, such as medically certified CircMon BT101 (impedance cardiograph), provided by JR Medical Ltd (Tallinn, Estonia) for the experiments conducted by authors, together with medical personnel of East Tallinn Central Hospital, and its modernized version CircMon BT101A. But there is both need and possibility to improve the instrumentation further. The method used by the CircMon device is called direct carrier compensation DCC [5]. The so-called feedback compensation principle can be used alternatively [6]. There is also a family of novel derivative solutions enabling separation of the basal value of the impedance from the changing part, before the digitalization with differential sampling which can be easily integrated into wearable solution [7] and with synchronous integration [8]. Both are tested with good results. Nevertheless, they rely on the underlying impedance

acquisition and should ideally work in two parallel channels for simultaneous acquisition of the real and imaginary values of the complex EBI. The number of required channels can be even larger if the simultaneous acquisition of voltage and current values is considered. It brings a new set of problems with the similarity of these channels, and obviously adds to energy consumption. In reality the imaginary part is often neglected, as the phase angle of the impedance vector at the frequencies of interest is low – around 4° and does not vary much in time. The resulting error between the estimation of the true impedance vector length and the value of the real part of the said vector is therefore below one percent and is sometimes considered acceptable. Alternatively, a small adjustment can be applied to the phase of the multiplying signal of the synchronous demodulator, slowly correcting it if necessary. Could it be possible to recover the full complex value of the EBI without said simplifications, and without added the complexity of multiple parallel demodulation channels? It turns out to be possible, and even relatively simple.

2 Proposed Method

The basic formula of the complex EBI will be considered, with slight adjustments. First, the complex division will be replaced with complex multiplication by the complex conjugate:

$$\dot{Z}(\omega) = \dot{V}(\omega)/\dot{I}(\omega) = \dot{V}(\omega) \cdot \dot{I}(\omega)^*/\dot{I}(\omega) \cdot \dot{I}(\omega)^* \quad (3)$$

In the resulting (mathematically exactly equal equation) the complex voltage $\dot{V}(\omega)$ is multiplied with the complex conjugate of the current $\dot{I}(\omega)^*$, and it is all divided with the multiplication of the complex current and its conjugate. It is known that the multiplication of some function in the frequency domain with its conjugate is equivalent to autocorrelation in the time domain, and that multiplication of one complex frequency-domain variable with conjugate of the other frequency domain complex variable is equal to the cross-correlation in the time domain. Given that current source based solutions are preferred for safety reasons in case of EBI acquisition the time domain voltage response signal has to be cross-correlated with the excitation current signal, and it has to be divided with the autocorrelated current signal. The later can be easily precalculated, since the excitation signal is given, and so is the autocorrelation value of it. Synchronous measurement solution using cross-correlation (Wiener-Khinchin theorem) is well known, and such a full shift correlation can be easily calculated in the digital domain, together with a follow-up Fourier transform for spectroscopy. It would be desirable to acquire it already in the analog domain before the analog to digital conversion. It would simplify requirements for the conversion, reduce required computing power, and ultimately enhance the embeddability of the method. So far, the simplicity of the solution may not yet be visible, since the cross-correlation of two different signals is at best hard to achieve with analog circuitry. By definition two signals have to be sliding in relation to each other, then they have to be multiplied and integrated:

$$(f \star g)(\tau) \triangleq \int_{-\infty}^{\infty} f(t)^* g(t + \tau) dt \quad (4)$$

The resulting correlation function will depict correlation results at arbitrary sliding time instances between two functions. It will have its positive maximum where two functions are best coinciding, i.e. have the highest measure of similarity, and zeros where they are orthogonal to each other.

In the case of the EBI measurement with the sinusoidal signal it means that the generated sinusoidal current signal will cause measurable voltage response, which will typically have a certain phase shift, because the EBI under investigation is complex by nature, and in fact slightly capacitive. Calculation of the correlation function maximum between sinusoidal current and sinusoidal voltage signals would give both the magnitude and displacement (phase) needed.

The classical solution to determine the length and phase angle of the resulting impedance vector is using two synchronous demodulation channels. The incoming voltage signal is multiplied with an in-phase reference signal (relative to the phase of the excitation current signal) and with quadrature, i.e. 90° shifted, reference signal. It will give real and imaginary components of the complex response voltage, and therefore completely determine its length and phase angle. The result should be divided with complex current value, but since the phase of the current signal coincides with one of the references, i.e. it is in phase with it, i.e. it is deliberately chosen to be in phase with it, the imaginary component of the complex current vector is zero and the complex division is reduced to the ordinary one with a rational number denominator. Therefore, the response voltage signal is directly proportional to the impedance signal of interest, since the current value can be considered constant, i.e. it is kept constant by the design of the current source circuitry. Such a quadrature synchronous demodulation can be considered also as getting cross-correlation values at two sliding angles, namely 0° and 90°.

Such a result can be accomplished in principle also with one single measurement channel, whereas the reference signal phase is suitably time multiplexed, and varies between 0° and 90°. Here the reduction in channel count is achieved with added complexity in reference generation, and care must be taken not to corrupt the result by transients at phase change moments.

The third possibility is to use single channel and introduce arbitrary sliding time interval τ , as it has been shown in several papers, including already referred [5], where it is denoted by changing phase difference $\Delta\phi$. Patent US7970461 is known in which a periodic excitation signal is applied to an object under study and the response received from the object is multiplied by a reference signal identical to the excitation signal but delayed by a fixed phase shift, the phase shift magnitude being selected according to the expected properties of the object. Such a τ should be then changed to get to the correlation function maximum.

Still, the circuitry needed to achieve a variable phase difference could be rather complex, it consumes excess energy, increases size and cost, and adds potential points of failure. Ideally, a certain amount of inherent automation should be built into the circuitry. In [5] the solution involved two similar AD9834 numerically controlled direct

digital synthesizers (DDS) from Analog Devices – one with frequency f and zero starting phase, and the other with the same frequency f and variable starting phase, which was then consequently changed to achieve the correlation function maximum. Effectively one synthesizer would generate excitation current signal:

$$I_{EXC} = A_I \cos(\omega_{EXC}t + \varphi_0), \text{ where } \varphi_0 = 0 \tag{5}$$

And the other synthesizer would generate a reference signal with varying starting phase:

$$V_{ref} = A_{ref} \cos(\omega_{EXC}t + \varphi_\tau), \text{ where } \varphi_\tau \text{ can change in full circle} \tag{6}$$

Important consideration to be noted here is trivial fact that the argument of cosine function (and also sine function) is phase, so that it could be written as:

$$\cos(\omega_1t + \varphi_0) = \cos(\varphi_1(t)) \tag{7}$$

If the typically constant starting phase is also changing in time the equation may take the following form:

$$\cos(\varphi_1(t)) = \cos(\omega_1t + \varphi(t)) \tag{8}$$

And if a said phase change is a linear function of the time it could be rewritten in the following form:

$$\cos(\omega_1t + \varphi(t)) = \cos(\omega_1t + \Delta\omega t) = \cos((\omega_1 + \Delta\omega)t) = \cos(\omega_2t) \tag{9}$$

So, the final conclusion here is that if slight change in the frequency is introduced between two oscillators, it is equal to automatically changing the phase difference between said oscillators in time, or in fact it is known phenomena called beating. From another angle it could be viewed as two oscillators having a slight difference in the period of signal repetition, i.e. one of them is slightly squeezed or expanded in time (see Fig. 1).

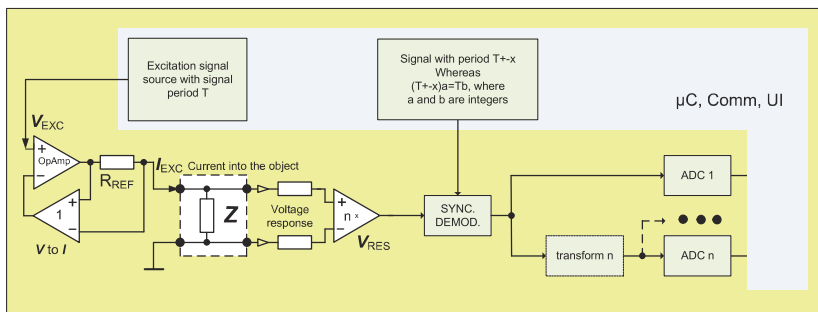


Fig. 1. A block diagram for EBI measurement unit using single synchronous demodulation channel.

If such a signals are used in single synchronous measurement channel, i.e. excitation signal having slightly different frequency than the reference signal at the multiplier, then the demodulator output will periodically cover full circle of phase differences between said two signals, and it can be viewed as having automatic phase shift, or automatically varying delay τ between these signals.

There are several considerations for the speed of this delay variation. First of them is related to the nature of the EBI, and to the sources of its variation. It should be considerably faster than the maximum speed of the EBI change, so that the EBI can be considered time-invariant in the window of the delay period. This sets a lower limit. The higher limit is related to the EBI acquisition frequency itself. In between there is an interesting time interval of 1 ms. In many cases the instruments for the acquisition of the biologically relevant varying data can be synchronized to sample simultaneously at 1 kHz. It is believed to be reasonable repetition frequency also for EBI measurement. It means that the excitation signal source frequency has to be exactly 1 kHz apart from the multiplier reference signal. As a result, the correlation maximum appears in exactly 1 ms intervals, it can be digitized, and used for consequent signal processing or analyzing task. Said maximum in the 1 ms window has to be found also in the current case, but it is a relatively straightforward and easy task, and can be left for the digital circuitry.

3 Conclusion

A novel method for wearable acquisition of EBI has been proposed. It reduces the complexity of the acquisition channel and reduces energy consumption. By using only a single synchronous demodulation channel for the acquisition of the full complex impedance vector it also eliminates errors caused by channel mismatch. Fully automatic operation reduces complexity and speed required for operation. In follow up embodiments it is also possible to compensate the correlation waveform before analog to digital conversion (ADC). It would enhance the available dynamic range of the circuitry, much like in the case for DCC, but at considerably lower (compared to the carrier) frequency. The method can be used for wearable acquisition of the EBI on the radial artery, and for the other system identification tasks outside of the EBI scope.

Acknowledgment. The research is supported by Estonian Research Council grants IUT1911, PRG737 and EAG34 and by European Regional Development Fund in frames of the Estonian ICT Center EXCITE and Mobilias Plus ERA-NET support project Chist-ERA JEDAI (through Estonian Research Council MOBERA20). Also, by the EU project H2020-WIDESPREAD-2014-2-668995-Cognitive Electronics and by Estonian ICT programme “IT Academy” (EU European Social Fund).

Conflict of Interest. The authors declare that they have no conflict of interest.

References

1. Kennelly, A.E.: Impedance. *Trans. Am. Inst. Electr. Eng.* **X**, 172–232 (1893). <https://doi.org/10.1109/T-AIEE.1893.4768008>
2. Barsoukov, E., Macdonald, J.R.: *Impedance Spectroscopy: Theory, Experiment, and Applications*, 3rd edn. Wiley, Hoboken (2018)
3. Grimnes, S., Martinsen, Ø.G.: *Bioimpedance and Bioelectricity Basics*. Elsevier, Boston (2014)
4. Brown, B.: Impedance surprises. *J. Electr. Bioimpedance* **6**, 1 (2015). <https://doi.org/10.5617/jeb.1520>
5. Annus, P., Lamp, J., Min, M., Paavle, T.: Design of a bioimpedance measurement system using direct carrier compensation. In: *Proceedings of the 2005 European Conference on Circuit Theory and Design*, Cork, Ireland, pp. 23–26. IEEE (2005)
6. Min, M., Parve, T., Ronk, A., Annus, P., Paavle, T.: Synchronous sampling and demodulation in an instrument for multifrequency bioimpedance measurement. *IEEE Trans. Instrum. Meas.* **56**, 1365–1372 (2007). <https://doi.org/10.1109/TIM.2007.900163>
7. Annus, P., Land, R., Priidel, E., Metshein, M., Min, M., Märtens, O.: Quantization of the response signal differences for the electrical bioimpedance measurement. In: Eskola, H., Väisänen, O., Viik, J., Hyttinen, J. (eds.) *EMBEC & NBC 2017*, pp. 290–293. Springer, Singapore (2018)
8. Priidel, E., Annus, P., Metshein, M., Land, R., Martens, O., Min, M.: Lock-in integration for detection of tiny bioimpedance variations. In: *2018 16th Biennial Baltic Electronics Conference (BEC)*, Tallinn, Estonia, pp. 1–4. IEEE (2018)

Appendix 5

Publication V

Priidel, E.; Annus, P.; Krivošei, A.; Rist, M.; Land, R.; Min, M.; Märtens, O. (2020). Methods for detection of bioimpedance variations in resource constrained environments. *Sensors*, 20 (5). DOI: 10.3390/s20051363.



Article

Methods for Detection of Bioimpedance Variations in Resource Constrained Environments

Eiko Priidel ^{*}, Paul Annus ^{*}, Andrei Krivošei, Marek Rist, Raul Land, Mart Min and Olev Märtens

Thomas Johann Seebeck Department of Electronics, Tallinn University of Technology, 12616 Tallinn, Estonia; andrei.krivošei@ttu.ee (A.K.); marek.rist@ttu.ee (M.R.); raul.land@ttu.ee (R.L.); mart.min@ttu.ee (M.M.); olev.martens@ttu.ee (O.M.)

* Correspondence: eiko.priidel@ttu.ee (E.P.); paul.annus@ttu.ee (P.A.)

Received: 21 December 2019; Accepted: 24 February 2020; Published: 2 March 2020



Abstract: Changes in a certain parameter are often a few magnitudes smaller than the base value of the parameter, specifying significant requirements for the dynamic range and noise levels of the measurement system. In case of electrical bioimpedance acquisition, the variations can be 1000 times smaller than the entire measured value. Synchronous or lock-in measurement of these variations is discussed in the current paper, and novel measurement solutions are presented. Proposed methods are simple and robust when compared to other applicable solutions. A common feature shared by all members of the group of the proposed solutions is differentiation. It is achieved by calculating the differences between synchronously acquired consecutive samples, with lock-in integration and analog differentiation. All these methods enable inherent separation of variations from the static component of the signal. The variable component of the bioimpedance can, thus, be acquired using the full available dynamic range of the apparatus for its detection. Additive disturbing signals and omnipresent wideband noise are considered and the method for their reduction is proposed.

Keywords: bioimpedance; dynamic range; synchronous measurement; lock-in detection; differentiation; cardiovascular system; non-invasive measurements; wearable devices

1. Introduction

Assessments of the working of human cardiovascular system has been one of the key tasks of medicine. It requires sensing as any other data acquisition task. The first truly non-invasive pulse recorder was introduced and patented by German physiologist Karl von Vierordt in 1855 - a sphygmograph. A “modern” mercury sphygmomanometer was not developed until 1896 and works of Scipione Riva-Rocci [1]. The first truly automatic measurement and recording devices showed up only in the late 20th century. Yet, the mercury sphygmomanometer has not disappeared from the scene. One of the key wishes has been formulated by the Research Professor and Director of Sleep Apnea Center of Kyushu University Hospital, Shin-ichi Ando: “I would like to have a blood pressure (BP) meter that is worn like a light wristwatch without any sensible pressure. . . . If such data can be transferred directly and easily to an electronic medical chart and be combined with other data, it would be very useful for the treatment of the patient and any kind of clinical research” [2]. Better diagnostic means and methods are clearly needed for ubiquitous early detection of the BP and its variation. There are a number of devices for acquisition of the static value of the BP, including some wearables. Variations are typically neglected in these devices. Probably, the best known tonometry device, which analyses the actual pressure curve is SphygmoCor [3], extensively evaluated in Mayo Clinic (Rochester, MN, USA) and other places [4]. Unfortunately, the method is rather complicated and operator-dependent, and can be used only by well-trained personnel, making it unsuitable for

unobtrusive wearable acquisition. There is also a verifiable link between the actual pressure variations and ballistocardiographic (BCG), and photoplethysmographic (PPG) signals presented in [5].

Authors of the present paper consider the electrical bioimpedance (EBI) sensing over the radial artery to be very promising competitive solution, and can back it up with years of research and development. Introduction to the complex topic of the EBI and its acquisition can be found in [6], and discussions on how the acquired EBI values can be related to the state of the cardiovascular system are comprehensively introduced in [7]. One of the earliest devices envisioned by the authors, which reached eventually medical certification for noninvasive acquisition of the EBI, is presented in [8]. It was used during the clinical research phase in the East-Tallinn Central Hospital (ITK) for over 100 human experiments. It has been validated against the invasive “golden standard” procedure. It has also been validated against the SphygmoCor device in the clinical experiments carried out in the ITK. The conclusion is that it is less operator-dependent than the SphygmoCor of AtCor Medical and does produce valid results reliably. EBI based assessment of central aortic pressure is not new, Herscovici and Roller published their groundbreaking research in 1980's [9]. Measurement was accomplished with four conductive Velcro electrodes, which were used together with inflatable standard pressurized cuff. Impedance plethysmography was promising for the assessment of the mean arterial pressure, and the used calculations resulted in acceptable correlation between direct and indirect measurements. Rudolf A. Hatschek has patented a non-invasive blood pressure measuring device and method in 1994 [10]. According the claims, blood pressure can be determined by acquiring the varying pulsatile volume and a speed of the pulse wave. For volume measurement, the EBI is suggested in addition to other possible means. J. Sola et al. provided experimental proof of usefulness of the electrical impedance tomography (EIT) on descending aorta on thorax in 2011 [11]. Many researchers have experimented with the EBI for central pressure in the aorta (CAP) assessment since then. Unfortunately, it has not yet resulted in widespread use of the method or development of relevant instrumentation. One of the reasons lies in the complexity of the task, including the need for advanced electronics. Current paper will not discuss relationships between EBI and cardiovascular parameters. Instead it will focus on the instrumentation for the ubiquitous acquisition of the EBI. This will be discussed in the following sections of paper.

2. EBI Acquisition

The topic is complex, and this explains the short list of success stories and modest number of developed devices, unless novel cardiac pacemakers are concerned where the sheer power of the EBI measurement method is used extensively. Two large problem areas are inherent, first, to the EBI acquisition electrode system, and second, to the electronics of the EBI measurement device itself. The device must operate reliably in rather harsh conditions, whereas minute variations of the EBI, which carry valuable information regarding the state of the cardiovascular system, can be masked by large motion caused artifacts, and the dynamic diapason required from the tiny wearable is huge. Electrodes play here crucial role. As stated in [6]: “around 85% of the problems in EBI measurement can be associated with the electrodes.” To acquire the EBI, one must let the current flow through the tissue and gather the voltage difference caused by the said current flow. The electrode system is used for coupling with the body. Four options could be considered in general [12]: Two electrode systems, both monopolar and bipolar, three electrode monopolar configuration and the tetrapolar four electrode or Kelvin connection. The names of the systems may be somewhat confusing. In case of the two and three electrode systems, the distinction between monopolar and bipolar refers to sensitivity distribution. Monopolar system should have only one significant region of high sensitivity and bipolar consequently two ideally equally sensitive regions. Situation is much more complex in case of the four-electrode connection to the object. The current flows through two of them and the voltage is monitored with the aid of two remaining electrodes. Sensitivity distribution, due to reciprocity [13], is cumbersome as it has negative sensitivity areas, and depends on the matter under electrodes. Having said that, the Kelvin method, essentially measuring transfer impedance between pairs of electrodes, drastically reduces the impact of the electrode-skin interface impedance to the results.

In the following only four electrode measurement is discussed, and only the instrumentation aspects, not the electrodes and electrode systems themselves, which are discussed elsewhere. All of the instrumentation solutions are presented in this manner, even though they could be easily adapted for other configurations as well. The impedance is a complex ratio between the voltage on the object and the current through that object. Excitation with the voltage output source and current measurement can be used, or current excitation and voltage measurement applied. A generally arbitrary source is acceptable, if both the voltage and current are acquired during the measurement. For medical applications, current excitation prevails mostly for safety reasons, but it also minimizes the impact of the electrode impedances. Also, a sinusoidal excitation signal allows the simplification of the calculations, and the impedance is determined by the response voltage magnitude and phase (Figure 1), by taking advantage that $\sin(0^\circ) = 0$, $\cos(0^\circ) = 1$ and $\sin(90^\circ) = 1$ and $\cos(90^\circ) = 0$. Quadrature signal can be expressed in complex plane as vector with the length of M and angle φ where real and imaginary components can be expressed as $I = M \cdot \sin(\varphi)$ and $Q = M \cdot \cos(\varphi)$. As the modulus of the signal is $M = \sqrt{I^2 + Q^2}$ we can see that on excitation signal phase angles 0° and 180° modulus equals to the imaginary part of the complex signal and on phase angles 90° and 270° modulus equals to the real part of the complex signal. The sampling, which is exactly on 0° , 90° , 180° and 270° phase angles, as seen in Figure 1, eliminates the need to calculate trigonometric functions in software resulting in lower CPU clock frequency and power consumption [14].

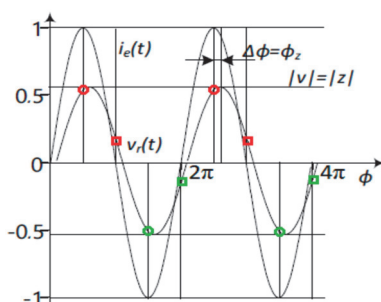


Figure 1. The unity-magnitude excitation current $i_e(t)$ with a zero-value initial phase, and the voltage response $V_r(t)$ with its magnitude, and phase shift. The normalized magnitudes of current and voltage in relative units given on vertical axis, and the phase on the horizontal axis. The samples related to the real part of the complex response of the i -th period $s(i,1)$ and $s(i,3)$ are designated by orange, and green circles, respectively, and samples corresponding to the imaginary part of the complex response of the i -th period $s(i,2)$ and $s(i,4)$ are designated by orange and green squares respectively.

Capacitively behaving bioimpedance is typically acquired in the range from kilohertz to hundreds of kilohertz. Therefore, EBI measurement on the radial artery (Figures 2 and 3) is performed accordingly. As it can be seen slightly capacitive impedance has very modest variation. The biomodulation is caused mostly by pulsating blood flow.

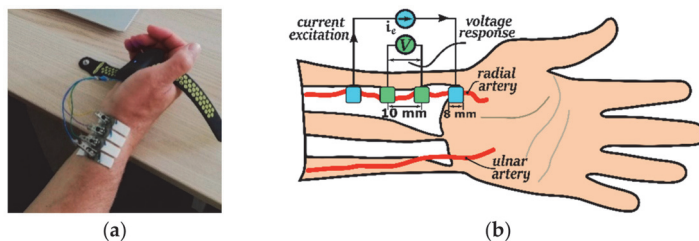


Figure 2. Electrodes (b) and their placement (a) during acquisition of the EBI.

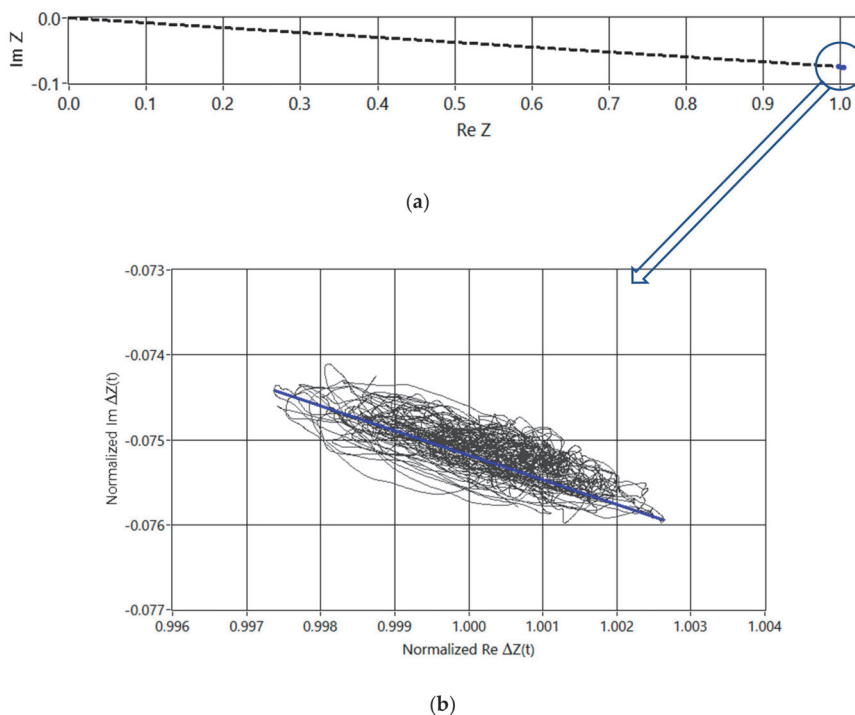


Figure 3. Normalized Nyquist plot of the impedance on the radial artery during several cardiac cycles. Real and imaginary parts of the base vector (dashed line, see (a)) together with modulation (blue dot at the end of the vector), and a zoomed-out modulation around the top of the base vector with average blue line (b).

Very small changes have to be acquired and this requires a wide dynamic range from the measurement apparatus. Abrupt changes in impedance of the contacts between the skin and the electrodes require close attention as well, otherwise the motion caused artifacts may saturate the measurement channel for a longer time and cause some slow signal wanderings afterwards.

3. Closer Inspection of the Measurement Situation

A set of measurements is conducted on the radial artery to illustrate the problem. Actual measurements were conducted multiple times with several different electrodes including gold plated printed circuit board (PCB) electrodes and standard electrocardiography (ECG) electrodes. The setup with the ECG electrodes is shown on Figure 2a. Placement of the electrodes in relation with the wrist and radial artery is further depicted on Figure 2b. Size, distance, location and the construction of the electrodes has been experimented with and refined during longer research period and described in different papers, such as [8] and [15]. In brief summary it can be said that the optimal setup for repeatable results consists of four equally spaced electrodes of 2–4 mm diameter roughly. The measurement results are normalized for two reasons. First, the results vary depending on the exact position and coupling of the electrodes. Secondly, the relationship between the base value and the periodic blood pulsation caused change is of interest here. The measurement results acquired from the radial artery are presented in Figure 3. Impedance values on real and imaginary axis are divided with average value of the real component as it is visible on the figure. Signal is taken from single measurement during several cardiac cycles on the radialis of volunteer. Normalization is done by dividing measurement results by center value of the samples. As seen from Figure 3 phase of the response signal is in the range of 4.27 to 4.33 degrees and $\text{Re}(\Delta Z)$ variation is 0.52%. Base level of the bioimpedance is normally in the range of

100 Ω to 1 k Ω depending on electrode material, distance and location. Impedance base level and phase is similar between subjects – large scale study of over 220,000 persons in Germany [16] defines average impedance of the human body, which shows very similar phase angles to Figure 3, even though it is measured at different location and only at 50 kHz. The reference study of dielectrical properties of tissues [17] marks the magnitude of the variability of readings between different subjects. Impedance variation on the radialis caused by cardiac activity can be considered small, around 0.5%, compared to base impedance and is in the range of some hundreds of milliohms. Impedance measurements on the hand of the author on Figure 3 and comparison with measurement results from other works are shown in the Table 1. Variability of bioimpedance measures in normal adults discussed in detail in [18] shows also remarkably similar phase angles as in [16], but now at 100 kHz. Also, the changing part of the bioimpedance measured in [19] on the wrist falls very close to the results acquired when conducting measurement depicted on Figure 3.

Table 1. Impedance measurement base values, variations due to cardiac activity and phase angle.

	Z [Ω]	ΔZ [Ω]	ΔZ [%]	Φ [deg]
Meas. Figure 3	70.39	0.35	0.5	4.3
Reference [18]	264.57			5.6
Reference [15]	102.8	0.12	0.11	
Reference [19]		0.326		

A signal was acquired with a well-known Zurich Instrument, AG HF2LI 50 MHz Lock-in Amplifier, together with HF2TA Current Amplifier, to ensure the results are repeatable elsewhere. The gathered information was analyzed and presented in the custom made LabView-based environment. The measurements were conducted in a wider scale at frequencies 10 kHz, 25 kHz, 50 kHz and 120 kHz in different conditions. The measurements with frequency of 120 kHz had the best signal quality and showed less motion artefacts compared to lower frequency measurements. The results presented here are from the single measurement frequency of 120 kHz, as it was determined to be the most viable for future experiments, and with the author sitting in quiet resting position in the chair with armrests. Actual impedance values and their dependence from the electrodes and their placement is not the subject of the investigation here. Instead relationship between the base value of Z_0 and magnitude of the change $\Delta Z(t)$ on top of it is emphasized:

$$Z(t) = Z_0 + \Delta Z(t), \quad (1)$$

Question may rise regarding representativeness of Figure 3, since it is measured on a single person. It has been shown however by Camelia Gabriel in her reference work (together with colleagues from the Brooks Air Force Base (USA)) [17] that: “Biological tissues are inhomogeneous and show considerable variability in structure or composition and hence in dielectric properties. Such variations are natural and may be due to physiological processes or other functional requirements. The spread of values ranges from about $\pm 5\%$ above 100 MHz to $\pm 15\%$ at the lower end of the frequency scale.” Therefore, it is reasonable to assume that the variation is not larger than presented by C. Gabriel, and Figure 3, can be considered sufficient as it is only showing the scale of the problem and not exact values. Moreover, minimal change of the bioimpedance of 0.1% is assumed, which is very conservative compared to 0.5% in Figure 3 and is considered to have sufficient margin of five times compared to the worst-case deviation of $\pm 15\%$, i.e., max 30%. In the following sections it is often called “small change” instead of actual number.

4. Two Devices for Comparison

Several methods have been proposed to overcome these graphically presented difficulties. Simplest is capacitive AC decoupling in analogue domain. To minimize the distortion of the waveform of

roughly 1 Hz signal (which is typical heart beat frequency) the corner frequency of the high pass filter (HPF) must be substantially lower, which results in large time constant. Even though the described approach works rather well, it has a serious drawback very slow reaction to the possible large changes of the input signal. Such changes can easily appear due to the movement of the system. Ideally the final solution should be free of that kind of lag. The second method is used for the acquisition of the EBI signal during the ITK experiments in the clinical device CircMon BT101 (JR Medical OY, Tallinn, Estonia) (Figure 4)—the direct carrier compensation (DCC) [20] (Figure 5), where DDS is Direct Digital Synthesizer, μC is microcontroller, Comm denotes communication interface, in current case Universal Serial Bus (USB) together with Bluetooth low energy (BLE), LPF is Low Pass Filter, ADC is Analog to Digital Converter, V_{exc} is excitation voltage, I_{exc} is excitation current, V_{res} is response voltage, R_{ref} is current determining reference resistor, and UI is User Interface. DCC, while working very well, requires usage of several synchronized oscillators, which complicates the schematic, requires rather complex adjustment software and ultimately results in larger, more expensive device with higher energy consumption than optimal. DCC is acceptable for the medical device used in the clinical surroundings, but unobtrusive and pervasive monitoring of the cardiovascular system would certainly benefit from more streamlined solution. Another example of the complex multifunctional device for laboratory use is given in [21]. Multi-frequency instrument for simultaneous multisite EBI acquisition is described. Essentially high-speed sample by sample compensation is used. Again, method is good but not suitable for wearable electronics.

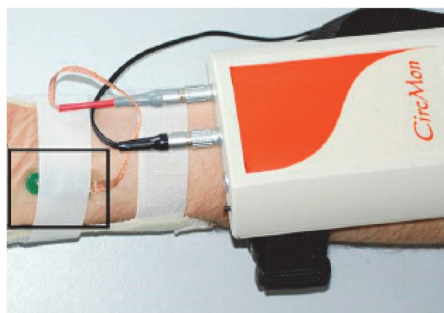


Figure 4. Noninvasive cardiovascular circulation monitor CircMon.

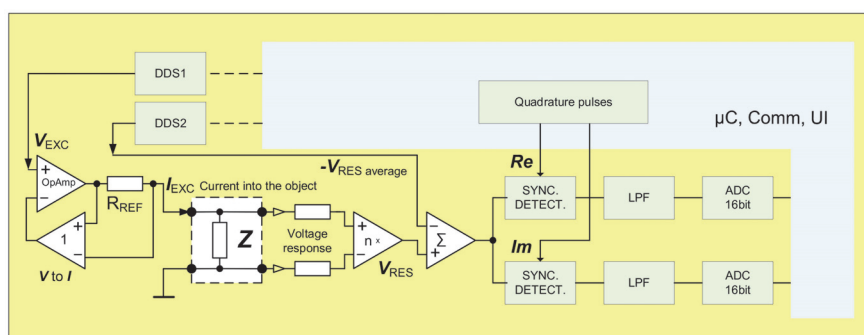


Figure 5. Block diagram of the EBI measurement device using direct carrier compensation method.

The second contender stepping up in current comparison between different methods was the “brute force device” with the best possible modern analog to digital converters (ADC) on board (Figure 6). Atmel AVR microcontroller XMEGA256, one of the latest 32-Bit Linear Technology Over-Sampling ADC’s the LTC2508-32 (Norwood, MA, USA), and the BLE Version 4.0 + radio module were used. Energy supply is from an on-board lithium-ion battery to minimize parasitic coupling issues. The

ADC has reasonably low noise and low power (for more information please refer to the datasheet of the used ADC), as well as integrated configurable digital filter, which enables immediate suppression of the unwanted disturbances. Digital synchronous demodulation is problematic due to the slow output data rate (3.9 kSa/s) of the converter, and limited computing power of the used microcontroller, and therefore analogue synchronous demodulators were used instead, as in the previous case of DCC. Therefore, the detection occurred in the analogue domain without the compensation. When compared to the DCC method, the multiplication in the analogue domain with following direct conversion does not have roughly 6–8 effective bits added to the nominal resolution of the digitizer (ADC). It was amply compensated with the double-up bit count of the following ADC. Both, real and imaginary quadrature channels were used in the previously described devices. Careful examination of the Figure 3a would suggest that the imaginary channel might be omitted, either by compensating the tiny phase error of roughly four degrees, or even ignoring it altogether, because the error introduced is not significant in the current application. That is exactly the path taken in design of following three competing novel solutions.

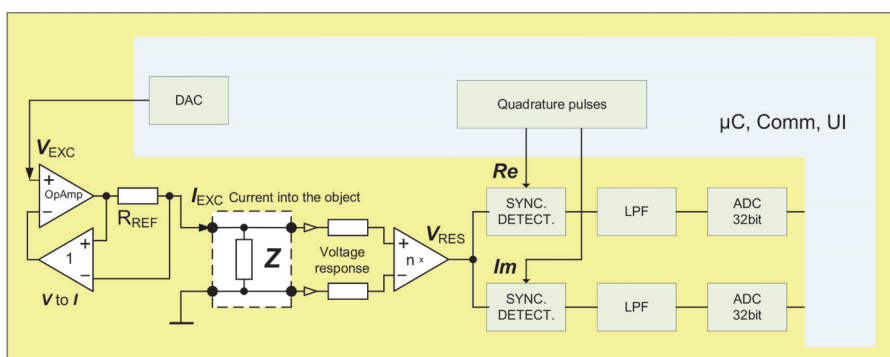


Figure 6. Main components of the “brute force device” using high resolution ADCs for detection of the EBI.

5. Three Novel Solutions, Materials, Methods, Preliminary Results and Discussion

Three different methods for the separation of the base value of the impedance from the time varying biomodulation were proposed, examined, simulated, and to a various extent prototyped. A common feature shared by all members of the group of the proposed solutions is differentiation. First, realization [22] is based on the calculation of differences between synchronously acquired consecutive samples. It has been shown that it is possible to demodulate the signal with simple additions and subtractions when using quadrature samples shown also on Figure 1. It has been described in several papers, but the most comprehensive overview is given in [21]. It was stated that the direct current (DC) component can be calculated as:

$$DC(i) = \frac{s(i,1) + s(i,3)}{2} = \frac{s(i,2) + s(i,4)}{2}. \quad (2)$$

The real and imaginary parts of the complex response signal (V) expresses impedance here could be computed according to:

$$Re(V(i)) = \frac{s(i,1) - s(i,3)}{2} \text{ and } Im(V(i)) = \frac{s(i,2) - s(i,4)}{2}. \quad (3)$$

And finally, the modulus and phase of the complex response signal V are found as:

$$|V(i)| = \sqrt{(ReV(i))^2 + (ImV(i))^2} \text{ and } \Phi(i) = \arctan \frac{ImV(i)}{ReV(i)}. \quad (4)$$

It is possible to decrease processing load and acquired samples even further by measuring only either positive or negative half period of I_mV and using calculated DC component in I_mV calculations:

$$I_mV(i) = (s(i,2)) - DC \text{ or } I_mV(i) = (s(i,4)) - DC. \quad (5)$$

In that case, only three measurements for the whole period are required in order to calculate the real and imaginary parts of the complex response signal.

In [21], the calculations were done in digital domain after conversion of the analog samples to their digital counterparts. These calculations can be done in analog domain when consecutive samples are held in separate sample and hold (SH) units, before they are finally quantized. The resulting R_eV , I_mV , and $|V|$ contain the sum of the base value and the modulation on top both, in analog and digital domain calculations. It becomes more interesting if we consider the actual DC shift to be equal to zero, which is easily achievable by high pass filtering the high frequency response signal, then Equation (2) will have entirely different meaning. Now, the calculated sums show the difference between the values of the samples, corresponding to real and imaginary parts of different half periods, or in fact it is equal to $\Delta V(i)$ for either, real part or imaginary part for that period. $\Delta X(t)/\Delta t$ when Δt is short enough can be viewed as derivative of the original response signal, hence the word differentiation in the description of the proposed three methods:

$$R_e\Delta V(i) = \frac{s(i,1) + s(i,3)}{2} \text{ and } I_m\Delta V(i) = \frac{s(i,2) + s(i,4)}{2}. \quad (6)$$

Removing DC shift simplifies sampling even further, in order to calculate response signal real and imaginary parts, only two samples per whole period is required. The differences can be calculated by using only samples belonging to either positive or negative half periods (Figure 7):

$$R_e\Delta V(i) = s(i,1) \text{ and } I_m\Delta V(i) = s(i,2). \quad (7)$$

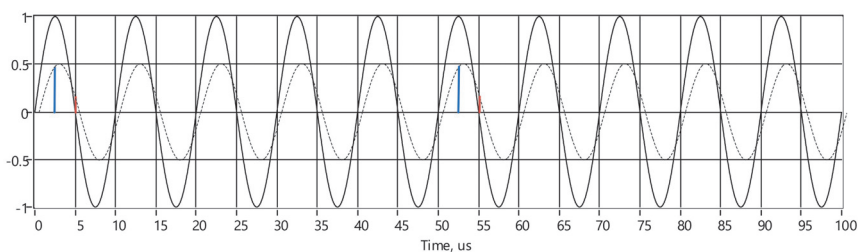


Figure 7. Down-sampling of the response signal using only positive half periods. Solid line is unity magnitude excitation current, dashed line is response voltage. Samples related to the $R_eV(i)$ and $I_mV(i)$ in blue color and red color respectively.

These differences can be calculated in many different ways leading to different realizations of the circuit. For example, prolonging the distance between two samples for integer number of whole periods can be considered, effectively resulting in slower sampling. Such an under-sampling may be beneficial for reduction of the energy required for sampling, and also when the sampling process has physical limitations due to cheaper components. The under-sampling rate is limited by the spectrum properties of the response signal. In usual bioimpedance measurement applications, the signal spectrum characteristics are related to the cardiovascular processes where signal spectral components are in kilohertz range. The under-sampling rate should satisfy Nyquist criteria and sampling rates over 2 kilo-samples per second are commonly sufficient. Compared to excitation signal frequency, sampling rates can be tens of times slower, which optimizes energy consumption and reduces the required computational power. Additionally excitation signal can be interrupted between sequential

sampling events that reduces power consumption even further. Obviously, transient processes must be taken into account between re-enabling excitation signal and acquiring next sample.

Device corresponding to first half of the Equation (6) is shown on Figure 8, where I_{EXC} ($+i_e$ and $-i_e$) is excitation current, V_{RES} is response voltage, DAC is Analog to Digital converter for excitation signal generation.

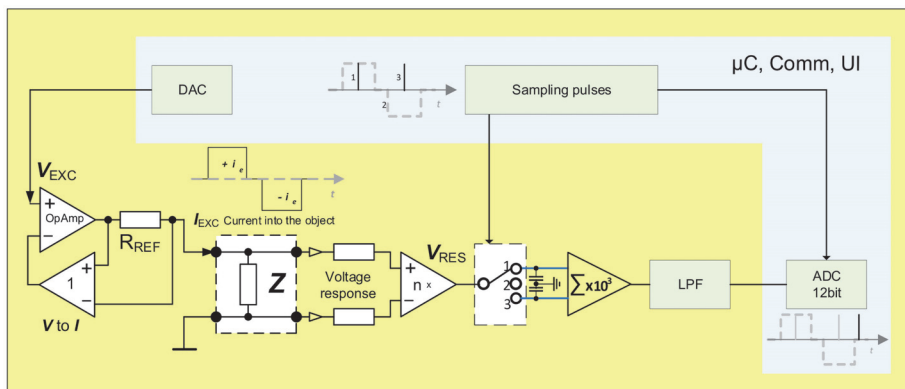


Figure 8. Simplified representation of the EBI measurement device with derivative sampling.

When proposing this realization, it is assumed that the phase angle of the impedance vector (shown on Figure 3a) is typically less than 4 degrees in case of excitation signal frequency of 120 kHz, and $R_e V(i)$ can be taken approximately equal to $|V(i)|$, without introducing large errors, at the same time considerably simplifying the physical realization of the device, (Figure 9).

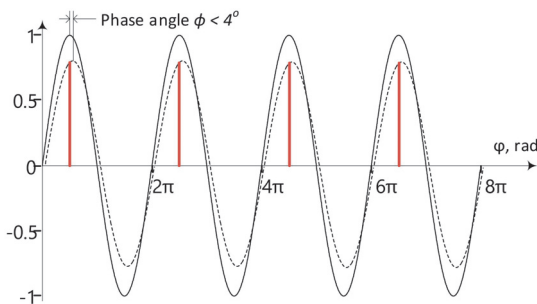


Figure 9. Sampling $|V(i)|$ in case of small phase angle of the impedance vector using only positive half periods. Solid line is unity magnitude excitation current, dashed line is response voltage. Samples related to the $R_e V(i)$ are in red color.

Maximum error introduced by discarding imaginary part of the response can be found as ratio of the modulus of the complex response signal to the real part.

Modulus of the complex response signal V is:

$$|V| = \sqrt{I^2 + Q^2}. \tag{8}$$

As real and imaginary components of the complex signal are:

$$I = R_e V = |V| \cdot \sin(\varphi) \text{ and } Q = I_m V = |V| \cdot \cos(\varphi). \tag{9}$$

It can be shown that:

$$\frac{V}{R_e V} = \sqrt{1 + (\tan(\varphi))^2}. \quad (10)$$

Estimated measurement error introduced by sampling only $R_e V$ in that case based on Equation (10) is approximately 0.24% (Figure 10). Actual response can also be easily calculated as:

$$|V| = \sqrt{R_e V^2}. \quad (11)$$

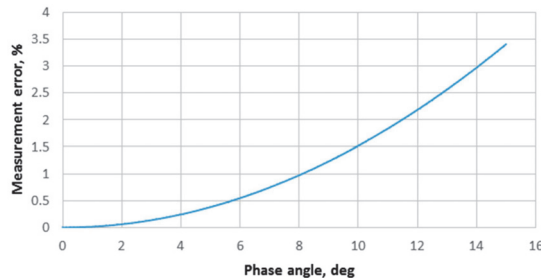


Figure 10. Measurement error compared to phase angle of the impedance vector.

Actual $R_e V(i)$ can be easily measured and calculated (3) and gives very good indications regarding the quality of the electrode attachment to the body. Why is the calculation of the $R_e \Delta V(i)$ more beneficial than direct calculation of the $R_e V(i)$? There is no real benefit, if the calculations are done entirely in digital domain. If the difference between consecutive samples is calculated in analog domain, things change considerably. Now, we need to digitize only tiny variations separately from large base value. Furthermore, these tiny variations are randomly around common mean, which is determined mainly by the omnipresent noise. It means that relatively slow variations in measured impedance caused by the biological processes, at least when compared to the fast-changing excitation signal, will not show up. Even large artifacts will disappear due to tiny change in short time window. Method has been extensively simulated in the LabView environment with convincingly good results [22] (Figure 11). Derivative sampling circuits can be made from discrete components, but more importantly they are easily integrated when purpose-made silicon is designed. As it is seen on the Figure 8 the differential sampling solution performs well, with or without an additive noise, even if only 12-bit converter is used. The 12-bit resolution was chosen for comparison, because many microcontrollers and digital signal processors (DSP) have similar ADC's.

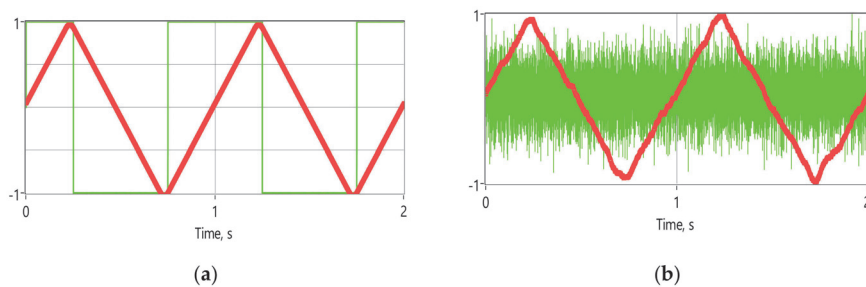


Figure 11. Normalized results of the differential sampling solution: without added noise (a), and the same signals with 0.1 mV noise added (typical situation during EBI acquisition) (b); all the curves are normalized for better readability.

In Figure 11, a carrier of 1 V amplitude is modulated by 0.1 mV and 1 Hz triangle wave. Normalized results are depicted as follows: A narrow green line square wave (normalized to unity magnitude) represents the calculated differences between adjacent samples, a bold red is normalized result of the 12-bit conversion of the differences integrated afterwards digitally. Note that the actual impedance modulation signal is fully restored, even while the derivative square wave has totally disappeared into the noise on Figure 11b.

There is also related patent application in process [23], which considers also an extension to the described method. The general sampling process acquires the value of the original signal plus some additive noise at the sampling point. Mathematically, the sampling instance is considered infinitely short in time. Immediately, it appears impossible to acquire samples in the described manner in real life. Instead of finite length sampling instances are present, typically very short, compared to the period of the maximum frequency component of the signal to be sampled, and at least twice faster than mentioned period according to well-known Witteraker-Kotelnikov-Shannon (WKS) sampling theorem. Naturally, the question may arise of what happens if we prolong the sampling instance? Real samplers obviously require some time to take the sample and settle afterwards, and therefore, have so-called aperture errors [24]. The sampler integrates the incoming signal to be sampled short while during, and after, the sampling pulse, as the sampling switch cannot change its state instantly. Generally, these aperture errors are considered harmful and should be minimized. From the other side, this integration can be viewed as filtering operation, which could help to improve the achievable signal to noise ratio (SNR).

That, in turn, brought up the idea of further investigating the performance of the system, when infinitely short samples are replaced with half-period integrals instead. Here, the answer is considered only in limited case of synchronous sampling, which is locked-in to the periodic excitation signal [25]. The basic principle can be seen on Figure 12. Modulation with linear ramp $a \cdot t$, where a is arbitrary constant and t is time, is considered for simplicity of the discussion.

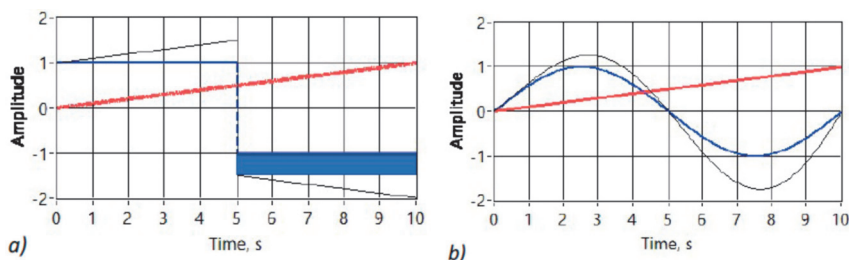


Figure 12. Synchronously integrating AM detection, when the carrier is square wave (a), and when the carrier is sinusoidal (b). Carrier is modulated in both cases with linearly growing ramp. Unmodulated carrier is wider blue line, modulated carrier is narrow black line, and modulating signal wide red.

That simplification seems to be valid, if we consider very slowly varying biomodulation (few Hz, with relevant bandwidth of the signal up to some hundred Hz) and compare it with relatively fast excitation (120 kHz excitation in current case of the EBI acquisition) signal. The case of the square wave carrier is easier to comprehend visually. As it can be seen in the Figure, the net integral over the full carrier period is zero, if the carrier is not changing during that time. Yet, one of the half periods has higher magnitude than the other when modulation of the carrier is present. A dark rectangle in Figure 12a) shows the difference in the area under the curve resulting in the integral being not zero anymore. Two parameters contribute to the changing area: Known and constant period of the carrier and the slope of the modulating signal. Slope of any linear function is equal to the derivative of this function. Visible dark rectangle, or the integral taken synchronously over the full period (or multiple periods) of the excitation signal is therefore linearly related to the derivative a of the modulating signal $a \cdot t$. More precisely, the negative value of the slope of the modulating signal ($-a$) must be considered.

It can be shown mathematically that the result is also valid for the sinusoidal excitation, which is modulated with linearly rising ramp $a \cdot t$ (12) (Figure 12b):

$$\int a \cdot x \cdot \sin(x) dx = a \cdot \sin(x) - a \cdot x \cdot \cos(x) + C. \quad (12)$$

When Equation (12) is evaluated over the full period from 0 to 2π the result will be the same $-a$. If x is replaced with more typical $\omega \cdot t$, where $\omega = 2\pi \cdot f$, and $f = 1/T$, where ω is angular frequency in rad/s, f is frequency in 1/s or Hz, and T is period in s, then there is additional constant scale factor $T^2/2\pi$ to be considered. As the result of the synchronous integration is linearly related to the derivative of the biomodulation of the EBI it can be restored with integration if required. The main benefit of the described method is in the automatic exclusion of the base value from the result due to differentiation. Given that the signal to be digitized is now only the slow biomodulation the ADC can be slower and with fewer bits than in the previous solution. Again, the method has been extensively studied in the LabView environment with convincingly good results [26] (Figure 13).

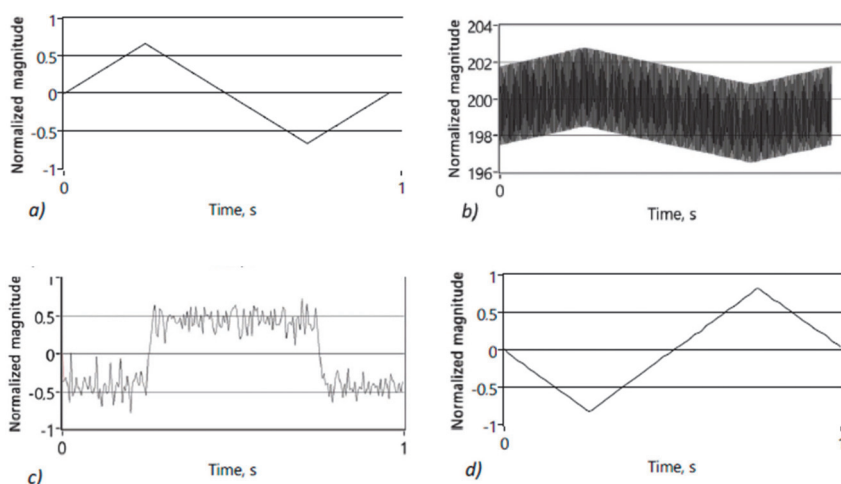


Figure 13. Modulating signal (a), signal after lock-in detector (b), synchronously integrated signal (c), signal after final integration (d). All signals are normalized for the sake of clarity. Please note that (d) is mirrored image of original (a), as predicted mathematically.

The “derivative peak-detectors” suffer from negative side effects. The peak detection is sensitive to all components of the detectable signals, i.e., it is not selective in the frequency domain. The user of the peak detection must be aware of the unwanted additive components or noise. The situation can be improved when pre-filtering of the acquired signal is used, as it considerably reduces the impact of possible additive disturbance. Since synchronous phase sensitive measurements are required the filter should be tuned exactly without any phase variations. A typical RLC filter is not suitable here, due to large variations. Instead synchronous lock-in filtering has to be used [25]. It serves the narrow band pass filter with rock stable parameters, and as a side effect gives the base impedance value, which is useful as an indicator for the quality of the electrode attachment. Many different realizations have been proposed, such as by Märtens [27]. Both presented solutions have something in common, the need for fast synchronized polyphase switches. It is easily achievable, when using application specific integrated circuit (ASIC) realizations of the principle, but harder to achieve with standard components.

The third derivative detector t is much simpler, yet performs very well (Figure 14):

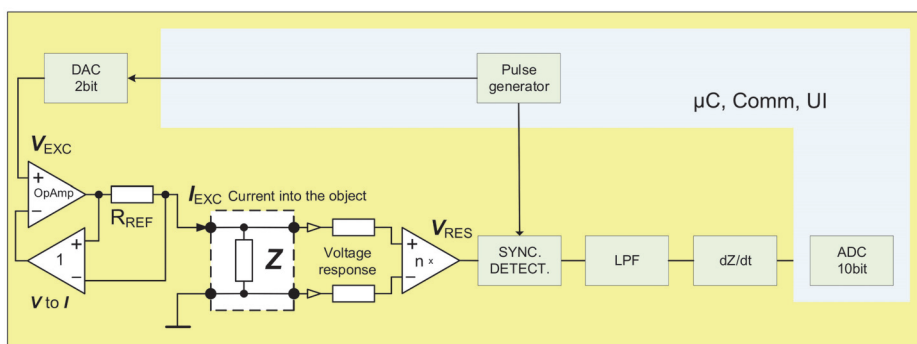


Figure 14. Simplified schematic of the EBI measurement device using filtering for derivation.

The block diagram is like the solution on Figure 6. It is also similar to the solution used in [19], with one major difference. Analog derivation is used over the frequency range of interest instead of having analog low pass filter at 0.1 Hz. While, the low pass filter has an inherently long settling time, in seconds, as it has been described also in number of other publications describing similar items, the derivative approach settles in milliseconds. It is crucial when wearable implementation is used during normal everyday activity instead of static sitting or lying position. The major difference is in the block of dZ/dt . The device uses same AVR ATXMEGA microcontroller, together with BLE 4.0 + module as on Figure 6, internal rather noisy low quality 10-bit ADC was used instead of high quality external 32-bit ADC. The quality of the solution is visible on the Figure 15, representing actual waveform acquired on top of the radial artery without any additional filtering or processing. It is quite clear and a good quality signal. dZ/dt in this case is achieved with simple high pass filtering, as discussed also earlier, but with much higher corner frequency, so that in the frequency range of the bioimpedance modulation caused by the beating heart the frequency response is rising 20 dB/dec, which is effectively equal to the mathematical derivative dZ/dt . Presented derivative detector was able to resolve impedance changes as small as 4 m Ω (ADC resolution 1 m Ω /LSB), which is in the range of 1% of impedance change caused by cardiac activity. Blue curve of the Figure 15 represents derivative signal caused by impedance change of approximately 300 m Ω . Picture of the demonstrator device is visible on Figure 16.

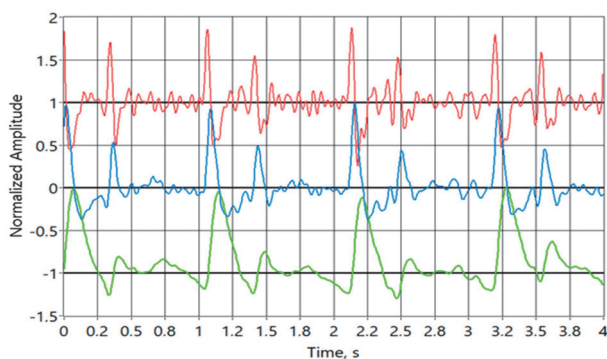


Figure 15. Bioimpedance signal, acquired with derivative technology, shown on Figure 11. All curves are normalized. Blue curve in the middle is the actual signal from the device, i.e., first derivative of the bioimpedance signal, upper red curve is second derivative of the bioimpedance signal shifted up by 1 unit, and lower green curve is integral of the incoming signal shifted down by 1 unit. It is also the actual bioimpedance signal.

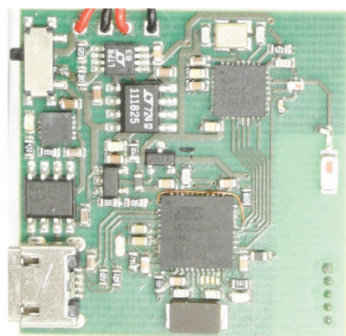


Figure 16. Image of the actual 10-Bit derivative bioimpedance acquisition system prototype.

Proposed derivative detector has several advantages compared to “Brute Force” and “Carrier Compensation” DCC method—it uses simpler hardware, has lower power consumption and requires less computational power. A comparison of the three different solutions is shown in Table 2.

Table 2. Comparison of the three different acquisition methods described.

Method	ADC Resolution	Excitation Signal Generation	Computational Power	Power Consumption	HW Complexity
DCC	16 bit	DDSx2	Medium	Hi	Hi
Brute Force	32 bit	Multibit DAC for sinusoidal signal	Hi	Medium	Medium
Derivative	10 bit	2 bit DAC for ternary signal	Low	Low	Low

6. Conclusions

Three derivative requiring methods for the EBI acquisition are presented. First two have been simulated in LabView environment with good results. The prototypes are being built and the last version is ready-made and tested. Differentiation implies improvement in the dynamic range of the useful signal at the input of ADC, as the variations can be 1000 times smaller than the whole measured value. Results show that the internal 10-bit analog-to-digital converter (ADC) of microcontroller is enough to achieve the signal quality, which is comparable to the one of the more complicated brute force device with 32-bit ADC's. The difference is that the output signal is the derivative of the measured EBI. While the original EBI signal can be restored relatively easily (Figure 15), it is not mandatory as many calculations, based on the acquired signals, require derivation before further indices can be calculated.

All three derivative solutions for acquisition of the EBI signal are believed to be novel and patentable. Very good results are obtainable when used together with lock-in filtering. They are key enablers for the design of simple analog front ends for pervasive EBI acquisition with enhanced protection against artefacts. The requirements for the ADC used after detection circuitry can be substantially relaxed. The current paper is focused only on the methods and basic technology research. In terms of technology readiness levels (TRLs) it ends before TRL 3. The actual prototypes for technology demonstration belonging to TRL 5 are currently being built and tested in the frames of commercial agreement.

Author Contributions: Conceptualization, P.A.; methodology, E.P., P.A.; software, E.P., A.K. and R.L.; validation, E.P., P.A., A.K. and R.L.; formal analysis, E.P., P.A. and R.L.; investigation, E.P. and P.A.; resources, O.M. and M.M.; data curation, E.P., P.A., A.K. and R.L.; writing—original draft preparation, P.A. and E.P.; writing—review and editing, E.P., P.A., A.K., R.L., M.R. and O.M.; visualization, E.P., P.A., A.K., M.R. and R.L.; supervision, P.A. and M.M.; project administration, P.A.; funding acquisition, M.M., O.M. and P.A. All authors have read and agreed to the published version of the manuscript.

Acknowledgments: The research was supported by Estonian Research Council grants IUT1911, PRG737 and EAG34 and by European Regional Development Fund in frames of the Estonian ICT Center EXCITE. Partly

also by the EU project H2020-2014-2-668995-Cognitive Electronics and Estonian Research Council Mobilitas+ grant Mobera20 for Chist-ERA JEDAI project. This work in the project “ICT programme” was supported by the Eu-ropean Union through European Social Fund”.

Conflicts of Interest: The authors declare no conflict of interest.

References

1. Roguin, A. Scipione Riva-Rocci and the men behind the mercury sphygmomanometer. *Int. J. Clin. Pract.* **2006**, *60*, 73–79. [CrossRef] [PubMed]
2. Ando, S. What does a perfect blood pressure meter look like from a clinician point of view? *IEEE Instrum. Meas. Mag.* **2014**, *17*, 15–20. [CrossRef]
3. AtCor Medical-SphygmoCor CVMS. Available online: http://www.atcormedical.com.au/sphygmocor_cvms.php (accessed on 15 April 2019).
4. Nelson, M.R.; Stepanek, J.; Cevette, M.; Covalciuc, M.; Hurst, R.T.; Tajik, A.J. Noninvasive Measurement of Central Vascular Pressures with Arterial Tonometry: Clinical Revival of the Pulse Pressure Waveform? *Mayo Clin. Proc.* **2010**, *85*, 460–472. [CrossRef] [PubMed]
5. Chen, Z.; Yang, X.; Teo, J.T.; Ng, S.H. Noninvasive monitoring of blood pressure using optical Ballistocardiography and Photoplethysmograph approaches. In Proceedings of the 2013 35th Annual International Conference of the IEEE Engineering in Medicine and Biology Society (EMBC), Osaka, Japan, 3–7 July 2013; pp. 2425–2428.
6. Grimnes, S.; Martinsen, Ø.G. *Bioimpedance and Bioelectricity Basics*; Elsevier: Boston, MA, USA, 2014; ISBN 978-0-12-411470-8.
7. Malmivuo, J.; Plonsey, R. *Bioelectromagnetism: Principles and Applications of Bioelectric and Biomagnetic Fields*; Oxford University Press: Oxford, UK, 1995; ISBN 978-0-19-984783-9.
8. Min, M.; Annus, P.; Koiv, H.; Krivosei, A.; Uuetoa, T.; Lamp, J. Bioimpedance sensing—a viable alternative for tonometry in non-invasive assessment of central aortic pressure. In Proceedings of the 2017 IEEE International Symposium on Medical Measurements and Applications (MeMeA), Rochester, MN, USA, 7–10 May 2017; pp. 373–378.
9. Herscovici, H.; Roller, D.H. Noninvasive Determination of Central Blood Pressure by Impedance Plethysmography. *IEEE Trans. Biomed. Eng.* **1986**, *6*, 617–625. [CrossRef] [PubMed]
10. Hatschek, R.A. Blood Pressure Measuring Device and Method. U.S. Patent No. 5,309,916, 10 May 1994.
11. Solà, J.; Adler, A.; Santos, A.; Tusman, G.; Sipmann, F.S.; Bohm, S.H. Non-invasive monitoring of central blood pressure by electrical impedance tomography: First experimental evidence. *Med. Biol. Eng. Comput.* **2011**, *49*, 409–415. [CrossRef]
12. Schreiner, S.; Bronzino, J.D.; Peterson, D.R. *Medical Instruments and Devices: Principles and Practices*; CRC Press: Boca Raton, FL, USA, 2015; ISBN 978-1-4398-7147-8.
13. Malmivuo, J. Principle of reciprocity solves the most important problems in bioimpedance and in general in bioelectromagnetism. *J. Phys. Conf. Ser.* **2010**, *224*, 012001. [CrossRef]
14. Min, M.; Parve, T.; Annus, P.; Paavle, T. A Method of Synchronous Sampling in Multifrequency Bioimpedance Measurements. In Proceedings of the 2006 IEEE Instrumentation and Measurement Technology Conference Proceedings, Sorrento, Italy, 24–27 April 2006; pp. 1699–1703.
15. Kõiv, H.; Rist, M.; Min, M. Development of bioimpedance sensing device for wearable monitoring of the aortic blood pressure curve. *Tm-Tech. Mess.* **2018**, *85*, 366–377. [CrossRef]
16. Bosy-Westphal, A.; Danielzik, S.; Dörhöfer, R.-P.; Later, W.; Wiese, S.; Müller, M.J. Phase Angle from Bioelectrical Impedance Analysis: Population Reference Values by Age, Sex, and Body Mass Index. *J. Parenter. Enter. Nutr.* **2006**, *30*, 309–316. [CrossRef] [PubMed]
17. Gabriel, C. Compilation of the Dielectric Properties of Body Tissues at RF and Microwave Frequencies, King’s College London. 1996. Available online: <https://apps.dtic.mil/docs/citations/ADA303903> (accessed on 17 February 2020).
18. Dittmar, M. Reliability and variability of bioimpedance measures in normal adults: Effects of age, gender, and body mass. *Am. J. Phys. Anthropol.* **2003**, *122*, 361–370. [CrossRef] [PubMed]
19. Huynh, T.; Jafari, R.; Chung, W.-Y. An Accurate Bioimpedance Measurement System for Blood Pressure Monitoring. *Sensors* **2018**, *18*, 2095. [CrossRef] [PubMed]

20. Annus, P.; Lamp, J.; Min, M.; Paavle, T. Design of a bioimpedance measurement system using direct carrier compensation. In Proceedings of the 2005 European Conference on Circuit Theory and Design, Cork, Ireland, 2 September 2005; pp. 23–26.
21. Min, M.; Parve, T.; Ronk, A.; Annus, P.; Paavle, T. Synchronous Sampling and Demodulation in an Instrument for Multifrequency Bioimpedance Measurement. *IEEE Trans. Instrum. Meas.* **2007**, *56*, 1365–1372. [[CrossRef](#)]
22. Annus, P.; Land, R.; Priidel, E.; Metshein, M.; Min, M.; Märten, O. Quantization of the response signal differences for the electrical bioimpedance measurement. In *EMBECE & NBC 2017*; Eskola, H., Väisänen, O., Viik, J., Hyttinen, J., Eds.; Springer: Singapore, 2018; Volume 65, pp. 290–293. ISBN 978-981-10-5121-0.
23. Annus, P.; Min, M.; Land, R.; Märten, O.; Priidel, E.; Metshein, M. Method and Device for Quantization of the Response Signal Differences during Synchronous Measurements, Patent. 2017. Available online: https://patentscope.wipo.int/search/en/detail.jsf?docId=EE236485554&_cid=P10-K4LYWP-55374-5 (accessed on 17 February 2020).
24. Kester, W.; Engineeri, A.D.I. *Data Conversion Handbook*; Elsevier: Boston, MA, USA, 2005; ISBN 978-0-7506-7841-4.
25. Meade, M.L. *Lock-in Amplifiers: Principles and Applications*; Peter Peregrinus Ltd.: London, UK, 1983; ISBN 0906048-94-X.
26. Priidel, E.; Annus, P.; Metshein, M.; Land, R.; Märten, O.; Min, M. Lock-in integration for detection of tiny bioimpedance variations. In Proceedings of the 2018 16th Biennial Baltic Electronics Conference (BEC), Tallinn, Estonia, 8–10 October 2018; pp. 1–4.
27. Märten, O. Precise synchronous detectors with improved dynamic reserve. *IEEE Trans. Instrum. Meas.* **2000**, *49*, 1046–1049. [[CrossRef](#)]



© 2020 by the authors. Licensee MDPI, Basel, Switzerland. This article is an open access article distributed under the terms and conditions of the Creative Commons Attribution (CC BY) license (<http://creativecommons.org/licenses/by/4.0/>).

Appendix 6

Publication VI

Priidel, Eiko; Min, Mart; Pesti, Ksenija; Ojarand, Jaan; Märten, Olev (2021). FPGA-based 16-bit 20MHz device for the inductive measurement of electrical bioimpedance. International Instrumentation and Measurement Technology Conference (IEEE I2MTC2021), Glasgow, Scotland, May 17-20, 2021, 1–5. DOI: [10.1109/I2MTC50364.2021.9460073](https://doi.org/10.1109/I2MTC50364.2021.9460073).

FPGA-based 16-bit 20 MHz device for the inductive measurement of electrical bio-impedance

Eiko Priidel, Ksenija Pesti, Mart Min, *Life Senior Member, IEEE*,
Jaan Ojarand, *Senior Member, IEEE*, Olev Martens, *Senior Member, IEEE*

T J Seebeck Department of Electronics
Tallinn University of Technology,
Ehitajate tee 5, Tallinn, 19086, Estonia
Email: eiko.priidel@taltech.ee

Abstract—A novel FPGA based 16-bit 20 MHz real-time electrical impedance measurement device has been developed. While such device can have several applications, then one of the purposes is to measure and monitor the human cardio-respiratory activity signals by inductive magnetic induction based coupling, where a fine resolution in relatively high frequency range is needed. As such a small form-factor device with affordable price and low power consumption is not commercially available, for wearable personal healthcare, the first prototype of such instrumentation device was developed. The solution uses the Altera Max10 FPGA and the external fast operating 16-bit analog-to-digital and digital-to-analog converters (ADC and DAC) with complementary analog components for signal generation, conditioning and handling. The WiFi data communication is based on a separate ESP8285 chip. The overall solution was tested in the frequency range of analog signals up to 20 MHz, getting 4000 measurement results during every second, what is certainly enough for the real-time presenting of impedance waveforms of such physiological processes as breathing and heart beating.

I. INTRODUCTION

Electrical impedance characterizes the properties of different materials, structures and processes as composition of metals, structures of materials, electro-chemical reactions as corrosion etc. [1]. Electrical bio-impedance (EBI) is the electrical impedance of biological matter, describing living biological materials (cells, tissues, organs) and such the physiological processes as breathing, heart beating, flowing of blood and tissue oxygenation. In summary, electrical bio-impedance allows to measure and analyze the cardiopulmonary and vascular dynamics, which are the most necessary physiological processes for medical diagnosing of human health [2]. To avoid serious electrode problems and reduce artefacts, the non-contact sensing methods are of interest [3] by using both capacitive and inductive coupling.

An important application of the impedance is monitoring of the hemodynamics of the person. One specific application could be impedance cardiography (ICG[4]), but more generally, monitoring of cardiac and respiratory data [5].

Impedance of the chest and head can be measured not only by electrically conductive electrodes placed on the body,

but also by using inductive (magnetic induction) coupling [6], enabling not only cardiovascular but also respiratory monitoring [7]. Compared to the measurement of metals, where the limited by the frequency - depth of penetration of the electromagnetic field suits for investigation of corrosion and the coating's depth [8], higher frequencies are preferred. E.g., 10 MHz instead of 100 kHz is used to obtain information on the β dispersion part of the body impedance and reduce the electrodes' series capacitance impact.

High frequency measurements are similarly preferable in many other cases and the developed instrumentation given in Fig. 1 is required more widely than in the bio-impedance measurement cases described above.

A. Existing solutions for impedance measurement

Well-known are the impedance measurement solutions based on using the single-chip integrated circuit AD5933 of Analog Devices Inc [9]. Such the solutions have both limited bandwidth (100 kHz) and also limited resolution because of only 12-bit analog-to-digital converter (ADC) in the input of it digital processing part. Though some DSP-based solutions for multifrequency impedance measurement devices have been developed [10], [11] in participation of authors of the present paper, these are not suitable for wearable devices by size, resolution, frequency range and cost limitations. There exist also high-resolution inductive impedance converter chips [12] of Texas Instruments, which can be considered for some applications, but the limited frequency range and required adaptive adjustment of the measurement range make them use almost impossible for higher precision measurements in the current task. Several bulky desktop impedance analyzers are available from Wayne Kerr [13] and Agilent and similar, for example, which are not applicable due to their cost and size, but mostly because of inability for real-time measurements.

II. PROPOSED SOLUTION

The block diagram in Fig. 1 depicts the proposed solution based on using the digital signal processing and synthesis

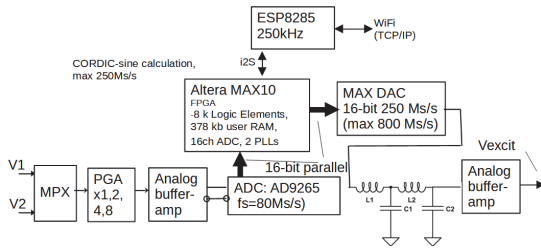


Fig. 1. Block diagram of the proposed solution

by the aid of field programmable gate array (FPGA) Altera MAX10. Analog signals are digitized by the aid of the 16-bit analog-to-digital converter (ADC) AD9265 from Analog Devices, and generated (synthesized) by using the 16-bit digital-to-analog converter MAX DAC. Input and output analog interfaces contain amplifiers, filters and a multiplexer at the input. A special integrated circuit ESP (8226) serves for wireless data communication (WiFi) with a standard computer.

A. Key components

The device includes the following electronic components:

- FPGA - Altera MAX 10 (*MAX10M16SAU169*), featured by the dual configuration flash memory, analog blocks (not used in the current project), DSP-blocks (including 18x18 bit multipliers), complex control management, single-core voltage support, user flash memory;
- Analog-to-digital converter (ADC) - AD 9265, featured by 16-Bit resolution, up to 125 MSPS sample-rate (utilized at 80 Ms/s in the current project);
- MUX: AD8184 (*700 MHz, 5 mA 4-to-1 Video Multiplexer*);
- PGA: THS7001 (*70-MHz High-Speed Programmable-Gain Amplifier, with max gain 20 dB*);
- AD8130, an ADC input driver buffer (*Low Cost 270 MHz Differential Receiver Amplifier*);
- Digital-to-analog converter (DAC): MAX5891, 16-Bit resolution, up to 600 MSPS sample-rate (utilized at 80 Ms/s in the current project);
- THS3215, DAC output driver buffer (*DC to 650-MHz, Differential-to-Single-Ended, DAC Output Amplifier*);
- The ESP8285 is a low-cost Wi-Fi microchip, with a full TCP/IP stack.

The ADC and DAC are connected to the FPGA by separate synchronous parallel 16-bit buses, giving the 80Ms/s data rates. The ESP8285 chip connected to the main FPGA by the I²S bus.

B. Algorithms used

Generation of sine/cosine waves (as excitation signal and as reference waveforms) for the Discrete Fourier Transform (DFT) is done by using of the CORDIC algorithm (COordinate

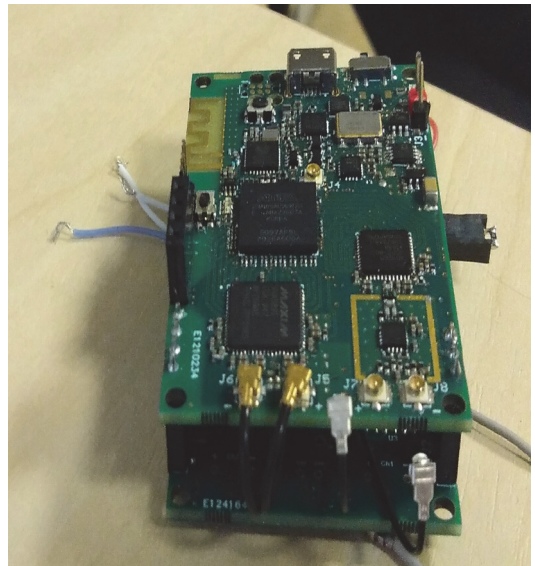


Fig. 2. Photo of the prototyped device

Rotation Digital Computer), known also as Volder's or "shift-and-add" algorithm [14].

C. Overall algorithm description

The overall impedance measurement consists of the following steps:

- The FPGA generates the excitation sinewave 2 V peak-to-peak amplitude and frequency from 100 kHz to 20 MHz;
- The excitation signal passes the circuit of series connected resistor $R=1K\Omega$ and unknown complex impedance $\tilde{Z}x$;
- Beside the sine wave, the chirp waveform signals can be synthesized for both, excitation and reference waveforms for performing Fourier analysis as proposed in the patented solution [15]. As a result, the spectral analysis of unknown impedances becomes possible.

III. APPLICATION EXAMPLE

In Fig. 3 it is given a schematic diagram for evaluation of functioning of human cardiopulmonary through simultaneous measurement of impedance variation of lungs, heart and vascular system of hand. The magnetic method is used for generating the induced measurement current i_i in the wrist by a generator G, incorporated in the prototyped measurement device (see Fig. 1 and 2) as a DAC based synthesizer of a magnetizing electrical current i_m . The induced current flow i_i passes through the hand and conductive belt and closes through both heart and lungs.

Fig. 3 and 4 demonstrate the work of inductive sensor in more detail. Magnetizing current $i_m = 10$ mA flows through

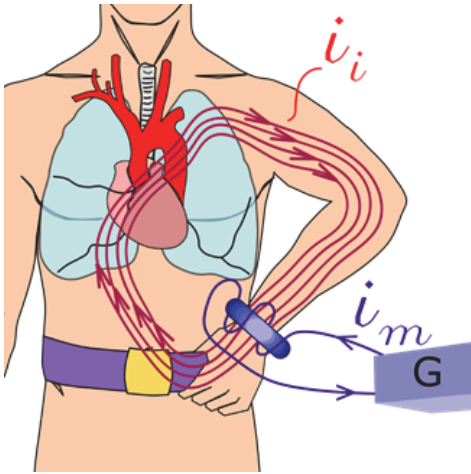


Fig. 3. Experimental evaluation of the cardiopulmonary system

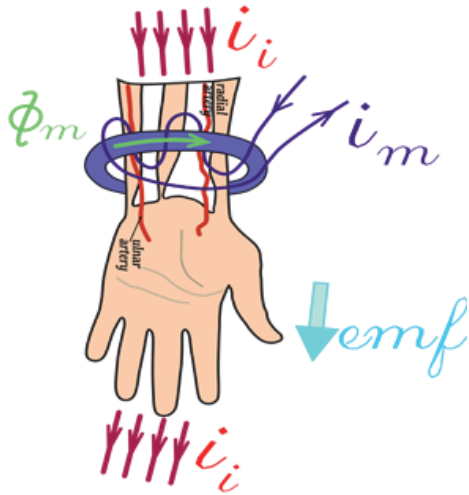


Fig. 4. Current density lines in case of the distal four-electrode placement

the coil winding ($N = 10$ turns) of a toroidal magnetic ring (flexible material, $\mu = 20$) and creates a magnetic induction Φ_m inside the magnetic ring. In turn, the magnetic induction Φ_m induces an electromotive force emf , which generates the inductive i_i , the level of which depends inversely on the impedance Z of the closed current circuit.

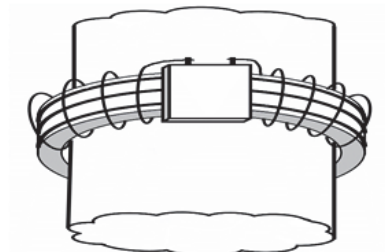
Construction of the toroidal magnetic coil is given in Fig. 5.

Breathing and heart beating together with blood flow modulate the impedance Z . Impedance modulation results in the output voltage of the device as illustrated in Fig. 6.

The acquired waveform of breathing satisfies the best

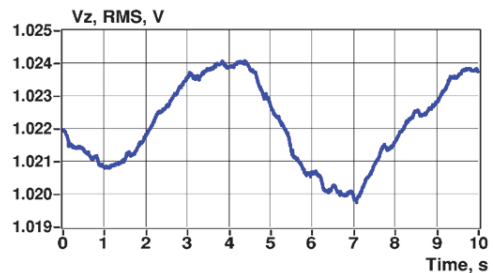


(a)

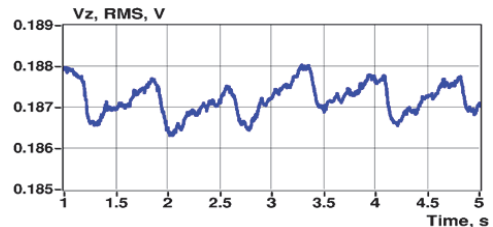


(b)

Fig. 5. Construction of the toroidal magnetic coil: a prototype (a) and principles of the design (b)



(a)



(b)

Fig. 6. Impedance caused demodulated waveforms of breathing (a) and heart beating (b) acquired with the prototyped device

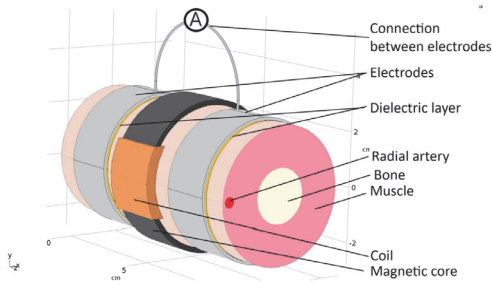


Fig. 7. Schematics of the sensor for sensing cardiac activities

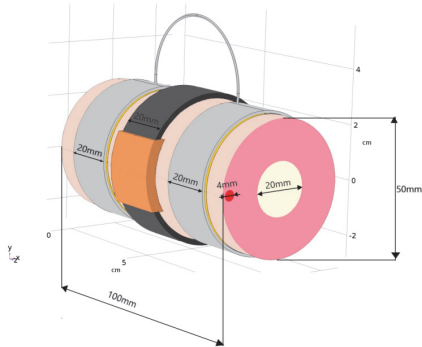


Fig. 8. Geometric data of the sensor model given in the previous figure

expectations, but heart-beating response in composite waveform remains too low and contains disturbances.

To overcome the problems, the following sensor schemes were proposed in Fig. 7 and 8 for sensor solutions.

In Fig. 7, the sensor model is supplemented with two capacitive electrodes connected with each other through a wire connection directly, not via body. Fig. 8 gives us the geometric data of the sensor. This enables us to measure the blood pulsation in the wrist area without taking into account other part of the body. Moreover, the capacitances of supplemented electrodes and inductance of the coil were tuned to have a serial resonance at the frequency of 10 MHz to measure the loss resistance directly.

The results show the modulation due to heart-beating $\Delta Z(t)$ up to 0.3% of basal value Z . Simulations using COMSOL Multiphysics software were carried out. The results in the form of magnet flux density and induced current density are given in the Fig. 9 and 10. The effect of electromagnetic induction penetrates about up to 5 mm into the wrist tissue (Fig. 9). There it induces the electromotive force emf (Fig. 4), which generates the induced current ii , inversely proportional to the tissue impedance Z . Distribution of the density of induced current ii shows clear concentration into the radial artery

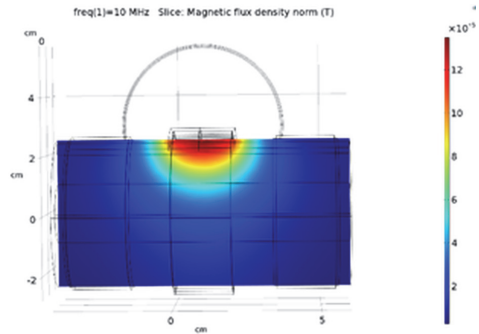


Fig. 9. Simulation results: distribution of the magnetic flux density

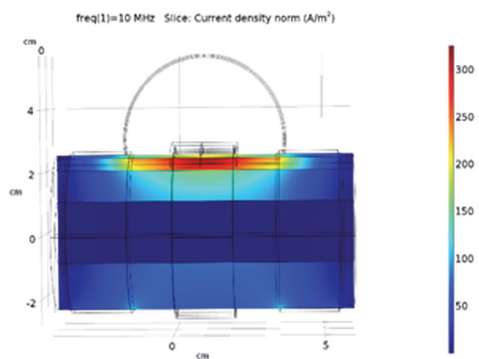


Fig. 10. Simulation results: distribution of the induced current density

because of a concentration of the electromotive force in this area, but mostly due to the fact that the electrical conductivity of blood is about three time higher than of surrounding tissues.

IV. RESULTS

The developed FPGA based impedance measurement electronics works, as expected. The evaluation showed the following results:

- resolution of the final impedance - better than 0.01%;
- full analog bandwidth of the system 60MHz;
- analog bandwidth for precise measurement to 30 MHz;
- signal-to-noise ratio: 80 dB (total measurement tract);
- noise level $40 \mu V$ in the whole bandwidth.

For evaluation, the purity of the output sinewave (generated by CORDIC algorithm) was tested at 1MHz, where the distortion and noise level is around $10 \mu V$ -better than 0.01% of the fullscale (Fig. 11). Also, the full (DAC - ADC) channel was independently tested (Fig. 12), showing still some nonlinearity on the 0.01% to 0.1% level, which is very reasonable result, as the harmonics are not giving any direct measurement error (except if multiple frequencies used simultaneously and the measurement frequencies are badly selected).

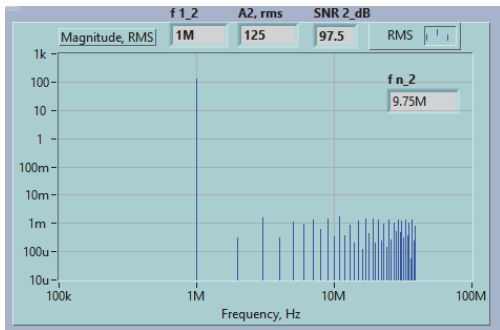


Fig. 11. Spectra of the output sinewave (showing harmonics and noise)

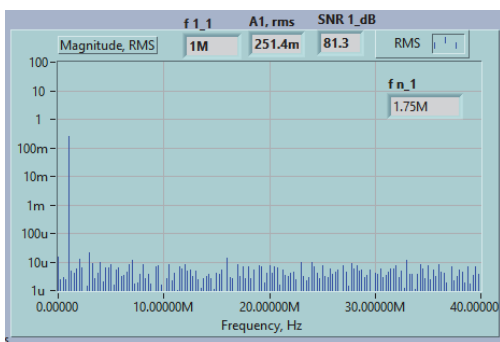


Fig. 12. Spectra of the input sinewave (total channel, showing harmonics and noise)

V. CONCLUSION AND FUTURE WORK

The dedicated device for inductive measurements of the conductivity and its changes and variation has been developed. Evaluation of the prototyped device fulfills the expected requirements in all aspects - by form factor, relatively simple construction and reasonable price of components. The future work involves further miniaturization of the present solution, careful tuning of the analog design and layout (to minimize noise and disturbances) and implementation of the multifrequency approach to get the impedance spectra simultaneously. While the simplest approach is to use a sum of two or more sinewaves for the excitation (and similar waveforms for the Discrete Fourier Analysis), interesting solution could be the usage of the chirp signals in both roles, as for excitation as well as for reference waveforms for Fourier analysis, as proposed in the patent description [15].

The proposed solution can be beneficially used in the wide range of bio-medical applications, like e.g. in bio-electrical impedance analysis (BIA), electrical impedance cardiography (ICG), electrical impedance tomography (EIT), electrical impedance spectroscopy (EIS), and magnetic induction tomography (MIT) [16].

ACKNOWLEDGMENT

Current work has been supported by grant EAG34 of Estonian Research Council, by Estonian Centre of Excellence in ICT Research EXCITE (TAR16013, EU Regional Development Fund) and Chist-ERA JEDAI (Mobilitas+ project *Mobera20*, EU Regional Development Fund) and finally by Estonian ICT program "IT Academy" (EU European Social Fund). The authors would like to thank also colleagues from TalTech impedance measurement group for their technical help.

REFERENCES

- [1] Y. Barsukov and J. Macdonald, *Impedance Spectroscopy: Theory, Experiment, and Applications*, 2nd Edn., 01 2005.
- [2] S. Grimmes and O. Martinsen, *Bioimpedance and Bioelectricity Basics*, 01 2008.
- [3] H. Sanier, S.E.J. Knobel, N. Shuetz, and T. Nef, "Contact-free signals as a new digital biomarker for cardiovascular disease: chances and challenges," *European Heart Journal – Digital Health*, vol. 1, no. 1, pp. 30–39, 2020.
- [4] W. Kubicek, R. Patterson, and D. Witsoe, "Impedance cardiography as a noninvasive method of monitoring cardiac function and other parameters of the cardiovascular system," *Annals of the New York Academy of Sciences*, vol. 170, pp. 724 – 732, 12 2006. First Published 1970.
- [5] D. Naranjo, J. Reina-Tosina, and M. Min, "Fundamentals, recent advances, and future challenges in bioimpedance devices for healthcare applications," *Journal of Sensors*, vol. 2019, pp. 1–42, 07 2019.
- [6] P. P. Tarjan and R. McFee, "Electrodeless measurements of the effective resistivity of the human torso and head by magnetic induction," *IEEE Transactions on Biomedical Engineering*, vol. BME-15, no. 4, pp. 266–278, 1968.
- [7] D. Teichmann, J. Foussier, and S. Leonhardt, "Respiration monitoring based on magnetic induction using a single coil," in *2010 Biomedical Circuits and Systems Conference (BioCAS)*, 2010, pp. 37–40.
- [8] J. García-Martín, J. Gómez-Gil, and E. Vázquez-Sánchez, "Non-destructive techniques based on eddy current testing," *Sensors*, vol. 11, no. 3, pp. 2525–2565, 2011.
- [9] *AD5933 1-MSPS, 12-Bit Impedance Converter, Network Analyzer: Datasheet*, Analog Devices, 2017, rev. F.
- [10] O. Martens, M. Min, R. Land, and P. Annus, "Multi-frequency and multi-channel bio-impedance measurement solution," in *Proceedings of the 7th Nordic Signal Processing Symposium - NORSIG 2006*, June 2006, pp. 178–181.
- [11] M. Rist, M. Reidla, M. Min, T. Parve, O. Martens, and R. Land, "Tms320f28069-based impedance spectroscopy with binary excitation," in *2012 5th European DSP Education and Research Conference (EDERC)*, Sep. 2012, pp. 217–220.
- [12] *Application Report: Optimizing L Measurement Resolution for the LDC161x and LDC1101*, Texas Instruments Inc, 2016, SNOA944.
- [13] *Technical Datasheet: Precision Impedance Analyzers*, Wayne Kerr Electronics, 2018, rev. E.
- [14] J. E. Volder, "The cordic trigonometric computing technique," *IRE Transactions on Electronic Computers*, vol. EC-8, no. 3, pp. 330–334, 1959.
- [15] O. Märtens, M. Min, R. Land, P. Annus, T. Saar, and M. Reidla, "Method and device for frequency response measurement," U.S. Patent 8,854,030, April, 20, 2010.
- [16] G. Singh, S. Anand, B. Lall, A. Srivastava, and V. Singh, "A technical review of various bioelectric impedance methods for health monitoring," in *2018 IEEE Long Island Systems, Applications and Technology Conference (LISAT)*, 2018, pp. 1–6.

Curriculum vitae

Personal data

Name: Eiko Priidel
Date of birth: April 16th, 1969
Place of birth: Tallinn, Estonia
Citizenship: Estonian

Contact data

E-mail: eiko.priidel@taltech.ee

Education

2015–2021 Tallinn University of Technology, Ph.D. student, Electronics and Telecommunication
2012–2014 Tallinn University of Technology, Electronics and Bionics, MSc
2010–2012 Tallinn University of Technology, Electronics and Bionics, BSc
2005–2011 Estonian Business School, IT-management, BSc

Language competence

Estonian Native
English Full professional proficiency
Finnish Professional working proficiency
Russian Professional working proficiency

Professional Employment

2010–... Teleplan Estonia Ltd., R&D Manager
2008–2010 IPTE Automation Ltd., R&D Manager
2004–2008 JOT Estonia Ltd., R&D Manager
2000–2004 Elektrobot Beijing Ltd., Vice General Manager/ Engineering Manager
1998–2000 JOT Automation Asia Pacific Ltd., Service Manager
1991–1998 JOT ESTONIA LTD., Engineer

Elulookirjeldus

Isikuandmed

Nimi: Eiko Priidel
Sünniaeg: 16.04.1969
Sünnikoht: Tallinn, Eesti
Kodakondsus: Eesti

Kontaktandmed

E-post: eiko.priidel@taltech.ee

Hariduskäik

2015–2021 Tallinna Tehnikaülikool, doktorant, elektroonika ja telekommunikatsioon
2012–2014 Tallinna Tehnikaülikool, elektroonika ja bioonika, magistratuur
2010–2012 Tallinna Tehnikaülikool, elektroonika ja bioonika, bakalaureus
2005–2011 Estonian Business School, IT-juhtimine, bakalaureus
1976–1987 Tallinna 44. Keskkool

Keelteoskus

Eesti keel emakeel
Inglise keel kõrgtase
Vene keel kesktase
Soome keel kesktase

Teenistuskäik

2010–... Teleplan Eesti OÜ, tootearendusjuht
2008–2010 IPTE Automation OÜ, tootearendusjuht
2004–2008 JOT Estonia Ltd., tootearendusjuht
2000–2004 Elektrobit Beijing Ltd., Vice General Manager/ Engineering Manager
1998–2000 JOT Automation Asia Pacific Ltd., Service Manager
1991–1998 OÜ JOT EESTI, insener

ISSN 2585-6901 (PDF)
ISBN 978-9949-83-890-5 (PDF)